



**Nanofabrication and characterisation of targeted drug  
delivery systems for liver cancer therapy**

**Sherif Hamdallah**

B.Sc. Pharmacy; M.Sc. Pharmaceutics

*Thesis submitted in fulfilment of the requirements for the degree of Doctor  
of Philosophy, University of East Anglia. Norwich, United Kingdom*

March 2023

©This copy of the thesis has been supplied on condition that anyone who consults it is understood to recognise that its copyright rests with the author and that use of any information derived therefrom must be in accordance with current UK Copyright Law. In addition, any quotation or extract must include full attribution.

## Abstract

Liver cancer (primarily hepatocellular carcinoma, HCC) is a leading cause of cancer-related mortality and morbidity worldwide, with a poor prognosis and limited treatment options. Sorafenib (Sf) is a multikinase inhibitor that is FDA-approved as the first line of treatment for advanced hepatocellular carcinoma (HCC). Despite its promising therapeutic outcomes, its low solubility, and oral bioavailability have limited its clinical application. Therefore, there is an urgent need for innovative and effective therapeutic strategies for liver cancer.

Nanotechnology-based drug delivery systems have emerged as promising platforms for the selective and controlled delivery of cytotoxic agents to cancer cells, minimising systemic toxicity and enhancing therapeutic efficacy. These nanocarriers can encapsulate, protect, and release drugs in a controlled manner and can be functionalised with ligands for targeted delivery to cancer cells. Among these, galactosylation of nanoparticles represents a potential strategy for liver-specific drug delivery.

The presented work herein involves the preparation, optimisation and characterisation of different galactosylated nanodrug delivery systems, including solid lipid nanoparticles (SLN), nanostructured lipid carriers (NLC), lipid nanocapsules (LNC), and polymeric micelles (PMs), for liver-targeted delivery of sorafenib to overcome its limited bioavailability and systemic side effects. The developed lipid-based delivery systems (SLN, NLC, and LNC) showed excellent colloidal properties with high drug entrapment efficiency (> 85%). Galactosylated LNC exhibited higher cytotoxicity and cellular uptake by HepG2 cells than untargeted LNC.

On the other hand, the developed Soluplus® based-polymeric micelles for oral administration have shown a tremendous enhancement of Sf solubility (>1100 times), translated into a 27-fold improvement in dissolution efficiency. Furthermore, these micelles exhibited an 8-fold increase in the cellular transport in the Caco-2 cell model compared to drug suspension. Lastly, galactosylated polymeric mixed micelles were formulated, exhibiting good colloidal properties and high Sf loading capacity (~15.5%). They demonstrated enhanced cellular cytotoxicity and receptor-mediated cellular uptake compared to untargeted counterparts.

## **Dedication**

I humbly give thanks and praise to our God for granting me the strength, resilience, and wisdom to overcome obstacles and achieve personal growth. I extend my sincere appreciation to my beloved parents (May they rest in peace), whose unwavering love and guidance have moulded me into the person I am today. Additionally, I acknowledge with deep gratitude all the individuals who have supported me along the way, embodying the virtues of kindness, compassion, and generosity. Finally, I pay tribute to my homeland, Egypt, which has provided me with a rich cultural heritage, invaluable life experiences and funded my PhD project.

## **Access Condition and Agreement**

Each deposit in UEA Digital Repository is protected by copyright and other intellectual property rights, and duplication or sale of all or part of any of the Data Collections is not permitted, except that material may be duplicated by you for your research use or for educational purposes in electronic or print form. You must obtain permission from the copyright holder, usually the author, for any other use. Exceptions only apply where a deposit may be explicitly provided under a stated licence, such as a Creative Commons licence or Open Government licence.

Electronic or print copies may not be offered, whether for sale or otherwise to anyone, unless explicitly stated under a Creative Commons or Open Government license. Unauthorised reproduction, editing or reformatting for resale purposes is explicitly prohibited (except where approved by the copyright holder themselves) and UEA reserves the right to take immediate 'take down' action on behalf of the copyright and/or rights holder if this Access condition of the UEA Digital Repository is breached. Any material in this database has been supplied on the understanding that it is copyright material and that no quotation from the material may be published without proper acknowledgement.

## **Acknowledgements**

I would like to express my sincere gratitude to my supervisors, Prof. Sheng Qi, and Prof. Maria O'Connell, for their continuous help, advice and invaluable support throughout my PhD. Also, I would like to thank Prof. Peter Belton and Dr. Christ Morris, for their generous help and consistent support during my PhD. Also, I would like to thank Mr. Bertrand Leze for his technical support during running some experiments in my PhD.

I would like to thank my colleague Dr. Randa Zoqlam for her valuable pieces of advice during the writing up of my thesis and for the fruitful collaboration during our PhD journey. Also, big thanks to my former and current PhD students Jehad, Fahad, Ibrahim and Ken, for always being there during my ups and downs. Special thanks to my friends in Norwich who became more than brothers within a short time Dr. Emad Shehata and ass. Prof. Amr El-Demerdash for their support and kindness.

To my supportive wife, Shahy, who was the best company during the whole journey till the end, giving all the support and encouragement to me. To my lovely son, Eyad, who gave me the meaning of unconditioned love and the motivation to do my best.

I would like to thank my dear brothers, Mohammed and Zeyad, I'm more than lucky to be gifted with such lovely and supportive brothers. Finally, I would like to extend my thanks to all my family members for their love and support.

# Table of Contents

<b>Abstract</b> .....	<b>ii</b>
<b>Dedication</b> .....	<b>iii</b>
<b>Acknowledgements</b> .....	<b>iv</b>
<b>Table of Contents</b> .....	<b>v</b>
<b>List of Figures</b> .....	<b>xiv</b>
<b>List of Tables</b> .....	<b>xxiii</b>
<b>List of abbreviations</b> .....	<b>xxvi</b>
<b>1. Chapter 1</b>	
<b>Introduction</b> .....	<b>1</b>
1.1. Hepatocellular carcinoma (HCC).....	2
1.1.1. Risk factors and epidemiology.....	2
1.1.2. Pathophysiology .....	5
1.1.3. Current HCC therapies .....	7
1.1.3.1. Ablation.....	9
1.1.3.2. Resection.....	9
1.1.3.3. Transplantation.....	9
1.1.3.4. Transarterial chemoembolisation (TACE).....	10
1.1.3.5. Systemic therapy .....	12
1.2. Nanomedicine in hepatocellular carcinoma (HCC) .....	14
1.3. ASGPR-mediated HCC targeting nanomedicines.....	20
1.4. Current state of sorafenib-loaded nanodelivery systems for HCC.....	24
1.5. Selected nanoparticles for sorafenib delivery .....	31
1.5.1. Solid lipid nanoparticles (SLN) and nanostructured lipid carriers (NLC) 31	
1.5.1.1. Composition of SLN and NLC.....	33
1.5.1.2. Preparation methods of SLN and NLC.....	34
1.5.1.3. Physicochemical properties of SLN and NLC .....	38
1.5.1.4. Nanotoxicology of lipid nanoparticles.....	42
1.5.1.5. Application of SLN and NLC for cancer therapy .....	43
1.5.2. Lipid nanocapsules (LNC).....	45
1.5.2.1. Composition of LNC .....	46
1.5.2.2. Preparation of LNC .....	46

1.5.2.3.	Phase inversion temperature (PIT) principle.....	48
1.5.2.4.	Applications of LNC for cancer therapy.....	49
1.5.3.	Polymeric micelles (PMs).....	52
1.5.3.1.	Preparation of polymeric micelles.....	53
1.5.3.2.	General properties of polymeric micelles.....	55
1.5.3.3.	Applications of polymeric micelles for cancer therapy .....	56
1.6.	Thesis objectives .....	58
<b>2.</b>	<b>Chapter 2</b>	
	<b>Materials and Methods .....</b>	<b>61</b>
2.1.	Introduction.....	62
2.2.	Materials .....	63
2.2.1.	Geleol™.....	63
2.2.2.	Precirol® ATO 5.....	63
2.2.3.	Compritol® 888 ATO .....	63
2.2.4.	Gelucires® .....	64
2.2.5.	Transcutol® P .....	64
2.2.6.	Solutol® HS 15.....	65
2.2.7.	Lipoid S 100.....	66
2.2.8.	Soluplus® .....	66
2.2.9.	D- $\alpha$ -tocopheryl polyethylene glycol succinate (TPGS) .....	68
2.2.10.	Tween 80 (Polysorbate 80).....	68
2.2.11.	Poloxamers (Pluronics).....	69
2.3.	Methods .....	70
2.3.1.	Nanoparticle preparation methods .....	70
2.3.1.1.	Preparation of SLN and NLC using emulsification/ultrasonication method	70
2.3.1.2.	Preparation of lipid nanocapsules (LNC) using the phase inversion temperature method:.....	71
2.3.1.3.	Preparation of polymeric micelles using the solvent evaporation method	71
2.3.2.	General physicochemical characterisation techniques .....	72
2.3.2.1.	Dynamic light scattering (DLS) .....	72
2.3.2.2.	Zeta potential ( $\zeta$ -potential).....	75

2.3.2.3.	Differential scanning calorimetry (DSC).....	76
2.3.2.4.	Thermogravimetric analysis (TGA) .....	78
2.3.2.5.	Powder X-Ray diffraction (PXRD) .....	78
2.3.2.6.	Attenuated total reflectance-Fourier transform infrared (ATR-FTIR) spectroscopy.....	79
2.3.2.7.	Proton nuclear magnetic resonance ( <sup>1</sup> H-NMR) .....	81
2.3.2.8.	Matrix-assisted laser desorption/ionization time-of-flight mass spectrometry (MALDI-TOF).....	82
2.3.2.9.	Critical micellar concentration (CMC) measurement .....	83
2.3.3.	Microscopy techniques .....	84
2.3.3.1.	Transmission electron microscopy (TEM) .....	84
2.3.3.2.	Scanning electron microscopy (SEM).....	85
2.3.3.3.	Inverted fluorescence microscopy (IFM).....	86
2.3.4.	<i>In-vitro</i> drug release .....	87
2.3.5.	<i>In-vitro</i> lectin agglutination assay .....	90
2.3.6.	<i>In-vitro</i> cellular studies.....	91
2.3.6.1.	MTS assay for cellular cytotoxicity assessment .....	91
2.3.6.2.	Flow cytometer.....	92
2.3.6.3.	Cellular transport studies .....	94
2.3.7.	Statistical analysis .....	96

### **3. Chapter 3**

#### **Preparation, optimisation, and in-vitro characterisation of galactosylated solid lipid nanoparticles and nanostructure lipid carrier for liver-targeted delivery of sorafenib..... 97**

3.1.	Introduction.....	98
3.2.	Materials and methods.....	100
3.2.1.	Materials .....	100
3.2.2.	Conjugation of stearylamine (SA) and lactobionic acid (LA) to form Gal-SA conjugate .....	100
3.2.3.	Characterisation of Gal-SA.....	101
3.2.4.	Sorafenib quantification using high-performance liquid chromatography (HPLC).....	101
3.2.5.	Determination of Sf solubility in different solid lipids and oils. ....	102
3.2.6.	Miscibility assessment of lipid ingredients.....	103

3.2.7. Preparation of SLN and NLC .....	103
3.2.8. Characterisation of SLN and NLC .....	104
3.2.9. Drug loading quantification .....	104
3.2.10. Solid state characterisation .....	105
3.2.10.1. Attenuated total reflection-Fourier transform infrared (ATR-FTIR) 105	
3.2.10.2. Differential scanning calorimetry (DSC).....	105
3.2.10.3. Powder X-Ray Diffraction (PXRD) .....	105
3.2.11. Solid redispersibility test .....	105
3.2.12. <i>In-vitro</i> drug release studies.....	106
3.2.13. <i>In-vitro</i> cellular cytotoxicity studies.....	107
3.3. Results and discussion .....	108
3.3.1. Synthesis and characterisation of Gal-SA .....	108
3.3.2. Sf quantification using HPLC method .....	111
3.3.3. Sf solubility in different lipid matrices.....	112
3.3.4. Preliminary screening of the type of solid lipids and surfactants for preparation of SLN .....	114
3.3.5. Miscibility assessment of lipid ingredients.....	116
3.3.6. Preparation and characterisation of Gal-Sf-SLN and Gal-Sf-NLC.....	118
3.3.7. Morphology of lipid nanoparticles using electron microscopy .....	121
3.3.8. Solid state characterisation .....	122
3.3.8.1. Attenuated total reflection-Fourier transform infrared (ATR-FTIR) 122	
3.3.8.2. Differential scanning calorimetry (DSC).....	123
3.3.8.3. Powder X-Ray Diffraction (PXRD) .....	125
3.3.9. Redispersibility of freeze-dried optimised lipid nanoparticles .....	126
3.3.10. <i>In-vitro</i> drug release studies.....	127
3.3.11. <i>In-vitro</i> cytotoxicity.....	132
3.4. Conclusion .....	135

#### **4. Chapter 4**

#### **Preparation and in-vitro appraisal of galactosylated Sorafenib-loaded lipid nanocapsules with lipiodol oil core as a liver-targeted theranostic agent..... 136**

4.1. Introduction.....	137
------------------------	-----

4.2. Materials and methods.....	139
4.2.1. Materials .....	139
4.2.2. Preparation of Sf-loaded lipid nanocapsules (Sf-LNC).....	139
4.2.3. Characterisation of lipid nanocapsules (LNC).....	140
4.2.4. Synthesis of galactosylated TPGS (Gal-TPGS).....	140
4.2.5. Characterisation of Gal-TPGS .....	141
4.2.6. Post-insertion of Gal-TPGS into Sf-LNC.....	142
4.2.7. Galactose surface accessibility (lectin-induced agglutination assay).....	142
4.2.8. Short-term shelf physical stability of Sf-LNC and Gal-Sf-LNC .....	143
4.2.9. Colloidal stability of Sf-LNC and Gal-LNC in physiological blood condition.....	143
4.2.10. <i>In-vitro</i> drug release study .....	143
4.2.11. <i>In-vitro</i> cellular study .....	144
4.2.11.1. Cellular cytotoxicity on HepG2 cells .....	144
4.2.11.2. Cellular uptake study using an inverted Fluorescence microscope.	144
4.2.11.3. Cellular uptake study using flow cytometer .....	145
4.3. Results and discussion .....	146
4.3.1. Preparation and characterisation of Sf-loaded Lipid nanocapsules (LNC) 146	
4.3.2. Characterisation of Gal-TPGS .....	148
4.3.2.1. ATR-FTIR.....	148
4.3.2.2. <sup>1</sup> H-NMR.....	149
4.3.2.3. MALDI-TOF.....	151
4.3.2.4. TGA .....	152
4.3.3. Conjugation efficiency of Gal-TPGS .....	153
4.3.4. Post-insertion of Gal-TPGS into LNC and Sf-LNC.....	154
4.3.5. Galactose surface accessibility (lectin-induced agglutination assay).....	157
4.3.6. Short-term shelf physical stability of Sf-LNC and Gal-Sf-LNC .....	158
4.3.7. Colloidal stability of Sf-LNC and Gal-Sf-LNC in physiological blood conditions .....	159
4.3.8. <i>In-vitro</i> drug release study .....	160
4.3.9. <i>In-vitro</i> cellular studies.....	162
4.3.9.1. Cellular cytotoxicity .....	162

4.3.9.2. Cellular uptake assessment by fluorescence microscope .....	164
4.3.9.3. Cellular uptake study using a flow cytometer.....	166
4.4. Conclusion .....	167

## 5. Chapter 5

### **Soluplus® and Soluplus®/TPGS mixed micelles for oral administration of Sorafenib ..... 168**

5.1. Introduction.....	169
5.2. Materials and methods.....	171
5.2.1. Materials .....	171
5.2.2. Preparation of sorafenib loaded Soluplus® micelles (Sf-SM) and Soluplus®/ TPGS mixed micelles (MM).....	171
5.2.3. Characterisation and optimisation of Sf-SM and Sf-MM .....	172
5.2.4. Drug loading (DL%) and encapsulation efficiency (EE%) .....	172
5.2.5. Critical micelles concentration determination .....	172
5.2.6. Morphology of micelles using transmission electron microscopy (TEM)	173
5.2.7. Short-term storage physical stability .....	173
5.2.8. Solid state characterisation .....	173
5.2.8.1. Attenuated total reflection-Fourier transform infrared (ATR-FTIR)	174
5.2.8.2. Differential scanning calorimetry (DSC).....	174
5.2.8.3. Powder X-Ray Diffraction (PXRD) .....	174
5.2.9. Physical stability in simulated gastric fluid (SGF) and simulated intestinal fluid (SIF).....	174
5.2.10. <i>In-vitro</i> drug release study .....	175
5.2.11. <i>In-vitro</i> cellular studies on Caco-2 .....	175
5.2.11.1. Cell viability studies .....	175
5.2.11.2. Cellular transport studies .....	176
5.3. Results and discussion .....	177
5.3.1. Preparation and characterisation of Sf-SM and Sf-MM.....	177
5.3.2. Critical micelles concentration determination .....	180
5.3.3. Morphology of micelles using transmission electron microscopy (TEM)	182

5.3.4. Short-term physical stability of Sf-SM and Sf-MM.....	183
5.3.5. Solid state characterisation .....	183
5.3.5.1. Attenuated total reflection-Fourier transform infrared (ATR-FTIR)	183
5.3.5.2. Differential scanning calorimetry (DSC).....	184
5.3.5.3. Powder X-Ray Diffraction (PXRD) .....	185
5.3.6. Physical stability in simulated gastric fluid (SGF) and simulated intestinal fluid (SIF).....	186
5.3.7. <i>In-vitro</i> drug release study .....	188
5.3.8. <i>In-vitro</i> cellular studies on Caco-2 cells .....	191
5.3.8.1. Cellular viability study.....	191
5.3.8.2. Cellular transport study.....	193
5.4. Conclusion .....	195

## **6. Chapter 6**

### **Preparation and characterisation of galactosylated TPGS/Soluplus® mixed micelles for liver-targeted delivery of Sorafenib..... 197**

6.1. Introduction.....	198
6.2. Materials and methods.....	200
6.2.1. Materials .....	200
6.2.2. Synthesis of Gal-TPGS.....	200
6.2.3. Characterisation and determination of conjugation efficiency of Gal-TPGS	200
6.2.4. Preparation of galactosylated Sf-loaded TPGS/Soluplus® mixed micelles (Gal-Sf-MM) .....	201
6.2.5. Particle size and Zeta potential .....	201
6.2.6. Encapsulation efficiency (EE%) and loading capacity (LC%).....	201
6.2.7. Short-term storage physical stability .....	201
6.2.8. Micellar colloidal stability under administration and physiological blood condition.....	201
6.2.9. Micelles morphology using transmission electron microscopy (TEM) ..	202
6.2.10. Critical micellar concentration (CMC) measurement .....	202
6.2.11. Solid state characterisation .....	202

6.2.11.1.	Attenuated total reflection-Fourier transform infrared (ATR-FTIR)	202
6.2.11.2.	Differential scanning calorimetry (DSC).....	202
6.2.11.3.	Powder X-Ray Diffraction (PXRD) .....	202
6.2.12.	Drug release study .....	203
6.2.13.	Surface accessibility (lectin-induced agglutination assay) .....	203
6.2.14.	<i>In-vitro</i> cellular studies .....	203
6.2.14.1.	<i>In-vitro</i> Cellular cytotoxicity.....	203
6.2.14.2.	Cellular uptake using an inverted fluorescence microscope .....	203
6.2.14.3.	Cellular uptake study using flow cytometer .....	204
6.3.	Results and discussion .....	204
6.3.1.	Synthesis and characterisation of Gal-TPGS.....	204
6.3.2.	Preparation and characterisation of Sf-MM and Gal-Sf-MM.....	204
6.3.3.	Morphology using transmission electron microscopy (TEM).....	206
6.3.4.	Short-term stability of Sf-MM and Gal-Sf-MM .....	207
6.3.5.	Colloidal stability in administration and physiological conditions.....	208
6.3.6.	Solid-state characterisation .....	210
6.3.6.1.	Attenuated total reflection-Fourier transform infrared (ATR-FTIR)	210
6.3.6.2.	Differential scanning calorimetry (DSC).....	211
6.3.6.3.	Powder X-ray diffraction (PXRD) .....	212
6.3.7.	Critical micellar concentration (CMC) measurement .....	213
6.3.8.	<i>In-vitro</i> dissolution in PBS at pH 7.4 .....	214
6.3.9.	Surface accessibility (lectin-induced agglutination) .....	216
6.3.10.	<i>In-vitro</i> cellular studies.....	217
6.3.10.1.	<i>In-vitro</i> cellular cytotoxicity .....	217
6.3.10.2.	Cellular uptake using an inverted fluorescence microscope .....	219
6.3.10.3.	Cellular uptake study using flow cytometer .....	221
6.4.	Conclusion .....	222

## 7. Chapter 7

### **Conclusion and future outlook .....** 224

#### 7.1. General conclusions..... 225

##### 7.1.1. Impact of formulation parameters on the properties of SLN and NLC... 225

7.1.2. Formulation of Gal-Sf-LNC using lipiodol® oil core.....	226
7.1.3. Development of single and mixed polymeric micelles to oral delivery of Sf 226	
7.1.4. Preparation of Galactosylated mixed micelles for liver-targeted delivery of Sf (Gal-Sf-MM).....	227
7.2. Future outlook.....	228
7.2.1. <i>In-vitro</i> cell cellular cytotoxicity studies for SLN and NLC .....	228
7.2.2. Further <i>in-vitro</i> cellular studies.....	228
7.2.3. <i>In-vitro</i> and <i>In-vivo</i> assessment of the contrasting potency of Gal-Sf-LNC containing lipiodol® oil core .....	229
7.2.4. Ex-vivo intestinal permeation study of oral polymeric single and mixed micelles (Sf-SM and Sf-MM).....	229
7.2.5. <i>In-vivo</i> animal studies.....	229
<b>References .....</b>	<b>230</b>

## List of Figures

Figure 1.1: The incidence and major aetiological factors of HCC worldwide. Figure was reprinted from GLOBOCAN 2018 <sup>27</sup> with data added from references <sup>3,9</sup> .....	5
Figure 1.2: The different proposed mechanisms of hepatocarcinogenesis. Figure was adapted with permission from reference <sup>28</sup> .....	6
Figure 1.3: HCC treatment strategy according to Barcelona Clinic Liver Cancer (BCLC) staging. Figure was adapted with permission from reference <sup>23</sup> .....	8
Figure 1.4: The Principle of trans-arterial chemoembolisation (TACE). Figure was adapted with permission from reference <sup>42</sup> .....	10
Figure 1.5: Molecular targets of Sorafenib as a multikinase inhibitor for treating unresectable advanced-stage HCC. Figure was adapted with permission from reference <sup>72</sup> .....	14
Figure 1.6: Schematic diagram of targeting strategies of nanomedicines for HCC therapy. Figure was adapted with permission from reference <sup>97</sup> .....	18
Figure 1.7: Summary of target biomarkers overexpressed on hepatoma cells and their ligands for active targeted therapy of HCC. Figure was adapted with permission from reference <sup>97</sup> .....	19
Figure 1.8: Schematic representation of ASGPR, demonstrating the hetero-oligomer composed of two H1 and H2 subunits. Figure was adapted with permission from reference <sup>108</sup> .....	20
Figure 1.9: Chemical structure of some saccharides and polysaccharides for ASGPR targeting. Figure was adapted with permission from reference <sup>97</sup> .....	22
Figure 1.10: Chemical structure of Sorafenib .....	24
Figure 1.11: Sorafenib-related side effects compared to placebo in the SHARP trial. Patients received oral Sf 400 mg twice daily (n=297) or placebo (n=302). Figure was adapted with permission from reference <sup>130</sup> . p = 0.04, ** p =0.007, *** p <0.001 .....	25

Figure 1.12: Structural differences of SLN and different types of NLC. ....	32
Figure 1.13: Schematic representation of different preparation methods of SLN and NLC. Figure was adapted with permission from reference <sup>157</sup> .....	35
Figure 1.14: Different drug incorporation models in SLN.....	40
Figure 1.15: Schematic representation of the typical composition of LNC.....	45
Figure 1.16: Schematic representation of the formation of lipid nanocapsules (LNC) by the PIT method. Figure was modified with permission from reference <sup>204</sup> . ....	47
Figure 1.17: Schematic representation of the self-assembly process of polymeric micelles above CMC.....	53
Figure 1.18: Method selection for the preparation of polymeric micelles.....	55
Figure 2.1: Transcutol® chemical structure.....	65
Figure 2.2: Chemical structure of Solutol® HS 15. ....	66
Figure 2.3: Typical chemical structure of phosphatidylcholine phospholipid (PC).....	66
Figure 2.4: Chemical structure of Soluplus®. Figure was adapted with permission from reference <sup>259</sup> . ....	67
Figure 2.5: Chemical structure of TPGS. Figure was adapted with permission from reference <sup>293</sup> . ....	68
Figure 2.6: Chemical structure of Tween 80. Figure was adapted with permission from reference <sup>307</sup> . ....	69
Figure 2.7: General chemical structure of Poloxamers.....	70
Figure 2.8: The working principle of dynamic light scattering for measuring particle size of nanoparticles.....	73
Figure 2.9: Number, volume, and intensity size distributions of a bimodal mixture of 10 and 100 nm nanoparticles present in equal numbers. ....	74

Figure 2.10: Typical DSC thermogram showing peaks associated with different thermal kinetic events.....	76
Figure 2.11: Schematic design of heat flux DSC.....	77
Figure 2.12: Schematic presentation of the working principle of XRD instrument (a) and X-ray diffraction through the crystalline lattice (b).....	79
Figure 2.13: Schematic of ATR-FTIR working principle.....	80
Figure 2.14: The effect of micellisation of surfactants/polymers on the different physical properties.....	83
Figure 2.15: Schematic of the operation principle of transmission (TEM) and scanning (SEM) electron microscopes.....	85
Figure 2.16: Schematic of the inverted fluorescence microscope. Figure was adapted with permission from reference <sup>334</sup> .....	87
Figure 2.17: Enzymatic reduction of MTS into formazan dye by metabolically active cells. Figure was adapted with permission from reference <sup>354</sup> .....	92
Figure 2.18: HepG2 gating strategy used in this study. SSC is a side scattered channel, FSC is a forward scattered channel and FITC-A is a Fluorescein isothiocyanate channel for coumarin-6 detection.....	93
Figure 2.19: Schematic representation of the cellular transport study design for assessment of Sf permeation through Caco-2 cells monolayer.....	94
Figure 3.1: Schematic representation of the workflow for the preparation and characterisation of Gal-Sf-SLN and Gal-Sf-NLC.....	99
Figure 3.2: Synthesis of Gal-SA conjugate.....	101
Figure 3.3: Solidified lipid in vial after centrifugation at 10,000 rpm for 10 min in falcon tube containing hot water at 80°C to allow slow solidification during centrifugation.....	102

Figure 3.4: FTIR absorbance spectra of SA, LA, and Gal-SA.....	108
Figure 3.5: <sup>1</sup> H-NMR spectra of (a) SA, and (b) Gal-SA recorded in CDCl <sub>3</sub> .....	109
Figure 3.6: Galactose standard solutions after adding 1 ml of 5% phenol and 5 ml of sulphuric acid and incubation at 25°C for 20 mins.....	110
Figure 3.7: UV/Vis spectrum of standard galactose solution at a concentration of 100 µg/mL (a) and the calibration curve of galactose standard solutions (at concentrations from 20-200 µg/mL) using phenol/sulfuric acid colourimetric assay (b).....	110
Figure 3.8: HPLC chromatograms (a) and calibration curve (b) of Sf standard solutions, UV absorbance was measured at a wavelength of 265 nm within a linearity range between 0.2-50 µg/mL. ....	111
Figure 3.9: DSC thermograms of Precirol® ATO 5 with different Gelucire® 48/16 percentages (w/w) after heating for 1 h at 80° C followed by cooling at room temperature (~ 25°C) for 24 h (a), the effect of Gelucire® 48/16 on the peak onset and melting point of Precirol® ATO 5 (b). ....	117
Figure 3.10: DSC thermograms of Precirol® ATO 5 with different Transcutol® P percentages (w/w) after heating for 1 h at 80° C followed by cooling at room temperature (~ 25°C) for 24 h (a), the effect of Transcutol® P percentages on the peak onset and melting point of Precirol® ATO 5 (b), and the filter paper of paper smear method for detection of phase separation (c). ....	118
Figure 3.11: TEM images of blank Gal-SLN (a), Gal-Sf-SLN (b), blank Gal-NLC (c), and Gal-Sf-NLC (d). ....	121
Figure 3.12: SEM images of blank Gal-SLN (a), Gal-Sf-SLN (b), blank Gal-NLC (c), and Gal-Sf-NLC (d). ....	122
Figure 3.13: FTIR absorbance spectra of Gal-Sf-SLN (a), and Gal-Sf-NLC (b) with their raw materials and physical mixtures. ....	123
Figure 3.14: DSC thermograms of Gal-Sf-SLN (a), and Gal-Sf-NLC (b) with their raw materials and physical mixtures. ....	124

Figure 3.15: PXRD patterns of Gal-Sf-SLN (a), and Gal-Sf-NLC (b) with their raw materials and physical mixtures. ....	125
Figure 3.16: The influence of the addition of 5% trehalose on the particle size of the freeze-dried optimised lipid nanoparticles after redispersion in MilliQ water. ....	126
Figure 3.17: Sorafenib release profiles from different solvents employing dialysis bag method using 1% Tween 80 in PBS at pH 7.4 as release medium and kept under shaking at 100 rpm at 37° C. ....	129
Figure 3.18: Sorafenib diffusion scenarios from different solvents through the dialysis membrane. ....	129
Figure 3.19: <i>In-vitro</i> Sorafenib release profiles from Gal-Sf-SLN and Gal-Sf-NLC using 1% Tween 80 in PBS at pH 7.4 as release medium and kept under shaking at 100 rpm at 37° C. ....	130
Figure 3.20: Cell viability plot of HepG 2 cells after incubation for 48 h at 37°C with free Sf solution, blank and Sf-loaded SLN and NLC, and their galactosylated counterparts (both blank formulations were diluted similarly to the Sf-loaded counterparts). ....	132
Figure 3.21: Cytotoxicity profiles of (a) blank Precirol® ATO 5-based SLN using different surfactants, (b) free surfactant solutions, and (c) blank Compritol® 888 ATO-based SLN using different surfactants after incubation with HepG2 cells for 48 h. ....	134
Figure 4.1: Schematic abstract for the preparation of galactosylated Sf-loaded lipid nanocapsules (Gal-Sf-LNC).....	138
Figure 4.2: The chemical scheme of the synthesis of Gal-TPGS.....	141
Figure 4.3: FTIR spectra of TPGS, LA, and Gal-TPGS.....	149
Figure 4.4: <sup>1</sup> H-NMR spectra of Gal-TPGS (a) and TPGS (b) dissolved in DMSO-d <sub>6</sub> . ....	150
Figure 4.5: MALDI-TOF mass spectra of LA (a) and TPGS (b), and Gal-TPGS (c). .	151

Figure 4.6: TGA curves of TPGS and Gal-TPGS (heating from 25°C to 500° C at a heating rate of 20°C/min) .....	152
Figure 4.7: FTIR spectra of DSPE-PEG2000-NH <sub>2</sub> , LA, and DSPE-PEG2000-Gal....	154
Figure 4.8: Schematic representation of the different spatial conformation of PEG arms at the surface of lipid nanocapsules. ....	156
Figure 4.9: TEM images of Sf-LNC (a and b) and Gal-Sf-LNC (c and d).....	157
Figure 4.10: RCA120-induced agglutination of Sf-LNC and Gal-Sf-LNC. 100 µL of LNC dispersions were incubated with 100 µL of RCA120 (1 mg/mL) for 20 min with continuous absorbance measurement at 450 nm at 2 min intervals. The reversibility of agglutination was verified by adding free D-galactose (10 mg/mL) at the 20 <sup>th</sup> min. ....	158
Figure 4.11: The effect of short-term storage of Sf-LNC and Gal-Sf-LNC at 4° C for one month on particle size (a), size distribution PDI (b), and EE% (C). ....	159
Figure 4.12: DLS reports of 5.4% BSA in PBS at pH 7.4 (a), Sf-LNC in 5.4% BSA in PBS at pH 7.4 (b), and Gal-Sf-LNC in 5.4% BSA in PBS at pH 7.4 (c) after incubation for 72 h at 37° C.....	160
Figure 4.13: <i>In-vitro</i> Sf release profiles from Sf solution, Sf-LNC and Gal-Sf-LNC into PBS at pH 7.4 containing 1% tween 80 under shaking at 100 rpm for 5 days. ....	161
Figure 4.14: Cell viability plot of HepG2 cells after incubation for 48 h at 37° C with free Sf solution, Sf-LNC, Gal-Sf-LNC and Gal-Sf-LNC in the presence of free galactose (10 mg/mL). ....	162
Figure 4.15: Cytotoxicity profiles of blank Labrafac® WL 1349 LNC (standard LNC) and lipiodol oil LNC (the blank LNC were diluted in the same manner as Sf-loaded LNC). ....	164
Figure 4.16: Fluorescence microscope images using 40X objective lens of HepG2 cells after incubation for 4 h with different C6-loaded LNC at 37° C.....	165

Figure 4.17: Histogram overlay (a) and GeoMean fluorescence intensities (b) of HepG2 cells after incubation for 4 h at 37°C with different LNC formulations containing C6 at a concentration of 0.2 µg/mL. ** (P < 0.01), ***(P < 0.001), and ns (P > 0.05). Error bars represent the standard deviation and n=3. ....	166
Figure 5.1: DLS reports of particle size and Zeta potential of Sf-SM (a and b), and Sf-MM (c and d).....	178
Figure 5.2: Sf apparent solubility (Sa) in single and mixed micelles comprised of Soluplus® and/or TPGS in MilliQ water at 25°C. (n = 3) .....	179
Figure 5.3: The measurement of CMC of Soluplus® single micelles (a) and Soluplus®/TPGS mixed micelles at different ratios 45:5 (b), 40:10 (c), and 30:20 (d) using the iodine UV-Vis spectroscopy method. ....	181
Figure 5.4: TEM images of Sf-SM (a and b) and Sf-MM (c and d) at different scales	182
Figure 5.5: Short-term physical stability, of (a)P.S., (b)PDI and (c) EE%, for Sf-SM and Sf-MM at 4°C for 14 days .....	183
Figure 5.6: FTIR absorbance spectra of Sf-SM (a) and Sf-MM (b) with their raw materials, physical mixtures, and blank micelles .....	184
Figure 5.7: DSC thermogram of Sf-SM (a) and Sf-MM (b) with their raw materials, physical mixtures, and blank micelles .....	185
Figure 5.8:PXRD patterns of Sf-SM (a) and Sf-MM (b) with their raw materials, physical mixtures, and blank micelles .....	186
Figure 5.9: Cumulative Sf release from Sf-suspension, Sf-SM and Sf-MM in SGF over 2 h at 37° C under shaking at 100 rpm using the dialysis bag method. ....	189
Figure 5.10: Cumulative Sf release from Sf-suspension, Sf-SM and Sf-MM in SIF over 72 h at 37° C under shaking at 100 rpm using the dialysis bag method. ....	190
Figure 5.11: Dissolution efficiency (DE%) values of Sf-suspension, Sf-SM and Sf-MM. *P < 0.05, **P < 0.01, ***P < 0.001, and ns = not significant (P > 0.05).....	190

Figure 5.12: Cytotoxicity of Blank SM and MM on Caco-2 cells after incubation for 6 h .....	192
Figure 5.13: Cytotoxicity of Blank SM and MM on Caco-2 cells after incubation for 24 h .....	192
Figure 5.14: Cytotoxicity of Blank SM and MM on Caco-2 cells after incubation for 48 h .....	193
Figure 5.15: Time-dependent Caco-2 cell influx (AP-BL) of Sf from Sf-suspension, Sf- SM, and Sf-MM over 4 h .....	194
Figure 5.16: Time-dependent Caco-2 cell efflux (BL-AP) of sf from Sf-suspension, Sf- SM, and Sf-MM over 4 h .....	195
Figure 6.1: DLS reports of the particle size of Blank Gal-MM (a) Gal-Sf-MM (b). ...	206
Figure 6.2: DLS reports of the Zeta Potential of Blank Gal-MM (a) and Gal-Sf-MM (b). .....	206
Figure 6.3: TEM images of (a) blank MM, (b) Sf-MM, (c) blank Gal-MM, and (d) Gal- Sf-MM.....	207
Figure 6.4: The effect of short-term storage of Sf-MM and Gal-Sf-MM at 4°C for 14 days on particle size (a), polydispersity index, PDI (b), and EE% (C).....	208
Figure 6.5: DLS reports of 5.4%BSA in PBS at 7.4 (a), Sf-MM in 5.4% BSA in PBS at 7.4 (b), and Gal-Sf-MM in 5.4% BSA in PBS at 7.4 (c) after incubation for 72 h at 37° C.....	210
Figure 6.6.6: FTIR spectra of Soluplus®, Gal-TPGS, Sf, Physical mix, Blank-Gal-MM, and Gal-Sf-MM. ....	211
Figure 6.7: Thermograms of Sf, Soluplus, Gal-TPGS, Physical mix, Blank-Gal-MM and Gal-Sf-MM.....	212
Figure 6.8: PXRD patterns of Soluplus, Gal-TPGS, Sf, physical mixture, Blank and Gal-Sf loaded MM. ....	213

Figure 6.9: Determination of critical micelle concentration (CMC) of MM (A) and Gal-MM(B) using iodine UV-Vis spectroscopy method.....	214
Figure 6.10: <i>In-vitro</i> sorafenib release profiles of Sf solution, Sf-MM, and Gal-Sf-MM in PBS at pH 7.4 containing 1% tween 80 at 37° C under shaking at 100 rpm for 5 days. ....	215
Figure 6.11: RCA <sub>120</sub> induced agglutination of Sf-MM and Gal-Sf-MM when 100 µL of micellar dispersion (10 mg/mL) was incubated with 100 µL of RCA120 (1 mg/mL) for 20 min with continuous measurement of the absorbance at 450 nm at 2 min intervals. The reversibility of agglutination was verified by adding free D-galactose (10 mg/mL) at the 20 <sup>th</sup> min. ....	217
Figure 6.12: Cell viability plot of HepG2 cells after incubation for 48 h at 37° C with free Sf solution, Blank MM, blank Gal-MM, Sf-MM, Gal-Sf-MM and Gal-Sf-MM in the presence of free galactose (10 mg/mL). (both blank formulations were diluted similarly to the Sf-loaded counterparts).....	218
Figure 6.13: Fluorescence microscope images using 10X objective lens of HepG2 cells after incubation for 4 h with different C6-loaded mixed micelles at 37°C.....	220
Figure 6.14: Fluorescence microscope images using 40X objective lens of HepG2 cells after incubation for 4 h with different C6-loaded mixed micelles at 37° C.....	220
Figure 6.15: Histogram of the green fluorescent events using Fluorescein isothiocyanate channel (FITC-A) detecting cells that have uptaken C6-loaded micelles (a), and GeoMean fluorescence intensities of HepG2 cells after incubation for 4 h at 37° C with different C6-loaded micelles formulations at a concentration of 0.5 µg/mL (b). ** (P < 0.01), and ns (P > 0.05). Error bars represent the standard deviation and n=3. ....	222

## List of Tables

Table 1.1: Examples of commercially available nanomedicines for cancer therapy.....	16
Table 1.2: Representative examples of different Sf-loaded nanodelivery systems for HCC. ....	27
Table 1.3: The most commonly used SLN and NLC components <sup>149,151-154,156</sup> .....	34
Table 1.4: Factors affecting the formulation and stability of LNC produced using the phase-inversion temperature (PIT) process.....	46
Table 2.1: Physicochemical properties of Soluplus®.....	67
Table 2.2: Properties of Poloxamers 188 and 127.....	70
Table 2.3: The equations of different mathematical models of drug release. ....	89
Table 3.1: Sf solubility in different solid lipid ingredients. ....	112
Table 3.2: Sf solubility in different liquid lipids and liquid solubilisers. ....	113
Table 3.3: Particle size (P.S.), Polydispersity index (PDI), Zeta potential (Z.P.), Entrapment efficiency (EE%), and Loading capacity (LC%) of Geleol <sup>TM</sup> -based SLN using different surfactant at lipid to surfactant ratio of 5:1.....	114
Table 3.4: The effect of surfactant type and concentration on the particle size (P.S.), Polydispersity index (PDI), Zeta potential (Z.P.), Entrapment efficiency (EE%), and Loading capacity (LC%) of 5% Precirol® ATO 5-based SLN.....	115
Table 3.5: The composition of different screened lipid nanoparticles formulations....	119
Table 3.6: The effect of lipid composition on the particle size (P.S.), Polydispersity index (PDI), Zeta potential (Z.P.), Entrapment efficiency (EE%), and Loading capacity (LC%) of the formulated lipid nanoparticles. ....	119

Table 3.7: Particle size (P.S.), Polydispersity index (PDI), Zeta potential (Z.P.), Entrapment efficiency (EE%), and Loading capacity (LC%) of the optimised galactosylated SLN and NLC formulations. ....	121
Table 3.8: Redispersibility index of optimised lipid nanoparticles after freeze-drying and redispersion with and without using 5% trehalose as cryoprotectant. ....	127
Table 3.9: Sorafenib solubilities in different proposed release media at 37°C. ....	127
Table 3.10: Difference factors ( $f_1$ ) and Similarity factors ( $f_2$ ) of the release profiles of Sf solution, Gal-Sf-SLN, and Gal-Sf-NLC. ....	131
Table 3.11: <i>In-vitro</i> drug release kinetic models of Sf solution, Gal-Sf-SLN and Gal-Sf-NLC.....	131
Table 4.1: Different oil compositions of LNC. ....	140
Table 4.2: The effect of variable oil composition on P.S., PDI, ZP and drug load of Sf-LNC.....	147
Table 4.3: The effect of lipiodol oil: Solutol® HS ratio on P.S., PDI, ZP and drug load of Sf-LNC.....	148
Table 4.4: The effect of post-insertion of Gal-TPGS into LNC on P.S., PDI, ZP and EE% of Sf-LNC.....	156
Table 4.5: Mean dissolution time (MDT) of Sf solution, Sf-LNC, and Gal-Sf-LNC. .	161
Table 4.6: Difference ( $f_1$ ) and similarity factors ( $f_2$ ) of Sf release profiles from Sf solution, Sf-LNC and Gal-Sf-LNC.....	161
Table 4.7: IC <sub>50</sub> values of Sf solution, Sf-LNC, Gal-Sf-LNC, and Gal-Sf-LNC in the presence of free galactose on HepG2 cells after incubation for 48 h. ....	163
Table 5.1: Particle size analysis and drug loading of Sf-loaded micelles with different compositions.....	178

Table 5.2: Sf apparent solubility ( $S_a$ ) and solubility factors ( $f_s$ ) for single and mixed micellar dispersions in MilliQ water at 25° C. (n = 3).....	179
Table 5.3: Theoretical and Experimental critical micellar concentration of micelles with different Soluplus®: TPGS ratios.....	181
Table 5.4: The colloidal stability of Sf-SM in SGF over 2 h and SIF for 6 h at 37° C.	187
Table 5.5: The colloidal stability of Sf-MM in SGF over 2 h and SIF for 6 h at 37° C. .....	188
Table 5.6: <i>In-vitro</i> drug release kinetic models of Sf-suspension, Sf-SM and Sf-MM	191
Table 5.7: Apparent Permeability values and Efflux ratio of Sf suspension, Sf-SM and Sf-MM (n=3). .....	194
Table 6.1: Particle size, polydispersity index (PDI) and Zeta potential of blank and Sf loaded MM and Gal-MM. ....	205
Table 6.2: Particle size (PS), polydispersity index (PDI), and zeta potential (ZP) of Sf-MM and Gal-Sf-MM before and after incubation in 0.9% NaCl at 25°C for 30 min (n=3).....	209
Table 6.3: Particle size (PS), polydispersity index (PDI), and zeta potential (ZP) of Sf-MM and Gal-Sf-MM before and after incubation in 5% dextrose at 25°C for 30 min (n=3).....	209
Table 6.4: Difference factors ( $f_1$ ) and Similarity factors ( $f_2$ ) of the release profiles of Sf solution, Sf-MM, and Gal-Sf-MM.....	216
Table 6.5: <i>In-vitro</i> drug release kinetic models of Sf solution, Sf-MM and Gal-Sf-MM. .....	216
Table 6.6: IC <sub>50</sub> values of different Sf formulations after incubation with HepG2 cells for 48 h.....	218

## List of abbreviations

$\mu$ -CT	Micro-computed tomography
$^1\text{H-NMR}$	Proton nuclear magnetic resonance
5-FU	5-fluorouracil
AF	Asialofeutin
AFB1	Aflatoxin B1
ASGPRs	Asialoglycoprotein receptors
ASOR	Asialoorosomuroid
AT-FTIR	Attenuated total reflectance Fourier transforms infrared spectroscopy
BCLC	Barcelona Clinic Liver Cancer
BCS	Biopharmaceutical classification system
BSA	Bovine serum albumin
C6	Coumarin 6
CD 44	Cluster of differentiation 44
CDCL <sub>3</sub>	Deuterated chloroform
CDI	Carbonyldiimidazole
CMC	Critical micelle concentration
C <sub>p</sub>	Heat capacity
CRDs	Carbohydrate recognition domains
DDS	Drug delivery system
DE%	Dissolution efficiency
DEBs	Drug eluting beads
DHAA	Dehydroascorbic acid
DLS	Dynamic light scattering
DMF	Dimethyl formamide
DMSO	Dimethyl sulfoxide
DMSO-d <sub>6</sub>	Deuterated dimethyl sulfoxide
DOPE	Dioleoyl phosphatidylethanolamine
DSC	Differential scanning calorimetry
DSPE	1,2-Distearoyl-sn-glycero-3-phosphorylethanolamine
EDA	Ethylenediamine

EDC	1-Ethyl-3- (3-dimethylaminopropyl) carbodiimide
EE%	Entrapment efficiency %
EMA	European Medicines Agency
EPR	Enhanced permeation and retention
ER	Endoplasmic reticulum
ESR	Electron spin resonance
FA	Folic acid
FBS	Fetal bovine serum
FDA	Food and drug administration
FSC	Forward scattering channel
GA	Glycyrrhetic acid
Gal	Galactose
GalNAc	N-acetyl-galactosamine
GAR	Glycyrrhetic acid receptor
Gd	Gadolinium
GMS	Glyceryl monostearate
GPC3	Glypican-3
GRAS	Generally Recognised as Safe
HA	Hyaluronic acid
HBSS	Hanks' Balanced Salt Solution
HBV	Hepatitis B virus infection
HCC	Hepatocellular carcinoma
HCV	Hepatitis C virus infection
HIV	Human immunodeficiency virus
HLB	Hydrophilic lipophilic balance
HPH	High-pressure homogenisation
HPLC	High performance liquid chromatography
HSA	Human serum albumin
IFM	Inverted fluorescence microscope
IL1 $\beta$	Interleukin-1 $\beta$
LA	Lactobionic acid
LC%	Loading capacity %

LNC	Lipid nanocapsules
MAB	Monoclonal antibody
MALDI-TOF	Matrix-assisted laser desorption/ionization coupled to time-of-flight mass spectroscopy
MCT	Medium chain triglycerides
MDR	Multiple drug resistance
MDT	Mean dissolution time
MPS	Mononuclear phagocyte system
MRI	Magnetic resonance imaging
MTS	3-(4,5-dimethylthiazol-2-yl)-5-(3-carboxymethoxyphenyl)-2-(4-sulfophenyl)-2H-tetrazolium
NAFLD	Non-alcoholic fatty liver disease
NASH	Non-alcoholic steatohepatitis
NEAA	Non-essential amino acids
NHS	N-hydroxysuccinimide
NLC	Nanostructured lipid carriers
NPs	Nanoparticles
NSCLC	Non-small cell lung carcinoma
ORR	objective response rate
OS	Overall survival
PAMAM	Polyamidoamine
PBS	Phosphate buffer saline
PC	Phosphatidylcholine
PDGFR	Platelet-derived growth factor receptor
PDI	Polydispersity index
P-gp	P-glycoprotein
PIT	Phase inversion temperature
PLGA	Poly Lactic-co-Glycolic Acid
PS	Particle size
PTA	Phosphotungstic acid
PXRD	Powder X-ray diffraction
RA	Retinoic acid

RCC	Renal cell carcinoma
ROS	Reactive oxygen species
SA	Stearylamine
SD	Standard deviation
SEER	Surveillance Epidemiology End Results
SEM	Scanning electron microscope
Sf	Sorafenib
SGF	Simulated gastric fluid
SHARP	Sorafenib Hepatocellular Carcinoma Assessment Randomized Protocol
SIF	Simulated intestinal fluid
SLN	Solid lipid nanoparticles
SSC	Side scattering channel
TACE	Transarterial chemoembolisation
TEA	Triethylamine
TEER	Transepithelial electrical resistance
TEM	Transmission electron microscope
TfR	Transferrin receptors
TGA	Thermogravimetric analysis
TNF $\alpha$	Tumour necrosis factor $\alpha$
TPGS	D- $\alpha$ - tocopheryl polyethylene glycol 1000 succinate
VEGFR	Vascular endothelial growth factor receptor
WHO	World Health Organisation
ZP	Zeta potential



# **Chapter 1**

## *Introduction*

## **1.1. Hepatocellular carcinoma (HCC)**

Primary liver cancer is the sixth most common cancer worldwide, with 905,700 new reported liver cancer cases in 2020, and the third in mortality rates among all cancer types with 830,00 reported deaths<sup>1-3</sup>. The World Health Organisation (WHO) predicts that liver cancer will be responsible for more than one million deaths by 2030. Indeed, according to Surveillance Epidemiology End Results (SEER), liver cancer has been the fastest-growing cause of cancer-related mortality in the USA since the early 2000s. If current trends continue, liver cancer will be the third highest cause of cancer-related death by 2030<sup>4</sup>.

Hepatocellular carcinoma (HCC) is a cancer form in the hepatocytes, constituting around 90% of total liver cells. Thus, HCC makes up between 85% and 90% of primary liver cancers (followed by cholangiocarcinoma ~15% and angiosarcoma ~ 1-2%)<sup>3</sup>. The 5-year survival rate of HCC patients is around 18%, making it the second most fatal tumour after pancreatic cancer<sup>5</sup>.

Besides the global health burden of HCC, it has a significant impact on the global economy. Generally, the estimated global economic cost of all cancer types from 2020 to 2050 is about \$25.2 trillion. Whereas liver cancer (mainly HCC) is ranked fourth among the top five cancer types with the highest costs, accounting for 6.5% (~\$1.7 trillion) of the total cost<sup>6</sup>. Notably, approximately 70% of liver cases are thought to be associated with modifiable risk factors<sup>7</sup>. Therefore, global efforts to counteract these risk factors and enhance therapeutic outcomes could potentially reduce the economic burden of HCC.

### **1.1.1. Risk factors and epidemiology**

Over 90% of HCC cases are associated with chronic liver disease. Cirrhosis, regardless of cause, is the most significant risk factor for HCC which is considered the primary cause of mortality in cirrhotic patients<sup>8</sup>. The key risk factors for HCC involve Hepatitis B virus infection (HBV) or Hepatitis C virus infection (HCV) infection, chronic alcohol intake, and metabolic disorders such as diabetes or obesity.

- **Hepatitis B virus (HBV) infection**

HBV is a DNA virus that can integrate into the host genome, causing insertional mutagenesis and activating oncogenes. HBV is the most common risk factor of HCC in the world (33%)<sup>9</sup>. Around 60% of HCC cases in Asia and Africa are attributed to HBV infection, which is responsible for less than 20% in western countries<sup>3,9</sup>.

- **Hepatitis C virus (HCV) infection**

HCV, in contrast to HBV, is an RNA virus that does not integrate into the host genome; hence, the risk of HCC is mainly restricted to people who experience cirrhosis or chronic liver injury with bridging fibrosis. HCV is the world's third most common risk factor for HCC (21%)<sup>9</sup>. Chronic HCV infection is the most prevalent underlying liver disease in North America, Europe, and Japan in patients with HCC<sup>10</sup>. With the help of direct-acting antiviral (DAA) therapy, a growing number of patients with HCV infection have been successfully treated. This has led to a 50–80% reduction in the risk of HCC<sup>11</sup>. But some patients, especially racial minorities, ethnic minorities, and people from low-income areas, have not been tested for HCV and remain unaware of their infection till HCC manifestations show up<sup>12</sup>.

- **Alcohol intake**

Alcoholic cirrhosis is the second most common risk factor for HCC worldwide<sup>9,13</sup>. It accounts for 15%-30% of HCC cases depending on the geographical location<sup>14</sup>. Chronic alcohol consumption can also raise the risk of HCC from other factors; for instance, several studies indicate that HBV carriers who consume alcohol have a higher risk of HCC than those who do not consume alcohol<sup>3,15</sup>.

- **Non-alcoholic fatty liver disease (NAFLD)**

Non-alcoholic fatty liver disease (NAFLD) is a range of health conditions caused by the build-up of fat in the liver, including diabetes mellitus and obesity. Among NAFLD cases, 20-30% are estimated to develop non-alcoholic steatohepatitis (NASH), which then progresses into cirrhosis in 10-20% of cases. Nowadays, NASH is the most common

hepatic disease and a key risk factor for HCC in most developed countries. One study suggested that NASH was linked to a 2.6-fold higher risk of HCC<sup>16</sup>. Since 2010, the proportion of HCC attributable to NASH has significantly grown, and currently accounts for 15–20% of cases in the west<sup>3,17,18</sup>.

- **Aflatoxin B1 (AFB1)**

Aflatoxins are hepatocarcinogenic mycotoxins that contaminate several staple cereals and oil seeds. Aflatoxin B1 (AFB1) produced by *Aspergillus* sp. is the predominant form of aflatoxin implicated in liver carcinogenesis<sup>19</sup>. It is believed that exposure to aflatoxin is, at least, partly responsible for the early start of HCC in several sub-Saharan African countries<sup>18</sup>. AFB1 induces mutations at codon 249 of the TP53 tumour suppressor gene (AGG to AGT), resulting in the substitution of arginine for serine (R249S), which is rarely identified in cancers other than HCC<sup>20</sup>. The R249S mutation is responsible for 50–90% of TP53 mutations in HCCs from places with substantial aflatoxin exposure, whereas this proportion drops to 6% in HCCs from patients in USA<sup>18,20</sup>.

Some reports suggested a synergistic effect between HBV and aflatoxin exposure. Chronic HBV infection may induce cytochrome P450 enzymes to convert inactive AFB1 to the mutagenic AFB1–8,9-epoxide form. Additionally, hepatocyte necrosis and regeneration caused by chronic HBV infection enhance the likelihood of AFB1-induced TP53 mutations. In addition, HBV oncogenic protein inhibits nuclear excision repair which is usually responsible for eliminating AFB1–DNA adducts<sup>21,22</sup>.

Due to the prevalence of risk factors, the global incidence of HCC varies from region to region. Most HCC cases (~80%) arise in eastern Asia and sub-Saharan Africa, where the primary risk factors are chronic hepatitis B and aflatoxin B1 exposure<sup>23,24</sup>, followed by USA, Europe and Japan, where Hepatitis C and excessive alcohol intake are the major risk factors<sup>23</sup> (Figure 1.1).

It is worth mentioning that the epidemiology of HCC changes with time because of the variations in the time and quantity of exposure to environmental and infectious risk factors, healthcare resource availability, and the capability to diagnose early-stage HCC and offer potentially curative treatment<sup>25,26</sup>. For instance, in Japan and Europe, where the

hepatitis C virus spread earlier than in the USA, the incidence of HCC has almost hit a plateau and is even receding in certain places. On the contrary, in the United States, where the hepatitis C virus spread later, the incidence continues to rise<sup>25</sup>. In developed areas, non-alcoholic fatty liver disease is becoming a significant cause of hepatocellular cancer<sup>25,26</sup>.

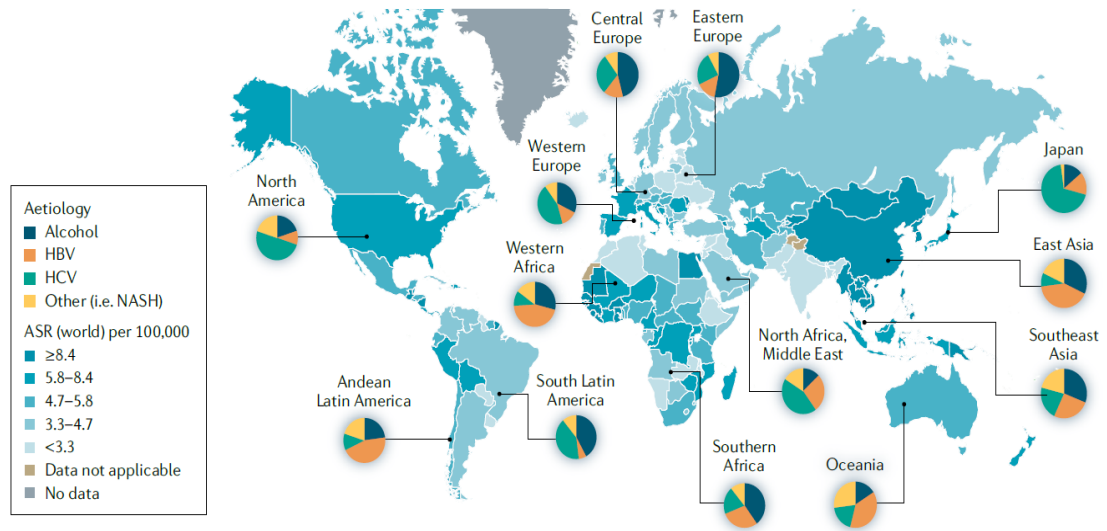


Figure 1.1: The incidence and major aetiological factors of HCC worldwide. Figure was reprinted from GLOBOCAN 2018<sup>27</sup> with data added from references<sup>3,9</sup>.

### 1.1.2. Pathophysiology

Hepatocellular carcinoma development is a complicated, multistep process involving prolonged inflammatory damage, hepatocyte necrosis and regeneration, and fibrotic deposition. When cirrhosis is present, hepatocellular carcinoma risk arises and grows in tandem with increasing liver function impairment. The immense molecular heterogeneity of hepatocellular carcinoma is due to the accumulation of somatic genomic mutations in passenger and driving genes as well as epigenetic modifications<sup>23</sup>. Despite certain shared molecular alterations, the cellular and molecular basis of hepatocarcinogenesis is believed to vary widely among aetiological factors (Figure 1.2).

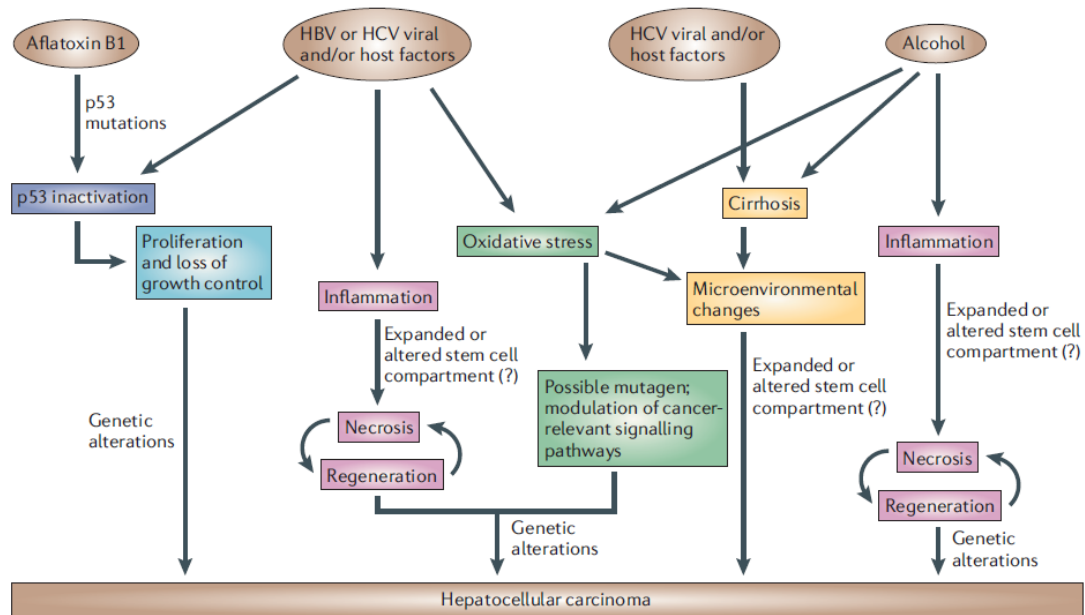


Figure 1.2: The different proposed mechanisms of hepatocarcinogenesis. Figure was adapted with permission from reference<sup>28</sup>.

In the case of viral infections, host-viral interactions appear to contribute to hepatocarcinogenesis. A strong T-cell immune response is apparently induced to combat viral infection; this response leads to hepatocyte necrosis, inflammation, and regeneration, and ultimately these necrosis-regeneration cycles lead to carcinogenesis. Another proposed mechanism is by viral-endoplasmic reticulum (ER) interaction which stimulates the growth and survival-signalling pathway resulting in mutations through the formation of free radicals and activation of stellate cells<sup>28,29</sup>. Moreover, viral infections are believed to induce mutations and inactivation of certain genes such as p53, a tumour suppressor gene that promotes apoptosis and induces cell-cycle arrest upon DNA damage to escape the host's immune response<sup>29</sup>. Finally, since HBV is cytopathic (in contrast to HCV), it is potentially proposed that direct integration of viral DNA to the host genome causes alternations in cancer-relevant genes.

On the other hand, Chronic alcohol consumption has been linked to the production of pro-inflammatory cytokines via monocyte activation<sup>30</sup>, as well as increased levels of circulating endotoxin, activation of Kupffer cells, and the release of numerous chemokines and cytokines (including TNF $\alpha$ , interleukin-1 $\beta$  (IL1 $\beta$ ), IL6, and prostaglandin E<sub>2</sub>) with detrimental effects on hepatocyte survival<sup>31</sup>. Moreover, with high

alcohol exposure, hepatocytes become more sensitive to the cytotoxic effect of TNF $\alpha$  which induces chronic hepatocyte necrosis–regeneration cycles, stellate cell activation, cirrhosis and eventually HCC.

Additionally, alcohol may damage the liver through different oxidative stress mechanisms including promoting fibrosis and cirrhosis which are key factors in promoting the HCC microenvironment<sup>32</sup>. Also, alcohol-induced oxidative stress might impact HCC-relevant signalling pathways such as inhibiting tyrosine phosphorylation. Finally, oxidative stress may lead to the accumulation of oncogenic mutations such as p53 mutation<sup>32</sup>.

In aflatoxin B1-induced hepatocarcinogenesis, Aflatoxin B1 seems to be a mutagen, as it is linked to a particular p53 mutation and involved in the mutational activation of oncogenes<sup>33</sup>. Although the understanding of the pathogenesis and drivers of HCC has improved, this knowledge is yet to be interpreted into clinical practice or employed to predict disease progression or recurrence<sup>23</sup>.

### **1.1.3. Current HCC therapies**

Over the last decade, the management of HCC has greatly improved. The management of HCC requires a complicated decision-making process that considers not only the tumour extent and patient comorbidities, but also the extent of liver dysfunction, since most of HCC therapies might worsen underpinning liver disease. Furthermore, for any management system to be clinically effective, the prognostic prediction must be coupled with therapy indication. For that, different cancer staging systems have been proposed considering different factors to help choose the best intervention according to the tumour stage. From which, Barcelona Clinic Liver Cancer (BCLC) system has been extensively validated and is the most frequently used staging system for HCC since it was first introduced in 1999 with continual updating<sup>34</sup>.

According to the most recent version of BCLC depicted in Figure 1.3., for very early-stage (BCLC 0) and early-stage (BCLC A) hepatocellular carcinoma patients, having a single lesion or up to three nodules with a diameter of less than 3 cm (no macrovascular

invasion or extrahepatic dissemination) and maintained liver function, different treatment interventions could be used, such as resection, transplantation, and ablation<sup>34</sup>.

Patients with HCC in the intermediate stage (BCLC B), exhibiting no symptoms but having large, multifocal tumours without vascular invasion or metastasis outside the liver, are candidates for transarterial chemoembolisation (TACE) if their liver function is preserved. Patients with advanced stage (BCLC C), who show extrahepatic and portal invasion with maintaining liver functions, have only the option of systemic therapy using tyrosine kinase inhibitors (such as Sorafenib and regorafenib). Finally, for the end-stage patients, having poor liver function with extrahepatic tumour invasion, the only available intervention is the supportive care<sup>34</sup>.

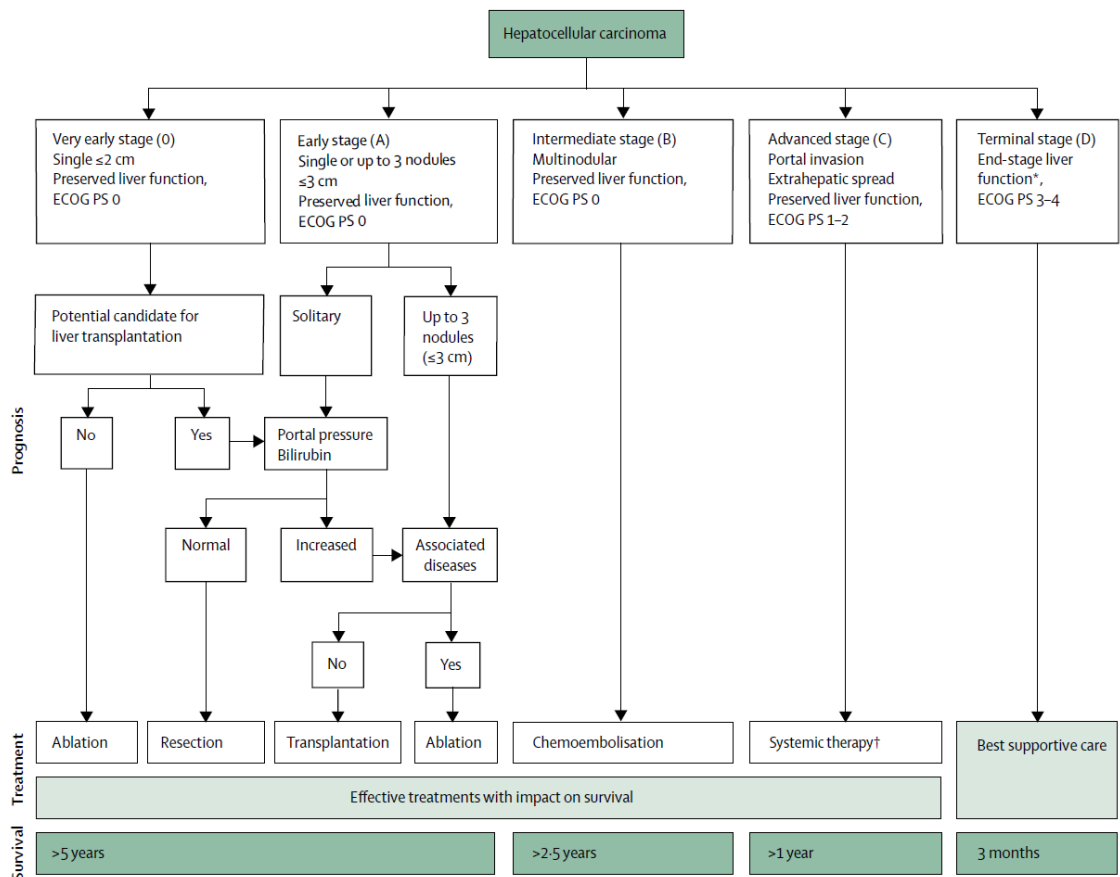


Figure 1.3: HCC treatment strategy according to Barcelona Clinic Liver Cancer (BCLC) staging. Figure was adapted with permission from reference<sup>23</sup>.

### **1.1.3.1.Ablation**

Tumour ablation is a generally approved therapy option for early-stage hepatocellular carcinoma patients. Ablation induces tumour necrosis through temperature alteration (radiofrequency, microwave, laser, or cryo-ablation) or chemical agent injection (most commonly ethanol)<sup>35</sup>. Ablation is reported to be as efficient as a resection for HCC nodules less than 2 cm (very early stage) with comparable survival rates<sup>36</sup>.

### **1.1.3.2.Resection**

Hepatic resection is the surgical removal of the tumour tissues from the liver that could be done through open or laparoscopic surgery<sup>37</sup>. It is the treatment of choice for patients with HCC who do not have cirrhosis or clinically significant portal hypertension, and for whom postoperative hepatic decompensation is not a significant problem. By applying these criteria, only 5-10% of early-stage HCC patients are candidates for surgical resection. On the other hand, adherence to these criteria reduced preoperative mortality to <3% with a 5-year survival of around 70% of patients<sup>37</sup>.

Although surgical resection is a potentially curative treatment of HCC, approximately 70% of patients experience recurrent HCC within 5 years after resection<sup>38</sup>. However, One of the benefits of surgical resection is the availability of the surgical histopathological specimen, which can aid in predicting the risk of HCC recurrence<sup>18</sup>.

### **1.1.3.3.Transplantation**

Liver transplantation is the most effective therapeutic option for HCC since it removes the tumour and the diseased liver, which has limited functionality and a propensity to produce new metachronous HCCs within the cirrhotic tissue area susceptible to carcinogenesis<sup>18,39,40</sup>. Considering the most restrictive criteria for selecting candidate HCC patients, liver transplantation can achieve long-term therapeutic outcomes with more than 70% of patients with a 5-year overall survival<sup>41</sup>. Nevertheless, the primary constraint of liver transplantation is donor shortage. This shortage necessitates a waiting period before transplantation, during which the tumour may develop and impede transplantation, reducing the treatment efficacy<sup>39</sup>.

#### 1.1.3.4. Transarterial chemoembolisation (TACE)

TACE is an efficient locoregional treatment option in intermediate-stage HCC patients (with large or multinodular HCC lesions and preserved liver function). It comprises two fundamental steps: intra-arterial infusion of cytotoxic chemotherapeutic agents dispersed in oil emulsion followed by the delivery of embolisation particles into the tumour-feeding artery, cutting off the blood supply resulting in ischemic necrosis of the tumour tissue (Figure 1.4). The most commonly used chemotherapeutic agents during TACE are doxorubicin, cisplatin, and epirubicin<sup>41</sup>.

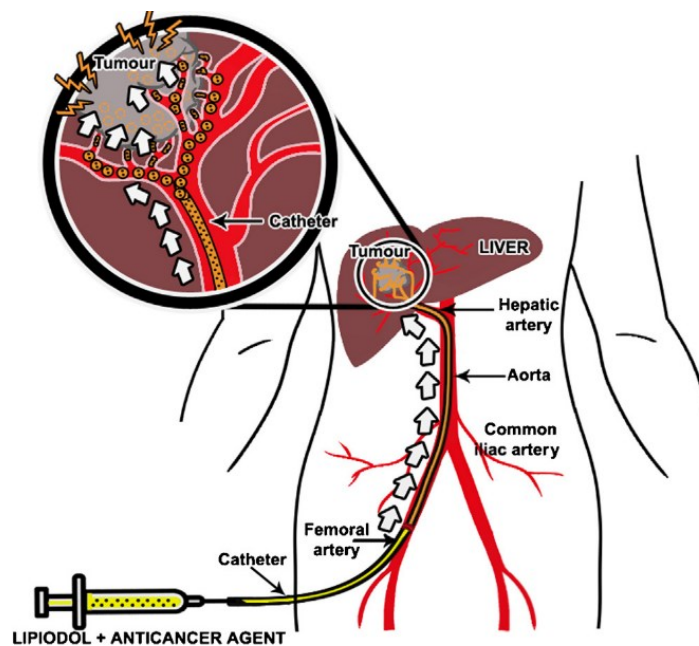


Figure 1.4: The Principle of trans-arterial chemoembolisation (TACE). Figure was adapted with permission from reference<sup>42</sup>.

There are two major TACE techniques: conventional TACE (cTACE) and TACE using drug-eluting beads (DEB-TACE). In cTACE, the cytotoxic drug is emulsified into oily radio-opaque agent Lipiodol (Lipiodol® Ultra-Fluid, Guerbet) injected intra-arterially followed by the injection of an embolic agent such as gelatin sponge or polyvinyl alcohol particles<sup>43</sup>. On the other hand, drug-eluting beads (DEBs) are non-resorbable embolic microspheres, mostly of hydrophilic ionic polymers, that could be loaded with cytotoxic agents through ion exchange mechanisms. They were designed to provide sustained drug release with concurrent embolisation of the tumour-feeding artery<sup>43</sup>.

- **Lipiodol® oil**

Lipiodol® was initially synthesised by the French pharmacist Marcel Guerbet early in 1901 in the School of Pharmacy Chemistry Laboratory in Paris<sup>44</sup>. Lipiodol® is an iodinated (480 mg iodine/ml) oil developed from poppy seed oil (ethylated esters of linoleic (73%), oleic (14%), palmitic (9%) and stearic (3%) acids). Nevertheless, the precise molecular composition of Lipiodol® in terms of the iodine molecular position is unclear<sup>45</sup>. It has a high viscosity of 25 mPas at 37 °C with a density of 1.28 g/cm<sup>45</sup>. The use of Lipiodol® oil in cTACE was first introduced in the early 1980s and became widely adopted after randomised control trials and meta-analysis asserting the superiority of lipiodol TACE. Lipiodol exhibits distinctive potentials for selective absorption and retention in hyperarterialised liver<sup>46-50</sup>. lipiodol® was reported to be retained by HCC for months, even up to a year, while it is cleared from normal hepatocytes within only 4 weeks<sup>51</sup>. The suggested mechanisms for lipiodol® accumulation in tumour cells are as follows: (i) cell membrane pumps; (ii) pinocytosis; (iii) decreased degradation by lysosomes; or (iv) a combination of these mechanisms<sup>42</sup>.

Besides serving as a vehicle for drug delivery, Lipiodol® may also function as an imaging biomarker to monitor treatment delivery and tumour response, as necrosis is proportional to the fraction of tumour volume opacified by Lipiodol® on computed tomography (CT)<sup>52</sup>. In typical cTACE procedures using lipiodol oil, a cytotoxic agent (commonly, doxorubicin) is dissolved/dispersed in an aqueous medium and emulsified into lipiodol oil extemporaneously forming W/O emulsion before injection. The formulation composition and emulsification procedures vary from one practitioner to another. However, the stability of the formulated emulsion is always a concern to guarantee a homogenous delivery and retention of the cytotoxic agent in tumour tissues<sup>53-56</sup>. Several studies investigated the stabilisation of lipiodol oil emulsions for the use in TACE<sup>45,54,57-60</sup>.

Additionally, few trials have been carried out for incorporating lipiodol oil as a vehicle in nanodrug delivery systems exploiting its tumour-seeking, retention properties and its radio-opacity serving as a contrasting agent<sup>57,59,61-63</sup>. For instance, Oh, M. H. et al. formulated a radio-opaque nanoemulsion containing paclitaxel and Bcl-2 small interfering RNA (siRNA) for synergistic anticancer theranostic applications<sup>64</sup>. The

nanoemulsion was prepared by dissolving paclitaxel in lipiodol oil and emulsified in an aqueous solution using a mixture of cholesterols, linear polyethyleneimine grafted with cholesterols, and PEGylated phospholipids. The nanoemulsion induced markedly higher levels of apoptosis and cytotoxic activity in breast adenocarcinoma compared to single treatments. Furthermore, the *in-vivo* delivery and accumulation of the therapeutic payload into liver tissues were successfully tracked by micro-computed tomography (micro-CT) owing to the presence of lipiodol® oil<sup>64</sup>. Similarly, Le Kim, T. H. *et al.* prepared theranostic nanoemulsions containing paclitaxel and lipiodol oil as a contrasting agent using linear polyglycerol-poly( $\epsilon$ -caprolactone) diblock copolymers (PG-b-PCL)<sup>59</sup>. Paclitaxel-loaded nanoemulsion exhibited excellent anti-cancer activity when tested on Hela cells. Besides, micro-CT images of nanoemulsions confirmed the efficiency of formulation to serve as a contrasting agent<sup>59</sup>.

From the aforementioned examples, the incorporation of lipiodol oil into nanodelivery systems serving as a vehicle and a contrasting agent for tracking the delivery of the therapeutic payload seems to be a promising application that needs further investigation.

#### **1.1.3.5. Systemic therapy**

Systemic therapy is the only therapeutic option for advanced-stage HCC patients or for whom other treatments have failed. Unfortunately, around 80% of HCC cases are diagnosed at advanced stages with a median survival time of 6-8 months only<sup>65,66</sup>. Until 2007, different conventional chemotherapeutic agents were used for HCC as a single or regime therapy. Doxorubicin has long been regarded as the reference chemotherapeutic agent among single-agent chemotherapeutic agents. However, it has shown limited efficiency (response rate, 0% to 29%) with no clinically relevant survival benefits<sup>67</sup>. Other drugs are even less efficient such as 5-fluorouracil (5-FU; response rate, 0% to 10%), etoposide (18%), and Cisplatin (6-17%)<sup>67</sup>. On the other hand, several regimen chemotherapies have been employed such as epirubicin/etoposide, oxaliplatin/gemcitabine (GEMOX), and 5-FU/oxaliplatin. However, the therapeutic activity was poor (response rate 15%-20%). HCC is considered a chemoresistant tumour. This could be partially attributed to the high expression of the multidrug resistance (MDR) gene<sup>66</sup>.

Due to the poor therapeutic outcome of the conventional chemotherapeutic agents and the advancement in the understanding of the molecular pathogenesis of HCC, many molecular alternations in HCC showed potential targets for molecular targeted drug therapy. Hence, a new group of therapeutic agents called “**molecular target therapy**” was first introduced in 2007. Molecular target therapy is a vast anticancer agent group targeting cancer-specific molecules or gene mutations. From which, protein kinase inhibitors and monoclonal antibodies are the most commonly used groups. Multikinase inhibitors are a group of protein kinase inhibitors that inhibits several kinase enzymes involved in many pathogenic pathways of HCC.

Sorafenib (Sf) was first approved by FDA (food and drug administration) in November 2007 as the first line of treatment for advanced-stage unresectable HCC based on SHARP (Sorafenib Hepatocellular Carcinoma Assessment Randomized Protocol) study in which sorafenib demonstrated a 2.8-month survival advantage over placebo, with a median overall survival (OS) of 10.7 months compared to 7.9 months in placebo<sup>68</sup>. Sorafenib inhibits several tyrosine kinases involved in tumour angiogenesis and progression such as vascular endothelial growth factor receptor (VEGFR-2/3), platelet-derived growth factor receptor (PDGFR- $\beta$ ), c-Kit, FLT-3, and RET. Also, it suppresses the downstream pathway kinases (Ras/Raf/MEK/ERK, JAK/STAT), and other targets (c-Raf, B-Raf)<sup>68,69</sup> (Figure 1.5). However, the complete molecular mechanisms by which sorafenib exerts its action are not yet fully understood.

Following the sorafenib FDA approval, regorafenib, having a similar structure and function to Sf, was FDA approved in April 2017 as a second line of treatment for advanced HCC after clinical studies showed enhancement in the overall survival from 7.6 to 10.6 months<sup>70</sup>. Furthermore, Lenvatinib, which widely targets VEGFR 1–3, KIT, and PDGFR, demonstrating non-inferiority to sorafenib regarding overall survival (OS) in clinical studies, received FDA approval as a first-line therapy for advanced liver cancer in 2018<sup>71</sup>.

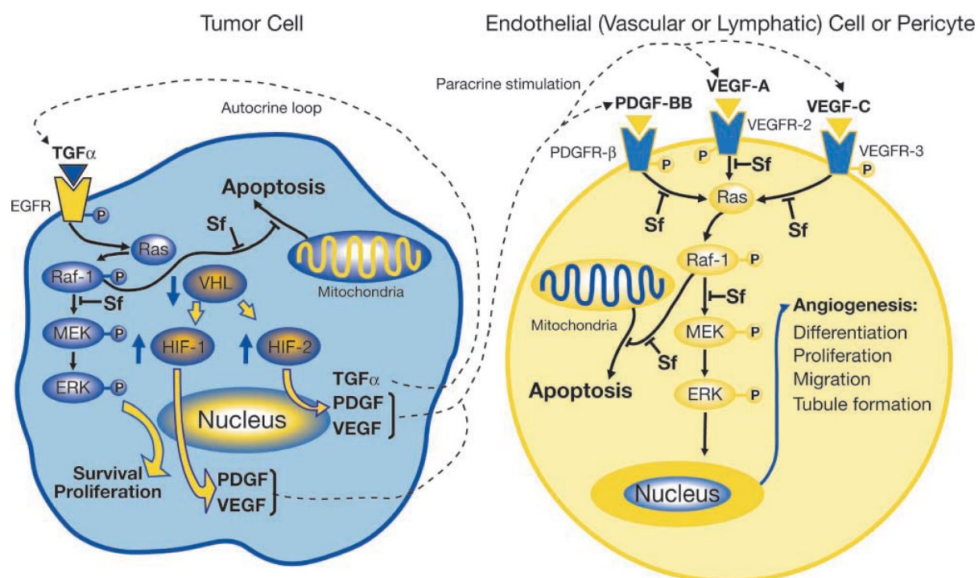


Figure 1.5: Molecular targets of Sorafenib as a multikinase inhibitor for treating unresectable advanced-stage HCC. Figure was adapted with permission from reference <sup>72</sup>.

Despite the encouraging results of clinical studies, molecular target therapies still face obstacles such as low objective response rate (ORR) and adaptive or acquired resistance. These disappointing results are primarily attributable to the heterogeneity of HCC resulting from its morphological complexity, signal transduction network, and microenvironmental disparities<sup>73</sup>.

Moreover, their poor aqueous solubility and pharmacokinetics with undesirable side effects make this approach challenging to be adopted widely in HCC patients. Conclusively, the treatment of HCC signifies an unmet medical need with the urgency to develop effective pharmaceutical therapies.

## 1.2. Nanomedicine in hepatocellular carcinoma (HCC)

The immense development of nanotechnology over the past few decades has profoundly impacted the medical field. Nanomedicine is an emerging area of nanotechnology that uses nanoscale or nanostructured materials in medicine to fulfil special medical requirements<sup>74,75</sup>. Nanomedicines can enhance the therapeutic efficiency of anticancer

agents due to their distinctive features, such as improving the pharmaceutical properties of anticancer agents including stability, solubility, and bioavailability with the avoidance of using toxic solvents. Also, the nanosize allows easy penetration of physiological barriers and modulates the physicochemical properties of the loaded anticancer agents using biodegradable and biocompatible ingredients. Furthermore, the massive surface area allows the loading of innumerable drug molecules as well as surface engineering of the nanocarrier to actively target molecular biomarkers of tumour cells.

Nanomedicines can improve systemic circulation, biodistribution and tumour accumulation of anticancer agents<sup>74-77</sup>. Moreover, the submicron size of nanomedicines enables nanoparticles to evade capturing by the mononuclear phagocyte system (MPS) or reticuloendothelial system (RES) and be cleared by the liver and spleen<sup>78</sup>. Although there is no strict cut-off size, larger particles are suggested to be more prone to be uptaken by MPS/RES than smaller ones<sup>78-80</sup>.

On the other hand, cancerous tissues have very distinguishing attributes that could be employed to allow more efficient delivery of anticancer agents such as the leaky vasculature due to the rapid growth and high angiogenesis of the tumour tissue leading to the formation of new blood vessels that lack smooth muscle layer with the larger lumen and wider fenestrations (up to 4.7  $\mu\text{m}$ , while fenestrations size in normal vessels ranges between 1-100 nm<sup>81</sup>). In junction with impaired lymphatic drainage, this vasculature abnormality increases the permeability and retention of nanoparticles inside the tumour tissues; this phenomenon is known as “Enhanced Permeation and Retention (EPR)”<sup>82,83</sup>. Also, due to poor oxygenation inside the solid tumour resulting from impaired vascular growth, hypoxia is a hallmark of the tumour. The median  $\text{pO}_2$  (partial pressure of oxygen) in the solid tumour was reported to be about 15 mmHg, while the median  $\text{pO}_2$  of the respective adjacent normal tissues was 35 mmHg<sup>84</sup>. Furthermore, tumour tissues exhibit a lower extracellular pH (between 6.0 – 7.0) than normal tissues (pH 7.4). This acidic condition arises from the high anaerobic glycolysis under hypoxic conditions of the tumour microenvironment<sup>85</sup>.

Due to the intensive research in nanomedicine applications in cancer therapy, some nanomedicine products have received approvals for commercialisation. Table 1.1

includes some representative examples of marketed nanomedicines for cancer therapy<sup>86-</sup>

88

Table 1.1: Examples of commercially available nanomedicines for cancer therapy.

<b>Generic name and /or proprietary name</b>	<b>Nanomedicine platform</b>	<b>Active pharmaceutical ingredient</b>	<b>Cancer type</b>	<b>Approval status (year)</b>
Liposomal doxorubicin (Doxil®)	Pegylated liposome	Doxorubicin	HIV-related Kaposi sarcoma, ovarian cancer, and multiple myeloma	FDA (1995) EMA (1996)
Liposomal daunorubicin (DaunoXome®)	Liposome	Daunorubicin	HIV-related Kaposi sarcoma	FDA (1996)
Liposomal cytarabine (DepoCyt®)	Liposome	Cytarabine	Lymphomatous meningitis	FDA (1999)
Liposomal doxorubicin (Myocet®)	Liposome	Doxorubicin	Metastatic breast cancer	EMA (2000)
Liposomal vincristine (Marqibo®)	Liposome	Vincristine sulfate	Acute lymphoblastic leukaemia	FDA (2012)
Liposomal irinotecan (Onivyde®)	Pegylated liposome	Irinotecan	Post-gemcitabine metastatic pancreatic cancer	FDA (2015)
Liposomal mifamurtide (Mepact®)	Liposome	Muramyl tripeptide phosphatidyl-ethanolamine	Nonmetastatic, resectable osteosarcoma, Breast cancer	EMA (2009)
Nab-paclitaxel (Abraxane®)	Albumin NP	Paclitaxel	Breast, lung and pancreatic cancer	FDA (2005) EMA (2008)

Polymeric micelles Leuprolide acetate (Eligard®)	Polymeric micelles (PLGA)	Leuprolide acetate	Prostate cancer	FDA (2002)
Polymeric micelles paclitaxel (Genexol®-PM)	Polymeric micelle	Paclitaxel	Breast cancer and NSCLC	Korea (2007)

\*HIV= human immunodeficiency virus, NSCLC= non-small cell lung carcinoma

In the case of HCC, although the uptake of nanomaterials to the liver by macrophages seems to be beneficial for delivering therapeutic agents to the liver, it comprises a barrier for the delivery of nanomedicine into the diseased tissues rather than healthy ones<sup>89,90</sup> as it has been reported that the resident phagocytosing Kupffer cells of the liver, not hepatocytes, potentially uptake and remove the systemically circulating nanoparticles based on several factors including particle size and charge<sup>91,92</sup>. Moreover, the occurrence of HCC accompanied by cirrhosis alters drug pharmacokinetics affecting their metabolism in the liver<sup>91</sup>. Fortunately, HCC has common features with other solid malignant tumours, such as acidosis, hypoxia, leaky vascular structure (EPR), and overexpression of certain biomarkers, which might be exploited for selective delivery and controlled release of nanomedicines<sup>92-94</sup>.

Conceptionally, the employment of nanomedicines in HCC relies on two distinctive strategies: passive targeting and active targeting<sup>95</sup> (Figure 1.6). In the passive targeting strategy, the accumulation of the nanomedicine in the HCC tissues depends on the enhanced permeation and retention phenomenon (EPR) in tumour tissues. Several nanomedicines relying on passive targeting have been developed to treat HCC<sup>96</sup>.

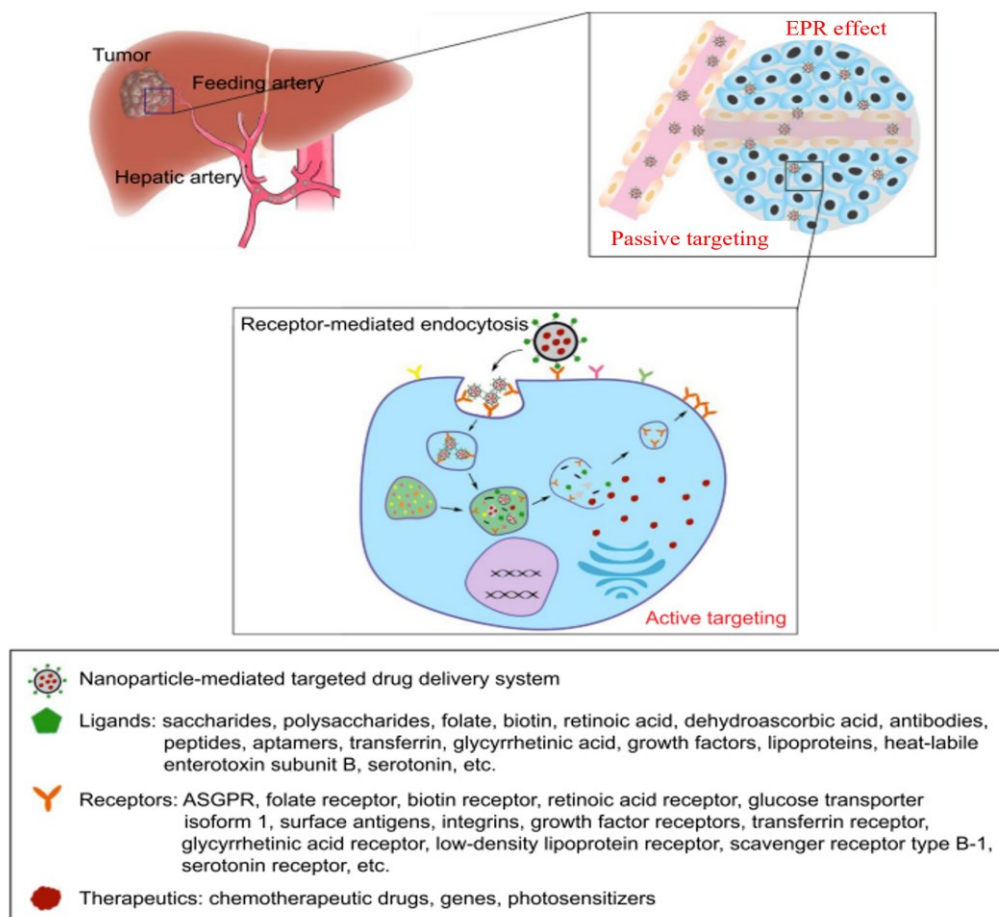


Figure 1.6: Schematic diagram of targeting strategies of nanomedicines for HCC therapy. Figure was adapted with permission from reference<sup>97</sup>.

Despite its widespread applicability in nanomedicines, passive targeting has several shortcomings. First, passive targeting is driven by concentration gradients (Fickian diffusion), greatly impeded by high interstitial pressure, tumour growth, and abnormal matrix-induced solid stress, resulting in inefficient targeting<sup>98</sup>. In addition, passive targeting tends to promote multiple drug resistance (MDR), which is an adaptation of cancer cells to drugs and leads to treatment failure<sup>99</sup>. Lastly, this basic targeting strategy cannot address the heterogeneity inside tumour tissues, which implies it cannot be effective in all circumstances<sup>87</sup>. As revealed by several studies, these restrictions result in less than 1% of systemically delivered nanoparticles reaching tumours<sup>98,100,101</sup>, hence accelerating the development of active targeting is much needed.

On the other hand, active targeting utilises a targeting ligand on the surface of nanoparticles that selectively binds to overexpressed biomarkers (receptors or antigens) on the surface of the target cells, which induces receptor-mediated endocytosis. This

allows the delivery of therapeutic agents to the tumour with high specificity and efficiency<sup>102,103</sup>. Active targeting can potentially overcome the constraints of passive targeting<sup>74</sup>. Nanomedicines adopting this targeting strategy have been widely studied to treat HCC achieving improved anticancer efficiency and reduced adverse effects<sup>91,104–106</sup>.

For active targeting of HCC cells, many overexpressed biomarkers have been employed for targeting hepatocytes using different ligands (Figure 1.7), such as asialoglycoprotein receptor (ASGPR) using galactose bearing polysaccharides, Glypican-3 (GPC3) using an anti-GPC3 monoclonal antibody, transferrin receptors (TfR) using transferrin, glycyrrhetic acid receptor (GAR) using glycyrrhizin or glycyrrhetic acid (GA), and a cluster of differentiation 44 (CD 44) using hyaluronic acid (HA). In addition, due to the rapid proliferation and high metabolic activity of cancer cells, some vitamin receptors are upregulated such as folic acid (FA), biotin, retinoic acid (RA), and dehydroascorbic acid (DHAA) that could be employed as targeting ligands<sup>97</sup>. Other possible target biomarkers have been reported for targeting HCC<sup>96,101,106</sup>. However, among all these biomarkers of hepatocytes, the asialoglycoprotein receptors (ASGPRs) have demonstrated a great potential for targeting hepatocellular carcinoma cells<sup>107</sup>.

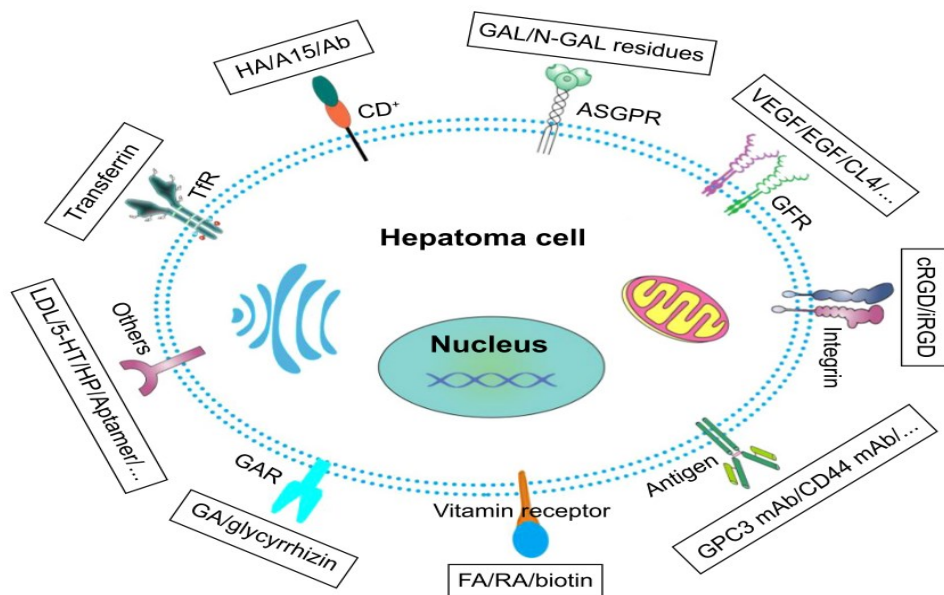


Figure 1.7: Summary of target biomarkers overexpressed on hepatoma cells and their ligands for active targeted therapy of HCC. Figure was adapted with permission from reference<sup>97</sup>.

### 1.3. ASGPR-mediated HCC targeting nanomedicines

ASGPR was first recognised by Morell and Ashwell in 1965 as a 40–50 kDa noncovalent hetero-oligomer comprised of two homologous polypeptides with the major and minor subunits HL-1 (hepatic lectin, or ASGPR1, ASGR1) and HL-2 (ASGPR2 or ASGR2), respectively<sup>108</sup>. Each subunit is a C-type II transmembrane protein, having a short amino terminal in the cytoplasmic domain and a neck region which links the internal signal membrane to calcium ( $\text{Ca}^{+2}$ ) dependent carbohydrate recognition domains (CRDs) on the outside<sup>107,108</sup> (Figure 1.8).  $\text{Ca}^{+2}$  is essential to enable the interaction between ASGPR and glycoprotein with maximum activity above pH 6<sup>107</sup>.

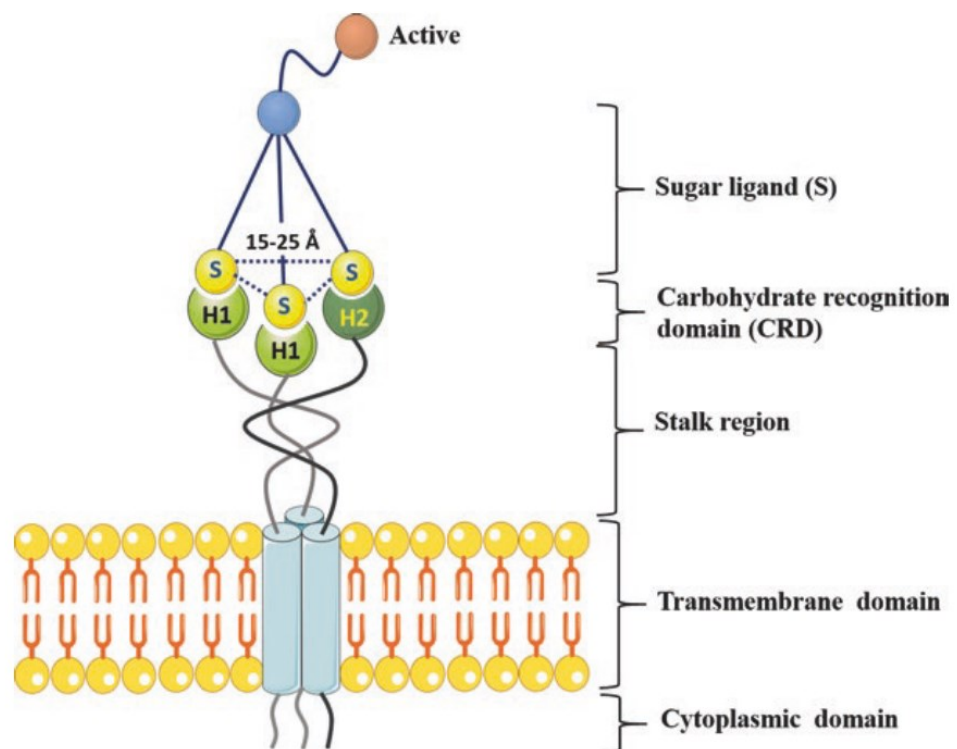


Figure 1.8: Schematic representation of ASGPR, demonstrating the hetero-oligomer composed of two H1 and H2 subunits. Figure was adapted with permission from reference<sup>108</sup>.

ASGPR is mainly expressed on hepatocytes (500,000 ASGPR/hepatocyte), mainly expressed on the sinusoidal and basolateral hepatocellular membrane, with minimal extrahepatic expression<sup>107</sup>. Moreover, ASGPR expression level was found to be about 80% in the well-differentiated tumour, while its expression in poorly differentiated HCC

is around 20%<sup>109</sup>. *In-vitro*, ASGPR was found expressed in human hepatoma cell line HepG2 at a density of 76,000 ASGPR/cell, HepAD38 cells (17,000 ASGP/cell) and at a lesser extent on HuH-6 and HuH-7 (~3000 ASGPR/cell)<sup>110</sup>. The expression of ASGPR could be impaired by ethanol, carbon tetrachloride and lipopolysaccharide. Besides, diabetes and partial hepatectomy can also cause ASGPR impairment<sup>107</sup>.

The hepatic ASGPR plays an essential function in the endocytosis and lysosomal breakdown of desialylated proteins in the serum. Moreover, hepatic ASGPR participates in the binding, internalisation through clathrin-mediated endocytosis, and breakdown of extracellular glycoproteins with exposed terminal galactose (Gal), lactose, or N-acetyl-galactosamine (GalNAc) residues, making it a potential receptor for galactose-mediated delivery of anti-cancer agents to the liver. The natural endogenous ligands of ASGPR include asialoorosomuroid (ASOR, a high-affinity ligand with an inhibition constant  $K_i = 1.7$  nM, contains 20 Gal), asialoceruloplasmin ( $K_i = 86$  nM, contains 12 Gal), asialofectin ( $K_i = 17$  nM contains 12 Gal with 3 GalNAc), and asialotransferrin ( $K_i = 3300$  nM, contains 5 Gal)<sup>91</sup>. ASGPR ligand binding affinity is impacted by the quantity, location and branching of the terminal galactose residues on the ligand<sup>108</sup>. It was found that increasing galactose density on the surface of galactosylated liposomes increased their cellular uptake by HepG2 cells<sup>111</sup>. Moreover, it was reported that the affinity of Gal binding increased by 100-1000 fold from mono- to tri-antennary Gal structure due to cluster effect<sup>107</sup>.

For ASGPR-mediated active targeting of HCC, various natural and synthetic targeting ligands have been explored. Natural ligands include asialoorosomuroid (ASOR) and asialofeutuïn (AF), endogenous glycoproteins bearing terminal galactose moieties. Also, Lactoferrin, an iron-binding glycoprotein of the transferrin family, exhibited high affinity to ASGPR ( $K_i \sim 80$  nM). Besides, Gal- and GalNAc-bearing carbohydrates, such as arabinogalactan (AG) and pectin, are also considered potential ASGPR-targeting carbohydrates. It is worth mentioning that Pullulan, a glucose-based carbohydrate polymer, represents an excellent ASGPR ligand due to the inability of ASGPR to differentiate between Gal and D-glucose<sup>107,112</sup>. The chemical structure of some ASGPR carbohydrate ligands is depicted in Figure 1.9.

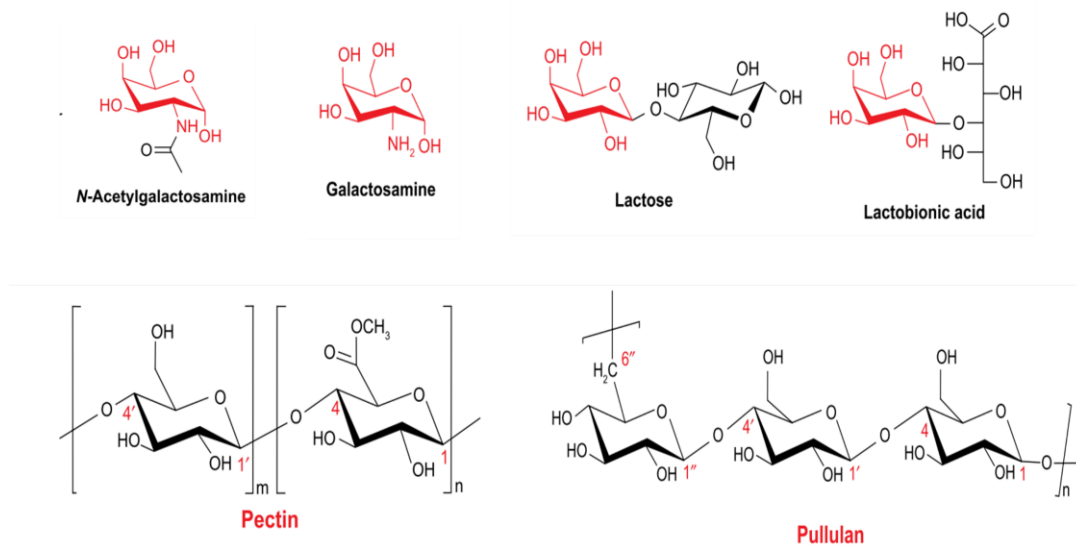


Figure 1.9: Chemical structure of some saccharides and polysaccharides for ASGPR targeting. Figure was adapted with permission from reference<sup>97</sup>.

On the other hand, synthetic ASGPR ligands are produced through galactosylation of polymers (such as poly-glutamic acid, poly-L-lysine, and chitosan), lipids (such as cholesterol) and proteins (bovine serum albumin, Gal-BSA) using versatile chemical conjugation reactions such as amidation reaction, reductive amination, and esterification employing primarily lactobionic acid, galactosamine or lactose as galactose bearing moieties<sup>97,107,108</sup>.

Several nanodelivery systems have been developed using galactosylated synthetic ligands for active targeting delivery of different anticancer agents to HCC<sup>97,107,108</sup>. For instance, L. Q. Thao et al. prepared galactosylated BSA NPs to co-deliver doxorubicin and paclitaxel using albumin-bound (nab<sup>TM</sup>) technology. Galactosylation of naïve BSA (Gal-BSA) was done through an amidation reaction between lactobionic acid and free amine groups of BSA<sup>113</sup>. Gal-BSA-NPs exhibited enhanced cellular uptake and higher cytotoxicity compared to untargeted counterpart nanoparticles<sup>113</sup>. In another study, galactosamine was conjugated through an amidation reaction with free carboxylic groups of BSA for targeted delivery of Doxorubicin<sup>114</sup>.

Furthermore, galactosylated liposomes (Gal-Lip) have been developed using galactosylated cholesterol for the liver-targeted delivery of doxorubicin<sup>115,116</sup>. From *in-vivo* studies, Gal-Lip was found to have 3 times higher liver targetability compared to

unmodified liposomes. In another study, galactosylation of liposomes was achieved by the reaction of lactose with dioleoyl phosphatidylethanolamine (DOPE) through reductive amination and utilised for the selective delivery of small interfering RNA (siRNA) to liver cancer cells<sup>117</sup>.

Galactosylated solid lipid nanoparticles (SLN) and nanostructured lipid carriers (NLC) have also been developed for targeting HCC. For example, Varshosaz J. et al. prepared galactosylated NLC to deliver 5-fluorouracil (5-FU). The galactosylation was achieved using an amidation reaction for conjugation between lactobionic acid and stearylamine<sup>118</sup>. It was found that galactosylated LNC exhibited higher cellular uptake and cytotoxicity on HepG2 cells than unmodified LNC<sup>118</sup>. Similar results were observed by Xu, Z. *et al.* after galactosylated DOPE was employed as a targeting ligand for the delivery of docetaxel using SLN<sup>119</sup>.

Due to their biocompatibility, galactosylated poly(lactide-co-glycolic acid) (PLGA), prepared by direct esterification between the terminal carboxylic groups of PLGA and the anomeric hydroxyl group of galactose, was utilised to fabricate Gal-PLGA polymeric NPs for liver-targeted delivery of apigenin<sup>120</sup>. Confirmed by *in-vitro* and *in-vivo* studies, Gal-PLGA NPs showed a superior therapeutic efficiency than unmodified PLGA NPs. Another study conducted by Liang et al. used galactosamine to develop paclitaxel-loaded galactosylated poly ( $\gamma$ -glutamic acid)-poly(lactide) nanoparticles as a targeted drug delivery system against HepG2 Cells. The study findings confirmed the high selectivity of the galactosylated nanoparticles demonstrated by the enhanced cellular uptake and the reduced systemic toxicity<sup>121</sup>.

Moreover, several dendrimer-based delivery systems have adopted galactosylation for liver-targeted delivery of anticancer agents. For instance, Gal-G4-polyamidoamine (PAMAM) sorafenib-loaded dendrimers were developed by Lacobazzi et al. through an amidation reaction between lactobionic acid and terminal amine groups<sup>122</sup>. The study demonstrated a higher binding and uptake ability of the Gal-G4-PAMAM dendrimers in well-differentiated and ASGPR-expressing human liver cancer cell line, HepG-2, compared to non-expressing HLE cells<sup>122</sup>.

Therefore, these studies, besides several other studies in the literature<sup>97,107,108</sup>, demonstrate that galactosylation of nanodelivery systems has shown ample potential as a promising strategy for targeting HCC.

#### 1.4. Current state of sorafenib-loaded nanodelivery systems for HCC

Sorafenib is a dual aryl urea oral multikinase inhibitor. It was FDA approved in 2007 as the first line of treatment for unresectable advanced-stage HCC<sup>123</sup> and also got FDA approval in 2009 for its use in advanced renal cell carcinoma (RCC)<sup>124</sup>. It has the chemical name 4-[4-[[4-chloro-3-(trifluoromethyl)phenyl]carbamoylamino]phenoxy]-N-methylpyridine-2-carboxamide and its chemical structure is depicted in Figure 1.10. Commercially, it is marketed as oral tablets in the form of tosylate salt, to enhance its solubility, under the brand name Nexavar® tablets (contain sorafenib tosylate (274 mg) equivalent to 200 mg of sorafenib).

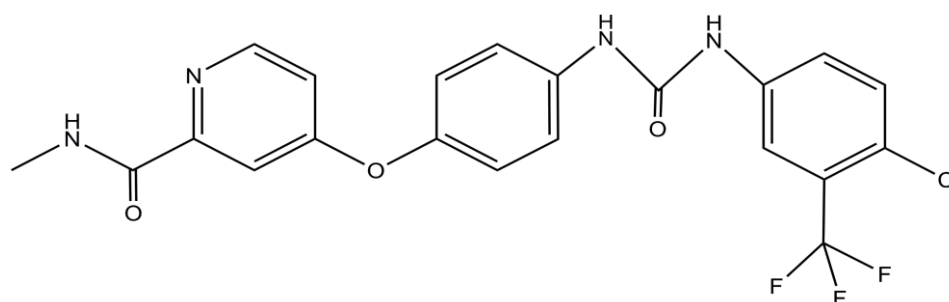


Figure 1.10: Chemical structure of Sorafenib

Sf is a white to yellowish solid powder with a molecular weight of 464.825 g/mol. It is practically insoluble in aqueous media ( $\sim 1.7 \mu\text{g/mL}$ )<sup>125</sup>, slightly soluble in ethanol and acetone, and soluble in dimethyl sulfoxide (DMSO), dimethyl formamide (DMF) and PEG 400<sup>126</sup>. It is classified as a class II drug in the biopharmaceutical classification system (BCS) with low solubility and high permeability<sup>127</sup>. It is very lipophilic (Log P = 3.8) with a strong crystal lattice ( $T_m = 205^\circ\text{C}$ )<sup>125</sup>.

Regarding Sorafenib pharmacokinetics, oral Sf tablets (Nexavar®) have a mean relative bioavailability of 38 - 49% compared to oral solution and absolute oral bioavailability of  $\sim 8.43\%$ <sup>128,129</sup>. While there is no other route of administration available due to limited Sf

solubility. Sf absorption decreased by 30% when administered high-fat meals compared to the fasted state. Sf has a high plasma protein binding (99.5%). It is primarily metabolised in the liver through CYP3A4-mediated oxidation and UGT1A9-mediated glucuronidation<sup>130</sup>.

Due to the very low oral bioavailability of Sf, the typical oral dose of sorafenib (Nexavar®) for HCC is 400 mg twice daily. However, high Sf oral dose and the non-specific uptake by normal cells have been reported to develop some side effects such as diarrhoea, hand-foot skin reactions, anorexia, alopecia and weight loss according to SHARP clinical trials<sup>68</sup> (Figure 1.11).

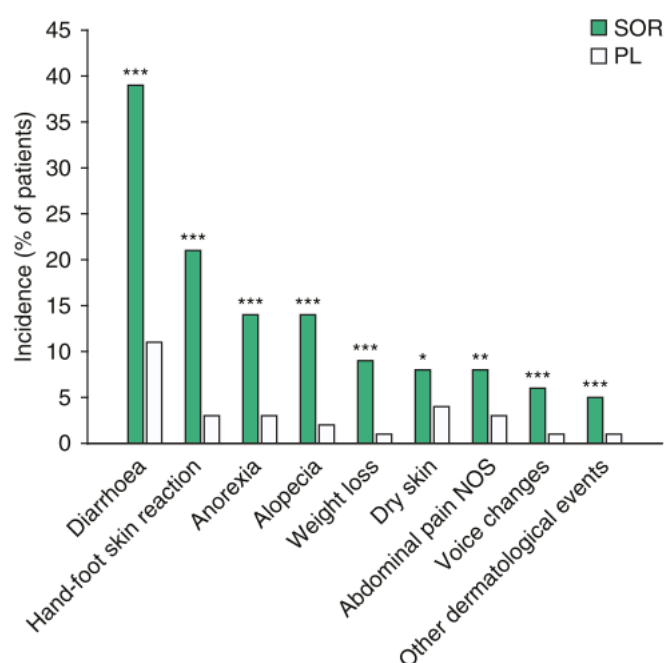


Figure 1.11: Sorafenib-related side effects compared to placebo in the SHARP trial. Patients received oral Sf 400 mg twice daily (n=297) or placebo (n=302). Figure was adapted with permission from reference<sup>130</sup>. p = 0.04, \*\* p = 0.007, \*\*\* p < 0.001

Consequently, several trials have been conducted to develop Sf-loaded nanoparticles (NPs) to overcome its limited bioavailability and side effects<sup>131,132</sup>. For instance, Xiao, Y. et al. co-loaded Sf and gadolinium into liposomal platform (Sf/Gd-liposomes) to serve as a theranostic agent for Sf delivery and MRI-guided therapy<sup>133</sup>. Sf/Gd-liposomes were prepared using the thin film hydration method and showed good nanosize ( $180 \pm 1$  nm) and size distribution (PDI = 0.2) with high Sf loading (Loading capacity LC%= $4.3 \pm$

0.1%). Sf/Gd-liposomes demonstrated higher antitumor activity with higher signal enhancement with MRI than free solutions of Sf and gadolinium<sup>133</sup>.

As a lipophilic drug, Sf is considered a good candidate for loading into solid lipid nanoparticles (SLN). For example, Sf has been loaded into Galactosylated solid lipid nanoparticles (GAL-Sf-SLN) made of glyceryl monostearate (GMS) and stearic acid to enhance Sf oral bioavailability<sup>128</sup>. GAL-Sf-SLN was prepared using the emulsification/solvent evaporation method showing particle size (P.S.) of  $111 \pm 6.99$  nm with PDI of  $0.354 \pm 0.024$  and zeta potential (ZP) of  $-19.8 \pm 1.11$  mV. The entrapment efficiency (EE%) of Sf was  $95 \pm 1.8\%$ . In *in-vitro* cellular studies, GAL-Sf-SLN exhibited higher cytotoxicity and apoptosis rate than unmodified Sf-SLN and free Sf solution. While GAL-Sf-SLN had a higher relative bioavailability compared to unmodified Sf-SLN and free Sf solution after oral administration to BALB/c mice<sup>128</sup>.

Additionally, polymeric NPs have also been employed for the delivery of Sf. Zheng, N. *et al.* prepared CXCR4-targeted poly (lactic-co-glycolic acid) (PLGA) NPs using solvent evaporation method for co-delivery of Sf and metapristone<sup>134</sup>. SF-loaded PLGA-PEG NPs had P.S. of  $145.1 \pm 2.08$  nm with PDI of  $0.113 \pm 0.012$  and ZP of  $-15.47 \pm 2.44$  mV. The loading capacity (LC%) of Sf was  $1.03 \pm 0.07\%$ . The combinatory delivery of Sf and mifepristone-loaded CXCR4-targeted PLGA NPs has synergistically suppressed the proliferation of HCC cell lines (HepG2, Huh7, and SMMC-7721 cells) and induced their apoptosis. Moreover, PLGA NPs showed prolonged circulation and selective accumulation in tumour tissues, thus suppressing tumour growth in the tumour xenograft mice model after intravenous administration<sup>134</sup>.

In addition, Due to the enormous merits of albumin-based NPs as nanocarriers, several studies investigated the employment of these systems to enhance the therapeutic efficiency of Sf for HCC. One such example is the preparation of folic acid-targeted Sf-loaded albumin NPs (FA-HSA-Sf-NPs) for targeted delivery to HCC. FA-HSA-Sf-NPs were prepared by chemical crosslinking producing NPs with P.S. of  $85.4 \pm 3.3$  nm, ZP of  $-22.5 \pm 0.9$  mV, and Sf loading capacity (LC%) of  $3.83 \pm 0.26\%$ . FA-HSA-Sf-NPs exhibited enhanced cytotoxicity against hepatocellular BEL-7402 cells (FA receptor-overexpressing cells) with minimal cytotoxicity on normal liver LO2 cells. Furthermore, FA-HSA-Sf-NPs had a superior antitumor efficacy, manifested as inhibition in tumour

proliferation and suppression of angiogenesis, with enhanced accumulation of Sf in the liver after intravenous administration in nude mice bearing xenograft tumors<sup>135</sup>. Table 1.2 includes some representative examples of different Sf-loaded NPs of various natures for improving Sf pharmacokinetics and its therapeutic efficiency.

Table 1.2: Representative examples of different Sf-loaded nanodelivery systems for HCC.

Nanocarrier	Delivery strategy	Colloidal properties	Drug loading	Remarks	Ref
Liposomes	Sf and Gadolinium co-delivery for drug delivery and MRI-guided therapy (Sf/Gd-liposomes)	PS = 180 ± 1 nm PDI = 0.2 ZP = -7 ± 1 mV	EE% = 96 ± 2% LC% = 4.3 ± 0.1 %	Sf/Gd-liposomes showed a superior antitumor efficiency to Sf solution (oral and iv) with longer imaging time and higher signal enhancement at the tumour tissue.	<sup>133</sup>
	Co-delivery of Sf and GPC3 siRNA using liposomes	P.S. =143.8 nm ZP = 7.5 mV	EE% = 85.48 ± 0.56% LC% = 5.85 ± 0.04%	Significant (p< 0.05) downregulation of GPC3 and cyclin D1 proteins in HepG2, increasing sensitivity to Sf. <i>In-vivo</i> study revealed a remarkable antitumor activity of Sf/siGPC3-liposomes compared to the Sf solution.	<sup>136</sup>

	PEGylated hyaluronic acid-coated liposome for efficient Sf delivery (PEG-HA-Sf-Lip)	PS = 130 ± 7.95 nm PDI = 0.26 ± 0.01 ZP = -12.6 ± 1.25 mV	EE% = 92.6 ± 3.94 %	PEG-HA-Sf-Lip exhibited higher cytotoxicity and cellular uptake in MDA-MB-231 cells than unmodified liposomes. Furthermore, <i>in-vivo</i> studies showed enhanced systemic exposure (3 folds) and improved tumour growth inhibition.	137
Solid lipid nanoparticles (SLN)	Galactosylated SLN for site-specific oral delivery (GAL-SSLN)	P.S. = 111 ± 6.99 nm PDI = 0.354 ± 0.024 ZP = -19.8 ± 1.11 mV	EE% = 95 ± 1.8%	GAL-SSLN exhibited superior cytotoxicity and apoptosis in HepG2. In addition, <i>in-vivo</i> studies showed better accumulation in the liver compared to unmodified SLN.	128
	Sf-loaded SLN to improve oral bioavailability	P.S. = 77.16 nm PDI = 0.28 ZP = -18.1 mV	EE% = 89.87% LC% = 5.39%	Sf-SLN exhibited a 66.7% enhancement in the area under the curve of Sf compared to Sf suspension after oral administration in rats.	138
	Sf-loaded SLN	P.S. = 108.23 ± 7.01 nm PDI = 0.25 ± 0.02 ZP = -16.37 ± 0.65 mV	EE% = 93.49 ± 1.87%	Enhanced pharmacokinetics after intravenous injection in rabbits compared to Sf solution.	139

	Magnetically targeted Sf-loaded SLN (Sf-Mag-SLN)	P.S. = 248 ± 113 nm PDI = 0.2 ± 0.1 ZP = -23.0 ± 5.3 mV	EE% = 90%	Sf-Mag-SLN showed enhanced accumulation and localisation of Sf on HepG-2 cells with the ability to function as a negative contrasting agent using magnetic resonance imaging (MRI).	<sup>140</sup>
Polymeric NPs	Dual loading of Sf and Doxorubicin in PLGA and PEG-PLGA NPs	P.S. (142.2 – 177.2 nm) PDI (0.076 – 0.203)	EE% (55-88%) LC% (4.35-5.03%)	Compared to the drug solution, there is comparable cytotoxicity from PLGA NPs on HT-29 cells, but PEG-PLGA showed higher cytotoxicity due to quicker drug release.	<sup>141</sup>
	CXCR4-targeted lipid-coated PLGA nanoparticles	P.S. = 175.25 ± 1.82 nm PDI = 0.148 ± 0.004	EE% ~ 85%	Enhanced cellular uptake and angiogenic effect with delay in tumour progression and increased overall survival in orthotopic HCC model compared to free Sf.	<sup>142</sup>

	Codelivery of Sf and metapristone by CXCR4-targeted PLGA-PEG nanoparticles.	P.S. = 145.1 ± 2.08 nm PDI = 0.113 ± 0.012 ZP = -15.47 ± 2.44 mV	EE% = 52.17 ± 3.92% LC% = 1.03 ± 0.07%	PLGA-PEG NPs showed a synergistic effect of Sf and metapristone in suppressing HCC proliferation and enhancing colony inhibition and apoptosis. NPs also displayed enhanced suppression of tumour growth in xenograft animal models compared to free Sf solution.	134
Albumin based NPs	Folate-decorated albumin NPs (FA-HSA-Sf-NPs)	P.S. = 85.4 ± 3.3 nm ZP = -22.5 ± 0.9 mV	EE% = 91.09 ± 6.14% LC% = 3.83 ± 0.26%	FA-HSA-Sf-NPs exhibited enhanced cytotoxicity, apoptosis induction and cellular uptake in BEL-7402 cells. From <i>in-vivo</i> studies, FA-HSA-Sf-NPs showed the most efficient antitumor activity with a remarkably improved Sf accumulation in tumour tissues.	135
	Lactobionic acid targeted Sf-loaded albumin lipid NPs (LA-Sf-HAS NPs)	P.S. = 280.1 ± 4.4 nm ZP = -12.3 ± 0.9 mV	EE% = 97.6 ± 2.2 %	LA-Sf-HAS NPs demonstrated more cytotoxicity and cellular uptake in HepG2 cells compared to untargeted counterparts.	143

	Codelivery of Paclitaxel (PTX) and Sorafenib (Sf) by albumin NPs (PTX–Sf-BSA-NPs)	P.S. = 154.93 ± 4.31 nm PDI = 0.16 ± 0.04 ZP = -10.93 ± 1.22 mV	EE% = 94.34 ± 1.3%	PTX–Sf-BSA-NPs demonstrated significantly (p< 0.05) lower haemolysis and myelosuppression compared to the drug solution.	144
--	---	---	--------------------	--	-----

## 1.5. Selected nanoparticles for sorafenib delivery

### 1.5.1. Solid lipid nanoparticles (SLN) and nanostructured lipid carriers (NLC)

Solid lipid nanoparticles (SLN) were first developed at the beginning of the 1990s by Müller et al. as an alternate drug nanocarrier to emulsions, liposomes, and polymeric nanoparticles. SLN are produced by replacing the liquid oily core of o/w emulsions with a solid lipid or a mix of solid lipids which are solid at both room and body temperature. SLN are submicron nanodispersion, with mean particle size ranges from 40 to 1000 nm, typically composed of 0.1% up to 30% solid lipid dispersed in an aqueous medium containing 0.5% to 5% surfactant to stabilise the dispersion<sup>145</sup>.

SLN have several advantages such as biocompatibility, biodegradability, low toxicity as they are made from Generally Recognised as Safe (GRAS) ingredients, protection of drugs from chemical degradation and controlling drug release. Also, they are suitable for industrial production because they are easy to scale up and stable under sterilisation conditions with good *in-vivo* stability<sup>146</sup>. On the other hand, SLN also have limitations, principally attributed to the risk of polymorphic transitions (from  $\alpha$  polymorph, which is less crystalline with high energy, to  $\beta$  polymorph, which is more crystalline with low energy) upon storage that may cause drug expulsion and drop in the drug loading.

Nanostructured lipid carriers (NLC) were introduced as a second generation of SLN with improved stability and drug encapsulation capability. In NLC, the lipid dispersion is composed of a blend of solid and liquid (oils) lipids with an oil content of up to 30% w/w of solid lipid (Figure 1.12). NLC were developed to overcome some limitations related

to SLN<sup>145,147–149</sup>. Unlike SLN, NLC exhibit a higher drug loading capacity and minimise/avoid potential drug expulsion during storage associated with solid lipid recrystallisation. According to the proposed structure of NLC, it is categorised into three different types (imperfect crystal type, multiple type, and amorphous type)<sup>145,147–149</sup>. In imperfect LNC, structurally dissimilar lipids are used to create imperfections in the crystal order allowing more voids to accommodate more drug molecules. While in multiple NLC type, the solid lipid contains nanosized liquid oil compartments.

These nanoparticles' structure can enhance drug loading especially if the drug is more soluble in the liquid lipid. Finally, in amorphous LNC type, special lipids (such as hydroxyoctacosanyl hydroxystearate or isopropyl myristate) that do not crystallise and exist in an amorphous state are carefully mixed with the solid lipid to form a homogenous amorphous mix which minimises drug expulsion due to lipid recrystallisation<sup>145,147–150</sup>.

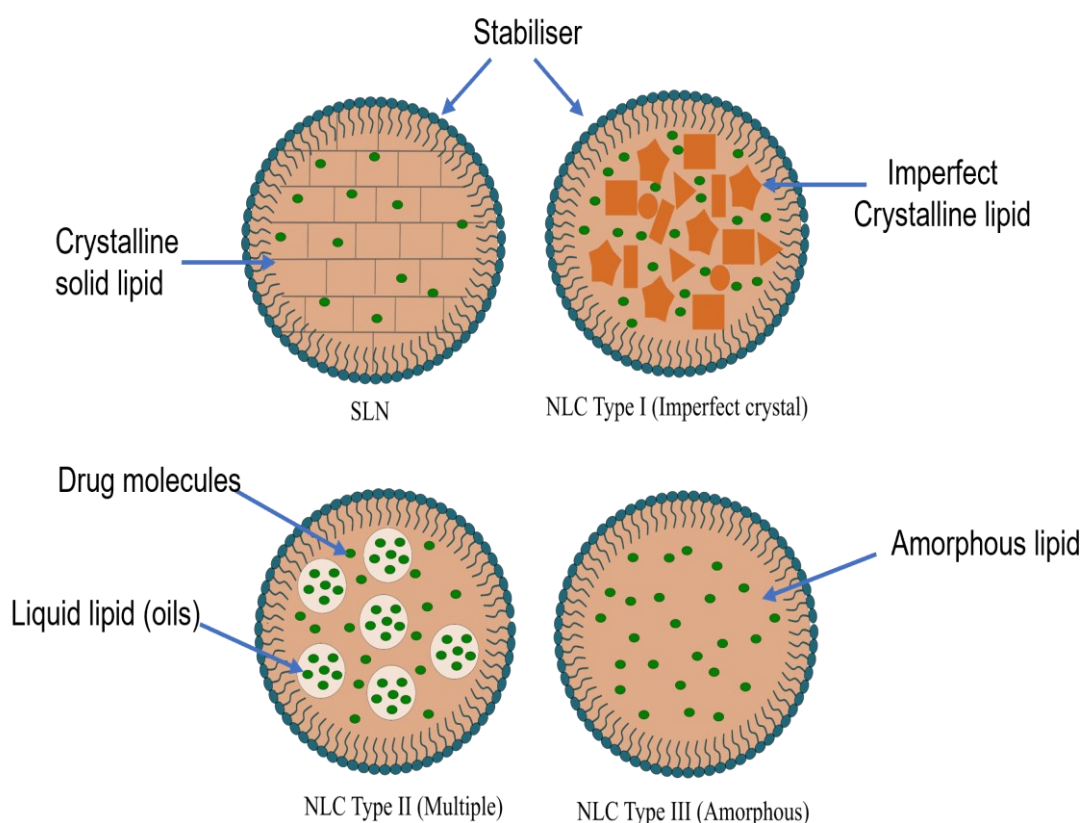


Figure 1.12: Structural differences of SLN and different types of NLC.

### 1.5.1.1. Composition of SLN and NLC

Generally, SLN are composed of solid lipids, surfactants, and drugs, while LNC contain liquid lipid (oil) beside the solid lipid (Figure 1.12). Solid lipid is a broad class that has fatty acids (e.g. Stearic acid), triglycerides (e.g. tristearin), partial glycerides (Compritol® 888ATO), and waxes (e.g. cetyl palmitate)<sup>149,151</sup>. In the case of NLC, the most commonly employed oils are Caproyl™900 and medium chain triglycerides (MCT), such as Miglyol® 812<sup>152,153</sup>. During the choice of the suitable lipid matrix, some factors should be considered, such as drug solubility in the lipid matrix that determines the drug loading capacity, the miscibility of the used solid and liquid lipids, which is a crucial determinant of the stability of the nanoparticles and the drug payload as well, and finally the ease of production of nanometric particles by having low viscosity and/or interfacial tension during the emulsification process<sup>154,155</sup>.

All classes of stabilisers/emulsifiers (concerning charge and molecular weight) have been employed to stabilise the lipid dispersions during the emulsification step and after solidification<sup>149,154,156</sup>. The choice of the emulsifier relies mainly on the administration route which is more limited for parenteral administrations. Preferably, non-ionic surfactants are intensively employed for stabilising lipid nanoparticles as they are more hydrophobic than other surfactants with higher capacity to solubilise hydrophobic drugs, non-irritant or toxic to biological membranes and several non-ionic surfactants may affect the pharmacokinetics of the drug through modulating efflux pumps such as P-glycoproteins and multi-drug resistance of anticancer agents<sup>149</sup>. It was reported that using a combination of emulsifiers might be more efficient in preventing particle aggregation than a single emulsifier. Table 1.3 includes the most commonly used ingredients in SLN and NLC.

Table 1.3: The most commonly used SLN and NLC components<sup>149,151–154,156</sup>.

Component	Examples	
Solid lipids	Fatty acids and alcohols	Lauric acid (C12), Myristic acid (C14), Palmitic acid (C16), and Stearic acid (C18).
	Partial triglycerides	Glyceryl monostearate (Imwitor® 900), Glyceryl monooleate (GMO), Glyceryl palmitostearate (Precirol® ATO5), and Glyceryl behenate (Compritol® 888 ATO)
	Triglycerides	Tristearin (Dynasan® 118), Tripalmitin (Dynasan® 116), Trimyristin (Dynasan 114), and Trilaurin
Liquid lipids (oil)	Miglyol® 812, Labrafac lipophile® WL, Labrafac PG, Capmul MCM, Castor oil, Soyabean oil, Propylene glycol caprylate (Capryol™90), and Decanoic acid, Peceol™	
emulsifiers	Non-ionic surfactants	Tween (20, 60, and 80), Poloxamers (188 and 407), and Span (20 and 80).
	Ionic surfactants	Sodium glycocholate, Sodium deoxycholate, sodium taurocholate, and Sodium lauryl sulphate.
	Amphoteric surfactants	Soybean lecithin (Lipoid S 75 and lipoid S 100) Egg lecithin (Lipiod® E 80) Phosphatidylcholines (Epikuron® 170)

### 1.5.1.2. Preparation methods of SLN and NLC

Several methods have been developed and optimised for the preparation of SLN and NLC (Figure 1.13), including:

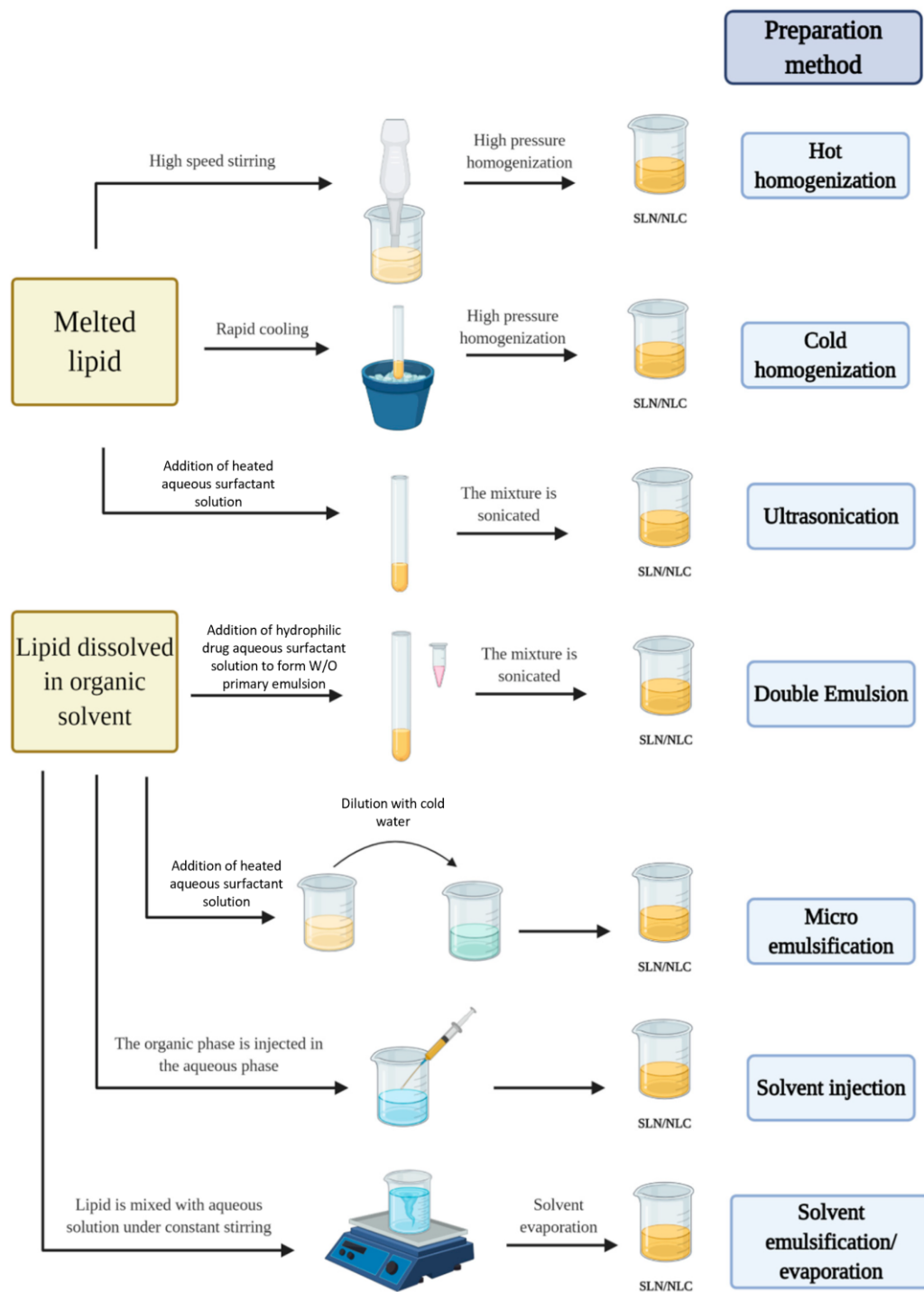


Figure 1.13: Schematic representation of different preparation methods of SLN and NLC. Figure was adapted with permission from reference<sup>157</sup>.

- **High-pressure homogenisation (HPH)**

In HPH, the particle size for the lipid particles is reduced by passing the coarse dispersion with high force (100-2000 bar) through a small orifice (few microns) by which the fluid is accelerated at extremely high speed ( $> 1000$  Km/h) which induces enormously high shear pressure and cavitation resulting in the formation of droplets/nanoparticles. HPH encompass two different techniques, hot and cold HPH. In hot HPH, the lipid phase (solid and liquid) and drug are mixed and heated above the melting point of the solid lipid. Next, lipid phase is mixed with an aqueous surfactant solution at the same temperature and homogenised using a high shear homogeniser (around 10,000-20,000 rpm) at the same temperature for a short time to get the pre-emulsion (coarse emulsion), which is further passed through high-pressure homogeniser for a number of cycles at a definite pressure (In most cases, 3-5 homogenisation cycles at 500-1500 bar are sufficient)<sup>154</sup>. Finally, the nano-emulsion is continuously stirred at room temperature ( $\sim 25^{\circ}\text{C}$ ) till lipid droplets solidify.

On the other hand, Cold HPH is employed for thermolabile drugs in which heating is minimised. In cold HPH, after mixing the drug with the melt lipid phase, they are left to cool up to solidification. Afterwards, the solid material is ground and dispersed into an aqueous surfactant solution at room temperature ( $\sim 25^{\circ}\text{C}$ ), followed by HPH as in the hot method. Increasing the number of cycles or homogenisation pressure often leads to an increase in the particle size owing to particles coalescence as a consequence of the high kinetic energy of the particles<sup>154</sup>. The main advantages of HPH are the rapid processing and scalability with the avoidance of organic solvents while the key drawbacks are drug degradation and loss into the aqueous phase<sup>158</sup>.

- **Emulsification-ultrasonication method**

Similar to hot HPH, the surfactant aqueous phase is added to melt the lipid phase containing the drug and homogenised by a high shear homogeniser to obtain the pre-emulsion followed by ultrasonication using a probe sonicator to get nano-emulsion that are left to cool up under stirring at room temperature ( $\sim 25^{\circ}\text{C}$ ) to solidify producing SLN or NLC. It is considered a straightforward scalable solvent-free method but the downside is the prospect of drug degradation due to high temperature with the risk of metal contamination from probe sonicator<sup>154,157-159</sup>.

- **Solvent injection (solvent displacement) method**

In this method, both drug and lipid matrix are dissolved in a single or a mixture of water-miscible organic solvents at elevated temperature with the aid of sonication. Afterwards, the hot lipid phase solution is mixed with an aqueous surfactant solution at the same temperature under constant mixing. Finally, the dispersion is under stirring to cool down to room temperature ( $\sim 25^{\circ}\text{C}$ ), allowing the solvent to evaporate, forming the lipid nanoparticles<sup>158</sup>.

- **Solvent emulsification-evaporation**

This method is similar to the solvent diffusion method except for a water-immiscible organic solvent, such as chloroform and dichloromethane, which is used instead of a water-miscible one. The main drawback of this method is the existence of residual solvents, especially chloroform and dichloromethane are known to be carcinogenic, which necessitates an additional solvent removal step<sup>158</sup>.

- **Microemulsion method**

This method comprises the formation of microemulsion by mixing the lipid phase (containing melt lipid and the drug) with an aqueous surfactant solution at the same temperature followed by dilution (25 to 50 times) with cold water ( $\sim 2^{\circ}\text{C}$ ). Upon dilution, a nanoemulsion is formed and lipids immediately solidify forming SLN and NLC. Microemulsion method is a simple, scalable, and solvent-free method. However, its limitations are using a large volume of water and the production of diluted dispersions<sup>153,157</sup>.

- **Double emulsion method**

The double emulsion method provides a means of hydrophilic drugs and biomolecules (such as peptides and proteins) of encapsulation into SLN and NLC. Particularly, it has been widely employed to fabricate insulin-loaded SLN and NLC for oral delivery<sup>160-162</sup>. According to this method, a hydrophilic drug and a stabiliser are dissolved in an aqueous medium and emulsified in a water-immiscible organic phase containing dissolved lipids

forming a primary W/O emulsion that is dispersed in an external aqueous phase containing hydrophilic surfactant to produce W/O/W emulsion. Finally, the emulsion is left under stirring to allow solvent evaporation and the precipitation of the lipid-forming SLN and NLC<sup>150,158</sup>. The main drawback of this method is the propensity of hydrophilic drugs to leak out to the external water phase during solvent evaporation resulting in low drug loading<sup>158</sup>.

### 1.5.1.3. Physicochemical properties of SLN and NLC

Physicochemical properties of SLN and NLC, such as particle size, polydispersity, zeta potential, drug entrapment efficiency and stability are very crucial parameters that determine the quality of the nanoparticles.

Particle size (PS) of lipid nanoparticles is considered the first and far most crucial parameter examined during the development of the nanoparticles. As aforementioned, the particle size of nanoparticles determines their biofate and *in-vivo* distribution. Ideally, the PS of nanoparticles is preferred to be between 50 and 200 nm<sup>163</sup>. The polydispersity index (PDI) is also essential to show the presence or the absence of aggregations in the sample. Several formulation parameters (such as lipid composition and concentration, surfactants nature and attention, and also the incorporated drug) and preparation conditions (such as time, temperature, stirring velocity and pressure) could affect the particle size and polydispersity of the produced SLN and NLC. In most reported studies, the higher the lipid concentration used, the bigger the nanoparticles produced<sup>154</sup>. On the contrary, increasing surfactant concentration was found to produce smaller nanoparticles to a certain limit after which increasing surfactant concentration will not affect particle size<sup>163,164</sup>. Moreover, the nature of the lipid matrix has a profound impact on the particle size of produced nanoparticles by the influence of its molecular weight, structure complexity and the viscosity of its melt lipid<sup>154,163</sup>. For instance, NLC produced using glyceryl monostearate (GMS) showed particle sizes between 33 nm and 179 nm, while using Precirol® ATO5 and compritol® 888 ATO produced larger NLC with particle sizes ranging from 108 to 400 nm, and 129 to 323 nm, respectively. This significant difference ( $p < 0.05$ ) could be attributed to the higher melting points and structural complexity of Precirol® ATO5 and Compritol® 888 ATO compared to GMS<sup>153</sup>. Method conditions

also substantially impact the particle size for lipid nanoparticles. For instance, cold-HPH was reported to produce larger particles compared to hot-HPH<sup>163</sup>. Additionally, increasing sonication time in the emulsification ultrasonication method was proven to reduce the particle size till a certain limit beyond which a marginal effect was noticed<sup>165,166</sup>.

Zeta potential (ZP) is another critical parameter that influences the produced nanoparticles' long-term stability; the higher the zeta potential, the higher the electrostatic repulsion between the nanoparticles, rendering them more resistant to aggregation. According to the literature, a zeta potential higher than 30 mV is considered ideal to guarantee the electrostatic stability of nanoparticles<sup>146,163</sup>. Most SLN and NLC have a negative zeta potential due to the lipid matrix's carboxylic acid groups of free fatty acids. However, the nature of the used surfactant may also affect the value of ZP, particularly in the case of ionic surfactants. Furthermore, the incorporated drug may also influence the ZP due to the surface deposition of drug molecules<sup>163,167</sup>.

Entrapment efficiency (EE%), which measures the extent of drug incorporation into lipid nanoparticles, is another vital factor during the development and optimisation stage that is meant to be maximised. EE% is primarily influenced by the drug solubility in the lipid matrix. Also, it was found that the complexity of the lipid structure could affect the EE%. For instance, Andalib et al. found that using cholesteryl stearate instead of cholesterol increased the EE% of 5-FU into NLC<sup>168</sup>. Similarly, using a blend of structurally different lipids can increase EE% by introducing more voids in the lipid structure to accommodate more drug molecules<sup>169</sup>. Furthermore, using the appropriate surfactant nature and concentration can enhance the stability of the incorporated drug by creating a protective layer around the nanoparticles<sup>153</sup>. However, it was reported that high surfactant concentrations might increase drug solubility in the aqueous phase, resulting in repartitioning the incorporated drug to the dispersion medium<sup>163</sup>. In addition, the initial drug amount can affect EE%<sup>163,170</sup>. Negi and co-workers reported that increasing the initial irinotecan amount resulted in increasing EE% but this was declined once the lipid had reached its maximum limit of drug accommodation<sup>171</sup>.

Depending on the position of the drug incorporation in the SLN, there are three different models of drug incorporation: homogenous matrix model, drug-enriched core model and

drug-enriched shell model (Figure 1.14). In the homogenous matrix model, also known as the solid solution model, the drug molecules are homogeneously distributed in the lipid matrix either molecularly or in the form of amorphous clusters. This model is common with the cold-HPH method without surfactants<sup>150,155</sup>. While in the drug-enriched core model the drug molecules are concentrated in the central core of the lipid nanoparticle. This model happens when the drug precipitates before lipid solidification. One way to make that is to dissolve the drug in the liquified lipid till its saturated solubility followed by emulsification. When the emulsion cools down, the drug becomes supersaturated in the core of the melt lipid and precipitates before lipid solidification. This model usually exhibits prolonged drug release governed by Fick's first law of diffusion<sup>150</sup>. On the contrary, drug molecules are condensed in the outer layer of the lipid nanoparticles in the drug-enriched shell model. This model occurs in Hot-HPH when the drug molecules partition from the lipid phase into the aqueous phase at a high temperature. During the cooling step, drug molecules repartition to the lipid phase due to the drop in aqueous solubility resulting in the concentration of the drug molecules on the lipid nanoparticle shell, making nanoparticles show burst drug release<sup>155</sup>.

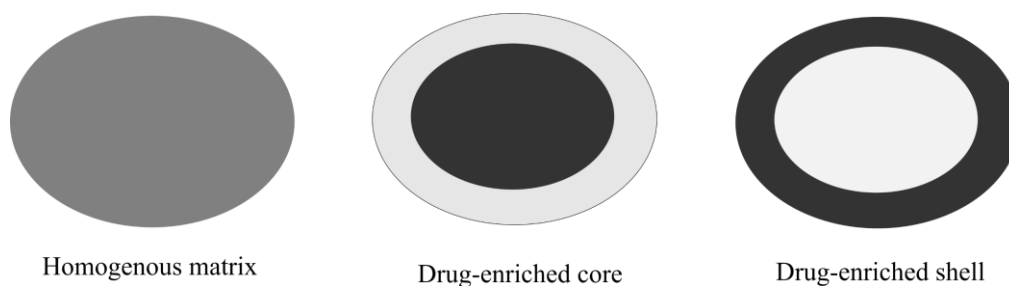


Figure 1.14: Different drug incorporation models in SLN.

Although SLN and NLC offer several advantages compared to other nanodelivery systems, they have some drawbacks that may impede their clinical applications, such as the high risk of polymorphic transitions (from  $\alpha$  to  $\beta'$  and finally to the stable  $\beta$  form), which is also known as recrystallisation<sup>146</sup>. This causes stability challenges during administration or storage, resulting in drug expulsion and particle size growth<sup>146</sup>. As mentioned before, the incorporation of liquid lipids, as in the case of NLC, and the use of

structurally different solid lipids as well as the proper surfactant may retard the polymorphic transition<sup>145,154,172</sup>.

Another limitation during the preparation of lipid nanoparticles is the possibility of the formation of supercooled lipid melt, which is the phenomenon that lipid crystallisation (solidification) may not occur although the sample is stored at a temperature lower than the melting point of the lipid. In other words, the lipid remains in a liquid state, forming nanoemulsions rather than solid lipid nanoparticles<sup>154</sup>. The main reason behind that is the size dependence of the crystallisation process, as crystallisation requires a critical number of nuclei to be initiated. This essential number is less likely to exist in small nanosized droplets. Besides the size, the type of surfactant and incorporated drugs can affect the crystallisation. The solid-state of the lipid could be confirmed by NMR, X-ray, or DSC<sup>154</sup>.

The co-existence of different colloidal structures (such as micelles, liposomes, supercooled melts, and drug nanoparticles) is another concern during the preparation of lipid nanoparticles which may affect the stability, the kinetics of drug release and *in-vivo* behaviour after administration. These different colloidal structures could be formed due to the complex structure of SLN and NLC that may involve the employment of surfactants, and phospholipids beside the solid and the liquid lipids. Unfortunately, this phenomenon is unavoidable but could be minimised by using appropriate proportions of the ingredients. The coexistence of different nanostructures could be detected by magnetic resonance techniques, such as nuclear magnetic resonance (NMR) and electron spin resonance (ESR)<sup>172</sup>.

Also, gelation of lipid nanoparticles dispersion could happen by the transformation of the low-viscosity lipid dispersion into a viscous gel. This phenomenon could be induced by the exposure of the lipid dispersion to other surfaces (such as a syringe needle) or shear forces. This irreversible process makes it life-threatening if that happens during i.v. injection<sup>167</sup>. Freitas reported that high storage temperatures, light exposure and mechanical stress can promote gelation of 10% Compritol® with 1.2% Poloxamer<sup>160</sup>. In another study, the same research group found that high lipid concentrations and high ionic strength also promote gelation<sup>173</sup>. On the other hand, the use of co-emulsifying surfactants with high mobility (such as glycocholate) can retard or prevent gelation<sup>167,174</sup>.

#### 1.5.1.4. Nanotoxicology of lipid nanoparticles

The toxicology of nanomaterials is a growing concern nowadays, particularly about nanoparticles found in the environment and nanomaterials intended for medicinal application. The nanotoxicology of SLN and NLC has two aspects, physical and formulary<sup>175</sup>. Like any other nanoparticles, the physical aspect includes particle size and surface charge. As mentioned before, particles with sizes larger than 200 nm are prone to opsonisation and recognition by the mononuclear phagocyte system (MPS) and reticuloendothelial system inducing the immune responses. Also, positively charged nanoparticles are well reported to induce cytotoxic effects with cells due to the electrostatic interaction with the negatively charged phospholipids of cellular membrane<sup>175,176</sup>. So, extra caution should be considered when using cationic ingredients to prepare lipid nanoparticles, such as cetyltrimethylammonium bromide (CTAB) as cationic surfactant<sup>177</sup> or Stearylamine as a lipid matrix<sup>178</sup>.

On the other hand, SLN and NLC are considered relatively safe colloidal carriers compared to different nanocarriers, such as polymeric nanoparticles<sup>154,179</sup>, as they are produced from physiological, biocompatible and biodegradable lipids. However, the status of SLN and NLC excipients must be considered in the context of the administration routes<sup>146,172</sup>. The topical and oral administration of SLN and NLC are free of excipient-related issues. All excipients currently utilised in formulating pharmaceutical and cosmetic ointments and creams may be used for topical SLN. For oral SLN and NLC, all lipids and surfactants employed in conventional dosage forms, such as tablets, pellets, and capsules, can be utilised. In addition, all chemicals with GRAS or GRAS-accepted status may be used. For parenteral administration, the situation is slightly different. Currently, no parenteral injectable products on the market contain solid lipid particles. Consequently, a toxicological investigation would be required.

To formulate parenteral SLN and NLC, surfactants accepted for parenteral use such as lecithin, Poloxamer 188, Tween 80, and sodium glycocholate should be employed. Generally, surfactants are considered the decisive ingredient in the toxicity of nanoparticles<sup>180–182</sup>. According to the literature, poly-vinyl alcohol (PVA) and sodium dodecyl sulphate (SDS) used as surfactants lead to higher cytotoxicity than Poloxamers and Tween 80<sup>183</sup>. However, there are some discrepancies about whether the cytotoxicity

of surfactants is attributed to the free or the bound portion on nanoparticles; some reports found that binding surfactants on the surface of nanoparticles increase their tolerability<sup>180,184</sup> while other studies suggested that bound surfactants are more toxic than free ones<sup>182</sup>.

#### **1.5.1.5. Application of SLN and NLC for cancer therapy**

Since SLN/NLC were first introduced by Müller et al.<sup>148,172</sup>, both systems have been employed to deliver many hydrophilic and hydrophobic drugs using different routes of administration including oral<sup>156</sup>, dermal, parenteral<sup>185</sup> and pulmonary<sup>186</sup>. Recently, many studies have been investigating the potential of using SLN/NLC in the delivery of anticancer agents.

Both systems have inherent distinctive properties that could be exploited to enhance the therapeutic outcomes of anticancer agents, such as the submicron particle size that enables the intravenous administration of hydrophobic anticancer agents, avoiding the side effects evolved from the use of solvent systems (such as Cremphor EL to dissolve paclitaxel)<sup>187–189</sup>. Also, small particle size (<500 nm) and the hydrophilic surface of nanoparticles are well reported to enable the evasion of the uptake by the mononuclear phagocyte system (MPS) and reticuloendothelial system (RES), allowing prolonged circulation time enough for the passive accumulation of anticancer agents in tumour tissue due to their leaky vasculature (EPR)<sup>190,191</sup>.

In addition, encapsulation of anticancer agents into lipophilic matrix imparts a sustained and controlled drug release character regardless of the pH environment<sup>192</sup>. Fontana et al. developed stable Tamoxifen citrate-containing SLN that demonstrated sustained release in various *in-vitro* aqueous environments. Tamoxifen SLN displayed a more prolonged release of the drug in plasma, which increased its bioavailability. *In-vitro* cytotoxicity studies on MCF-7 cell lines demonstrated that the cytotoxic impact of the drug-loaded SLN was significantly ( $p < 0.05$ ) greater than that of the free drug without compromising bioavailability<sup>193</sup>.

Conventional anticancer agents are well known to exert non-specific side effects due to their poor bioavailability and detrimental impact on healthy cells. For instance, docetaxel,

a widely used broad-spectrum anticancer agent for solid tumours such as non-small-cell lung carcinoma, has serious side effects including neutropenia, myelosuppression and anaemia. Yuan et al. encapsulated docetaxel in SLN to reduce its side effects and augment its anticancer potency. A trimyristin lipid matrix stabilised by soyabean lecithin was employed to prepare the SLN using a high-pressure homogenisation method. Docetaxel-loaded SLN exhibited a superior antiproliferative effect on MCF-7 cell lines with less inflammatory effect on primary mouse bone marrow cells than free drugs. Additionally, the encapsulation of docetaxel in SLN demonstrated low myelosuppression toxicity when tested in beagle dogs<sup>194</sup>.

Moreover, lipid nanoparticles can serve for the co-delivery of a combination of anticancer agents for synergetic effects. For example, both paclitaxel (PTX) and doxorubicin (DOX) were co-encapsulated into NLC made of Compritol® 888 ATO and oleic acid (PTX-DOX NLC) producing nanoparticles with a mean size of  $129.3 \pm 4.2$  nm. PTX-DOX NLC exhibited enhanced cytotoxicity *in-vitro* on NCL-H460 cell line and augmented antitumor activity *in-vivo* in BALB/c nude mice bearing human non-small cell lung carcinoma xenograft tumor model compared to individual anticancer agent solutions<sup>195</sup>. Furthermore, lipid nanoparticles have a potential theranostic function by co-loading different contrasting agents (such as superparamagnetic iron oxide, gadolinium 'Gd' and quantum dots 'QD') beside the anticancer agents<sup>196,197</sup>. For instance, SLN was used to deliver Paclitaxel and siRNA for lung cancer therapy by incorporating QD as an in-situ imaging agent. Paclitaxel and QD were dispersed throughout the solid lipid matrix, whereas the anionic siRNA was electrostatically coupled to the cationic outer surface. The combination of paclitaxel and siRNA loaded in SLN rapidly accumulated in lung carcinoma and demonstrated a synergistic antitumor activity. Significantly, the QD fluorescence in SLN made it feasible to detect the increased *in-vivo* cellular uptake of SLN on-site while reducing the uptake by off-site cancer cells<sup>198</sup>.

Surface modification of SLN/NLC can also be used to modulate plasma circulation time and target the delivery of anticancer agents for certain tissues. Madan and colleagues noted a higher plasma concentration of the anticancer agent noscapipe following intravenous injection of drug-loaded SLN decorated with PEG to mice compared to the unmodified carrier and free drug. This was ascribed to the presence of a PEG brush on the surface of the nanoparticles, which impeded their uptake by the reticuloendothelial

system (RES)<sup>199</sup>. Additionally, the surface conjugation of SLN/NLC with active targeting ligands (such as folic acid, hyaluronic acid, transferrin and monoclonal antibodies) can confer an improved and selective accumulation of anticancer agents into tumour tissue, not healthy ones, lowering their systemic toxicity. Yassemi, A. et al. developed folic acid-targeted SLN loaded with letrozole (FA-LTZ-SLN) using the emulsification evaporation method for breast cancer therapy<sup>200</sup>. It was found that FA-LTZ-SLN was significantly ( $p < 0.05$ ) more cytotoxic than untargeted SLN and free drug against MCF-7 cancer cells *in-vitro* with negligible cytotoxicity toward MCF-10A normal cells<sup>200</sup>.

### 1.5.2. Lipid nanocapsules (LNC)

Lipid nanocapsules are lipid-based biomimetic nanocarriers that mimic lipoproteins. LNC were first developed and patented by Heurtault et al.<sup>201,202</sup>. They have a hybrid structure between polymer nanocapsules and liposomes. In contrast to liposomes, which are manufactured via techniques utilising organic solvent and are leaky and unstable in biological fluids, LNC are produced by a solvent-free, low-energy approach and exhibit a high level of stability (with physical stability up to 18 months)<sup>203</sup>. Typically, they comprise an oily core composed of medium-chain triglycerides surrounded by a shell of lecithin and a pegylated surfactant (Figure 1.15). Their preparation relies on the phase-inversion temperature (PIT) phenomenon, used originally for the preparation of emulsions, which results in the creation of lipid nanocapsules with excellent monodispersity<sup>203</sup>.

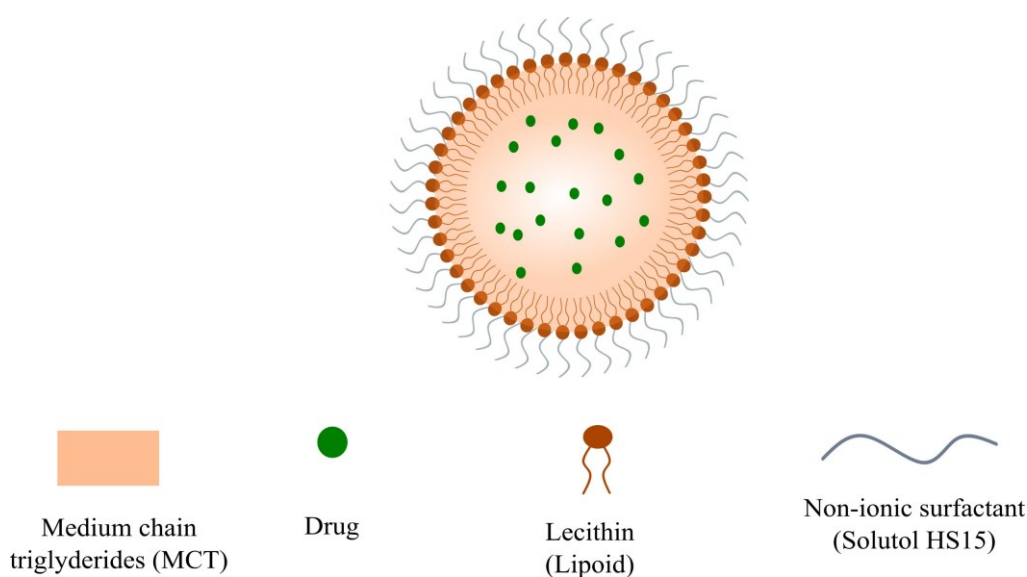


Figure 1.15: Schematic representation of the typical composition of LNC.

### 1.5.2.1. Composition of LNC

LNC formulation consists principally of at least three major components: an oily phase, an aqueous phase, and a non-ionic surfactant. The oily phase is mainly composed of medium-chain triglycerides of capric and caprylic acids marketed commercially as Labrafac® WL 1349. The primarily used non-ionic surfactant is Solutol® HS 15. The aqueous phase is made up of Milli-Q® water and sodium chloride salt (NaCl). Furthermore, Lipoid®, a lipophilic surfactant made of 69% phosphatidylcholine soya bean lecithin, is employed in modest amounts to improve LNC stability significantly. All LNC components are FDA approved for topical, oral and parenteral administration<sup>203</sup>. The role of each component of LNC is summarised in Table 1.4.

Table 1.4: Factors affecting the formulation and stability of LNC produced using the phase-inversion temperature (PIT) process.

<b>Factors</b>	<b>Effect</b>
Non-ionic surfactant (Typically, Solutol® HS)	Essential for the formation of LNC, stability and prolonged blood circulation.
Heating-cooling cycles	Formation of LNC and enhancing its quality
Oily phase (Typically, Labrafac®)	Accommodation of the hydrophobic drugs, construction of the core, and increase LNC size.
NaCl	Lowering PIT
Lipophilic surfactant (lipoid®)	Construction of the rigid LNC shell and enhancement of stability

### 1.5.2.2. Preparation of LNC

This kind of lipid nanocapsules requires a two-step technique to prepare as described by Heurtault et al <sup>202</sup>. The first step entails the formation of a W/O emulsion by heating the mixture of all the components (whose proportions change according to the study) from ambient temperature to T2 temperature, which is higher than the phase-inversion temperature (PIT). After this, the temperature is lowered to T1, much below the PIT, where an O/W emulsion is formed. The phase-inversion zone (PIZ) is crossed many times during the temperature cycling between T2 and T1. The second step is conducted during

the last cooling cycle at the phase inversion zone via an irreversible shock induced by sudden dilution with cold water (2° C) added to the mixture. This results in the formation of stable nanocapsules by breaking the microemulsion system formed in the PIZ (Figure 1.16).

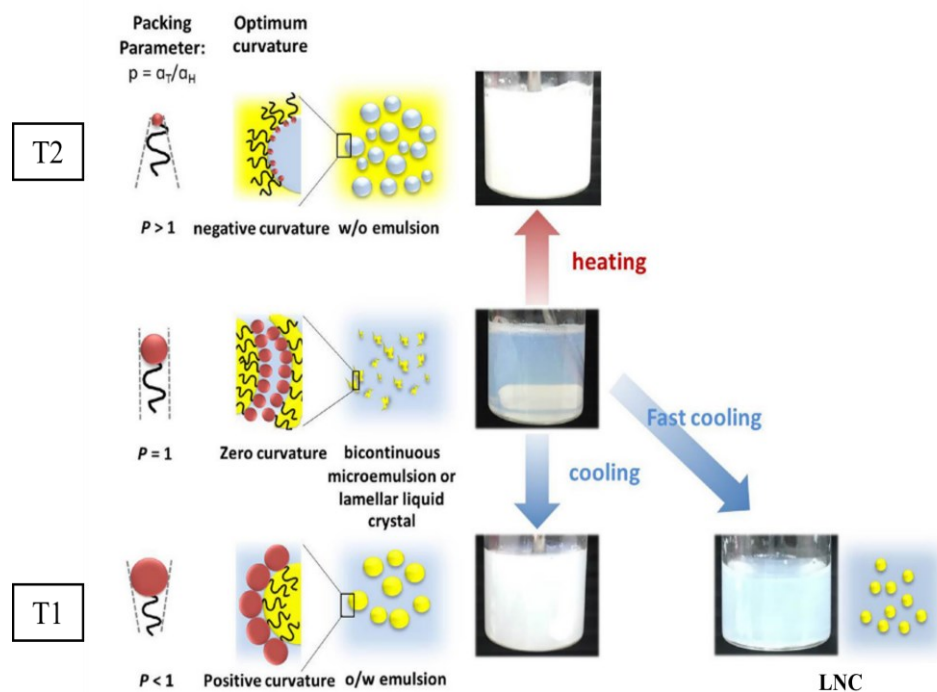


Figure 1.16: Schematic representation of the formation of lipid nanocapsules (LNC) by the PIT method. Figure was modified with permission from reference<sup>204</sup>.

The impact of using different composition proportions on the formation and the physical properties of the formed LNC have been intensively investigated<sup>201,205,206</sup>. Previous studies showed that increasing the Solutol HS15 ratio results in decreasing particle size of LNC<sup>202</sup>. Moreover, replacing Solutol HS with other non-ionic surfactants (namely, Cremphor EL, TPGS, Simulsol 4000, Tween 20, and Tween 80) did not influence the feasibility zone of LNC with a minimal change in their particle size<sup>206</sup>. Furthermore, the temperature cycles across the PIZ play a crucial role in LNC formation. Increasing the number of cycles promotes LNC production and enhances the size and dispersion of LNC. Though, at high surfactant concentrations, several cycles do not seem to be required<sup>207</sup>. Additionally, increasing NaCl concentration was found to lower the phase-inversion temperature, which could be advantageous for encapsulating thermolabile hydrophobic drugs<sup>202</sup>. Furthermore, within the screened oils (Labrafac® WL 1349, Ethyl palmitate, Ethyl oleate, Ethyl myristate, Isopropyl myristate, and Octyldodecyl myristate), it was

found that changing the length of the carbon chain of fatty acids (C<sub>14</sub> and C<sub>18</sub>) or oil hydrophilic-lipophilic balance (HLB) affected neither particle size of LNC nor phase inversion temperature<sup>202</sup>. Nevertheless, other studies conducted to form nanoemulsions by PIT found that increasing the alkyl chain length of hydrocarbon oil led to increasing the PIT and more heat-cooling cycles were required for the formation of stable nanoemulsions<sup>204,208</sup>. Lastly, increasing the phosphatidylcholine content (between 40% and 90%) in the lecithin (lipophilic surfactant) increased the particle size of LNC. However, the use of charged lecithin did not allow nanocapsules formation<sup>202</sup>.

Generally, LNC exhibit particle sizes ranging from 20 to 100 nm with a very narrow range of dispersity (PDI < 0.3). Also, LNC have a negative zeta potential (ZP) due to the presence of phospholipids molecules<sup>209</sup> and the PEG dipoles in their shell<sup>210</sup>.

### 1.5.2.3. Phase inversion temperature (PIT) principle

The PIT method was first reported by Shinoda and Saito<sup>211</sup> and is now commonly used in industry. PIT is the “temperature or temperature range at which the hydrophilic and lipophilic properties of a non-ionic surfactant just balance”<sup>208</sup>. This method is based on the temperature-dependent changes in the solubility of non-ionic polyoxyethylene-type surfactants. As the temperature increases, this kind of surfactant becomes lipophilic owing to the dehydration of polyoxyethylene chains caused by the breakage of hydrogen bonds with water molecules<sup>204</sup>. As depicted in Figure 1.16, At low temperature (T<sub>1</sub>), the surfactant monolayer has a broad, spontaneously positive curvature (packing parameter < 1) that forms O/W emulsions with high conductivity. By raising the temperature, the spontaneous curvature becomes negative (packing parameter > 1), resulting in developing W/O emulsion with a sharp drop in conductivity. This indicates that a phase inversion from an O/W to a W/O emulsion occurs in the PIZ. This zone displays a continuous fluctuation in conductivity between W/O and O/W emulsions ascribed to bicontinuous microemulsion structures in which the spontaneous curvature goes near zero<sup>204,207</sup>.

Although both nanoemulsions and lipid nanocapsules (LNC) could be prepared using PIT, the rigid shell of LNC comprised of crystallised lecithin and the non-ionic surfactant, since the final formulation temperature is lower than the melting point of the non-ionic surfactant (around 30° C), inhibits the coalescence of the droplets and leads to the

formation of stable LNC suspensions at an ambient temperature allowing their freeze-drying with the aid of cryoprotectants such as mannitol, glucose and trehalose<sup>201,212</sup>. Among all employed cryoprotectants, trehalose provided the best polydispersity index after redispersion<sup>201,212</sup>. In contrast, nanoemulsions are only kinetically stable, and one of their major instability issues is the increase in the Ostwald ripening rate during storage resulting in oil diffusion from small to larger droplets<sup>213</sup>.

#### **1.5.2.4. Applications of LNC for cancer therapy**

The availability of such nanoparticulate formulations allows for the encapsulation of many types of molecules with anti-cancer activity employing various drug delivery strategies to the tumour<sup>214-222</sup>. In addition, these nano-cargos provide an effective drug-loading mechanism with high encapsulation rates. LNC provide highly intriguing characteristics that might be exploited to improve the efficacy of anticancer agents such as:

##### **a. P-glycoprotein inhibition**

P-glycoprotein (P-gp), an ATP-dependent drug efflux pump, functions as a transporter for numerous lipophilic and cationic drugs/substrates, limiting intestinal absorption and constraining the accumulation of anticancer agents in adequate quantities inside cells<sup>223</sup>. This is one of the primary causes of tumour cell resistance to several anticancer drugs such as paclitaxel, doxorubicin, and etoposide<sup>224</sup>. Interestingly, LNC demonstrate good P-gp inhibiting properties owing to their components, particularly Solutol®<sup>225,226</sup>. Subsequently, Paclitaxel-loaded LNC were studied for the impact of their P-gp inhibitory effect on inhibiting intestinal efflux promoting the oral bioavailability of paclitaxel after oral administration<sup>216,227</sup> and on mitigating the multidrug resistance towards Paclitaxel after intravenous administration allowing more drug accumulation in cancerous cells<sup>216</sup>. Furthermore, etoposide-loaded LNC demonstrated higher levels of cytotoxicity on glioma cell lines compared to free etoposide solution. This observation was proposed to be due to enhanced cellular uptake due to the P-gp inhibitory effect of LNC<sup>221</sup>. The same observations were reported after treating small cell lung cancer (SCLC) with etoposide-loaded LNC<sup>228</sup>.

## **b. Prolonged blood circulation and passive targeting**

As previously mentioned (in section 1.2), colloidal drug nanocarriers are prone to rapid clearance from systemic circulation after intravenous administration based on their sizes<sup>229,230</sup>. Besides the particle size of nanoparticles, the nature of the particles' surface also influences the rate of nanoparticles elimination; it was found that neutral and hydrophilic surfaces, like in the case of PEG, are more resistant to opsonisation by plasma proteins allowing prolonged circulation time in bloodstream<sup>78,231</sup>.

Consequently, the grafting of LNC with longer PEG chains using PEG1500 stearate instead of PEG 660 stearate (Solutol® HS15) resulted in prolonging plasma elimination half-life after intravenous injection into healthy rats<sup>232</sup>. In addition, it has been shown that LNC may be retained longer in systemic circulation by post-inserting distearoyl phosphatidylethanolamine DSPE-PEG 2000 or DSPE-PEG 5000 at their surface, with half-lives of over 6 h following intravenous administration<sup>233</sup>.

Additionally, size also plays a crucial influence in the penetration and accumulation of nanocarriers in diseased tissues, particularly tumours. Increasing the size of nanocarriers is known to have a detrimental effect on their vascular penetration. For tumour tissues, the enhanced permeation and retention (EPR) effect, which is commonly relevant to nanoparticles ranging in size from 30 to 200 nm, is responsible for the passive accumulation of nanocarriers in tumour tissues<sup>78,234</sup>. In this context, docetaxel-loaded LNC coated with DSPE-PEG 2000 accumulated markedly and substantially in subcutaneous tumours of C26 colon adenocarcinoma, while uncoated LNC exhibited poor tumour uptake. Tumour docetaxel concentrations rose throughout a 12-hour sampling period and were significantly ( $p < 0.05$ ) higher than those of a Taxotere® control formulation<sup>235</sup>. LNC seem to meet these essential parameters due to their nanoscale size range (20-100 nm) and their high-density PEG 660 surface-coating shell allowing both prolonged blood circulation and passive accumulation in the tumour tissues<sup>203</sup>.

In light of that, Morille, M. *et al.* designed a long-circulating DNA lipid nanocapsules for passive tumour targeting<sup>217</sup>. In this study, DNA was complexed with cationic lipids and encapsulated into LNC that were furtherly coated with either DSPE-mPEG2000 or F108 poloxamer through post insertion method to make them stealthy. Although the shorter PEG arm of DSPE-mPEG2000 compared to F108, DSPE-mPEG2000 coated LNC

showed a superior efficiency in evading the complement activation and phagocytosis which was translated into longer *in-vivo* circulation time in mice, 5-fold greater, than non-coated LNC<sup>217</sup>. Furthermore, *in-vivo* fluorescent imaging revealed an augmented tumour accumulation for these coated LNC due to passive targeting without causing liver damage<sup>217</sup>. The same finding was observed after surface coating of LNC with DSPE-PEG2000 to deliver small interfering RNA to malignant melanoma<sup>236</sup>. These features were confirmed by other studies, in which PEG-coated LNC exhibited enhanced biodistribution and extended blood circulation time after intravenous injection<sup>231,237,238</sup>.

### **c. Active targeting**

Active targeting, in contrast to passive targeting, includes the attachment of a targeting moiety, such as a monoclonal antibody (MAb) or a ligand, to selectively deliver the drug to diseased regions or to penetrate biological barriers based on molecular recognition mechanisms<sup>239</sup>. Accordingly, different studies have employed active targeting of LNC to tumour tissues. For instance, cRGD peptides, known to be recognised by  $\alpha_v\beta_3$  integrins expressed on tumour endothelium, were conjugated to DSPE-PEG<sub>2000</sub>-maleimide via thiol conjugation with the reactive maleimide group followed by post-insertion into LNC<sup>224</sup>. cRGD-LNC demonstrated improved binding and internalisation into U87MG glioma cells compared to unmodified LNC. Furthermore, after intravenous injection into mice bearing the same subcutaneous xenograft, cRGD-LNC remained in the blood circulation for up to 3 h with mitigated capture by the RES organs with a significantly ( $p < 0.05$ ) higher tumour accumulation compared to unmodified LNC<sup>224</sup>.

Finally, the surface grafting of LNC can also be achieved by simple physicochemical adsorption. This strategy was adopted by Karim et al.<sup>240</sup> for the functionalisation of the surface of ferrocifen-loaded LNC with the NFL peptide, which is known to preferentially penetrate glioblastoma cells and disrupt the microtubule network<sup>241</sup>. Because of this functionalisation, the uptake of the functionalised LNC by U87MG cells was greater than that of unmodified LNC and lower in astrocytes (normal human astrocytes). This uptake seemed to be a mix of micropinocytosis, clathrin-mediated, and caveolin-mediated endocytosis<sup>240</sup>.

### 1.5.3. Polymeric micelles (PMs)

During the last decades, polymeric micelles have attracted substantial interest as a multifunctional nanotechnology-based delivery strategy for poorly water-soluble drugs<sup>242–248</sup>. Micelles are typically formed by the self-aggregation/assembly of amphiphilic polymers, with the hydrophobic portion of the polymer in the inner core and the hydrophilic portion in the exterior shell (Figure 1.17). As a result of this property, the potential benefits of polymeric micelles as delivery vehicles are twofold: first, the hydrophobic core functions as a solubilisation depot for poorly soluble drugs and second, the hydrophilic shell provides some protection against opsonin adsorption, which contributes to a longer blood circulation time and improved blood stability<sup>247,248</sup>.

Polymeric micelles are composed of block-copolymers with hydrophilic and hydrophobic blocks. These blocks could be arranged in different configurations: A-B type copolymers (diblock copolymers), A-B-A type copolymers (triblock copolymers), and grafted copolymers. Grafted polymers are polymers with a hydrophilic backbone and one or more hydrophobic side chains or vice versa. The most frequently used polymers for hydrophobic core formation are polyesters, polyamino acids, and polyethers<sup>249</sup>. Commonly used core-forming molecules are poly(propylene oxide) (PPO), poly(D,L-lactic acid) (PDLLA), poly( $\epsilon$ -caprolactone) (PCL), poly(lactic-co-glycolic acid) (PLGA), poly(L-aspartate) and poloxamers<sup>249</sup>. In recent years, despite they are not strictly block copolymers, a variety of biomaterials have been utilised to produce micellar systems. D- $\alpha$ -tocopheryl polyethylene glycol 1000 succinate (TPGS) is a PEGylated vitamin E capable of loading hydrophobic pharmaceuticals<sup>250–253</sup> and inhibiting P-glycoprotein (P-gp)<sup>254</sup>. Furthermore, the *in-vitro* and *in-vivo* cytotoxic activity of TPGS on many cancer cell lines has been reported as it has apoptosis-promoting properties<sup>255–257</sup>. In addition, the polyvinyl caprolactam–polyvinylacetate–polyethylene glycol graft copolymer (Soluplus®) is a recently explored polymer with amphiphilic characteristics that has effectively solubilised several weakly water-soluble drugs. Owing to its low CMC value, Soluplus micelles have great dilution stability<sup>253,258–260</sup>.

Recently, the development of mixed micelles, by combining two or more distinct amphiphilic polymers, has evolved as an interesting approach for optimising micellar systems' properties and overcoming the disadvantages of single micelles. Compared to

single PMs, mixed micellar systems have the following benefits: better thermodynamic (lower CMC) and kinetic stability, increased drug loading capacity, more precise size control, and ease of surface functionalisation<sup>261</sup>.

### 1.5.3.1. Preparation of polymeric micelles

The main driving force behind amphiphilic polymer self-assembly is hydrophobic interactions, which decrease the system's free energy by removing the hydrophobic regions of the polymer from the aqueous environment. The critical micelle concentration (CMC) is the concentration at which unimers (non-assembled amphiphilic polymer molecules) begin to assemble into polymeric micelles. As shown in Figure 1.17, amphiphilic molecules exist separately in an aqueous environment below the CMC; above the CMC, unimers exist in equilibrium with polymer micelles<sup>242,261</sup>.

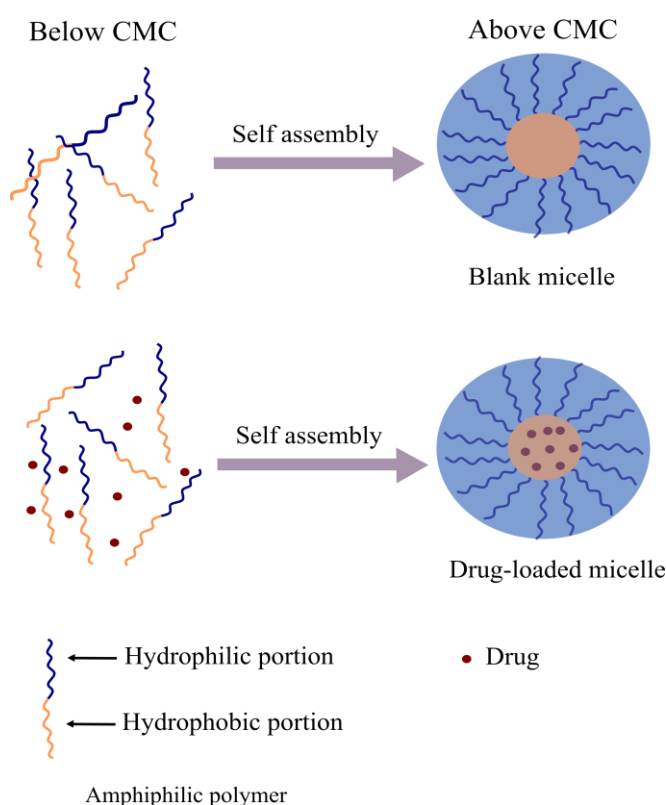


Figure 1.17: Schematic representation of the self-assembly process of polymeric micelles above CMC.

The closed association model is one of the finest models for describing micellar colloidal solutions. Supposing that each micelle is composed of  $n$  amphiphilic unimers ( $M$ ) and

micelle formation was in a single step which is:  $nM \rightarrow M_n$ . The equilibrium constant for this process could be described by Eq. (1.1):

$$K_{micellisation} = \frac{[M_n]}{[M]^n} \quad \text{Eq. (1.1)}$$

From Eq. (1.1), it could be concluded that the rate of micellisation is strongly dependent on the concentration of the unimers  $[M]$ . Moreover, the temperature also has an influence on the concentration at which micelles form (CMC), which could be derived from Eq. (1.2)

$$\Delta G^\circ = RT \ln(CMC) \quad \text{Eq. (1.2)}$$

Where  $\Delta G^\circ$  is the Gibbs free energy change, R is the gas constant, T is the temperature (in Kelvins), and CMC is the critical micelle concentration.

The practical significance of the equation is that increasing the temperature lowers CMC, allowing CMC to form at lower unimer concentrations. Clinically, introducing polymeric micelles into the physiological temperature would lessen their CMC suggesting better resistance to dissociation by dilution<sup>242</sup>.

The choice of the appropriate preparation method for polymeric micelles relies on the physicochemical properties of the polymer and the proposed organic solvent; for more hydrophilic polymers, polymers can directly be dispersed in the aqueous medium while the use of organic solvent is a must in case of more hydrophobic polymers<sup>261</sup>. As depicted in Figure 1.18, According to the organic solvent, the dialysis method is used with water-miscible non-volatile solvents, while both the solvent evaporation and thin film hydration method are applicable for volatile solvents. On the other hand, in the emulsification method, the polymer is dissolved in a water-immiscible solvent and physically entrapped in the solvent droplets during the formation of an O/W emulsion forming the micellar dispersion after solvent evaporation. In this case, the emulsification process parameters (such as O/W ratio, emulsification power and time) can influence the physical properties of the formed micelles<sup>247,261</sup>.

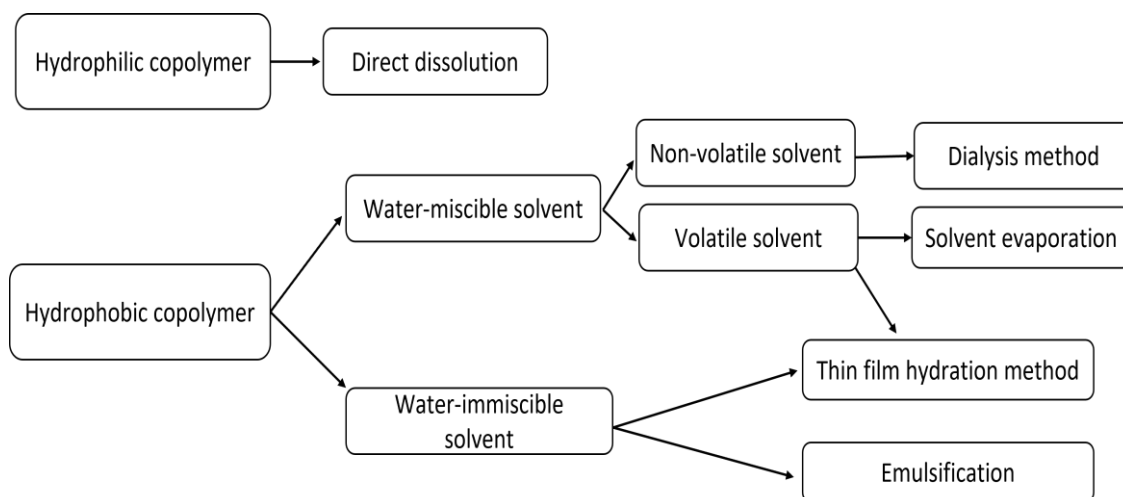


Figure 1.18: Method selection for the preparation of polymeric micelles.

### 1.5.3.2. General properties of polymeric micelles

The appropriate application of PM as nanocarriers for drug delivery relies on several parameters such as micellar size, micelles stability, drug loading capacity and the existence of functionalities<sup>262</sup>. The size of micelles is one of their key features. A successful performance as drug delivery systems is determined, depending on the route of administration, by a suitable size. For instance, micelles with a size range of 10–200 nm are able to avoid clearance at the kidney and avoid capture by the reticuloendothelial system (RES) in the liver and spleen, making them acceptable as drug delivery systems and are especially appropriate for intravenous administration<sup>263</sup>. On the other hand, it has been found that nanocarriers smaller than 300 nm may swiftly overcome gastrointestinal mucociliary clearance when used for oral delivery<sup>264</sup>. In addition, there are a variety of variables that may be used to control the size of the micelles, including the type of copolymer, molecular weight, and aggregation number. In the case of mixed micelles, the size may also rely on the type and proportion of their constituents<sup>261</sup>.

Critical micelle concentration (CMC) is another fundamental parameter that evaluates the stability of different micellar systems. It is a fundamental parameter, as micelles are often exposed to several environmental variations, such as changes in pH, ionic strength, exposure to various fluids containing proteins and cells, and significant dilution upon oral and intravenous administration. For these reasons, micelles should retain their integrity

as long as possible to prevent a rapid drug release and ensure the drug's delivery to its intended site of action. The lower the CMC value, the more stable the micellar system is. The CMC values depend on the balance between the hydrophilic and hydrophobic blocks of the polymers so that increasing the hydrophobicity and chain length of the hydrophobic block results in lowering the CMC and producing more stable micelles.

CMC values could be experimentally determined by monitoring sharp changes in different physical properties that happen upon reaching CMC, such as surface tension, particle size, optical clarity, and solubility. More details are discussed in Chapter 2 (section 2.3.2.9).

### **1.5.3.3.Applications of polymeric micelles for cancer therapy**

The bioavailability of anticancer agents administered orally is often limited due to poor absorption. In addition, intravenous administration of these medications is challenging and needs the utilisation of organic solvents and conventional surfactants (e.g. 50:50 ethanol and Cremphor® in Taxol®). This issue can be resolved by the solubilisation of hydrophobic drugs within micelles. For instance, Bernabeu, E. *et al.* have achieved a substantial increase in paclitaxel (PTX) solubility (38,000 folds) when encapsulated into soluplus/TPGS mixed micelles at a concentration of 5%w/v<sup>265</sup>. Another research group attained an even higher increase in PTX solubility by 82,947 folds by using Soluplus/Solutol HS15 mixed micelles at a concentration of 13.3%<sup>266</sup>.

By escaping the mononuclear phagocyte system (MPS) in the liver and by-passing the filtration of inter-endothelial cells in the spleen, the nanosize of polymeric micelles contributes to a prolonged blood circulation period which results in enhanced deposition of the drug at cancerous tissues with vascular anomalies (EPR). This final attribute is one of the greatest justifications for employing polymeric micelles to deliver anti-cancer agents, the majority of which are poorly soluble<sup>248,249</sup>.

In addition to passive targeting, the versatility of the chemical nature of polymers confers an excellent platform for functionalising polymeric micelles with different ligands for active targeting of tumour tissues. For instance, transferrin-conjugated PLGA nanoparticles were developed for the targeted delivery of docetaxel (Tf-DCT-PLGA) for

cancer therapy<sup>267</sup>. Tf-DCT-PLGA nanoparticles exhibited higher cytotoxicity on MCF-7 cell lines compared to untargeted nanoparticles. Furthermore, cellular uptake studies confirmed the enhanced cellular uptake through transferrin-mediated active transport<sup>267</sup>. Another study reported using folic acid conjugated PEG-PLGA nanoparticles for the active targeted delivery of 5-fluorouracil (5-FU-FOL-PEG-PLGA-NPs) for colon and breast cancers<sup>268</sup>. *In-vitro* cytotoxicity studies in folate-overexpressed HT-29 colon cancer cells and MCF-7 breast cancer cells displayed that the half maximal inhibitory concentration (IC<sub>50</sub>) of 5-FU-loaded FOL-PEG-PLGA NPs was approximately 4-fold less than that of untargeted counterpart<sup>268</sup>.

Moreover, some micelles (such as Soluplus®, TPGS, and Solutol® HS 15) exhibit an inhibitory effect on P-glycoprotein (P-gp) pumps which helps to overcome multidrug resistance (MDR) and enhance the oral bioavailability of drugs that are considered a strong P-gp substrate such as paclitaxel<sup>269</sup>. To address that, Zhang, J. *et al.* developed mixed micelles composed of dextran-g-poly(lactide-co-glycolide)-g-histidine (HDP) and folic acid-D- $\alpha$ -tocopheryl polyethylene glycol 2000 (FA-TPGS2K) copolymers for actively targeted delivery of paclitaxel (PTX) to PTX-resistant breast cancer MCF-7 cells (MCF-7/PTX)<sup>270</sup>. FA-TPGS2K/HDP mixed micelles exhibited more cytotoxicity against MCF-7/PTX cells than HDP micelles due to the synergistic effect of FA-receptor mediated cell endocytosis, and TPGS mediated P-gp inhibition<sup>270</sup>.

Overall, polymeric micelles have shown great promise as drug delivery vehicles for anticancer agents, and several micelle-based formulations have been developed and are under preclinical studies<sup>248,249,271,272</sup>. While some products have successfully reached the market, such as Genexol®-PM (poly(D, L-lactide) based micelles) for breast cancer and Eligard® (PLGA-based polymeric nanomicelles) for prostate cancer<sup>272</sup>.

## 1.6. Thesis objectives

Hepatocellular carcinoma (HCC) is considered one of the most fatal cancer types affecting the lives of hundreds of thousands annually. Currently, although locoregional treatments are standardly recommended clinical treatment choices for HCC, only a small percentage of patients are potential candidates for these approaches, while most patients are diagnosed at an advanced stage at which systemic chemotherapy is the only option. Therefore, the treatment of HCC comprises a health condition with an unmet therapeutic outcome. Since it was approved by FDA, Sorafenib (Sf) has shown promising results for the treatment of advanced-stage HCC. However, its low oral bioavailability and side effects considerably impede its clinical application. The application of nanomedicine in the delivery of poorly-soluble anticancer agents holds excellent potential for enhancing their physicochemical properties and hence improving their solubility, stability, bioavailability, and cytotoxicity, as well as lowering their side effects on normal tissues. In addition, active targeting through galactosylated nanodelivery systems comprises a promising strategy for the liver-targeted delivery of anticancer agents.

This project aims to study the development of different liver-targeted nanodelivery systems for Sf delivery. According to literature, few studies have used lipid nanoparticles for the delivery of sorafenib for HCC treatment<sup>128,138,139</sup>. However, none of them employed galactosylation as an approach for liver targeting. In Chapter 3, we prepared SLN and NLC for the delivery of Sf, in which the choice of the lipid matrices was carried out through systematic approach based on sorafenib solubility in lipid and lipid miscibility. The formulated lipid nanoparticles were then galactosylated for active targeting of hepatocytes using lactobionic acid as a galactose bearing moiety for targeting ASGPRs. On the other hand, in chapter 4, galactosylated lipid nanocapsules (LNC) were prepared for the active delivery of sorafenib to HCC cells using lipiodol oil to have a dual role as a main oil core replacing MCT and as a contrasting agent for diagnostic purposes and real-time monitoring of the dosage. From literature, only one study has reported the incorporation of sorafenib into LNC but was used for glioblastoma relying on passive targeting<sup>273</sup>.

Lastly, Polymeric mixed micelles were formulated using Soluplus® as a main polymeric matrix due to its high dissolution efficacy and was applied in two different administration routes (oral in Chapter 5, and parenteral in Chapter 6). In addition, TPGS was

incorporated into the mixed micelles to modulate the release profile of sorafenib, inhibit P-gp pumps enhancing cellular transport (Chapter 5), and to be employed in the surface grafting using galactosylation approach for active liver targeting after intravenous administration (Chapter 6).

So, the study includes the following:

### **Discussed in chapter 3**

- To Prepare a liver-targeting ligand using lactobionic acid-stearylamine conjugate.
- To develop and optimise liver targeted SLN and NLC for delivery of Sf.
- To study the impact of formulation parameters on the colloidal properties, drug loading, and drug release of the prepared lipid nanoparticles.
- To evaluate the cellular cytotoxicity on HepG2 cells of the blank and optimised liver targeted SLN and examine the impact of delivery system ingredients on cellular viability.

### **Discussed in chapter 4**

- To synthesise and characterise a lactobionic acid and TPGS conjugate to function as liver targeting ligand (Gal-TPGS).
- To fabricate of Sf-loaded lipid nanocapsules (Sf-LNC) and explore the impact of different formulation parameters of their physicochemical properties.
- To assess the post-insertion of Gal-TPGS into Sf-LNC on physical properties of LNC.
- To Appraise the colloidal stability of Gal-Sf-LNC during short-term storage and under physiological conditions.
- To examine the targeting efficiency, cytotoxicity, and cellular uptake of the developed Gal-Sf-LNC on HepG2 cells.

### **Discussed in chapter 5**

- To develop and optimise single Soluplus® micelles and mixed Soluplus®/TPGS micelles for the enhancement of Sf solubility and dissolution rate.

- To characterise the physicochemical properties of the Sf-loaded single and mixed micelles.
- To examine the colloidal stability of both single and mixed micelles under short-term storage conditions and gastrointestinal physiological conditions.
- To study the impact of using single and mixed micelles on Sf solubility and release kinetics under gastrointestinal physiological conditions.
- To evaluate the *in-vitro* cellular transport study of single and mixed micelles using Caco-2 cell line.

### **Discussed in chapter 6**

- To develop galactosylated Soluplus/TPGS mixed micelles for liver-targeted intravenous delivery of Sf.
- To characterise the physicochemical properties of galactosylated Sf-loaded mixed micelles (Gal-MM).
- To evaluate the colloidal stability of Gal-Sf-MM during short-term storage and under administration and physiological conditions and studying Sf release kinetics from Gal-Sf-MM.
- To appraise the targeting efficiency, cytotoxicity, and cellular uptake of the developed Gal-Sf-MM on HepG2 cells.



## **Chapter 2**

*Materials and Methods*

## 2.1. Introduction

This chapter provides insights into the materials, methodologies and characterisation techniques utilised throughout the project. During this project, different nanodelivery systems have been developed (namely, solid lipid nanoparticles SLN, nanostructured lipid carriers NLC, lipid nanocapsules LNC, and mixed polymeric micelles). For that, diverse nanofabrication methods have been adopted, including the ultrasonic hot emulsification method for the preparation of both SLN and NLC. In contrast, the phase inversion temperature method has been employed for the preparation of LNC. Lastly, the solvent evaporation self-assembly method was adopted to prepare mixed polymeric micellar systems. Many materials were used to prepare these nanocarriers, such as solid lipids (Geleol™, Compritol® 888 ATO and Precirol® ATO 5), oils (Medium chain triglycerides and lipiodol), Soluplus® and TPGS. Additionally, a group of excipients were involved comprising Transcutol® P, Solutol® HS, lipoid® S 100, Tween 80, and Poloxamers.

Furthermore, several characterisation techniques were employed to investigate and understand the crude materials' physicochemical properties and formulated nanoparticles. These techniques include dynamic light scattering (DLS), differential scanning calorimetry (DSC), thermogravimetric analysis (TGA), attenuated total reflectance Fourier transforms infrared spectroscopy (ATR-FTIR), scanning electron microscope (SEM), transmission electron microscope (TEM), powder X-ray diffraction (PXRD), proton nuclear magnetic resonance (<sup>1</sup>H-NMR), matrix-assisted laser desorption/ionization coupled to time-of-flight mass spectroscopy (MALDI-TOF MS), critical micellar concentration measurement using UV-VIS spectroscopy, drug encapsulation efficiency (EE%) and loading capacity (LC%) assay, phenol-sulfuric acid assay for carbohydrates, lectin agglutination assay, *in-vitro* drug release study.

Additionally, *in-vitro* cellular studies were carried out, such as cellular cytotoxicity assays using MTS reagent, cellular transport study, and cellular uptake study using both the inverted fluorescence microscope and flow cytometer, to investigate the cellular responses of the formulated nanoparticles.

## **2.2. Materials**

### **2.2.1. Geleol™**

Geleol™, also referred to as glyceryl monostearate (Type I) Eur.Ph., consists of a mixture of glyceryl mono- and distearate with monostearate ester content between 40-55%. It has a melting point between 54-64° C with a hydrophilic-lipophilic balance (HLB) of 3<sup>274</sup>. It is a white to cream-coloured, solid that is available in the form of beads, flakes, or powder. It has a faint greasy odour and taste and a waxy texture. Geleol™ is soluble in hot ethanol (at 60° C), chloroform and dichloromethane but insoluble in hexane, water, and mineral oils<sup>275</sup>. It has been widely employed as an emollient, plasticiser and lubricant in the food, pharmaceutical, and cosmetic fields. Moreover, it is intensively used as a matrix for sustained-release applications for tablets, suppositories, and implants<sup>274</sup>. It was also reported to be utilised as a solid lipid matrix for SLN and NLC<sup>276</sup>.

### **2.2.2. Precirol® ATO 5**

Precirol® ATO 5 (also known as Glyceryl palmitostearate) is a mixture of mono-, di-, and triglycerides of palmitic and stearic fatty acids. It is a solid lipid intensively used in the pharmaceutical and cosmetics industries. It is employed as a sustained drug-release matrix and lubricant in tablets prepared by granulation or hot-melt techniques. Precirol® is a fine white powder with a weak odour. It is freely soluble in dichloromethane and chloroform; practically insoluble in ethanol (95%), mineral oils, and water. It has a melting point of 50-60° C with an HLB of ~ 2<sup>277</sup>. Additionally, Precirol® has been employed as a solid matrix in preparing SLN and NLC for encapsulation of hydrophobic drugs<sup>278</sup>.

### **2.2.3. Compritol® 888 ATO**

Compritol (also known as Glyceryl behenate) is a hydrophobic mixture of glycerol of mono- and di-esters of behenic acid (docosanoic acid, C22 fatty acid) manufactured by Gattefosse (France)<sup>279</sup>. It is a white, almost odourless, tasteless, non-toxic, and non-irritating substance used as a carrier and excipient in the pharmaceutical industry. Compritol® has an HLB of ~ 2 with a melting point between 65-77° C. It is Soluble, when

heated, in chloroform and dichloromethane; slightly soluble in hot ethanol (96%); practically insoluble in cold ethanol (95%), hexane, and water<sup>274</sup>.

It is utilised in various medicinal formulations, including soft gel capsules, suppositories, and topical formulations. Furthermore, it is used as a carrier and excipient to increase drug stability, solubility, bioavailability and formulations' physical and chemical qualities. Due to its high melting point, Compritol® has been employed as a modified drug release matrix former, lubricant and coating agent in table manufacturing. Moreover, it was intensively used as a matrix for SLN and NLC<sup>279</sup>.

#### **2.2.4. Gelucires®**

Gelucires® are a family of lipid-based excipients that are used in the pharmaceutical industry. They are made from a mixture of glyceryl esters, fatty acids, and polyethylene glycol (PEG). They are commonly used in the formulation of oral solid dosage forms such as tablets, capsules, and powders to improve drug solubility, bioavailability, and stability of hydrophobic drugs. They can also help to control drug release rates and enhance drug permeation across biological membranes<sup>280</sup>. Their properties vary depending on their composition, which could be tailored to meet specific formulation needs. The name of Gelucires® always includes two numbers; the first indicates the melting point, and the second number represents the value of its HLB. Based on their HLB, Gelucires® can function as surfactants, such as Gelucire® 48/16, 50/13, and 44/14, or as matrix formers, such as Gelucire® 43/01<sup>281</sup>. Among all Gelucires®, Gelucire 48/16, which is composed of PEG-32 (MW 1500) esters of palmitic acid and stearic acid, is commonly employed as drug solubiliser in self-emulsifying lipid formulations as well as melt processes such as granulation, extrusion, and table compression<sup>280</sup>. In our study, Gelucire® 48/16 was employed as Sf solubiliser to improve drug loading into SLN.

#### **2.2.5. Transcutol® P**

Transcutol® P (Diethylene glycol monoethyl ether, DEGEE) is a penetration enhancer utilised in many pharmaceutical and cosmetic formulations (Figure 2.1). It is a colourless, transparent liquid often used as a solubiliser and cosolvent. Transcutol®P is often used to improve drug penetration into the skin in transdermal drug delivery systems and topical

formulations. Besides, increasing the solubility and spreadability of oils and other components in cosmetics and personal care products. It is water soluble and miscible in acetone, ethanol (95%), chloroform, ether, benzene, and pyridine. It is partially soluble in some vegetable oils and insoluble in mineral oils. It is also commonly used as a cosolvent in many lipid-based nanodelivery systems such as solid lipid nanoparticles (SLN), nanostructured lipid carriers (NLC), lipid nanocapsules (LNC) and self-microemulsifying drug delivery systems to enhance drug solubility and encapsulation efficiency<sup>273,282–286</sup>.



Figure 2.1: Transcutol® chemical structure.

#### 2.2.6. Solutol® HS 15

Solutol® HS 15 (also known as Kolliphor HS 15, Polyethylene glycol 660 12-hydroxystearate or Macrogol (15)-hydroxystearate) is a non-ionic solubiliser and emulsifier made by reacting 15 moles of ethylene oxide and 1 mole of 12-hydroxy stearic acid (Figure 2.2). Moreover, Solutol® HS 15 is marketed as a mixture of free PEG 660 and PEG 660 hydroxystearate. It is a yellowish-white paste at ambient temperature that turns into a liquid at around 30°C. It has an HLB between 14-16. It is soluble in water, ethanol, and isopropanol. However, its solubility in water decreases with increasing temperatures due to dehydration of its hydrophilic portion, making it more lipophilic. This phenomenon is employed in the formation of lipid nanocapsules (LNC) via the phase inversion temperature method<sup>203</sup>. Its critical micelle concentration (CMC) ranges between 0.005 – 0.02% with micelles typically in the 10-15 nm range. It has been used as a solubiliser and a viscosity-reducing agent in many formulations such as oral, topical, and injectable preparations<sup>287</sup> and as a structural component in LNC<sup>203,288</sup>.

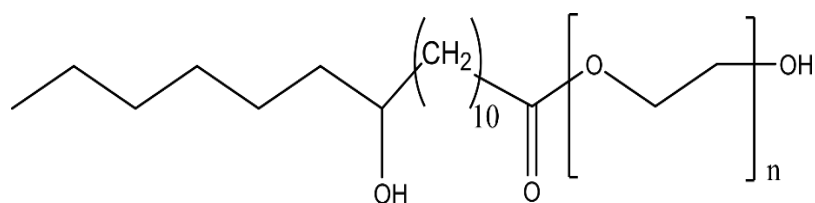


Figure 2.2: Chemical structure of Solutol® HS 15.

### 2.2.7. Lipoid S 100

Lipoid S 100 is a phosphatidylcholine (PC) from soybean. It is a zwitterionic phospholipid containing choline as a component of the polar head group and fatty acid as a lipophilic tail (Figure 2.3). According to manufacturer<sup>289</sup>, Lipoid S 100 is composed of different percentages of fatty acids; palmitic acid (12-17%), stearic acid (2–5%), oleic acid (7-12%), Linoleic acid (59-70%), and linolenic acid (5-8%). It is provided as yellowish coarse waxy agglomerates. It is dispersible in water and soluble in ethanol, chloroform, and dichloromethane. It offers several outstanding features, including biocompatibility, biodegradability, metabolic activity, and safety. Due to its amphiphilic properties, it has been intensively employed in the preparation and stabilisation of Lipid-based drug delivery systems such as liposomes, SLN, NLC, LNC and microemulsions (MEs)<sup>289</sup>.

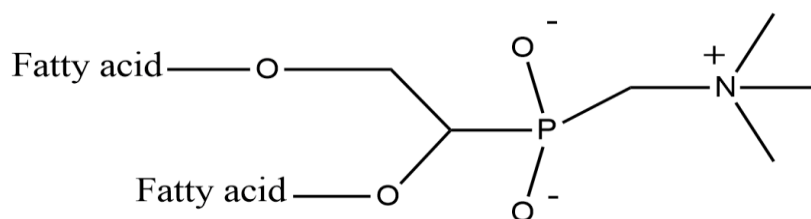


Figure 2.3: Typical chemical structure of phosphatidylcholine phospholipid (PC).

### 2.2.8. Soluplus®

Soluplus® is polyvinyl caprolactam–polyvinyl acetate–polyethylene glycol (57/30/13) graft copolymer (Figure 2.4) that was first introduced by BASF<sup>290</sup>. Due to its distinctive physicochemical properties, as shown in Table 2.1, Soluplus® has been used as a matrix polymer for solid solutions, primarily through hot-melt extrusion, to improve the aqueous

solubility and oral bioavailability of poorly soluble drugs such as danazol, fenofibrate and itraconazole<sup>260</sup>. It has amphiphilic properties consisting of a polyethylene glycol (PEG) backbone as the hydrophilic portion and vinyl caprolactam/vinyl acetate side chains as the hydrophobic portion. Thus, it can self-assemble into micelles in aqueous solutions above its CMC (7.6 mg/L). Soluplus® micelles have been intensively used to deliver hydrophobic drugs by encapsulating them within their core. Therefore, it could enhance solubility, stability, sustained drug release, target drug distribution, and increase therapeutic efficiency<sup>291</sup>.

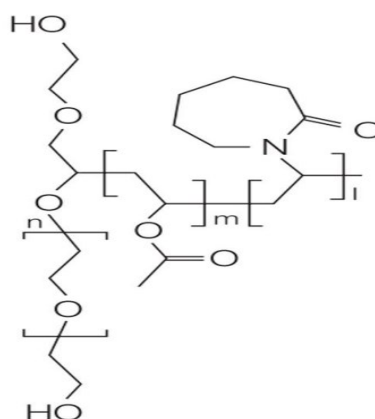


Figure 2.4: Chemical structure of Soluplus®. Figure was adapted with permission from reference<sup>259</sup>.

Table 2.1: Physicochemical properties of Soluplus®.

Physicochemical properties	Description/value
Appearance	White to slightly yellowish granules.
Molecular weight	Range of 90 000 – 140 000 g/mol (average 118,000 g/mol).
Critical micellar concentration (CMC)	7.6 mg/L in distilled water at 23°C.
HLB	~ 14.
Glass transition temperature	~ 70°C.
Solubility	Soluble in water, acetone (up to 50%), methanol (up to 45%), Ethanol (up to 25%) and dimethylformamide (up to 50%).
Lower critical solution temperature	~ 40°C.

### 2.2.9. D- $\alpha$ -tocopheryl polyethylene glycol succinate (TPGS)

TPGS is a water-soluble form of natural Vitamin E synthesised by esterifying Vitamin E succinate with polyethylene glycol (PEG) 1000 (Figure 2.5). It is a waxy solid (m.p.  $\sim$  37-41°C) with an average molecular weight of 1513 (g/mole) and an HLB of 13.2<sup>292</sup>. As a novel non-ionic surfactant with relatively low CMC (0.02 wt%), it exhibits amphiphilic properties and can form stable micelles in aqueous vehicles. It has been extensively studied and used for its emulsifying, dispersing, gelling, and solubilising potentials on poorly soluble drugs<sup>293</sup>. Additionally, TPGS has distinctive bifunctional properties that augment anticancer efficiency due to P-glycoprotein inhibition, counteracting multidrug resistance (MDR), enhancing drug absorption, inducing mitochondrial-associated apoptosis, and promoting drug permeation and tumour accumulation<sup>255</sup>. Since TPGS has received FDA approval as a safe pharmaceutical excipient, it has been employed in different TPGS-based DDS either by using the original TPGS<sup>294,295</sup>, TPGS-drug conjugates<sup>296-300</sup>, functionalised TPGS<sup>250,301-304</sup> or TPGS copolymer<sup>296</sup> for improving the therapeutic efficiency of different drugs<sup>305</sup>.

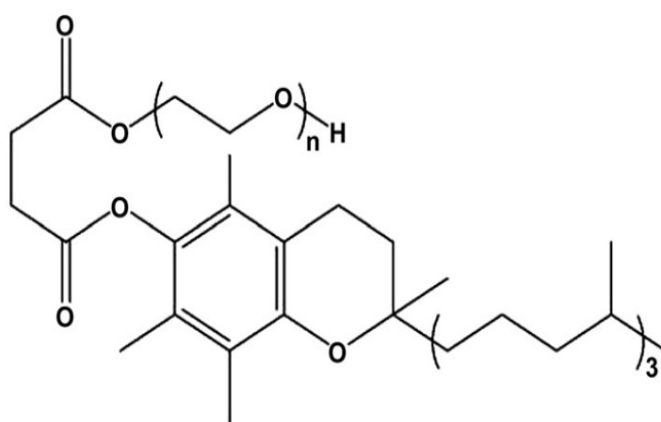


Figure 2.5: Chemical structure of TPGS. Figure was adapted with permission from reference<sup>293</sup>.

### 2.2.10. Tween 80 (Polysorbate 80)

Tween 80 (Polysorbate 80) is a synthetic surfactant of polyoxyethylene sorbitan fatty acid esters (Figure 2.6). The fatty acid content is dominated by oleic acid, but other fatty acids, such as palmitic or linoleic acid, may be present. It is a yellow oily liquid with a molecular

weight of 1309.7 g/mol and a density of 1.064 g/mL<sup>306</sup>. It has an HLB of 15 and forms micelles above a concentration (CMC) of 0.01%. Due to its appealing properties and biocompatibility, Tween 80 has been widely used in the pharmaceutical and food industries. Moreover, Tween 80 has been reported as an efficient stabiliser for many drug nanodelivery systems<sup>306,307</sup>.

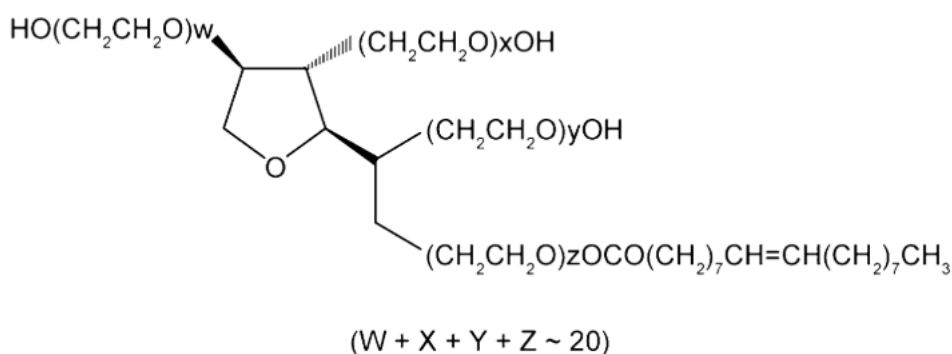


Figure 2.6: Chemical structure of Tween 80. Figure was adapted with permission from reference<sup>307</sup>.

### 2.2.11. Poloxamers (Pluronic)

The poloxamer polyols are a family of ethylene oxide and propylene oxide block copolymers with a general formula  $\text{HO}(\text{C}_2\text{H}_4\text{O})_x(\text{C}_3\text{H}_6\text{O})_y(\text{C}_2\text{H}_4\text{O})_x\text{H}$  (Figure 2.7). The polyoxyethylene segment represents the hydrophilic portion, while the polyoxypropylene segment is the hydrophobic one<sup>274</sup>. Poloxamers are a class of non-ionic copolymers used principally in pharmaceutical formulations as emulsifiers and solubilising agents. All the poloxamers are chemically similar, with the main difference being the relative quantities of propylene and ethylene oxides added during the production process that affect their physical properties (Table 2.2). Generally, poloxamers (mainly, Poloxamer 188 and 407) are widely used as stabilisers of different drug nanodelivery systems, including SLN, NLC and polymeric nanoparticles<sup>274</sup>. In our study, both Poloxamers 188 and 407 have been employed in the preparation of SLN and NLC.

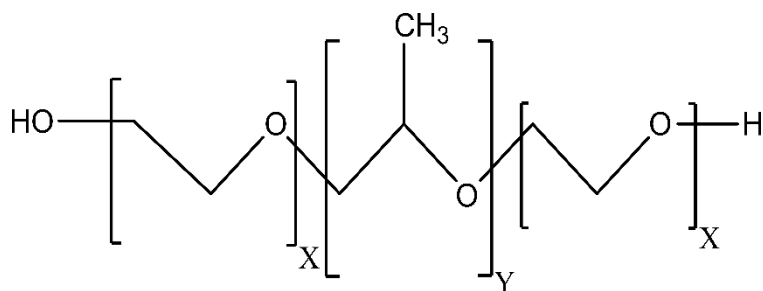


Figure 2.7: General chemical structure of Poloxamers.

Table 2.2: Properties of Poloxamers 188 and 127.

Poloxamer	non-proprietary name	Physical state	X	Y	Average molecular weight	HLB
188	F-68	Solid	80	27	7680 – 9510	29
407	F-127	Solid	101	56	9840 – 14600	18-23

## 2.3. Methods

### 2.3.1. Nanoparticle preparation methods

Several nanoparticles preparation methods for drug delivery have been reported in the literature<sup>308</sup>. In this study, the appropriate method was determined primarily based on the nature of the delivery system components and the intended application.

#### 2.3.1.1. Preparation of SLN and NLC using emulsification/ultrasonication method

As previously discussed in Chapter 1 (section 1.5.1.2.), SLN and NLC could be prepared by different methods such as high-shear homogenisation, high-pressure homogenisation, emulsification/solvent evaporation and microemulsion formation method. In this study, the ultrasonic emulsification method was employed to produce SF-loaded SLN and NLC due to the quick and easy preparation procedures. The influence of different components (lipid, oil, and surfactants) on the lipid nanoparticles' physicochemical properties and drug loading of the lipid nanoparticles has been thoroughly investigated in Chapter 4.

To prepare lipid nanoparticles, solid lipids were melted at a temperature around 10° C above their melting point. Then, the aqueous surfactant solution was added, followed by sonication using a probe sonicator (Fisherbrand™ 505 connected to a probe with 3 mm tip) at 20% amplitude for 3 min in a 20:5 sec on-off cycle. Finally, the nanoemulsion was left under stirring at room temperature (~ 25°C) for solidification and lipid nanoparticles formation.

### **2.3.1.2.Preparation of lipid nanocapsules (LNC) using the phase inversion temperature method:**

In this study, the phase inversion temperature method has been adopted to prepare and optimise Sf-loaded LNC using lipiodol oil as the internal core for its application as a contrasting agent<sup>203</sup>. The phase inversion temperature method is thoroughly discussed in Chapter 1 (section 1.5.2.2.). In this study, different components' ratios were screened to optimise the formulation. Furthermore, the post-insertion approach was used to graft galactosylated TPGS onto the surface of the optimised LNC to produce galactosylated LNC as a liver-targeted nanodelivery system for hepatocellular carcinoma (Chapter 5).

### **2.3.1.3.Preparation of polymeric micelles using the solvent evaporation method**

As discussed in Chapter 1 (section 1.5.3.1.), polymeric micelles can be prepared using different methods based on the nature of the polymer and the used organic solvent. In this study, the solvent evaporation method was employed due to its simplicity, short processing time, and suitability for maximizing the encapsulation of hydrophobic drugs<sup>261</sup>. Acetone was used as a solvent to dissolve the polymeric material and Sorafenib. Afterwards, the organic solution was dripped into MilliQ water. Using solvent displacement and evaporation, the polymer concentration in the mixture increases to a concentration higher than its CMC, inducing micelle formation. The detailed processes and screened parameters are discussed in Chapters 5 and 6.

## 2.3.2. General physicochemical characterisation techniques

### 2.3.2.1. Dynamic light scattering (DLS)

Dynamic Light Scattering (DLS) is a widely used technique for measuring nanoparticles' size and size distribution in a liquid. The principle of DLS is based on measuring the intensity of light scattered by the particles as a function of time. The scattered light intensity is analysed to determine the size of the particles in the sample. When measuring nanoparticles, DLS provides accurate measurements of the hydrodynamic diameter ( $d_H$ ) (i.e. the size of a hypothetical hard sphere that diffuses in the same fashion as that of the particle being measured) by monitoring the velocity of the Brownian motion of the particles which is called “translational diffusion coefficient” ( $D$ ). The translational diffusion coefficient ( $D$ ) can then be converted into a particle size using the Stokes-Einstein (Eq. (2.1)).

$$d_H = \frac{KT}{3\pi\eta D} \quad \text{Eq. (2.1)}$$

Where  $d_H$  is the hydrodynamic diameter of particles,  $K$  is Boltzmann's constant,  $T$  is the absolute temperature,  $\eta$  is the viscosity of the dispersion medium, and  $D$  is the translational diffusion coefficient<sup>309</sup>.

DLS employs a single-frequency laser-focused on the sample, where light interacts with particles causing light scattering in all directions. To monitor the motion of the particles, scattered light is recorded at a certain angle (typically  $90^\circ$  or  $173^\circ$ ) over a specific time interval (Figure 2.8). Detection at angle  $90^\circ$  represents side scattering and is usually used for diluted samples, while angle  $173^\circ$  represents back scattering and is generally used for concentrated turbid samples due to the short path length of the laser within the sample. The intensity of the scattered light changes over time, with smaller particles fluctuating quickly than the bigger ones. Conversely, bigger particles have larger amplitudes between the minimum and maximum scattering intensities. The initial intensity trace is typically used to generate a correlation function that specifies the time a particle spent at the same spot within the sample<sup>310</sup>.

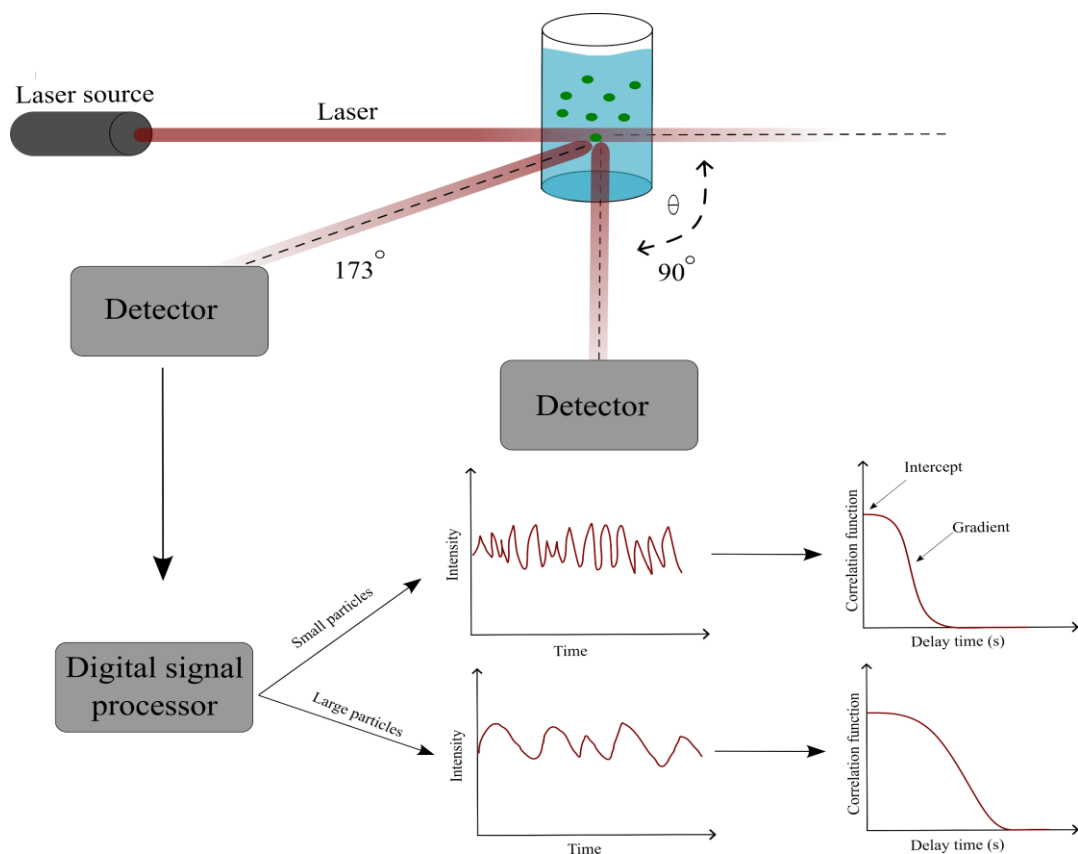


Figure 2.8: The working principle of dynamic light scattering for measuring particle size of nanoparticles.

The correlation function is linear at the start of the measurement, suggesting that the particle is still at the same position inside the sample. Later, an exponential decrease may be seen, representing the particle's movement. Small particles travel quickly; therefore, the decay is fast (steep slope), but large particles take a long time to alter their relative positions. As a result, the size-dependent movement is incorporated into the decay of the correlation function. Furthermore, the y-intercept can be employed to determine the signal-to-noise ratio from a measured sample and is thus typically used to evaluate data quality. It is commonly suggested that an ideal signal has a value of 1, while a good system has an intercept higher than 0.6, and great systems have intercepts higher than 0.9. Particle size is usually expressed as Z-average, with size distribution around this average. The size distribution, in turn, could be expressed in three different ways: intensity, volume, and number distribution (where both volume and number distributions are derived from the intensity measurement by inputting the refractive index of the particles)<sup>310</sup>. It is worth mentioning that both intensity and volume size distributions are

very sensitive to the presence of any aggregates in the sample as depicted in the example in Figure 2.9.

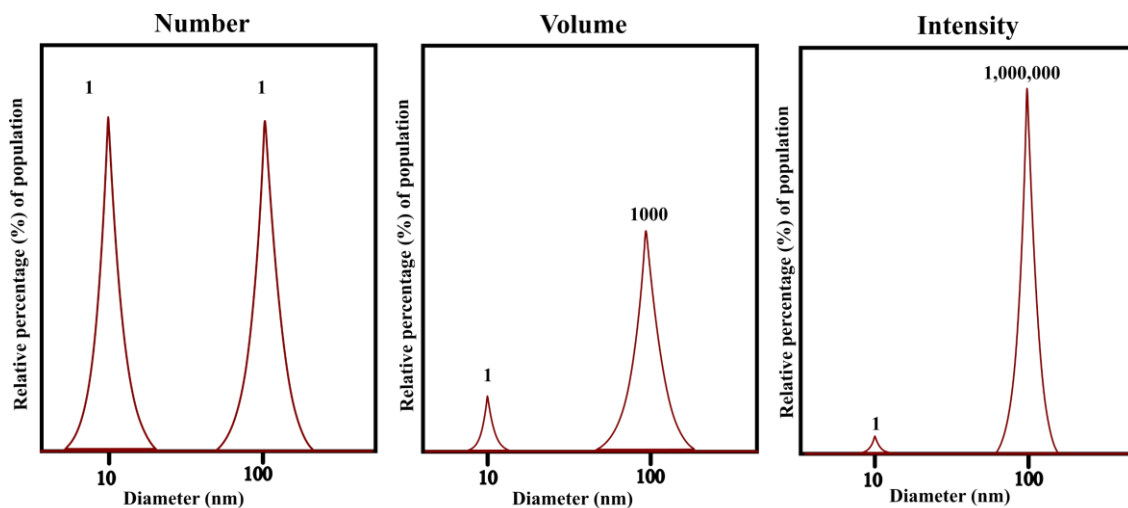


Figure 2.9: Number, volume, and intensity size distributions of a bimodal mixture of 10 and 100 nm nanoparticles present in equal numbers.

The polydispersity index (PDI) is another key parameter that indicates the breadth or the broadness of the particle size distribution. The values of PDI can range from 0 to 1 with values closer to 0 indicating a narrower size distribution and values closer to 1 indicating a broader size distribution. PDI is calculated using Eq. (2.2.2).

$$PDI = \left(\frac{\sigma}{d}\right)^2 \quad \text{Eq. (2.2.2)}$$

Where  $\sigma$  is the standard deviation of particle size distribution and  $d$  is the mean particle diameter<sup>310</sup>.

In this study, DLS was carried out to measure the mean particle size (Z-AVG) and polydispersity index (PDI) using Zetasizer Nano (Malvern Instruments Ltd, Malvern, UK). The dispersant (medium) was set to water with a viscosity (cP) of 0.8872 with an equilibration time of 120s at a temperature of 25 °C. All measurements were done in triplicates and expressed as mean  $\pm$  standard deviation (S.D.).

### 2.3.2.2. Zeta potential ( $\zeta$ -potential)

The zeta potential ( $\zeta$ -potential) measures the electrical potential at the shear plane of a particle suspended in a liquid. It is a measure of the charge at the interface between the particle and the liquid and is used to determine the stability of the particle suspension. The measurement of zeta potential is based on the concept of electrophoresis, which is the movement of charged particles in an electric field. Hence, a particle with a surface charge will experience a force in an electric field, causing it to move at a certain velocity. The zeta potential is then calculated from the particle's velocity using different techniques, one of which is laser Doppler electrophoresis (LDE) applied in Malvern zetasizer instruments<sup>310</sup>.

Several factors may affect  $\zeta$ -potential such as pH (which can change the ionisation state of the surface chemical groups) and ionic strength (as the ionic strength of the liquid increases, the  $\zeta$ -potential decreases). This is attributed to the increased concentration of ions in the liquid competing with the surface charge of the particles, reducing the net surface charge and the  $\zeta$ -potential), particle size (smaller particles generally have a higher  $\zeta$ -potential than larger ones of the same material), and the dispersion medium (conductivity and viscosity of the dispersion medium can affect the electrophoretic mobility of the particles hence affect the  $\zeta$ -potential<sup>309</sup>.

$\zeta$ -potential values can be employed to assess the stability of particle dispersion. Particles having a high zeta potential repel particles with the same charge, resulting in a stable suspension. Particles having a low zeta potential can assemble due to attraction interactions between particles with opposing charges, resulting in an unstable suspension. The  $\zeta$ -potential is an essential parameter for understanding particle behaviour under diverse situations and developing nanoparticulate drug delivery systems<sup>310</sup>. In this study, the  $\zeta$ -potential of all formulations was determined using Zetasizer (Zetasizer Nano, Malvern Instruments Ltd, Malvern, UK).

### 2.3.2.3. Differential scanning calorimetry (DSC)

Differential Scanning Calorimetry (DSC) is a commonly used technique to measure the thermal properties of materials. It works by heating the sample at a controlled rate and measuring the heat absorption or release by the sample as a function of temperature. This technique primarily identifies various thermal events, such as melting, glass transitions, and crystallisation, through controlled heating or cooling cycles (Figure 2.10).

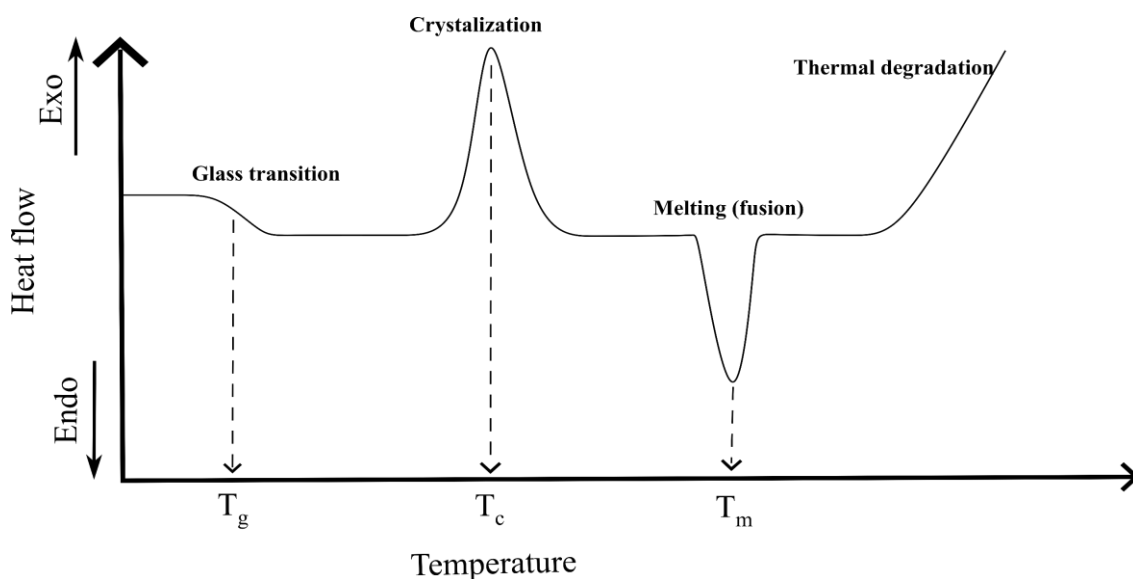


Figure 2.10: Typical DSC thermogram showing peaks associated with different thermal kinetic events.

Fundamentally, two types of DSC are commercially available: heat flux and power compensation. Heat flux DSC is the easier of the two techniques conceptually, as seen graphically in Figure 2.11. Generally, two crucibles are placed symmetrically within the furnace, one empty (reference) and one carrying the sample, with a thermocouple in close contact with each of them. The thermocouples are linked back-to-back such that the voltage generated by the pair directly indicates the temperature difference between the sample and the reference. The cell should guarantee that the heat paths from the furnace to the sample and reference are similar, stable, and well-defined.

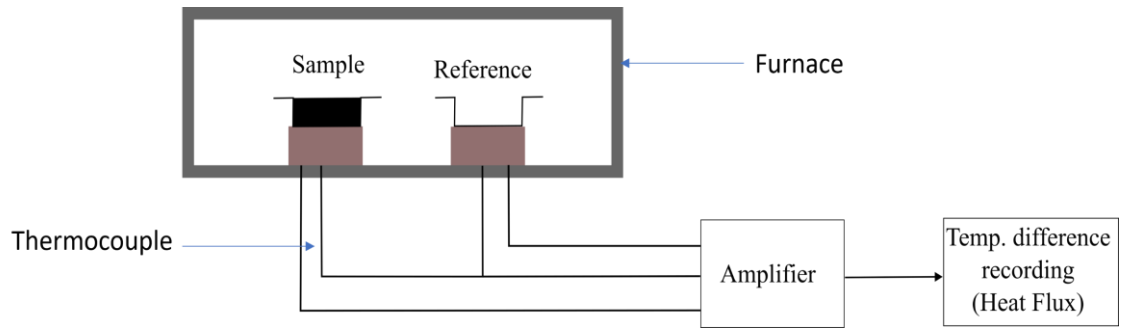


Figure 2.11: Schematic design of heat flux DSC.

The heat flow from the furnace to each crucible is calculated from Eq. (2.3)

$$\frac{dQ}{dt} = \frac{\Delta T}{R} \quad \text{Eq. (2.3)}$$

Where  $Q$  is the heat flow,  $t$  is time,  $\Delta T$  is the temperature difference between the crucible and the furnace, and  $R$  is the thermal resistance of the heat path between the crucible and furnace.

Consequently, the temperature difference between the sample and reference crucibles is converted into heat flow provided that all other influencing factors (such as heat absorption by the crucible, heat losses by convection and others) are kept constant for both crucibles. For accurate measurement of heat flow as a function of temperature difference, temperature difference signal ( $\Delta T$ ) needs to be calibrated using standard pure material with known melting enthalpy and heat capacity (such as indium, melting temperature = 156.6°C, melting enthalpy = 28.71 J/g, and heat capacity = 0.23 J/g.K)<sup>311</sup>.

Similarly, the heat flow can be calculated using heat capacity ( $C_p$ ), defined as the energy required to increase the temperature of one gram of certain material by one degree kelvin, using Eq. (2.4).

$$\frac{dQ}{dt} = C_p \times \frac{dT}{dt} \quad \text{Eq. (2.4)}$$

Regarding power compensation DSC, the first noticeable difference between this method and the heat flux instrument is that it employs two separate furnaces, one for the sample crucible and another for the reference crucible. However, both are set to go through the

same temperature profile, and the difference in electrical power provided to nullify (compensate) the difference in temperature between the two furnaces is monitored.

In this study, Discovery DSC 2500 differential scanning calorimetry (TA Instruments, Delaware, United States) that relies on the heat flux principle was used. The device was calibrated using standard Indium. Nitrogen purge gas with a flow rate of 50 (mL/min) was used during the experiments and TA Trios software was used for the data analysis.

#### **2.3.2.4. Thermogravimetric analysis (TGA)**

Thermogravimetric analysis (TGA) is a technique used to measure the weight change of a material as a function of temperature or time. The TGA instruments consist of a very sensitive balance and a heating furnace. It works by heating the sample at a controlled rate and monitoring the weight change as the sample undergoes thermal degradation or chemical reactions. TGA can be used to study a wide range of materials, including polymers, ceramics, metals, and biomaterials. It is a useful technique for characterising the thermal stability of a material, especially for those used in the formation of nanoparticles by methods involving thermal treatment (such as phase inversion temperature, as discussed in section 2.3.1.2). Moreover, TGA can be used to determine the water content, volatile content, and ash content of a sample<sup>312</sup>.

In this study, TGA 5500 (TA Instruments, Delaware, United States) was used with a heating rate of 20°C/min and TA Trios software was used for the data analysis.

#### **2.3.2.5. Powder X-Ray diffraction (PXRD)**

Powder X-ray diffraction (PXRD) is a technique used to investigate the crystallinity of a material. It works by directing an X-ray beam on a powdered sample and measuring the diffraction patterns created by the X-rays as they interact with the inner crystal lattice of the sample. This non-destructive technique is commonly used to determine crystallinity, characterise polymorphs and solvates, and study phase transitions<sup>310</sup>. The principle of X-ray diffraction is based on the constructive interference of monochromatic X-rays with a crystalline material as a cathode ray tube produces these X-rays, which are then filtered

to create monochromatic radiation, parallelled to concentrate, and directed into the sample (Figure 2.12a). In the crystalline material, the diffracted rays constructively interfere (Figure 2.12b) following Bragg's (Eq. (2.5)) and show up as diffraction peaks<sup>312,313</sup>.

$$n\lambda = 2d \sin \theta \quad \text{Eq. (2.5)}$$

Where  $n$  is an integer,  $\lambda$  is the wavelength of X-rays,  $d$  is the interplanar spacing creating the diffraction, and  $\theta$  is the diffraction angle.

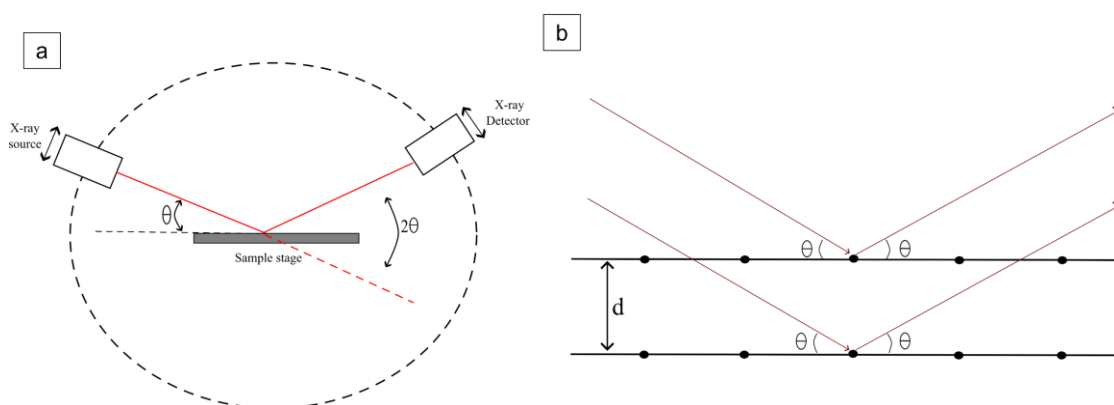


Figure 2.12: Schematic presentation of the working principle of XRD instrument (a) and X-ray diffraction through the crystalline lattice (b).

In this study, Rigaku Powder X-ray diffraction system (SmartLab SE/PC, Japan) with graphite-monochromated  $\text{CuK}\alpha$  radiation with a voltage of 40 kV and current of 50 mA was used to investigate the crystallinity of different lipid-based formulations (Chapter 3) and polymeric micellar systems (Chapter 5 and 6). The range of scanned ( $2\theta$ ) was from  $5^\circ$  to  $60^\circ$  at a scanning speed of  $4^\circ$  per minute and step of  $0.02^\circ$ .

### 2.3.2.6. Attenuated total reflectance-Fourier transform infrared (ATR-FTIR) spectroscopy

Fourier transforms infrared (FTIR) spectroscopy is an essential analytical technique for illustrating the chemical structure of different materials. It is widely used in the

pharmaceutical field for identifying and characterising unknown materials, detecting contaminants, identifying decomposition and oxidation, detecting chemical incompatibility, and inspecting chemical synthesis products<sup>314,315</sup>. It is a direct and non-destructive technique with easy sample preparation. Moreover, FTIR could be used for qualitative and quantitative purposes. The principle of the technique relies on the irradiation of the test sample with infrared radiation (typically in the mid-infrared region between 400-4000  $\text{cm}^{-1}$ ) and determining the fraction of the incident radiation that is absorbed by sample molecules (due to the vibration of atoms' bonds) at a particular frequency<sup>316</sup>. There are two modes of FTIR, either transmittance or reflectance mode, based on whether the absorbed fraction was determined via the transmitted or the reflected fraction of the incident light. In ATR-FTIR, the sample is placed directly on a diamond and irradiated by polarized IR radiation. The reflected fraction of radiation is directed to the IR detector by a set of mirrors<sup>317</sup> (Figure 2.13).

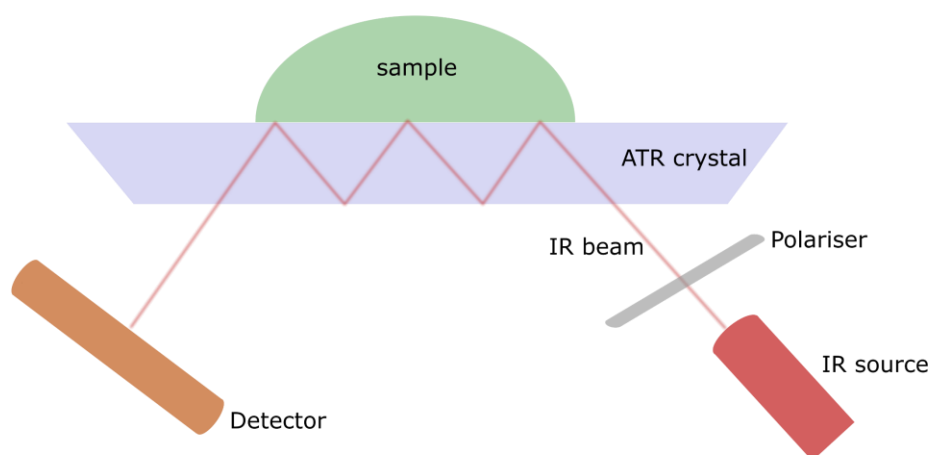


Figure 2.13: Schematic of ATR-FTIR working principle.

In this study, an FTIR spectrophotometer (Vertex 70, Bruker Optics Limited, United Kingdom) equipped with an internal reflection diamond Attenuated Total Reflectance (ATR) accessory (Specac Ltd., Orpington, United Kingdom) was utilized to illustrate the chemical structure of the synthesised galactosylated excipients and to check the chemical compatibility of the formulated nanoparticles. The spectra were acquired from 32 scans

in the range between 600-4000  $\text{cm}^{-1}$  at a resolution of 4  $\text{cm}^{-1}$ . All measurements were carried out in triplicate, and data were analysed using OPUS software.

### 2.3.2.7. Proton nuclear magnetic resonance ( $^1\text{H-NMR}$ )

Proton Nuclear Magnetic Resonance ( $^1\text{H-NMR}$ ) spectroscopy is a powerful analytical technique for identifying the chemical structure of a molecule. The fundamental principle behind H-NMR spectroscopy is that the nuclei of certain elements, such as hydrogen, have a feature known as spin. When these nuclei are exposed to a high magnetic field, they align either parallel or antiparallel to the magnetic field's direction. This is referred to as the ground state. When exposed to a radiofrequency (RF) pulse, the nuclei absorb energy and move to an excited state. As the nuclei return to their ground state, they emit energy in the form of RF radiation, which may be detected and quantified to establish the molecule's chemical structure<sup>312</sup>.

Three main parameters characterise the NMR spectrum, namely, chemical shift ( $\delta$ ), integration and peak splitting. The chemical shift ( $\delta$ ) is a measure of the difference in emitted resonance frequency between the hydrogen atom in the sample and the reference compound (usually tetramethylsilane (TMS)). The chemical shift ( $\delta$ ) is typically reported in units of parts per million (ppm). It is calculated using the following Eq. (2.6):

$$\delta (\text{ppm}) = \frac{\nu_H - \nu_s}{\nu_s} \times 10^6 \quad \text{Eq. (2.6)}$$

Where  $\delta$  (ppm) is the chemical shift expressed in ppm,  $\nu_H$  is the proton resonating frequency in the sample and  $\nu_s$  is the proton resonating frequency in the standard (TMS). The position of the peak (chemical shift ( $\delta$ )) relies on the chemical environment of the proton (low chemical shifts represent shielded protons while high chemical shifts represent deshielded protons)<sup>318</sup>. Furthermore, Peak integration is the number of protons represented by the peak relative to the total number of protons in the sample, while peak splitting indicates the neighbouring protons<sup>319</sup>.

H-NMR spectroscopy is frequently employed in chemistry, polymer science, and biological research. It may be employed to identify unknown chemicals, assess the purity

of a sample, and track changes in the chemical structure of a molecule over time. It may also be used to analyse the interactions and their dynamics for molecules in a sample. It is important to point out that H-NMR spectroscopy requires a sample in solution. The samples are usually dissolved in deuterated solvents to avoid or minimise the signals arising from the protonated solvents<sup>320</sup>.

In this study, H-NMR spectra were recorded in different solvents (DMSO-d<sub>6</sub> and CDCl<sub>3</sub>) using a 500 MHz spectrometer (Bruker Avance DRX 500) to investigate the structure of the galactosylated lipids (in Chapter 3) and galactosylated TPGS (in Chapter 4 and 6).

#### **2.3.2.8. Matrix-assisted laser desorption/ionization time-of-flight mass spectrometry (MALDI-TOF)**

MALDI-TOF MS is a technique used to measure the molecular masses of molecules such as proteins, peptides, polymers, and polysaccharides. It works by ionising molecules in the presence of a matrix material with a laser and then measuring the time that ions take to travel to the detector. The MALDI-TOF MS equipment comprises a laser source, a matrix application system, and a time-of-flight mass spectrometer. The molecules are mixed with a matrix component (depending on the nature of the sample) and put on a sample plate. The sample is then exposed to a laser beam (typically a nitrogen laser at 330nm) which ionises the sample molecules and desorbs them off the sample plate. The ions are then accelerated and transferred through a magnetic field, which separates them based on their mass-to-charge ratio. The time it takes for the ions to reach a detector is then measured and used to calculate the mass of the biomolecules<sup>319</sup>. This technique is commonly used in proteomics, metabolomics, and microbiology. Additionally, it is used to analyse synthetic polymers, small molecules and inorganic compounds<sup>319</sup>.

In this study, MALDI-TOF (AXIMA performance, Shimatzu, UK) was used, applying linear positive ionisation mode equipped with a 337 nm nitrogen laser operating at 50 Hz. It was utilized to check the molecular weight of the synthesised galactosylated TPGS after conjugation (Chapter 4, section 4.2.5.).

### 2.3.2.9. Critical micellar concentration (CMC) measurement

The micellar formation process is well-established in polymers that have the amphiphilic trait. Critical micellar concentration (CMC) is the concentration above which the polymer or surfactant starts to form a micellar structure instead of being molecularly dispersed in the aqueous medium<sup>245</sup>. In micellar form, there is a change in the physicochemical properties of the polymer/surfactant, such as surface tension, nanoparticulate structure formation, and solubilisation potency (Figure 2.14). Based on this notion, different methods have been developed for measuring the CMC. For instance, a tensiometer was used for measuring CMC based on the notion that after micellar formation, there is no further decrease in the surface tension of the micellar dispersion upon increasing polymer/surfactant concentration<sup>261</sup>. Another method depends on detecting the formation of nanoparticulate structures using the dynamic light scattering technique (DLS)<sup>321</sup>. Regarding the solubilisation potency of micelles, different hydrophobic materials have been used as probes to detect the concentration above which micelles solubilize the probes, which could be seen by fluorescence in case of using pyrene<sup>322-325</sup> or UV-Vis absorbance in case of using iodine<sup>326-331</sup>. In this study, iodine UV-Vis absorbance method was adopted.

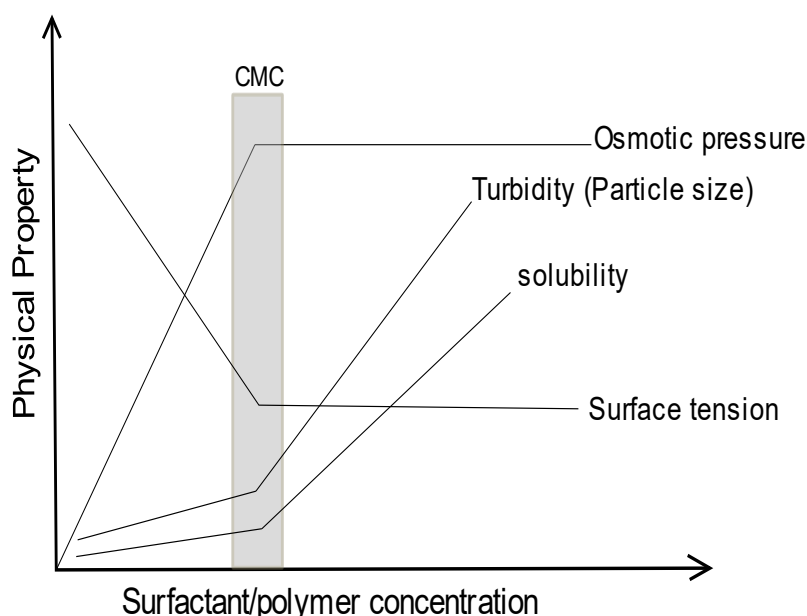


Figure 2.14: The effect of micellisation of surfactants/polymers on the different physical properties.

In the case of mixed micelles, both experimental and theoretical CMC values can be defined. The theoretical CMC value for mixed micelles can be calculated using Eq. (2.7).

$$\frac{1}{CMC} = \frac{X_1}{CMC_1} + \frac{X_2}{CMC_2} \quad \text{Eq. (2.7)}$$

Where,  $X_1$  and  $X_2$  are the molar fractions of the components 1 and 2, and  $CMC_1$  and  $CMC_2$  are the experimental CMC values for the corresponding components.

The deviation of the experimental values from the theoretical ones may be indicative of a favourable (negative deviation) and unfavourable (positive deviation) mixing in the micellar system<sup>332</sup>.

### **2.3.3. Microscopy techniques**

#### **2.3.3.1. Transmission electron microscopy (TEM)**

Transmission electron microscopy (TEM) is the most extensively used electron microscopy method for characterising nanoparticles. TEM produces high-resolution pictures with resolutions as low as a few angstroms<sup>333</sup>. The operating concept of TEM is based on passing an electron beam through a thin sample (placed on a grid) and detecting the electrons transmitted through the sample. The electrons that pass through the sample are then focused by an objective electromagnetic lens and projected onto a detector (Figure 2.15). As a result, TEM is more favourable for NPs characterisation than SEM because it offers accurate particle size in both bright and dark field pictures, as well as detailed information on the NPs morphologic, crystallographic, and compositional features<sup>310</sup>.

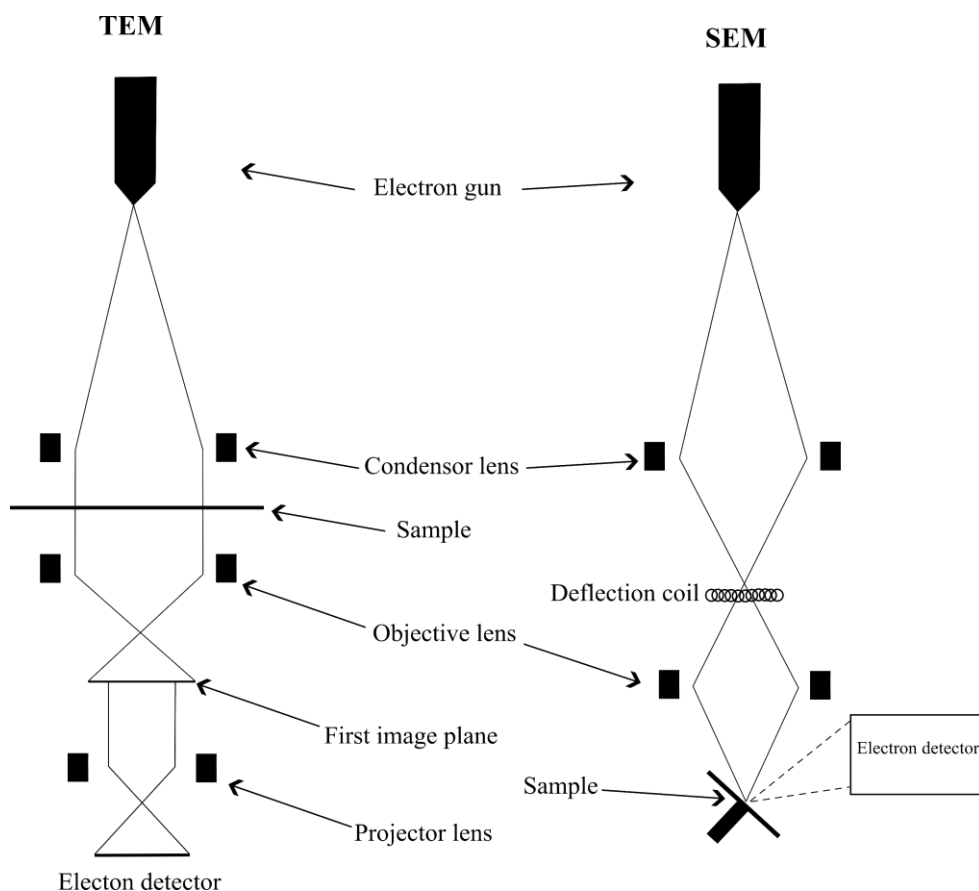


Figure 2.15: Schematic of the operation principle of transmission (TEM) and scanning (SEM) electron microscopes.

In this study, the TEM mode of a Gemini 300 series emission microscope (Zeiss, Germany) was used to analyze the particle size and morphologies of the produced nanoparticles. Samples were placed on the 400-mesh grid (Agar scientific, UK) and stained with phosphotungstic acid (2%, pH 6.8) to contrast the sample.

### 2.3.3.2. Scanning electron microscopy (SEM)

Scanning electron microscopy (SEM) is a high-resolution method for studying the surface topography of materials and the spatial variations in chemical compositions<sup>333</sup>. It works by scanning a focused electron beam over the sample surface and detecting the electrons that are emitted from the sample due to the interaction with the electron beam. These emitted electrons are then employed to build an image of the sample (Figure 2.15)<sup>310,333</sup>.

It is noteworthy that, unlike TEM, SEM does not require samples to be thin, but it does need samples to be conductive or covered with a conductive coating to minimise charging artefacts<sup>333</sup>.

In this study, the imaging was carried out using a Gemini 300 series emission microscope (Zeiss, Germany). Images were generated using 10 kV acceleration voltage. Samples for SEM mode were placed on coverslips that were fixed onto a brass stub using a double-sided adhesive tape and left for drying overnight. Afterwards, dried samples were made electrically conductive by coating them with a thin layer of gold (Au) by conventional Au sputter coating parameters: 30 sec at 2.2 kV and 20 mA. The samples were 55 mm from the gold target (Polaron SC 7640, Quorum Technologies, UK).

### **2.3.3.3. Inverted fluorescence microscopy (IFM)**

The inverted fluorescence microscope (IFM) is a type of microscope that visualises material using fluorescence. It is used in cell biology, microbiology, and developmental biology to image living cells and organisms. Unlike normal light microscopes, IFM has the light source above the sample and the objective lens below it (Figure 2.16). This inverted assembly provides simple access to the sample and allows the use of specialised equipment such as incubation chambers and environmental control systems<sup>334</sup>.

In an IFM, the sample is excited with a specified wavelength of light, and the emitted fluorescence is received by the objective lens and transmitted onto a detector. Depending on the type of detector employed, the fluorescence generated by the sample can be seen as a bright-field picture or a fluorescence image. IFMs are extensively used to image living cells as they enable the use of a wide set of fluorescent dyes and proteins to label specific components inside the cell, such as the cell membrane, cytoskeleton, or organelles. This may be used to investigate cell dynamics and the impact of various treatments on cells<sup>334</sup>.

It should be noted that the use of fluorescence in IFM necessitates labelling the material with a fluorescent dye or protein, and the sensitivity of the fluorescence signal is lower than that of other methods, such as confocal microscopy. Furthermore, photobleaching and phototoxicity might influence the fluorescence signal, reducing the fluorescence

signal over time<sup>334</sup>. In this study, fluorescence microscope (Zeiss Axiovert 200M, Germany) was used to visualise HepG2 cells after incubation with the Coumarin-6-labeled nanoparticles.

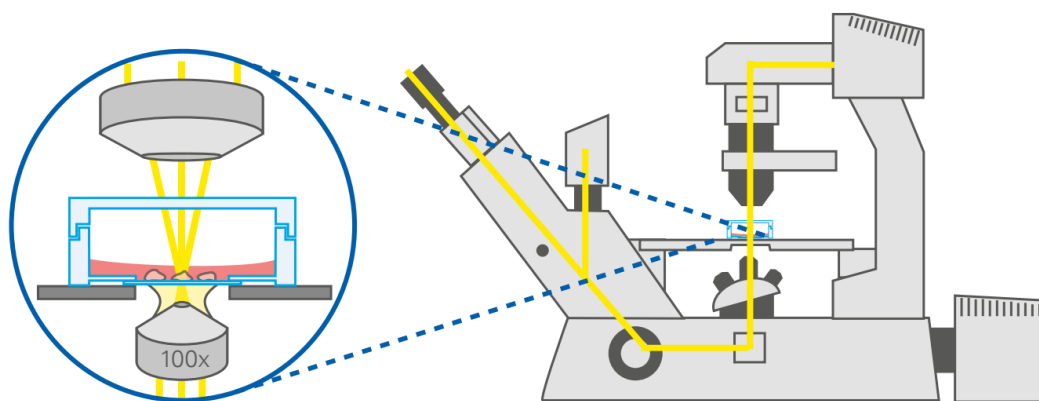


Figure 2.16: Schematic of the inverted fluorescence microscope. Figure was adapted with permission from reference<sup>334</sup>

#### 2.3.4. *In-vitro* drug release

*In-vitro* release testing is a key analytical tool employed to investigate and anticipate the behaviour of the pharmaceutical product during different development stages. When appropriately developed, an *in-vitro* release profile may disclose fundamental facts about the dosage form and its behaviour and offer information on the release mechanism and kinetics, providing a logical and scientific approach to manufacturing pharmaceutical products. *In-vitro* release testing is even more critical for nanosized-dosage forms, and the experiment design encompasses additional challenges. Since there are presently no compendial standards for assessing drug release from nanocarriers, drug release is evaluated using a range of techniques, including sample and separate (SS), continuous flow (CF), and dialysis membrane (DM) approaches<sup>335</sup>. The SS technique offers an easy setup and direct monitoring of drug release, although sampling is time-consuming and needs additional separation steps to separate the released drug from raw material. With the CF approach, sampling is simple, but setup takes effort. The DM makes setup and sampling simpler, but it might not be appropriate for medications that bind to the

membrane, and the presence of dialysis membrane as an additional barrier may be problematic in data interpretation<sup>336</sup>.

- ***In-vitro* drug release kinetic modelling**

It is crucial to know the precise mass transport processes involved in the drug release and make a quantitative prediction for the ensuing drug release kinetics to determine a precise drug release profile from a therapeutic system<sup>337</sup>. Many mathematical models have been employed to design simple and intricate drug delivery systems based on the predicted overall release behaviour. They permit the measurement of several crucial physical properties and the use of model fitting to analyse data from experimental releases<sup>338</sup>. The most commonly adopted models are listed in *Table 2.3* and include:

**Zero-order model** is employed when the drug release is constant over time and not affected by time or concentration. This situation applies to drug delivery systems with prolonged drug release (such as transdermal slow-release batches, and osmotic systems)<sup>337</sup>.

**The first-order model** is mainly used to describe the absorption, elimination and/or release of different drugs in which drug concentration increases/decreases exponentially depending on the remaining drug concentration at any time<sup>337</sup>.

**The Higuchi model** was initially proposed by Higuchi in 1961<sup>339</sup> as a trial to mathematically describe the drug release rate from ointment bases. This model best describes the drug release from neither swellable nor soluble matrices, so the drug release relies only on diffusion<sup>337</sup>.

**The Korsmeyer-Peppas model** is useful for studying drug release from polymeric matrices when the release mechanism is uncertain or when several drug release mechanisms (such as diffusion and dissolution) occur simultaneously<sup>338</sup>. Depending on the value of the release exponent ( $n$ ) in the equation, the drug release profile from the delivery system matrix categorizes into the fickian model ( $n=0.5$ ), where drug release is mainly governed by diffusion through the polymeric matrix, non-fickian ( $n=1$ ) where drug release corresponds to zero-order kinetics and primarily driven by polymer swelling,

and finally anomalous transport ( $0.5 < n < 1$ ) where the drug release is governed by both diffusion and swelling<sup>337</sup>.

**Hixson–Crowell model** assumes that drug release is constrained by dissolution velocity rather than diffusion, which can take place via the soluble polymeric matrix. Therefore, this model applies to pharmaceutical dosage forms like tablets, considering that dissolution happens in planes parallel to the active agent's surface if the tablet's dimensions decline proportionately while maintaining its geometrical properties<sup>337</sup>.

Table 2.3: The equations of different mathematical models of drug release.

<b>Model</b>	<b>Equation</b>
<b>Zero-order</b>	$f = k_0.t$
<b>First-order</b>	$f = 1 - \exp(-kt)$
<b>Higuchi</b>	$f = k_H . t^{0.5}$
<b>Korsmeyer-Peppas</b>	$f = k_{kp} . t^n$
<b>Hixson-Crowell</b>	$f = [1 - (1 - k_{HC} . t)^3]$

All mathematical modelling and release profile comparisons were made using the DDSolver add-in on Microsoft excel. The best fit of the drug release mathematical model was chosen based on the highest coefficient of determination (COD or  $R^2$ )<sup>340</sup>.

For drug release/dissolution profile comparison, different mathematical methods have been adopted in the last decade. Of which, difference factor ( $f_1$ ) and similarity factor ( $f_2$ ) are commonly employed. The difference factor ( $f$ ) estimates the percentage (%) difference between the two curves in comparison at each time point. It is a measurement of the relative error between the two curves (Eq. (2.8)). The similarity factor ( $f$ ) measures the similarity in the percentage (%) dissolution between the two curves. It is the logarithm of the reciprocal square root transformation of the sum of squared error (Eq. (2.9))<sup>337</sup>.

$$f1 = \left( \frac{\sum_{t=1}^n |R_t - T_t|}{\sum_{t=1}^n R_t} \right) \times 100 \quad \text{Eq. (2.8)}$$

$$f2 = 50 \times \log \left[ \frac{100}{\sqrt{1 + \frac{\sum_{t=1}^n (R_t - T_t)^2}{n}}} \right] \quad \text{Eq. (2.9)}$$

According to FDA regulatory guidelines<sup>341-343</sup>, release profiles are considered to show high similarity if  $f1 < 15$  and  $f2 > 50$ . While the release profiles are regarded dissimilar if  $f1 > 15$  and  $f2 < 50$ .

Another parameter commonly employed in describing release/dissolution profiles is mean dissolution time (MDT) which represents the sum of the different periods that drug molecules take to be released divided by the total number of drug molecules in the total dose<sup>344</sup>. MDT is calculated according to Eq. (2.10)<sup>340</sup>.

$$MDT = \frac{\sum_{t=1}^n \bar{t}_i \cdot \Delta M_i}{\sum_{t=1}^n \Delta M_i} \quad \text{Eq. (2.10)}$$

One more parameter was introduced by Khan & Rhodes (1972)<sup>345</sup> called dissolution efficiency (DE%). This is defined as the area under the dissolution curve up to a specific time,  $t$ , represented as a percentage of the area of the rectangle described by 100% dissolution at the same time (Eq. (2.11)). DE% is usually used to measure and compare the magnitude of enhancement of the dissolution rate of different formulations.

$$\text{Dissolution efficiency (DE\%)} = \frac{\int_0^t y \cdot dt}{y_{100} \cdot t} \cdot 100 \% \quad \text{Eq. (2.11)}$$

### 2.3.5. *In-vitro* lectin agglutination assay

Lectins are a class of proteins that bind to mono- and oligosaccharides reversibly and with high specificity. They serve as cell recognition moieties on cell surfaces of animals, plants, and microorganisms. They are categorized principally into five specificity groups, depending on the monosaccharide for which they show the highest affinity: mannose, galactose/N-acetylgalactosamine, fucose, N-acetylglucosamine, and N-acetylneuraminic

acid. Most lectins bind to two or more carbohydrate molecules presented on cells' surfaces, such as erythrocytes, inducing cross-linking of the cells and their consequent precipitation, in a phenomenon referred to as 'cell agglutination' <sup>346</sup>.

Based on that concept, Lectin, mainly from *Ricinus communis* Agglutinin 'RCA120', is used to assess the surface exposure or accessibility of galactose sugar on the surface of the nanodelivery system <sup>347,348</sup>. The test protocol involves the incubation of a small volume (100  $\mu$ L) of lectin solution in phosphate buffer at a certain concentration (mostly 1 mg/mL) with a small volume (100  $\mu$ L) of nanosystem dispersion for 20 mins. During that time, the turbidity of the mixture is monitored by measuring optical absorbance at 350 nm <sup>349,350</sup> or 450 nm <sup>351,352</sup>. The specificity of the reaction towards galactose moieties could be further confirmed by adding free excess galactose (100  $\mu$ L of 10 mg/mL Gal in PBS) to reverse the interaction and induce disaggregation <sup>350,353</sup>.

### **2.3.6. *In-vitro* cellular studies**

*In-vitro* cellular studies are laboratory-based experiments performed to examine nanoparticle interactions with cells. These studies are used to assess the safety and efficiency of nanoparticles as drug delivery methods, and to comprehend the mechanisms of nanoparticle cellular uptake and intracellular fate. Cells are generally cultured in the presence of nanoparticles and different biological responses, such as cell viability, proliferation, apoptosis, and gene expression, are measured. These studies may be carried out using various cell types, including cancer cells, primary cells, and immortalised cell lines.

Different cellular study techniques, including cellular cytotoxicity, transport and uptake using flow cytometry, were carried out to evaluate the performance of the formulations on HepG2 cell lines (human hepatoma cell lines that over express ASGPRs).

#### **2.3.6.1. MTS assay for cellular cytotoxicity assessment**

MTS, (3-(4,5-dimethylthiazol-2-yl)-5-(3-carboxymethoxyphenyl)-2-(4-sulfophenyl)-2H-tetrazolium), is a colourimetric assay that is commonly used to measure the cells'

metabolic activity. This assay relies on the ability of mitochondrial nicotinamide adenine dinucleotide phosphate (NADPH)-dependent dehydrogenase enzymes in metabolically active cells to reduce MTS, in the presence of phenazine methosulfate (PMS), into a formazan dye that is soluble in culture media (Figure 2.17)<sup>354</sup>. Afterwards, the formazan dye can be quantified by colourimetric absorbance measurement at 490-500 nm. MTS assay is regarded as an advancement of the typical MTT assay as it produces soluble formazan dye that enables the direct measurement of the dye without the need for intermittent steps for dissolving insoluble formazan dye produced in MTT assay. Therefore, the MTS assay is often described as a “one-step” MTT assay<sup>354</sup>.

In this study, the plate was read at 490 nm by microplate reader (CLARIOstar, BMG LABTECH, Germany). Data were collected from three biological replicates as triplicate measurements, and results are shown as the mean  $\pm$  standard deviation.

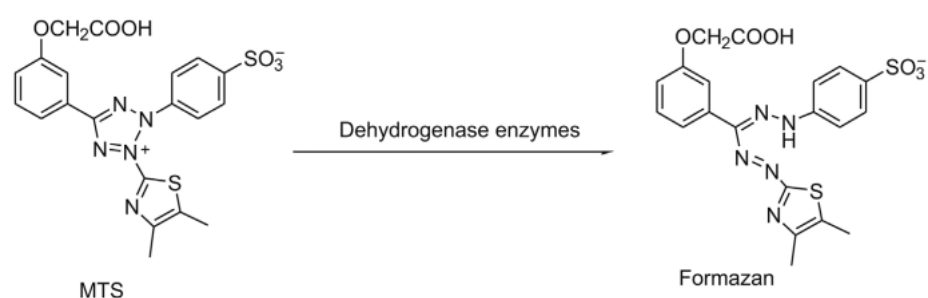


Figure 2.17: Enzymatic reduction of MTS into formazan dye by metabolically active cells. Figure was adapted with permission from reference<sup>354</sup>.

### 2.3.6.2. Flow cytometer

Flow cytometry is a sophisticated technique extensively used in clinical diagnostics and biomedical applications. It is a laboratory tool that measures the physical and biological properties of cells and particles moving in a fluid stream. These properties include relative size, relative granularity, and fluorescent intensity. It operates by passing a stream of cells or particles within a liquid (sheathing liquid) through a laser beam and detecting their scattering and fluorescence as they pass through<sup>355</sup>.

A flow cytometer's fundamental components are a fluidic system for suspending and carrying cells or particles to the laser beam, a laser light source for exciting the cells or particles and causing them to generate fluorescence, and a detection system for measuring

the scattering and fluorescence of the cells or particles as they pass through the beam<sup>355,356</sup>.

The light scattered in the forward direction is detected by the forward scattering channel (FSC), where the degree of scattering relies on the cellular membrane permeability, cell size and the refractive index. However, the scattered light at 90° is detected by a side scattering channel (SSC), where the degree of scattering depends on cellular granularity. Thus, the FSC channel is used to sort cells according to their relative sizes, while the SSC channel sorts the cells according to their relative granularity<sup>356</sup>.

Furthermore, the flow cytometer may be employed to detect the number of fluorochrome molecules in each cell by using a detector with proper fluorescence emission settings, the intensity of which is proportional to the number of fluorochrome molecules in each cell. This could be employed to selectively label a specific cell type or component<sup>356</sup>.

In this study, a flow cytometer (CytoFlex, Beckman Coulter, USA) was used to assess the cellular uptake of different nanoparticles by HepG2 cells. Data were acquired and analysed using CytExpert software (v2.3, Beckman Coulter, USA). The gates were assigned using control untreated cells as shown in Figure 2.18. The first gate (P1) was assigned based on both SSC and FSC to exclude cell debris while the second gate (P2) was determined based on the FSC width and height to exclude cell doublets and aggregates. The machine was programmed to record 10000 events in the second gate (P2).

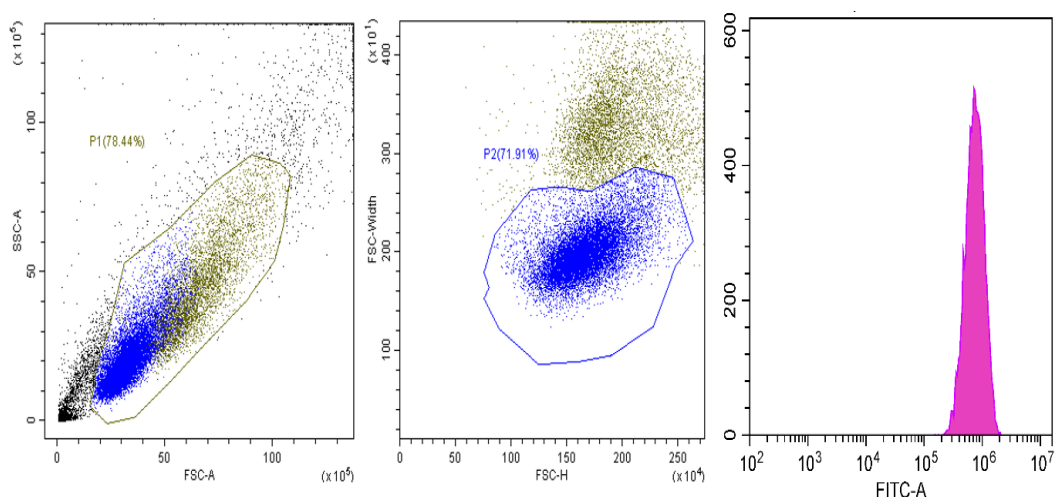


Figure 2.18: HepG2 gating strategy used in this study. SSC is a side scattered channel, FSC is a forward scattered channel and FITC-A is a Fluorescein isothiocyanate channel for coumarin-6 detection.

### 2.3.6.3. Cellular transport studies

In the gastrointestinal tract, a single layer of epithelial cells lines the inner intestinal wall and represents the rate-limiting barrier to drug absorption. As a result, the appropriate recreation of a human differentiated epithelial cell monolayer *in-vitro* allows for the prediction of oral drug absorption in humans. Caco-2, a human colon cancer cell line, has been demonstrated to be effective for this purpose<sup>357</sup>. The caco-2 cell line was obtained from a moderately differentiated colonic adenocarcinoma and is distinctive in that it spontaneously differentiates into a polarised columnar cell that mimics small intestine enterocytes morphologically and functionally<sup>358</sup>.

Caco-2 cells are cultured on semipermeable membrane inserts suspended in culture dish wells to form a three-compartment system that mimics the luminal, cellular, and basolateral parts of the mucosal epithelium (Figure 2.19). When cells reach a high confluency level (~ 90%), they begin to differentiate and form a tight barrier separating the apical and basolateral compartments after a few weeks (typically three weeks). To ensure efficient and prompt cell differentiation, cells with a high passage number, ideally between 95-105, is preferred<sup>359</sup>.

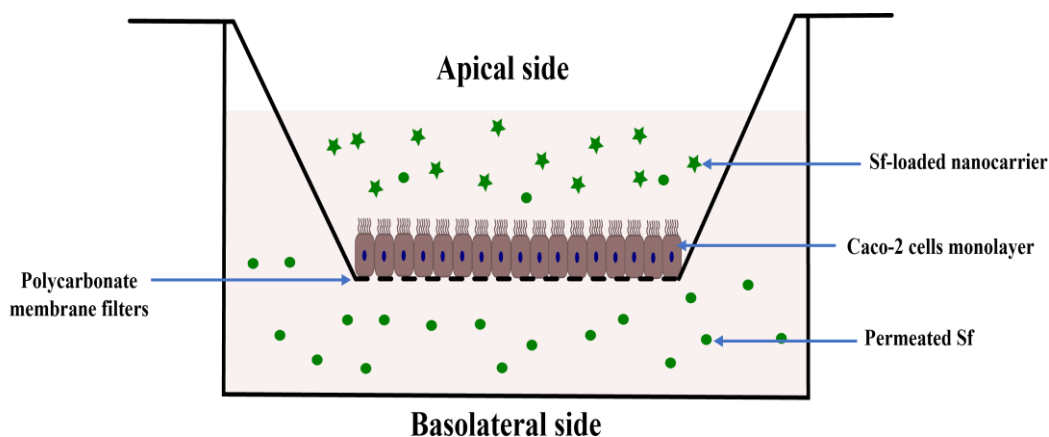


Figure 2.19: Schematic representation of the cellular transport study design for assessment of Sf permeation through Caco-2 cells monolayer.

This model allows for the study of apical to basolateral chemicals and metabolite transfer, as well as the impact of endogenous mediators on the transport and metabolism of compounds present in both the apical and basolateral compartments. Therefore, it is critical to verify monolayer barrier integrity when measuring apical to basolateral and

basolateral to apical flux for chemicals of interest. To verify monolayer integrity, transepithelial electrical resistance (TEER) and/or flow of chemicals transported across the monolayer paracellularly (e.g., mannitol, inulin, and fluorescent Lucifer yellow) are widely utilised<sup>358</sup>.

For studying the intrinsic passive permeability of poorly soluble hydrophobic drugs, they are often dissolved in DMSO. However, DMSO may affect the integrity of the Caco-2 cells monolayer. Therefore, it is recommended that the maximum DMSO concentration should not exceed 1%<sup>359</sup>. Moreover, the solubility of the permeated drug in the receiving compartment should be guaranteed to ensure sink conditions. For that, 4% BSA could be added to enhance drug solubility with complete medium replacement at each time interval. However, using BSA necessitates the pre-treatment of release samples before analysis to ensure drug extraction and BSA precipitation (by adding acetonitrile in 1:2 sample to acetonitrile ratios)<sup>359</sup>.

In this study, final volumes of 0.4 ml apically and 1.2 basolaterally were used during the experiment to ensure the same hydrostatic pressure between the two compartments<sup>359</sup>. For measuring the influx apparent permeability coefficient, the tested sample was placed in the apical side and the sampling was done from the basolateral side (as shown in Figure 2.19), while for efflux tested sample was placed in the basolateral side. The apparent permeability coefficient was calculated using the following Eq. (2.12):

$$P_{app} = \frac{V}{A \times C} \times \frac{dC}{dt} = \frac{1}{A \times C} \times \frac{dQ}{dt} \quad \text{Eq. (2.12)}$$

Where V is the volume of receiving compartment, A is the surface area of the cell monolayer (surface area of the semipermeable membrane), C is the initial concentration of the tested drug, dC/dt is the rate of the drug concentration change in the receiver compartment, and dQ/dt is the rate of drug amount change in the receiver compartment<sup>266</sup>.

In some cases, to assess the efflux inhibition potential of the tested samples, the efflux ratio is calculated using Eq. (2.13):

$$\text{Efflux ratio} = \frac{P_{app (BL-AP)}}{P_{app (AP-BL)}} \quad \text{Eq. (2.13)}$$

Where,  $P_{app (BL-AP)}$  is the apparent permeability of efflux direction, and  $P_{app (AP-BL)}$  is the apparent permeability of the influx direction. The lower the efflux value is, the more efflux inhibitor the tested sample is.

### **2.3.7. Statistical analysis**

Data were analysed using GraphPad 8 software. All measurements were done in triplicate, and the results were represented as mean  $\pm$  SD. Unpaired t-test was employed to evaluate the significance of the difference between the means of the two variables. The statistical differences were represented as \* $P < 0.05$ , \*\* $P < 0.01$ , \*\*\* $P < 0.001$ , and ns = not significant ( $P > 0.05$ ).



## **Chapter 3**

*Preparation, optimisation, and in-vitro characterisation of galactosylated solid lipid nanoparticles and nanostructure lipid carrier for liver-targeted delivery of sorafenib*

### 3.1. Introduction

The use of nanotechnology in cancer treatment has revolutionised the way we approach the delivery of cytotoxic agents. One of the most promising and widely studied nanocarriers is the solid lipid nanoparticle (SLN). SLN are composed of biocompatible lipids and can encapsulate a variety of drugs, including cytotoxic agents<sup>156,197,276</sup>. Their small size and unique surface properties allow efficient delivery to tumour sites, improved drug solubility, and sustained drug release. As a second generation of SLN, nanostructured lipid carriers (NLC) were developed to provide improved drug loading capacity, stability and drug release compared to SLN<sup>145,159,186,360</sup>.

Hepatocellular carcinoma (HCC) is one of the most common and deadly cancers worldwide. Unfortunately, most HCC cases are diagnosed in advanced stages in which surgical intervention is limited, and systemic therapy is the only option<sup>361</sup>. Sorafenib (Sf), a multi-tyrosine kinase inhibitor, has shown promising results in the treatment of HCC, but its clinical efficacy is limited by poor bioavailability and off-target effects<sup>68</sup>. To overcome these limitations, galactosylated solid lipid nanoparticles (SLN) and nanostructured lipid carriers (NLC) are considered a promising approach for targeted delivery of Sorafenib to liver cancer cells. Galactosylation allows for selective binding of the SLN and NLC to the asialoglycoprotein receptors (ASGP receptors) on the surface of HCC cells, leading to improved drug uptake and efficacy<sup>108</sup>. Overall, targeted drug delivery using galactosylated SLN and NLC has the potential to significantly improve the clinical outcomes of Sf for patients with HCC.

This chapter aims to systemically study the influence of the lipid composition on the physicochemical properties, and the drug loading capacity of Sf-loaded SLN and NLC. Consequently, the development of galactosylated SLN and NLC, based on the optimised formulations, followed by physicochemical characterisation and *in-vitro* cellular cytotoxicity studies (Figure 3.1).

The objectives of this chapter are to:

- To Prepare a liver-targeting ligand using lactobionic acid-stearylamine conjugate.
- To develop and optimise liver targeted SLN and NLC for delivery of Sf.
- To study the impact of formulation parameters on the colloidal properties, drug loading, and drug release of the prepared lipid nanoparticles.
- To evaluate the cellular cytotoxicity on HepG2 cells of the blank and optimised liver targeted SLN and examine the impact of delivery system ingredients on cellular viability.

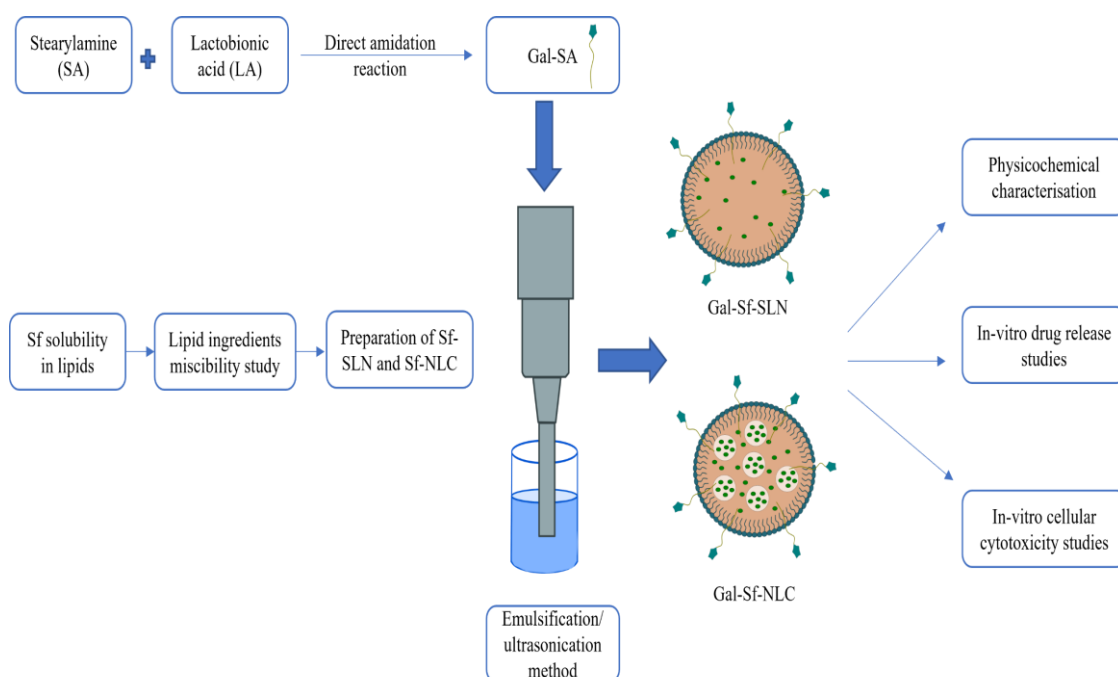


Figure 3.1: Schematic representation of the workflow for the preparation and characterisation of Gal-Sf-SLN and Gal-Sf-NLC

## **3.2. Materials and methods**

### **3.2.1. Materials**

Compritol® 888 ATO, Precirol® ATO 5, Geleol™, Gelucire® 48/0.1, 48/16, 44/14, and 50/13, Peceol™, Capryol® 90, Labrafac® WL 1349, Transcutol® P, Labrasol®, and Labrafil® M 1944 CS were kindly provided from Gattefossé (Saint-Priest, France). Tripalmitin (Dynasan® 116), trimyristin (Dynasan® 114), and tristearin (Dynasan® 118) were a kind gift from IOI Oleo (IOI Oleochemicals GmbH, Germany). Lipiodol® oil was purchased from Guerbet (UK). Sorafenib was obtained from LC Labs (USA). Lactobionic acid, Tween® 80, Poloxamer 188 (Pluronic® F-68), Poloxamer 407 (Pluronic® F-127), ethyl oleate, Soybean oil, Sunflower oil, deuterated dimethyl sulfoxide (DMSO-d<sub>6</sub>), deuterated chloroform (CDCl<sub>3</sub>), ethylenediamine (EDA), N-hydroxysuccinimide (NHS), 1-Ethyl-3-(3-dimethyl aminopropyl) carbodiimide (EDC), trypsin-EDTA solution, RPMI 1640 Medium, fetal bovine serum (FBS), phosphate buffer saline (PBS), 1% non-essential amino acids (NEAA), 1% penicillin–streptomycin solution, triethylamine (TEA), phosphotungstic acid (PTA), ethanol, acetonitrile HPLC grade were all purchased from Sigma-Aldrich (Sigma- Aldrich, UK). All chemicals were used without further purification. Double distilled water from Milli-Q systems (Millipore, Watford, UK) was used for all experiments.

### **3.2.2. Conjugation of stearylamine (SA) and lactobionic acid (LA) to form Gal-SA conjugate**

Galactosylated stearylamine (Gal-SA) was synthesised using a previously reported method<sup>118</sup> with some modifications (Figure 3.2). Briefly, 0.716 g of LA (2 mmol) was dissolved with 0.465 g of EDC (3 mmol) and 0.345 g of NHS (3 mmol) in 2 mL of DMSO and left under stirring for 2 h at 50° C for the activation of the carboxylic group of LA. Afterwards, 0.27 g of SA (1 mmol) dissolved in 15 mL of methanol at 70° C was added to the previous reaction mixture, which continued under refluxing at 70° C for 24 h. The product was then precipitated by adding Milli-Q and collected by filtration with a 0.45 µm Millipore filter (Millipore, Massachusetts, USA). Finally, the precipitate was washed

thrice with Milli-Q water to remove unreacted LA, followed by washing with methanol to remove unreacted SA and dried under a vacuum overnight.

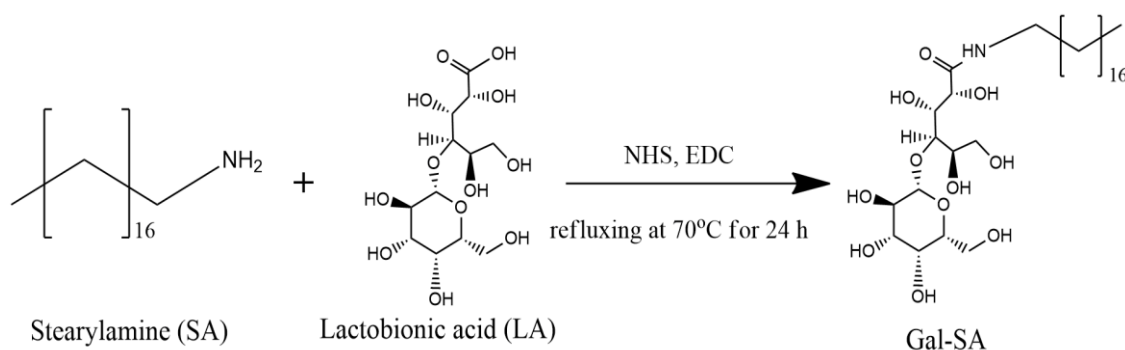


Figure 3.2: Synthesis of Gal-SA conjugate

### 3.2.3. Characterisation of Gal-SA

ATR-FTIR measurements were done as detailed in Chapter 2 (section 2.3.2.6.), while  $^1\text{H-NMR}$  spectra were acquired after dissolving LA in DMSO- $d_6$  and both SA and Gal-SA in  $\text{CDCl}_3$  and analysed using 500 MHz spectrometer (Bruker Avance DRX 500, UK). The conjugation efficiency was measured by quantifying galactose content in the conjugation product using the phenol/sulfuric acid assay method<sup>362</sup>. Briefly, 1 mL of 5% phenol solution was added to 1 mL of aqueous Gal-SA conjugate, followed by 5 ml of concentrated sulfuric acid. Then the mixture was kept at 25 °C for 20 min. The galactose content was quantified by measuring the UV absorbance at 490 nm using the calibration curve of standard galactose solutions within the concentration range (20-200  $\mu\text{g/mL}$ ). All measurements were done in triplicates.

### 3.2.4. Sorafenib quantification using high-performance liquid chromatography (HPLC)

The quantification of Sf was carried out using the HPLC method as previously reported<sup>363</sup>. The HPLC system is composed of a tertiary gradient mobile phase delivery pump (PU-1580, Jasco, Japan) connected to a degasser unit (DG-1580-53, Jasco, Japan) and equipped with a multi-wavelength UV-vis detector (UV-1570M, Jasco, Japan). The separation was done using a reverse-phase column (HC-C18, 4.6x250 mm, 5  $\mu\text{m}$ , 400

bar, Agilent, UK) connected to a guard column (HC-C18, 4.6x12.5mm, 5  $\mu$ m, 400 bar, Agilent, UK) and a mobile phase of acetonitrile/water (75:25, v/v) with 0.03% aqueous triethylamine at a flow rate of 1 mL/min. The Sf was detected at a wavelength of 265 nm. The calibration curve of Sf was established in the range of 0.2-50  $\mu$ g/mL using a standard Sf solution. All measurements were done in triplicates.

### 3.2.5. Determination of Sf solubility in different solid lipids and oils.

In order to choose the proper lipid matrix for SLN and NLC, the solubility of Sf in different solid and liquid lipid components was determined according to the previously reported method<sup>364</sup>. For solid lipids, 1 g of lipid was melted at 10° C above the melting point of each lipid and mixed under stirring with an excess amount of Sf for 4 h, followed by equilibration, without stirring, for another 2 h. Next, the melted lipids were swiftly centrifuged (Megafuge 16, Thermofisher scientific, UK) at 10,000 rpm for 10 min by placing the test vial in 15 mL falcon tube containing hot water (~80°C) to allow precipitation of excess undissolved Sf (Figure 3.3). Afterwards, 10 mg were scraped off of the solidified lipid's surface and dissolved in acetonitrile, followed by injection in the HPLC method. In the case of liquid ingredients, 1 mL of each liquid was mixed with an excess amount of Sf in a screw-capped vial. The vials were kept under shaking at 37°C for 72 h in a shaking incubator (KS 2000 i control, IKA, UK) at a shaking rate of 100 rpm. Afterwards, the dispersions were centrifuged at 10,000 rpm for 15 min to allow precipitation of excess undissolved Sf, followed by analysing the supernatant using the HPLC system after dilution with acetonitrile<sup>286</sup>. All samples were done in triplicate, and the solubilities were presented as mean  $\pm$  SD.



Figure 3.3: Solidified lipid in vial after centrifugation at 10,000 rpm for 10 min in falcon tube containing hot water at 80°C to allow slow solidification during centrifugation.

### **3.2.6. Miscibility assessment of lipid ingredients**

For determining the best proportions of lipid excipients that showed the best solubilising potential for Sf, the miscibility of excipients (Gelucire® 48/16 and Transcutol® P) with the main solid lipid Precirol® ATO 5 was investigated following the previously reported method<sup>282</sup>. Different excipient percentages (10, 20, 30, 40, and 50% w/w to Precirol® ATO 5) were mixed and agitated at 200 rpm for 1 h at 80° C. Afterwards, the samples were kept at room temperature (~ 25°C) for 24 h before investigation using differential scanning calorimetry (DSC) and paper smear methods.

DSC was used to monitor the depression in the melting point of Precirol upon mixing with different excipients. 5 mg of samples were weighed and placed in Tzero aluminium pans that were hermetically crimped using a lid with a pinhole. Then, samples were heated at a heating rate of 5° C/min from 25° C to 80° C. All other parameters were kept constant, as previously stated in Chapter 2 (section 2.3.2.3.). Additionally, the miscibility between Transcutol® P and Precirol® ATO 5 was further examined by smearing a cooled sample of the solid mixture onto hydrophilic filter paper, followed by visual inspection to determine the existence of any liquid droplets in the filter paper as an indication of phase separation.

### **3.2.7. Preparation of SLN and NLC**

SLN/NLC have been prepared using the emulsification/ultrasonication method. Briefly, the lipid phase mixture (solid lipid, and liquid lipid with/without solubiliser) was melted and mixed well at 5-10° C above the melting point of the solid lipid. Afterwards, 10 mg of Sf was dissolved in the melted lipid mixture with the aid of 0.5 mL of ethanol. Then, 10 mL of aqueous surfactant solution at the same temperature was added to the melted lipid phase and kept under stirring at 1000 rpm on a hot-stage magnetic stirrer for 5 min to form a pre-emulsion. The mixture was then sonicated for 3 min using a probe sonicator (Fisherbrand™ 505 sonicator, UK) at 20% amplitude, applying pulse “ON” for 20 s and pulse “OFF” for 5 s. The final dispersion was kept under stirring at 300 rpm at room temperature (~ 25°C) for 1 h to allow the solidification of lipid nanoparticles. Finally, the dispersions were filtered using a 1 µm syringe filter (glass filter, Kinesis scientific, UK) to remove the excess untrapped drug. Preliminary screening of selected lipids (solids

and liquids) based on Sf solubility using different surfactants was carried out to choose the optimised formulation. The Galactosylated SLN/NLC were prepared using the optimised formulations, adding 10 mg of Gal-SA to the lipid phase during preparation procedures.

### 3.2.8. Characterisation of SLN and NLC

The average particle size (P.S.), polydispersity index (PDI) and Zeta potential (Z.P.) of all formulations were measured using (Zetasizer Nano, Malvern Instruments, Malvern, UK) following the procedures described in Chapter 2 (sections 2.3.2.1. and 2.3.2.2. ). Particles' morphology was inspected using transmission electron microscopy (TEM) and scanning electron microscopy (SEM) following the procedures and conditions detailed in Chapter 2 (sections 2.3.3.1. and 2.3.3.2.).

### 3.2.9. Drug loading quantification

The direct assay method was adopted to determine entrapment efficiency (EE%) and loading capacity (LC%). Briefly, 50 µL of lipid nanoparticles dispersions were digested with 950 µL of acetonitrile with the aid of sonication for 5 min to extract the drug-loaded followed by filtration with 0.22 µm PTFE syringe filters (Fisherbrand™, UK). After 20-time dilution with acetonitrile, 20 µL of the solution was injected into the aforementioned HPLC system, and the amount of Sf was quantified. Entrapment efficiency (EE%) and Loading capacity (LC%) were calculated according to equations (3.1) and (3.2), respectively:

$$EE\% = \frac{W_{loaded\ Sf}}{W_{initial\ Sf\ amount}} \times 100 \quad \text{Eq. (3.1)}$$

$$LC\% = \frac{W_{loaded\ Sf}}{W_{loaded\ Sf} + W_{lipid\ components}} \times 100 \quad \text{Eq. (3.2)}$$

Where,  $W_{loaded\ Sf}$  is the weight of Sf loaded in the whole sample,  $W_{initial\ Sf}$  is the initial weight of Sf (=10 mg), and  $W_{lipid\ components}$  is the total weight of all lipid ingredients that comprise the nanoparticle matrix (= 500 mg).

### **3.2.10. Solid state characterisation**

For solid-state characterisation of the produced lipid nanoparticles (SLN/NLC), samples were frozen with liquid nitrogen and placed into a freeze-dryer (VirTis® Wizard 2.0, SP SCIENTIFIC, USA) at -80° C and under a vacuum for 24 h. The lyophilised samples were placed in a silica gel desiccator at room temperature (~ 25°C) until the analysis.

#### **3.2.10.1. Attenuated total reflection-Fourier transform infrared (ATR-FTIR)**

The Attenuated total reflection-Fourier transform infrared (ATR-FTIR) spectra of raw materials, physical mixtures, and freeze-dried galactosylated blank and Sf-loaded lipid nanoparticles (SLN and NLC) were obtained using FTIR spectrophotometer as mentioned in Chapter 2 (section 2.3.2.6). All measurements were done in triplicate using absorbance mode and were analysed using OPUS software.

#### **3.2.10.2. Differential scanning calorimetry (DSC)**

DSC was carried out for raw materials, physical mixtures, and freeze-dried galactosylated blank and Sf-loaded lipid nanoparticles (SLN and NLC) to investigate the impact of nanoformulation and Sf encapsulation on the thermal behaviour of the components. DSC scans were done as prescribed in Chapter 2 (section 2.3.2.3.). All measurements were performed in triplicate.

#### **3.2.10.3. Powder X-Ray Diffraction (PXRD)**

To identify any changes in the crystal lattice of the materials using in nanoformulation of SLN and NLC, PXRD studies were performed on raw materials, physical mixtures, and freeze-dried galactosylated blank and Sf-loaded lipid nanoparticles (SLN and NLC) following the procedures detailed in Chapter 2 (section 2.3.2.5.).

### **3.2.11. Solid redispersibility test**

To assess the redispersibility of the freeze-dried optimised lipid nanoparticles (blank Gal-SLN, Gal-Sf-SLN, blank Gal-NLC, and Gal-Sf-NLC) with and without the addition of

5% trehalose as a cryoprotectant, the particle size was monitored before and after the redispersion in MilliQ water by sonication for 5 min. Moreover, the redispersibility index was calculated using Eq. (3.3)<sup>365</sup>

$$RI = \frac{\text{Average particle size after redispersion}}{\text{Average particle size before freeze drying}} \quad \text{Eq. (3.3)}$$

### 3.2.12. *In-vitro* drug release studies

The sorafenib release profile was investigated using the dialysis bag method. Firstly, to prepare the Sf solution as a control, different solvents for Sf were screened to choose the solvent that permits the complete release of Sf without drug precipitation in the dialysis bag. Afterwards, 2 mL of Gal-Sf-SLN, Gal-Sf-NLC and free sorafenib solution (with equivalent total sorafenib content of 100 µg) were placed in a dialysis tube (Snakeskin™, M.W.C.O =10 KDa, regenerated cellulose, Sigma, UK). Then, the bag was immersed in 40 mL of 1% Tween 80 in PBS at pH 7.4 as a release medium (Sf solubility in release mediums was 72.3 ± 5 µg/mL) and incubated in a shaking incubator (KS3000 i control IKA®, UK) at 37°C with a shaking rate of 100 rpm. At predetermined intervals (0.5, 1, 2, 4, 8, 10, 24, 48, 72, 96, 120, and 144 h), samples of 0.5 mL were taken and replaced with 0.5 mL of fresh release medium. Released samples were filtered with a 0.22 µm syringe filter (Fisherbrand™, UK) and assayed by injecting 20 µL into the HPLC system as previously described. The experiments were carried out in triplicate and the average percent cumulative Sf amount released was expressed as mean ± SD.

Release profiles were established by plotting the percent of cumulative Sf released against the time. Furthermore, data were fitted into various drug release kinetic models (zero order, first order, Higuchi, Korsmeyer-Peppas, and Hixon-Crowell). The best fit was chosen based on the highest coefficient of determination (R<sup>2</sup>). In addition, for further comparison between different release profiles, mean dissolution time (MDT), the difference (*f*1), and similarity (*f*2) factors were calculated using Excel DD solver add-in.

### 3.2.13. *In-vitro* cellular cytotoxicity studies

The HepG2 cell line, purchased from (Sigma, UK), was used in the study as an *in-vitro* model of liver cancer cells with overexpression of ASGP receptors (76.000 receptor/cell)<sup>110</sup>. The cells were grown in T-75 flasks using RPMI 1640 medium supplemented with 10% fetal bovine serum (FBS), 1% penicillin–streptomycin solution and non-essential amino acids. HepG2 cells were incubated in a 5% CO<sub>2</sub> humidified (95%) incubator (AUTOFLOW, UK) at 37°C. Cell passages ranged from 9 to 20 and were passaged at 90% confluency using 0.25% trypsin-EDTA solution.

Cellular cytotoxicity studies were conducted using the MTS assay technique to determine the impact of sorafenib encapsulated into lipid nanoparticles and the surface galactosylation of optimised lipid nanoparticles (SLN and NLC) on the cytotoxicity efficiency of Sf on HepG2 cells. Briefly, HepG2 cells were seeded at a density of 7,000 cells/well/100 µL of the medium in a 96-well plate and incubated at 37°C for 24 h to allow cell attachment<sup>366</sup>. Afterwards, cells were treated with different formulations (Sf solution in 1% DMSO, blank SLN, blank NLC Sf-SLN, Sf-NLC, Gal-Sf-SLN and Gal-Sf-NLC) at Sf concentration ranges from 20 to 0.5 µg/mL. All formulations were sterilised by filtration using a 0.45 µm sterile syringe filter (Minisart, Sartorius, UK). After 48 h of incubation, the medium was replaced with a fresh one, containing 10 µL of MTS reagent and cells were further incubated in a dark incubator for another 3 h. The absorbance was measured by a microplate reader (CLARIOstar, BMG LABTECH, Germany) at wavelength 490 nm. Untreated cells were used as a control for 100% cell viability, and MTS without cells were used as a blank to calibrate the spectrophotometer to zero absorbance. Cell viability was calculated according to Eq. (3.4)

$$Cell\ viability\ (\%) = \frac{Abs_{(sample)} - Abs_{(blank)}}{Abs_{(control)} - Abs_{(blank)}} \times 100 \quad Eq. (3.4)$$

Where,  $abs_{(sample)}$  is the UV-Vis absorbance of cells treated with the sample,  $abs_{(blank)}$  is the UV-Vis absorbance of empty wells with MTS reagent, and  $abs_{(control)}$  is the UV-Vis absorbance of untreated cells (100% cell viability)

### 3.3. Results and discussion

#### 3.3.1. Synthesis and characterisation of Gal-SA

Galactosylation of SLN and NLC has been reported as a successful strategy for actively targeted drug delivery to hepatocytes through ASGP-R mediated cellular uptake<sup>118,367–369</sup>. In this study, conjugation between lactobionic acid (as galactose bearing-moiety) with Stearylamine (as lipophilic anchor moiety) has been carried out through an amidation reaction.

ATR-FTIR was used to confirm the conjugation between SA and LA. As depicted in Figure 3.4, SA exhibited its typical absorption bands of CH<sub>2</sub>, CH<sub>3</sub> at 2916, 2847, and 1460 cm<sup>-1</sup>; with another weak band at 3333 cm<sup>-1</sup>, which is ascribed to the terminal amine group<sup>370</sup>. In addition, LA spectrum showed a broad band around 3339 cm<sup>-1</sup>, which refers to OH groups of both the carboxylic group and the pyran ring and a sharp peak at 1736 cm<sup>-1</sup> that is attributed to the carbonyl group of the carboxylic acid. In Gal-SA conjugate spectrum, the distinctive amide bands at 1618 cm<sup>-1</sup> and 1580 cm<sup>-1</sup> beside the presence of LA hydroxyl groups peak at 3339 cm<sup>-1</sup> confirm the successful formation of the Gal-LA conjugation. These findings are consistent with the previously reported data<sup>118,367</sup>.

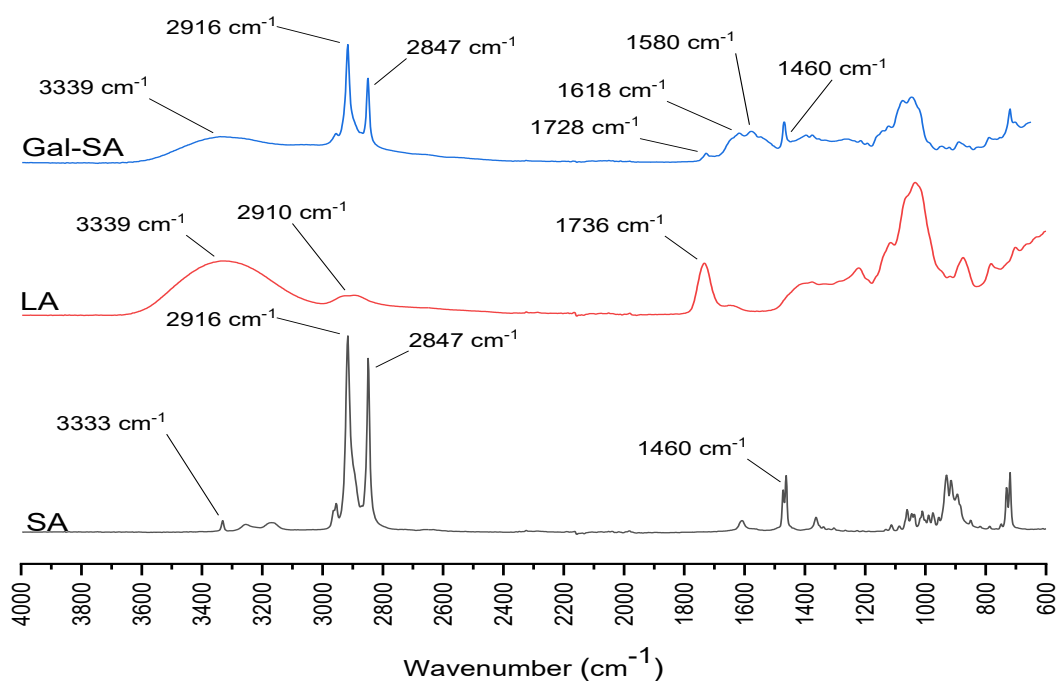


Figure 3.4: FTIR absorbance spectra of SA, LA, and Gal-SA.

On the other hand, the  $^1\text{H-NMR}$  spectrum ( $\text{CDCl}_3$ , 500 MHz) of SA (Figure 3.5a) showed several diagnostic signals including,  $\delta = 0.88$  ppm for terminal  $\text{CH}_3$ ,  $\delta = 1.26$  and  $1.30$  ppm for  $(\text{CH}_2)_n$  groups, and a small peak at  $\delta = 1.29$  ppm assigned to free  $\text{NH}_2$ . While the spectrum of Gal-SA (Figure 3.5b) exhibited additional small signals in the range between 2.70-4.00 ppm, corresponding to oxygenated protons of the pyran ring of LA. Furthermore, a new small signal was assigned at  $\delta = 8.31$  ppm corresponds to NH of the newly formed secondary amide group ( $\text{NH-C=O}$ ). The signals at  $\delta = 1.56$  ppm, and 7.26 ppm correspond to  $\text{H}_2\text{O}$  and  $\text{CHCl}_3$ , respectively. Finally, it is worth mentioning that the signals' integration of the conjugation product (Gal-SA) was relatively low compared to pure SA due to its poor solubility in  $\text{CDCl}_3$  compared to SA. Altogether, these results confirm the successful formation of Gal-SA.

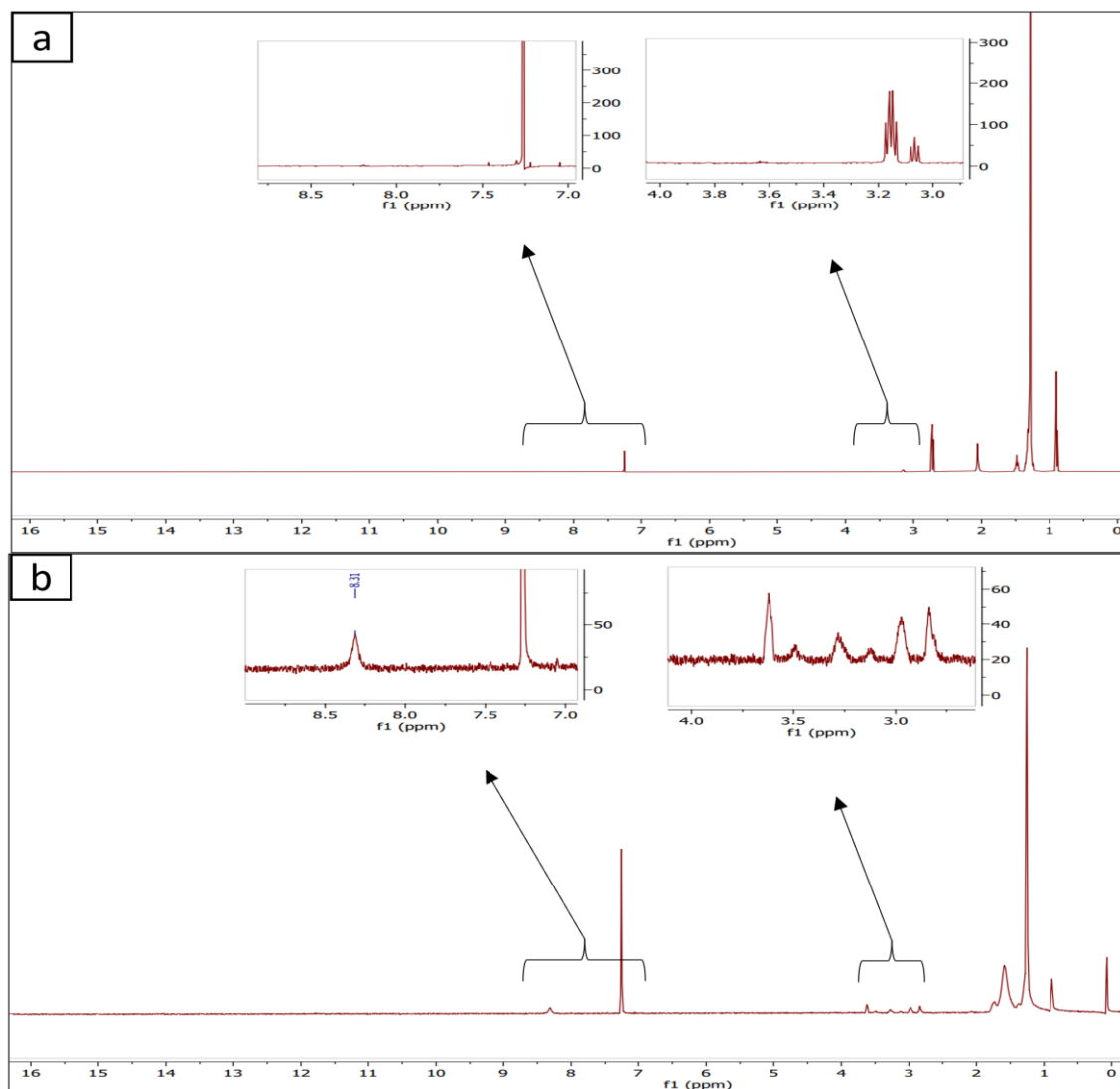


Figure 3.5:  $^1\text{H-NMR}$  spectra of (a) SA, and (b) Gal-SA recorded in  $\text{CDCl}_3$ .

For quantification of the conjugation efficiency of Gal-the SA, the phenol/sulfuric acid method was adopted. This method was first introduced by Dubois M. et al.<sup>362</sup> for quantifying sugar (simple, oligo and polysaccharides) in biological samples. In the assay, sulfuric acid is used to breakdown sugars into monosaccharides, followed by dehydration into furan derivatives that condense with phenol to produce yellow-golden coloured compounds (Figure 3.6) that could be assayed colourimetrically by measuring absorbance at  $\lambda = 490 \text{ nm}$ <sup>362</sup> (Figure 3.7a). Different standard galactose solutions have been prepared and used to construct a calibration curve (Figure 3.7b) in the concentration range (20 – 200  $\mu\text{g/ml}$ ), showing a good coefficient of determination ( $R^2 = 0.9916$ ).

Conjugation efficiency (number of conjugated SA moles to total number of moles) calculated was  $29.5 \pm 1.7 \%$ , giving galactose content of  $14.2 \pm 0.6 \%$  w/w.



Figure 3.6: Galactose standard solutions after adding 1 ml of 5% phenol and 5 ml of sulphuric acid and incubation at 25°C for 20 mins.

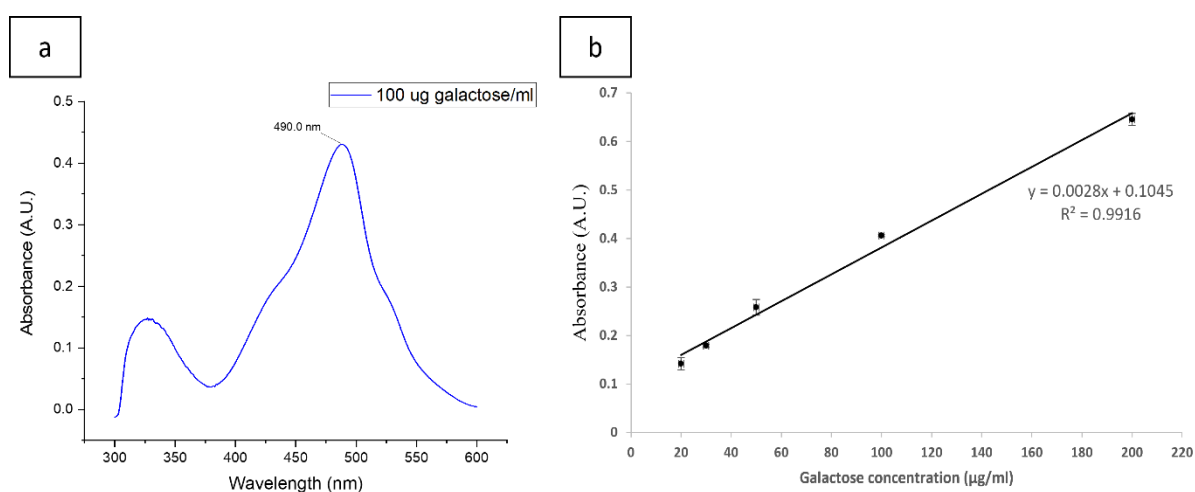


Figure 3.7: UV/Vis spectrum of standard galactose solution at a concentration of 100  $\mu\text{g/mL}$  (a) and the calibration curve of galactose standard solutions (at concentrations from 20-200  $\mu\text{g/mL}$ ) using phenol/sulfuric acid colourimetric assay (b).

### 3.3.2. Sf quantification using HPLC method

For quantification of Sf in different matrix systems, the HPLC method was adopted from a previously reported study<sup>363</sup>. Sf standard solutions demonstrated good sharp peaks at retention time  $R_t$  around 5.05 min (Figure 3.8a). Furthermore, Sf concentrations (x) showed a perfect linear correlation with peaks' areas with a regression equation ( $Y = 74254x - 109.63$ ) having  $R^2 = 1$  (Figure 3.8b).

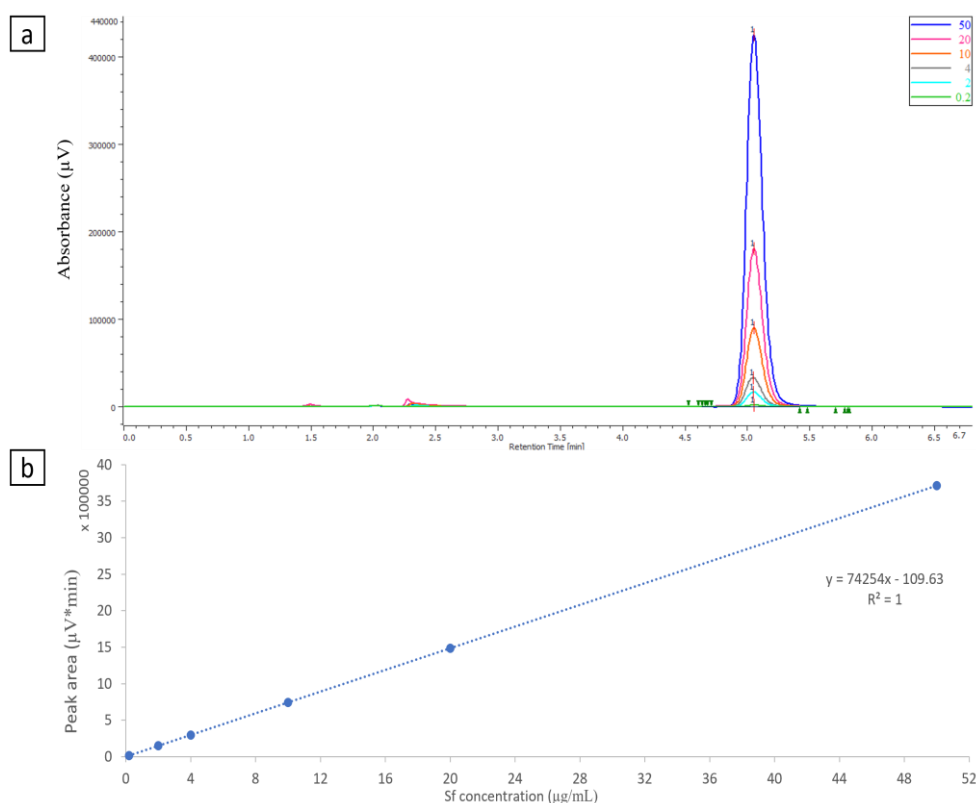


Figure 3.8: HPLC chromatograms (a) and calibration curve (b) of Sf standard solutions, UV absorbance was measured at a wavelength of 265 nm within a linearity range between 0.2-50 μg/mL.

For determining the limit of detection (LOD) and Limit of quantification (LOQ), equations 3.5 and 3.6 were used, respectively.

$$LOD = \frac{3.3 \sigma}{S} \quad \text{Eq. (3.5)}$$

$$LOQ = \frac{10 \sigma}{S} \quad \text{Eq. (3.6)}$$

Where  $\sigma$  is the standard deviation of the intercept, and S is the slope of the calibration curve. LOD was 0.01  $\mu\text{g/mL}$ , while LOQ was 0.03  $\mu\text{g/mL}$ .

### 3.3.3. Sf solubility in different lipid matrices

Drug solubility in the lipid matrix of SLN and NLC has been reported to be the primary determinant of drug loading in these systems<sup>151,153</sup>. However, due to the difficulty of the precise quantification of drugs within the lipid (either solid or viscous oil) matrix, limited studies have reported studying the solubility of drugs in lipid matrices as a systematic approach to choosing the lipid matrix. Different methods were utilised for that purpose, including semiquantitative methods such as visual inspection of undissolved drug particles<sup>371,372</sup> or using hot stage microscopy<sup>373</sup>, and the more accurate quantification methods such as HPLC<sup>364</sup>. Hence in our study, the HPLC method was adopted. As depicted in Table 3.1, Sf solubilities in different solid lipid ingredients were screened and came in the following order: Geleol<sup>TM</sup> > Precirol® ATO 5 > Compritol® 888 ATO > Trimyrustin > Stearic acid > Tristearin  $\geq$  Tripalmitin > Gelucire® 48/01. It was noted that Sf exhibited lower solubility in triglycerides (e.g. Tristearin, Tripalmitin, and Trimyrustin) compared to mono- and diglycerides. This could be attributed to their high crystalline structure, which does not have many voids to accommodate drug molecules<sup>374,375</sup>. Moreover, the high viscosity of the melted lipid of these triglycerides may hamper the efficient mixing between the drug and the lipid. Additionally, Sf solubility in lipophilic solid solubilisers showed a direct correlation with their HLB (Gelucire 48/16 > Gelucire 44/14 > Gelucire 50/13).

Table 3.1: Sf solubility in different solid lipid ingredients.

Lipid ingredient	Solubility (mg/g)
<b>Solid lipids</b>	
Geleol <sup>TM</sup>	6.56 $\pm$ 0.13
Precirol® ATO 5	3.96 $\pm$ 0.11
Compritol® 888 ATO	3 $\pm$ 0.07
Stearic acid	1.29 $\pm$ 0.09
Tristearin	0.72 $\pm$ 0.02

Tripalmitin	0.7 ± 0.01
Trimyristin	1.35 ± 0.02
Gelucire® 48/01	0.93 ± 0.01
<b>Lipophilic solid solubilisers</b>	
Gelucire® 48/16	69.47 ± 4.69
Gelucire® 44/14	49.22 ± 0.81
Gelucire® 50/13	41.86 ± 0.94

On the other hand, the solubility of Sf in different lipophilic liquid ingredients was examined. As shown in Table 3.2, the Sf solubility was found to be the highest in Peceol™ and Caproyl® 90 at  $15.68 \pm 0.51$  mg/mL and  $13.44 \pm 0.17$  mg/mL, respectively. However, Transcutol® P, which is well known to be a powerful solubiliser<sup>273</sup>, has exhibited the highest solubility of  $162.18 \pm 2.83$  mg/mL. These results partially agree with the previously reported data with a slight deviation that could be attributed to the use of sorafenib tosylate salt instead of the base<sup>286</sup>.

Table 3.2: Sf solubility in different liquid lipids and liquid solubilisers.

Lipid ingredient	Solubility (mg/mL)
<b>Liquid lipids (oils)</b>	
Peceol™	$15.68 \pm 0.51$
Caproyl® 90	$13.44 \pm 0.17$
Lipiodol® oil	$1.13 \pm 0.14$
Ethyl oleate	$0.27 \pm 0.05$
Soybean oil	$0.31 \pm 0.04$
Sunflower oil	$0.82 \pm 0.15$
Labrafac® WL 1349	$0.58 \pm 0.05$
<b>liquid solubiliser</b>	
Transcutol® P	$162.18 \pm 2.83$
Labrasol®	$85.6 \pm 1.63$
Labrafil® M 1944 CS	$2.87 \pm 0.13$

### 3.3.4. Preliminary screening of the type of solid lipids and surfactants for preparation of SLN

Firstly, to screen the feasibility of the formulation of SLN in terms of colloidal properties, stability and drug loading using the solid lipids that showed the highest dissolving capacity for Sf, SLN were prepared using Geleol<sup>TM</sup> as a main solid lipid matrix with different stabilisers (Tween 80 (T80), Poloxamer 188 (P188), and Poloxamer (P407)) at a lipid stabiliser ratio of 5:2 and initial Sf amount added of 10 mg. As shown in Table 3.3, Geleol<sup>TM</sup> produced solid lipid nanoparticles with all the screened surfactants with particle sizes between 86 and 128 nm and a moderate negative zeta potential (between -15.1 and -18.8 mV). However, it was remarkable that both poloxamers (P188 and P407) could produce smaller particles with narrower size distribution compared to T80 used at the same concentration. Furthermore, regarding drug loading, T80 showed statistically significantly ( $p < 0.05$ ) higher EE% ( $42.6 \pm 3.5\%$ ) than both poloxamers. This could be explained by the higher dissolving capacity of T80 compared to poloxamers.

Nevertheless, after 48 h of storage, all Geleol<sup>TM</sup>-based SLN using different surfactants exhibited massive gelation. The gelation phenomenon of SLN could be ascribed to many factors such as high lipid concentration, mechanical stress, insufficient surfactant coverage, low static stability (low zeta potential values), temperature, and light exposure<sup>160,173</sup>. Thus Precirol® ATO 5, having the second highest dissolving capacity for Sf, was employed as a main solid lipid matrix for the rest of the screening process.

Table 3.3: Particle size (P.S.), Polydispersity index (PDI), Zeta potential (Z.P.), Entrapment efficiency (EE%), and Loading capacity (LC%) of Geleol<sup>TM</sup>-based SLN using different surfactant at lipid to surfactant ratio of 5:1

Solid lipid	surfactant	P.S. $\pm$ SD (nm)	PDI $\pm$ SD	Z.P. $\pm$ SD (mV)	EE% $\pm$ SD (%)	LC% $\pm$ SD (%)
Geleol <sup>TM</sup>	T80	128 $\pm$ 6.1	0.4 $\pm$ 0.008	-15.1 $\pm$ 3.6	42.6 $\pm$ 3.5	0.85 $\pm$ 0.07
	P188	86 $\pm$ 5.6	0.142 $\pm$ 0.008	-18.8 $\pm$ 4.2	29.4 $\pm$ 2.1	0.58 $\pm$ 0.04
	P407	101.8 $\pm$ 7.2	0.146 $\pm$ 0.015	-15.7 $\pm$ 2.4	24.5 $\pm$ 4.7	0.49 $\pm$ 0.09

Secondly, the effect of surfactant type and concentration on the physicochemical properties and drug loading of the SLN using Precirol® ATO 5 as a solid lipid was studied. From Table 3.4, increasing the surfactant concentration from 1% to 3% decreased the particle size with no significant ( $p > 0.05$ ) impact on the polydispersity index (PDI). Similar to Geleol™-based SLN, 5% Precirol® ATO 5 SLN stabilised with 1% P188 gelled after a short preparation time which could be attributed to high lipid concentration with an insufficient surfactant to prevent particles aggregation<sup>376</sup>. Zeta potential did not show any significant ( $p > 0.05$ ) change between different surfactants and concentrations. Regarding drug loading, T80 showed higher EE% than Poloxamers (P188 and P407), which increased by increasing the T80 concentration from 1% to 2%. However, the EE% decreased by using 3% T80, which could be ascribed to the partitioning of Sf molecules towards the hot surfactant aqueous medium during the emulsification process due to the solubilising effect of T80 leading eventually to drug precipitation as microparticles upon cooling<sup>163</sup>.

Table 3.4: The effect of surfactant type and concentration on the particle size (P.S.), Polydispersity index (PDI), Zeta potential (Z.P.), Entrapment efficiency (EE%), and Loading capacity (LC%) of 5% Precirol® ATO 5-based SLN

Surfactant	Surfactant concentration (%)	P.S. ± SD (nm)	PDI ± SD	Z.P. ± SD (mV)	EE% ± SD (%)	LC% ± SD (%)
T80	1	182.6 ± 2	0.273 ± 0.015	- 21.6 ± 4.8	31.6 ± 2.9	0.63 ± 0.06
	2	139.2 ± 4.6	0.229 ± 0.007	-21.7 ± 6.2	38.3 ± 4.1	0.76 ± 0.08
	3	88.9 ± 1.4	0.219 ± 0.011	-19 ± 8.8	28.7 ± 3.5	0.57 ± 0.07
P188	1	Gelation				
	2	187.7 ± 3.4	0.27 ± 0.01	-27.6 ± 6.8	15.4 ± 2.8	0.31 ± 0.06
	3	117.2 ± 2.5	0.25 ± 0.09	-21.8 ± 5.8	16.3 ± 3.1	0.32 ± 0.06
P407	1	229.3 ± 2.3	0.226 ± 0.017	-23.4 ± 6	13.9 ± 2.8	0.28 ± 0.06

	2	177.3 ± 6.2	0.293 ± 0.018	-20.3 ± 5.8	16.6 ± 3.2	0.33 ± 0.06
	3	117.6 ± 1.2	0.245 ± 0.004	-20.4 ± 5.1	16.7 ± 3.5	0.33 ± 0.07

From this screening step, 5% Precirol ATO 5 and 2% tween 80 were chosen as a solid lipid and surfactant, respectively, for the next screening step.

### 3.3.5. Miscibility assessment of lipid ingredients

Due to the low Sf solubility in pure solid lipids and oils, adding solubilisers was considered to enhance drug loading. Therefore, based on the solubility study results (shown in a previous section), Gelucire® 48/16 and Transcutol® P were employed as solid and liquid solubilisers, respectively. For determining the proper ratios of Gelucire® 48/16 and Transcutol® P to be added with the solid lipid, the miscibility between these two excipients and Precirol® ATO 5 was assessed using the DSC method (for both) and paper smear method (for Transcutol® P)<sup>282</sup>.

The DSC method was used based on the fact that a depression in the melting point of Precirol® ATO 5 is expected following the incorporation of Gelucire® 48/16 and Transcutol® P into the lamellar structure of the solid lipid<sup>282,377</sup>. As depicted in Figure 3.9a, the thermal curve of Pure Precirol® ATO 5 before heating showed a single endothermic melting peak with the onset and maximum temperatures at 52.7° C and 57.2° C, respectively, ascribed to the melting of the stable  $\beta$ -polymorph form<sup>378</sup>. However, after exposure to heating at 80° C for 1 h and subsequent cooling to room temperature (~ 25° C), the thermal curve of resolidified lipid (red line) exhibited a small shoulder, peaked at 48.9° C, which may be assigned to the melting of the metastable  $\alpha$ -form, formed during the recrystallisation of Precirol® ATO 5<sup>378</sup>.

Furthermore, it was remarkable that increasing the Gelucire 48/16 percentage up to 20% w/w in the mixture resulted in a decrease in the onset, maximum temperatures (Figure 3.9b), and fusion enthalpy of Precirol® ATO 5. Above this percentage, no further depression in the onset and maximum peak temperatures was noticed. A new endothermic peak appeared around 43.3° C at high Gelucire® 48/16 percentages (> 30% w/w) that

could be attributed to the melting of Gelucire 48/16 indicating the incidence of phase separation.

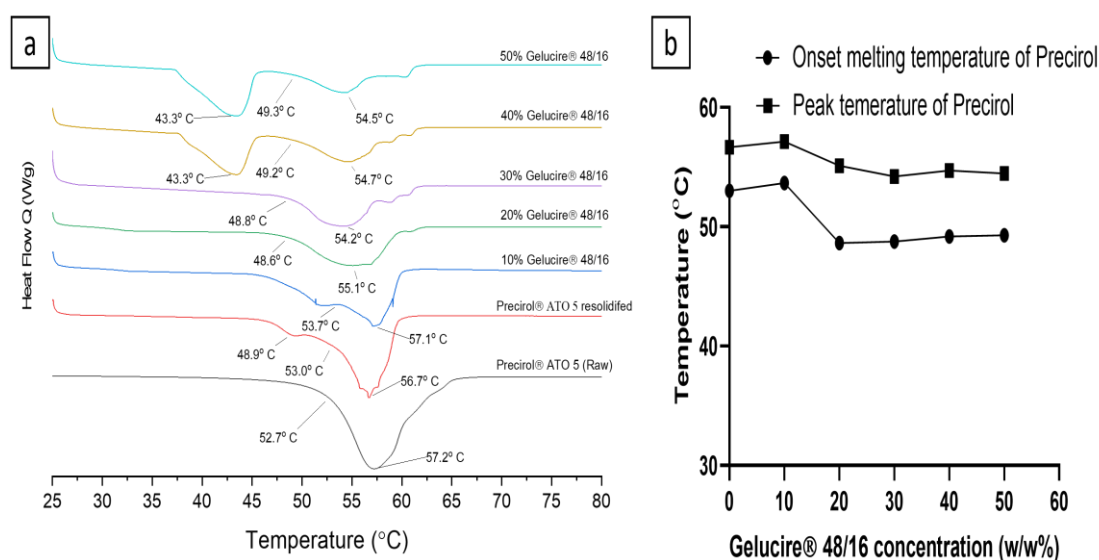


Figure 3.9: DSC thermograms of Precirol® ATO 5 with different Gelucire® 48/16 percentages (w/w) after heating for 1 h at 80° C followed by cooling at room temperature (~ 25° C) for 24 h (a), the effect of Gelucire® 48/16 on the peak onset and melting point of Precirol® ATO 5 (b).

Similarly, the onset and the maximum peak temperature of the melting of Precirol® ATO 5 decreased with increasing Transcutol® P amount up to a concentration of 20% (w/w) of the solid lipid (Figure 3.10a and b). Moreover, all solid-liquid lipid combinations demonstrated a noticeable increase in the intensity of the endothermic peak around 50.95° C related to the less crystalline  $\alpha$ -form (Figure 3.10a). This could be explained by the presence of Transcutol® P within the crystal structure of Precirol® ATO 5, favouring the formation of the less crystalline  $\alpha$ -form<sup>378</sup> and indicating a good miscibility between Precirol® ATO 5 and Transcutol® P reaching the maximum at Transcutol® P concentration of 20% w/w. It is well reported that lipid matrices with some degree of disorder (less crystalline) allow more voids for higher drug payload compared to the more ordered structures (more crystalline lipid)<sup>147,148,150,153,186</sup>. These results were further confirmed by visual inspection of samples smeared on filter paper as no droplets were spotted on the filter paper until reaching 30% w/w Transcutol® P (Figure 3.10c). These findings come in agreement with the previously reported data<sup>282</sup>.

Based on these results, 20% w/w of Gelucire 48/16 and Transcutol® P were chosen as appropriate concentrations of excipients to ensure good miscibility with the solid lipid (Precirol® ATO 5).

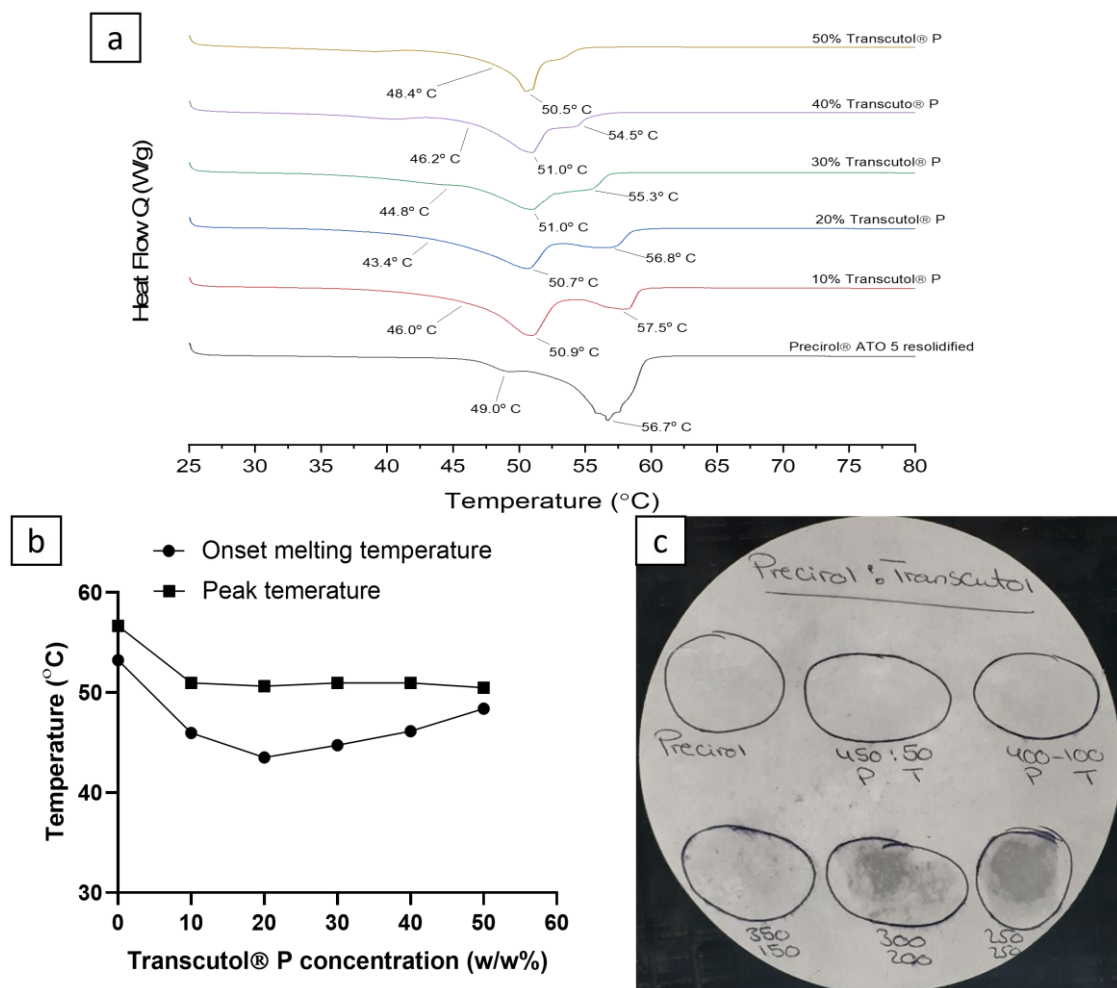


Figure 3.10: DSC thermograms of Precirol® ATO 5 with different Transcutol® P percentages (w/w) after heating for 1 h at 80° C followed by cooling at room temperature (~ 25° C) for 24 h (a), the effect of Transcutol® P percentages on the peak onset and melting point of Precirol® ATO 5 (b), and the filter paper of paper smear method for detection of phase separation (c).

### 3.3.6. Preparation and characterisation of Gal-Sf-SLN and Gal-Sf-NLC

As a final screening step to investigate the impact of lipid composition on the colloidal properties and drug loading of lipid nanoparticles, several formulations with different compositions, as elaborated in Table 3.5, were prepared. Peceol™ oil was included as an oil ingredient based on the Sf solubility studies.

Table 3.5: The composition of different screened lipid nanoparticles formulations

Formula code	Drug (mg)	Solid lipid (mg)	Liquid lipid (mg)	Solubiliser (mg)		Surfactant (mg)	Water (ml)
				Gelucire® 48/16	Transcutol® P		
	Sf	Precirol® ATO 5	Peceol™ oil			Tween 80	
F1	10	500				200	10
F2	10	400	100			200	10
F3	10	400		100		200	10
F4	10	400			100	200	10

From Table 3.6, the addition of liquid oil (Peceol™) to the solid lipid in F2 did not exhibit a significant ( $p > 0.05$ ) change in the particle size compared to the solid lipid alone (F1). In contrast, the incorporation of both Gelucire® 48/16 and Transcutol® P in the lipid composition resulted in a significant ( $p < 0.05$ ) reduction in the particles size due to the surface activity of these components that helps maintain the stability of the small nanodroplets during the emulsification process<sup>149</sup>.

Table 3.6: The effect of lipid composition on the particle size (P.S.), Polydispersity index (PDI), Zeta potential (Z.P.), Entrapment efficiency (EE%), and Loading capacity (LC%) of the formulated lipid nanoparticles.

Formula	P.S. ± SD (nm)	PDI ± SD	Z.P. ± SD (mV)	EE% ± SD (%)	LC% ± SD (%)
F1	139.2 ± 4.6	0.229 ± 0.007	-21.7 ± 6.2	38.3 ± 4.1	0.76 ± 0.08
F2	144.6 ± 4.3	0.25 ± 0.003	-39.7 ± 2.2	44.5 ± 4.6	0.88 ± 0.09
F3 (Sf-SLN)	82.9 ± 8.7	0.245 ± 0.011	-29.9 ± 1.6	86.2 ± 5.2	1.69 ± 0.1
F4 (Sf-NLC)	111.2 ± 3.4	0.224 ± 0	-34.2 ± 1.9	93.4 ± 5.7	1.83 ± 0.11

It is well reported that NLC were developed as a second generation of SLN by introducing liquid oils into the composition of SLN that impart imperfections in the crystalline structure of solid lipids conferring more voids to accommodate more drug load and

enhancing the loading stability<sup>159,360,375</sup>. However, the introduction of Peceol<sup>TM</sup> oil into the lipid structure showed a slight insignificant ( $p > 0.05$ ) increase in drug loading compared to solid lipid nanoparticles (F1). This could be attributed to the limited solubility of Sf in Peceol<sup>TM</sup>.

On the other hand, the incorporation of Gelucire<sup>®</sup> 48/16 as a solid solubiliser to enhance the drug loading of SLN has contributed to a significant ( $p < 0.05$ ) enhancement in the drug loading, having EE% of  $86.2 \pm 5.2\%$ . This could be ascribed to the high Sf solubility in Gelucire<sup>®</sup> 48/16 ( $69.47 \pm 4.69$  mg/g) and its good miscibility with Precirol<sup>®</sup> ATO 5. Similarly, the employment of Transcutol<sup>®</sup> P as a liquid solubiliser has remarkably increased the drug loading up to EE% of  $93.4 \pm 5.7\%$ , which could be attributed to both high Sf solubility in Transcutol<sup>®</sup> P and good miscibility of Transcutol<sup>®</sup> P with Precirol<sup>®</sup> ATO 5 in addition to the liquid nature of Transcutol<sup>®</sup> P.

Although Transcutol<sup>®</sup> P is not a typical liquid lipid (oil), several studies have employed it as a liquid ingredient to produce NLC<sup>282,379–383</sup>. Thus, based on the previous results, formulas F3 and F4 were chosen as the optimised composition of Sf-SLN and Sf-NLC, respectively.

To prepare liver-targeted lipid nanoparticles, the galactosylation of the optimised Sf-SLN and Sf-NLC was carried out by incorporating the previously synthesised Gal-SA at a concentration of (0.05% w/w to the total lipid weight) according to the previous study<sup>384</sup>. From Table 3.7, the incorporation of Gal-SA within Sf-SLN and Sf-NLC structure resulted in a statistically significant ( $p < 0.05$ ) decrease in the negative values of zeta potential, which could be ascribed to the presence of free unconjugated stearylamine (SA) that partially neutralised the negative charge by its protonated terminal amine groups. This confirms the surface exposure of the liver-targeting galactose moieties on Sf-SLN and Sf-NLC.

Table 3.7: Particle size (P.S.), Polydispersity index (PDI), Zeta potential (Z.P.), Entrapment efficiency (EE%), and Loading capacity (LC%) of the optimised galactosylated SLN and NLC formulations.

Formula	P.S. $\pm$ SD (nm)	PDI $\pm$ SD	Z.P. $\pm$ SD (mV)	EE% $\pm$ SD (%)	LC% $\pm$ SD (%)
Gal- SLN	77.38 $\pm$ 1.7	0.229 $\pm$ 0.013	- 20.5 $\pm$ 0.7	--	--
Gal- NLC	119.8 $\pm$ 1.4	0.219 $\pm$ 0.009	- 24.8 $\pm$ 0.2	--	--
Gal-Sf-SLN	79.4 $\pm$ 1.5	0.236 $\pm$ 0.022	- 16.1 $\pm$ 1.1	88.1 $\pm$ 4.7	1.73 $\pm$ 0.09
Gal-Sf-NLC	113.2 $\pm$ 3	0.187 $\pm$ 0.012	- 23.8 $\pm$ 1.1	92.4 $\pm$ 5.3	1.81 $\pm$ 0.1

### 3.3.7. Morphology of lipid nanoparticles using electron microscopy

The shape and surface morphology of blank and Sf-loaded Gal-SLN and Gal-NLC were inspected using TEM and SEM. From Figure 3.11, TEM images of all tested samples showed almost spherical nanoparticles with smooth surface morphology within the 70-120 nm particle size range, which was in agreement with the particle size data measured by DLS. It was also remarkable that no drug crystals were noticed in the drug-loaded specimens asserting that no unencapsulated Sf in the quantified amounts in drug-loading studies.

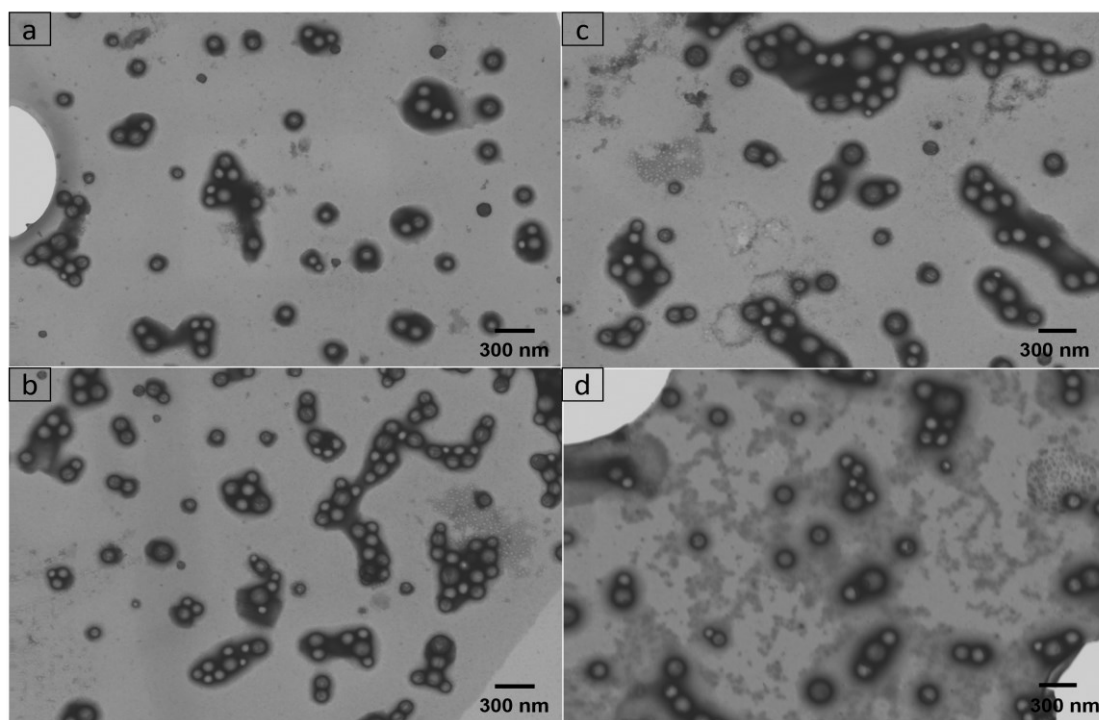


Figure 3.11: TEM images of blank Gal-SLN (a), Gal-Sf-SLN (b), blank Gal-NLC (c), and Gal-Sf-NLC (d).

Furthermore, SEM images (Figure 3.12) also showed aggregates of mostly spherical nanoparticles with some agglomeration that may be attributed to the lipid nature (stickiness) that affects its stability during the drying process besides the deposition of Au layer during sample preparation for SEM scanning.

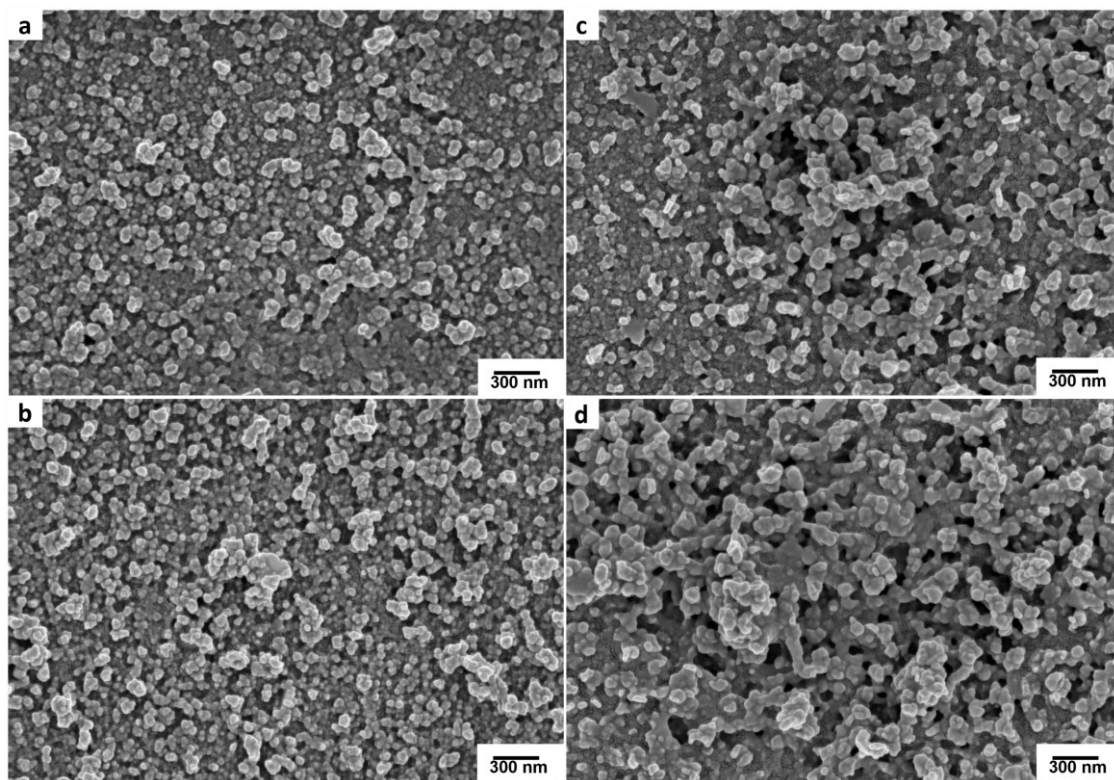


Figure 3.12: SEM images of blank Gal-SLN (a), Gal-Sf-SLN (b), blank Gal-NLC (c), and Gal-Sf-NLC (d).

### 3.3.8. Solid state characterisation

#### 3.3.8.1. Attenuated total reflection-Fourier transform infrared (ATR-FTIR)

FTIR analysis was conducted to inspect any chemical change in the lipid nanoparticles due to nanofabrication and drug encapsulation. As depicted in Figure 3.13, Precirol® ATO 5 IR absorbance spectrum exhibited the characteristic absorbance bands identified at  $1470\text{ cm}^{-1}$  (C-C stretching),  $1730\text{ cm}^{-1}$  (C=O stretching), and  $2851$  and  $2914\text{ cm}^{-1}$  (C-H stretching), as reported elsewhere<sup>385-387</sup>. For Gelucire 48/16, the spectrum showed a sharp band at  $1105\text{ cm}^{-1}$  (C-O stretching) of PEG moiety with overlapping bands around  $2885\text{ cm}^{-1}$  (C-H stretching) of PEG moiety, and stearic and palmitic acid moieties. Being an ether, Transcutol® P spectrum demonstrated bands at  $1107\text{ cm}^{-1}$  (C-O stretching), and

2784  $\text{cm}^{-1}$  (C-H stretching) with a broad band at 3424  $\text{cm}^{-1}$  (O-H stretching) of the terminal hydroxyl group<sup>388</sup>. Sf spectrum revealed two characteristic bands at 3298  $\text{cm}^{-1}$  and 3337  $\text{cm}^{-1}$  (N-H stretching) of amide and a band at 3074  $\text{cm}^{-1}$  (C-H stretching) with a characteristic band at 1705  $\text{cm}^{-1}$  (C=O stretching) of the amide group<sup>389</sup>. The physical mixtures of both Gal-Sf-SLN and Gal-Sf-NLC were prepared by mixing all their ingredients at the same ratios of the optimised formulations using a pestle and mortar. The spectra of the physical mixtures and SF-loaded lipid nanoparticles (SLN and NLC) did not show any observed changes or interactions between components confirming the chemical stability of the ingredients during nanoparticle preparation and drug encapsulation.

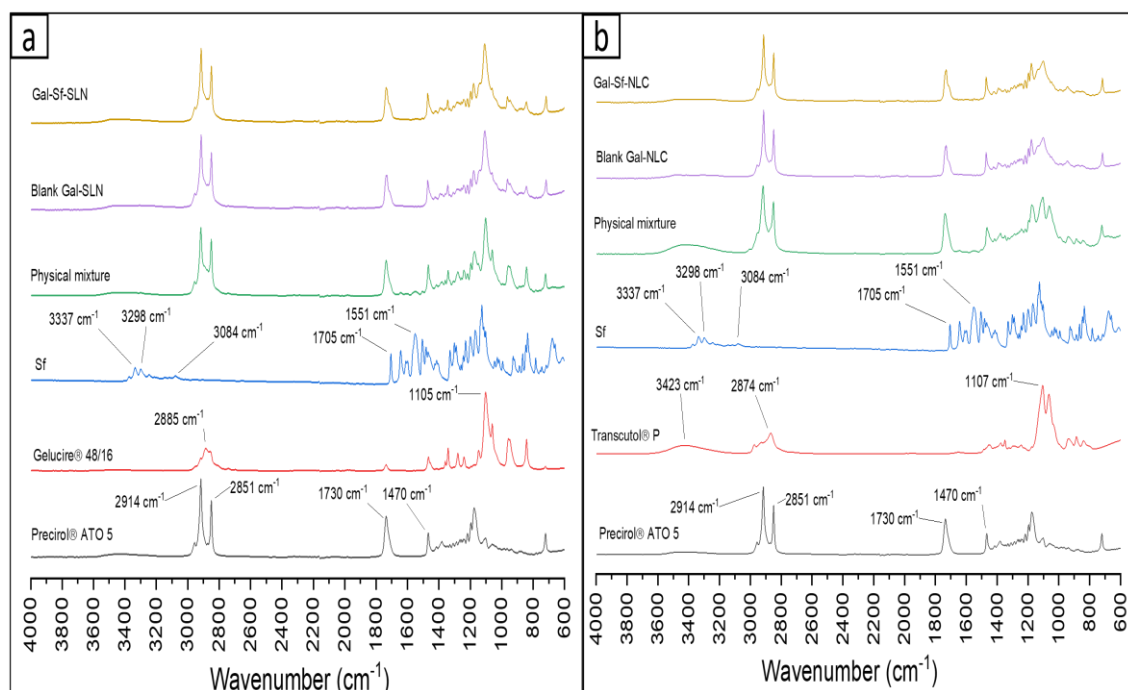


Figure 3.13: FTIR absorbance spectra of Gal-Sf-SLN (a), and Gal-Sf-NLC (b) with their raw materials and physical mixtures.

### 3.3.8.2. Differential scanning calorimetry (DSC)

DSC analysis was employed to investigate the thermal behaviour of the formulated lipid nanoparticles. As demonstrated in Figure 3.14 a and b, Sf showed its sharp endothermic melting peak at 209° C, while Precirol® ATO 5 and Gelucire® 48/16 exhibited their endothermic melting peak at 57.2° C, and 48° C, respectively. The physical mixtures of

both Gal-Sf-SLN and Gal-Sf-NLC showed the melting peaks of the corresponding ingredients with slight deviation due to the miscibility between different ingredients, as discussed in a previous section. At the same time, the sharp endothermic peak of Sf was not observed in the thermograms of both physical mixtures and freeze-dried lipid nanoparticles. This suggests that the drug was well dissolved in the molten lipid, which agrees with the solubility study of Sf in the lipid matrix. The same observation was reported by Teixeira, M. I. *et al.* during the preparation of lactoferrin functionalized lipid nanoparticles for Riluzole Delivery<sup>385</sup>. Notably, the thermograms of both Gal-Sf-SLN and Gal-Sf-NLC showed a broadening in the endothermic peak, accompanied by a shift of the onset and the melting point to a lower temperature. These changes are mainly attributed to the interactions of the solid lipid with the liquid Transcutol® P and the surfactant during the nanofabrication process. According to the Gibbs-Thompson effect, sub-micron sized solid lipid particles can get to thermodynamic equilibrium at lower temperatures compared to the larger crystals in their (bulk lipid) physical mixtures due to the higher surface-to-bulk free energy ratio of small particles<sup>385,386,390</sup>. In addition, polymorphic transformations and the recrystallisation process can be further distorted by the adsorption of surfactant molecules on the lipid particle surface<sup>376,391</sup>, explaining the changes in the melting and crystallisation profiles of lipid nanoparticles.

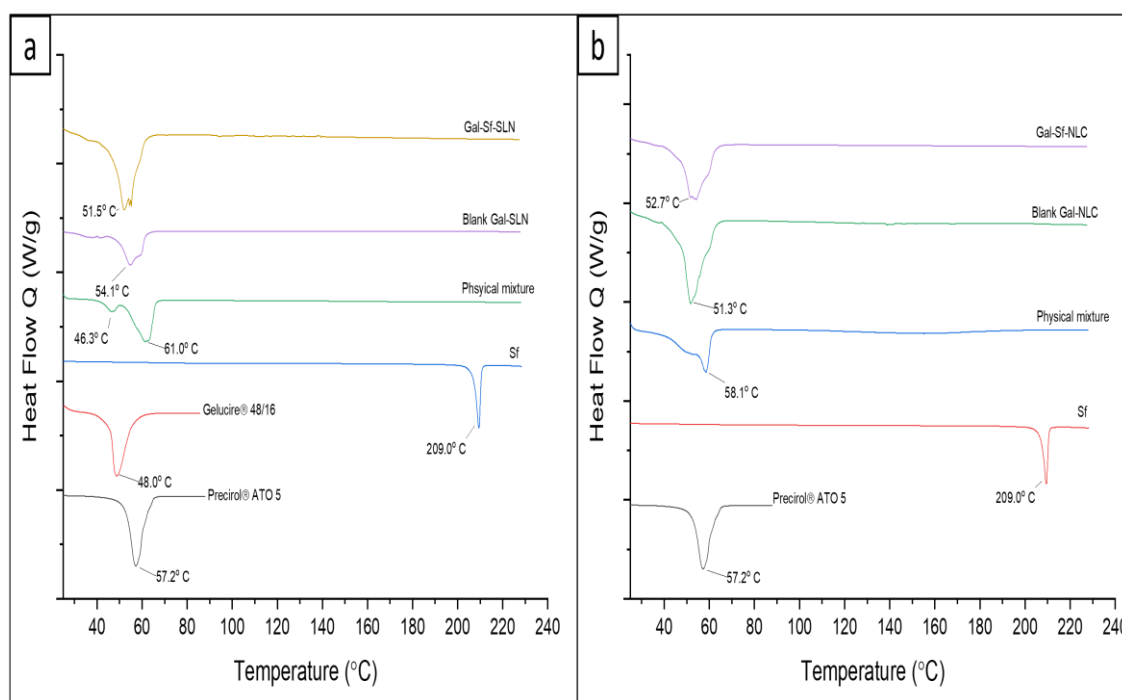


Figure 3.14: DSC thermograms of Gal-Sf-SLN (a), and Gal-Sf-NLC (b) with their raw materials and physical mixtures.

### 3.3.8.3. Powder X-Ray Diffraction (PXRD)

To further investigate any changes in the crystalline structure of the nanoparticles, PXRD experiments were carried out. As shown in Figure 3.15, Sf exhibited various characteristic diffraction peaks at  $2\theta$  of  $11.3^\circ$ ,  $18.5^\circ$ , and  $24.7^\circ$ , denoting its highly crystalline structure<sup>389,392</sup>. Moreover, the diffractogram of Gelucire 48/16 depicted two distinctive sharp diffraction peaks at  $2\theta$  of  $19^\circ$  and  $23.2^\circ$ <sup>393</sup>, while Precirol® ATO 5 showed a broad peak within the range between  $18^\circ$  and  $25^\circ$ <sup>394</sup>. The physical mixtures of both Gal-Sf-SLN and Gal-Sf-NLC showed all the distinctive diffraction peaks of the ingredients. However, the intensity of peaks was lessened in NLC due to the presence of a liquid ingredient (Transcutol® P)<sup>394</sup>. Furthermore, the diffractograms of Gal-Sf-SLN and Gal-Sf-NLC revealed diminished diffraction peaks indicating a significant decrease in the crystallinity of lipids with a complete disappearance of Sf peaks. The reduction of the crystallinity of the lipids could be attributed to the nanoformulation process, especially by using ultrasonication and the presence of surfactants that may impede lipid recrystallisation<sup>395</sup>. For Sf, the disappearance of its diffraction peak could be ascribed to the low drug content in the formulations to a level below the limit of detection of the instrument and the dissolution of the drug into the lipid matrix during the formulation.

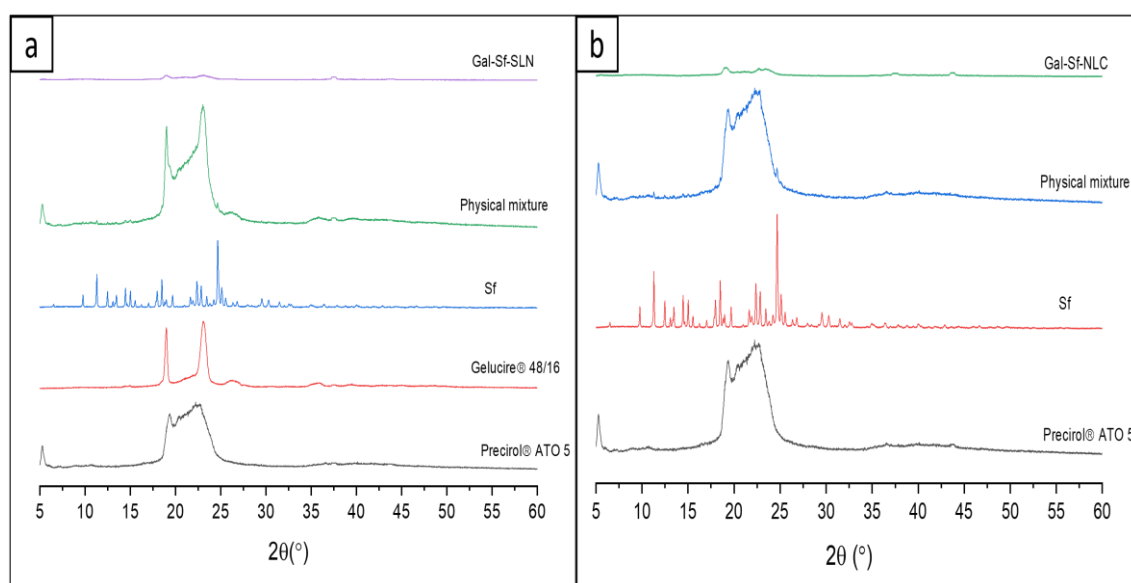


Figure 3.15: PXRD patterns of Gal-Sf-SLN (a), and Gal-Sf-NLC (b) with their raw materials and physical mixtures.

### 3.3.9. Redispersibility of freeze-dried optimised lipid nanoparticles

Solidification, by freeze-drying, is a key step to improve the stability of SLN and NLC for longer storage time compared to aqueous dispersion. However, maintaining the colloidal characteristics of nanoparticles during freeze-drying and redispersion processes is essential. To help with that, different cryoprotectants are reported to be used during freeze drying, such as trehalose, mannitol, and sucrose. Cryoprotectants are known to act by embedding nanoparticles in an amorphous matrix that minimise the interaction between nanoparticles with ice crystals during the freezing step and the intimate interaction between nanoparticle themselves<sup>396</sup>. Among all employed cryoprotectants, trehalose was reported to be the most efficient in maintaining the colloidal properties<sup>396,397</sup>. Thus, the effect of using 5% of trehalose to preserve the particle size of lipid nanoparticles during the freeze-drying step was assessed.

As shown in Figure 3.16, the impact of freeze drying was more profound on NLC formulations than SLN, which could be ascribed to the presence of a liquid ingredient in NLC, rendering it stickier and more resistant to redispersion compared to SLN. Furthermore, the addition of 5% trehalose helped to maintain the particle size after redispersion represented in lower redispersibility index (RI) values, in Table 3.8, with a more substantial impact in the case of NLC compared to SLN.

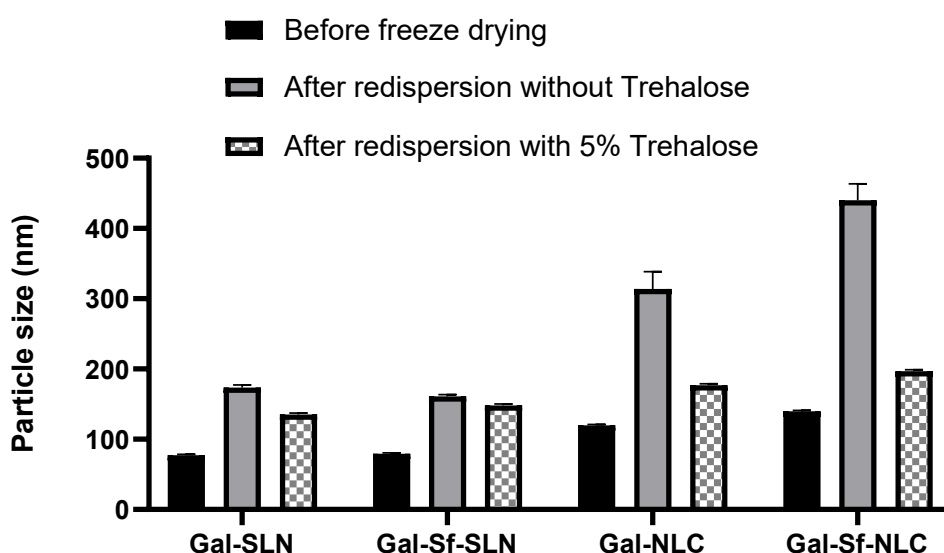


Figure 3.16: The influence of the addition of 5% trehalose on the particle size of the freeze-dried optimised lipid nanoparticles after redispersion in MilliQ water.

Table 3.8: Redispersibility index of optimised lipid nanoparticles after freeze-drying and redispersion with and without using 5% trehalose as cryoprotectant.

	Gal-SLN	Gal-Sf-SLN	Gal-NLC	Gal-Sf-NLC
Without 5 % trehalose	2.24	2.03	2.62	3.15
With 5 % trehalose	1.75	1.87	1.477	1.41

### 3.3.10. *In-vitro* drug release studies

Drug release studies from Gal-Sf-SLN and Gal-Sf-LNC were carried out to investigate the influence of Sf encapsulation and oil incorporation on sustaining Sf drug release. Firstly, the equilibrium solubility of Sf in different media was determined to ensure the sink condition during the release study. Due to the very low solubility of Sf in PBS at pH 7.4 at 37° C ( $4.3 \pm 1.2 \mu\text{g/mL}$ ), most of the reported studies used surfactants to increase Sf solubility in the release medium from which Tween 80<sup>122,398</sup> and Sodium dodecyl sulphate (SDS)<sup>399</sup> were the most commonly used. As shown in Table 3.9, Tween 80 demonstrated higher dissolution capacity for Sf compared to SDS. Hence, 40 mL of 1% Tween in PBS at pH 7.4 was chosen as a release medium<sup>366,398</sup>.

Table 3.9: Sorafenib solubilities in different proposed release media at 37°C.

Medium	Sf solubility ( $\mu\text{g/mL}$ )
PBS at pH 7.4	$4.3 \pm 1.2$
1% Tween 80 in PBS at pH 7.4	$72.3 \pm 5$
2% Tween 80 in PBS at pH 7.4	$147.0 \pm 9.0$
1% SDS in PBS at pH 7.4	$35.2 \pm 3.1$
2% SDS in PBS at pH 7.4	$72.4 \pm 3.6$

Additionally, including Sf solution as a control in the experiment design was considered to demonstrate the dialysability (the ability of Sf molecules to diffuse out of the dialysis membrane) and to represent the immediate release profile of Sf (negative control). From the literature, some studies did not include Sf solution as a control<sup>363,400</sup>, while others included drug solution without specifying the used solvent<sup>401–403</sup>. Due to low Sf solubility,

Yang, S. *et al.* used a Cremophor EL–ethanol (1:1, v/v) mixture to dissolve Sf<sup>366</sup>. However, the Sf solution showed only around 34% drug release after 48 h. This observation could be explained by the solvent diffusion out of the dialysis bag. In contrast, PBS (from the release medium) diffuses in leading to drug precipitation inside the dialysis bag. To investigate this point, Sf release from Sf solutions using different solvents (namely, ethanol, DMSO, PEG 400, 50:50 v/v ethanol: PBS at 7.4, and 1% Tween 80 in PBS at 7.4) was studied. As depicted in Figure 3.17, around 7% of Sf was released from 1% Tween 80 in PBS at pH 7.4 (the release medium). This could be attributed to the encapsulation of Sf molecules inside Tween 80 micelles that exhibited a very sustained release. Furthermore, the use of 50:50 v/v ethanol: PBS showed a higher released amount of Sf compared to Tween 80. Still, it only reached 54% after 10 h, followed by a very low release rate, suggesting Sf precipitation may have happened due to solvent diffusion.

On the other hand, using pure solvents resulted in reaching higher release levels of Sf due to the higher solubility of Sf in these solvents. However, both ethanol and DMSO only released 81% and 72% of Sf after 10 h from ethanol and DMSO, respectively, followed by a prolonged release, which also could be attributed to the rapid diffusion of the small molecules of solvents that led to Sf precipitation inside dialysis bag (scenario I in Figure 3.18). However, due to the high molecular weight and viscosity of PEG 400, its diffusion through the dialysis membrane was relatively slower than the diffusion rate of Sf (scenario II in Figure 3.18), allowing the complete Sf release after almost 20 h. Thus, PEG 400 was chosen as a solvent for Sf in the release studies.

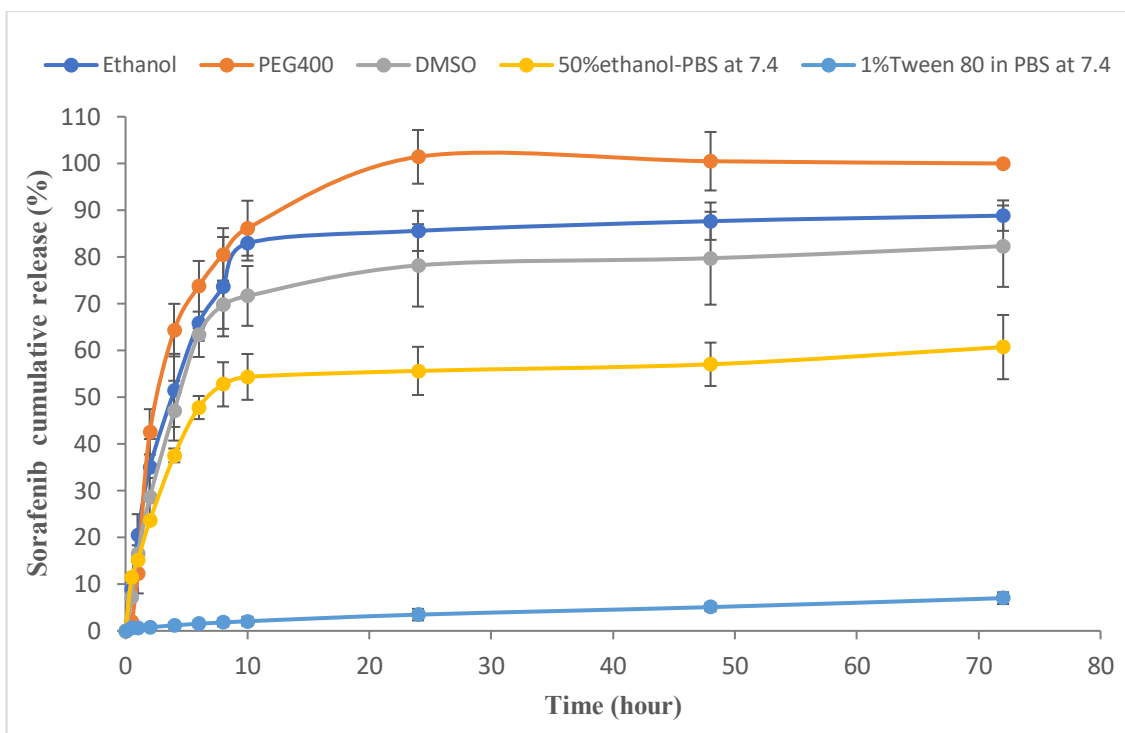


Figure 3.17: Sorafenib release profiles from different solvents employing dialysis bag method using 1% Tween 80 in PBS at pH 7.4 as release medium and kept under shaking at 100 rpm at 37° C.

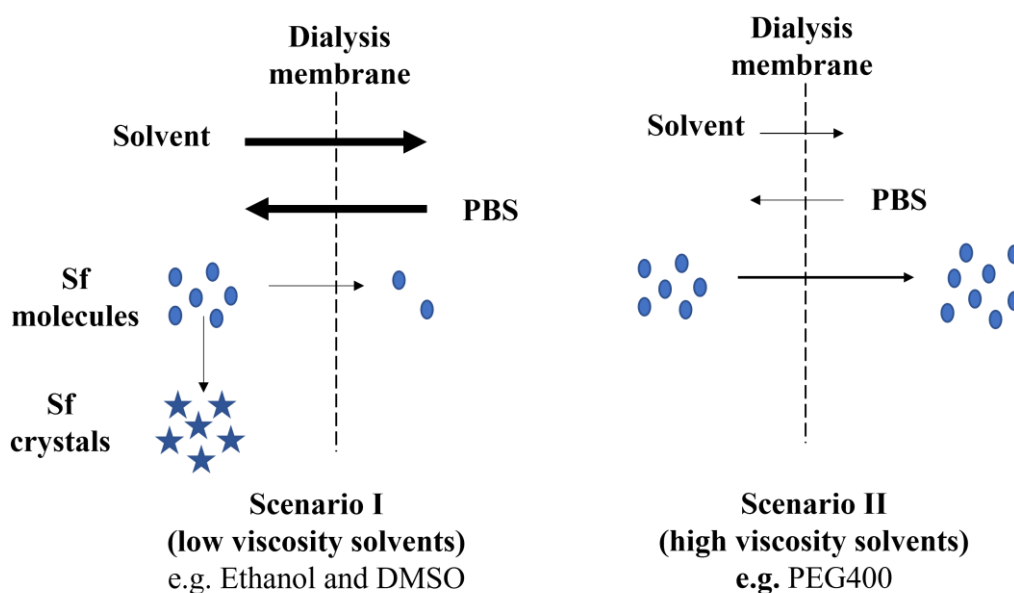


Figure 3.18: Sorafenib diffusion scenarios from different solvents through the dialysis membrane.

Figure 3.19 demonstrates Sf release profiles from Gal-Sf-SLN and Gal-Sf-NLC. Both profiles exhibited a sustained release with  $20.4 \pm 0.3\%$  and  $27.7 \pm 1.3\%$  of Sf released from Gal-Sf-SLN and Gal-Sf-NLC, respectively. Moreover, the data reveal that Sf release from both SLN and NLC is biphasic, with an initial burst release observed within the first hour followed by slower and more sustained release. The initial burst release suggests the presence of Sf-enrich shell, as discussed in Chapter 1 (section 1.5.1.3), due to the formation of a surfactant-lipid boundary layer enriched with Sf as previously reported<sup>382,404</sup>. It is noteworthy that Gal-Sf-NLC showed a relatively faster release than Gal-Sf-SLN, which could be attributed to the presence of a liquid lipid compartment (Transcutol® P) that confers a more rapid diffusion pathway to Sf molecules compared to the solid lipid. Moreover, the MDT (mean dissolution time) of Gal-Sf-SLN and Gal-Sf-NLC were  $51.8 \pm 0.3$  h and  $54 \pm 2.8$  h, respectively, which were almost 11.4 times higher than that of the Sf solution ( $4.6 \pm 3.5$  h). This asserts the potential of Sf encapsulation into SLN and NLC to sustain the drug release.

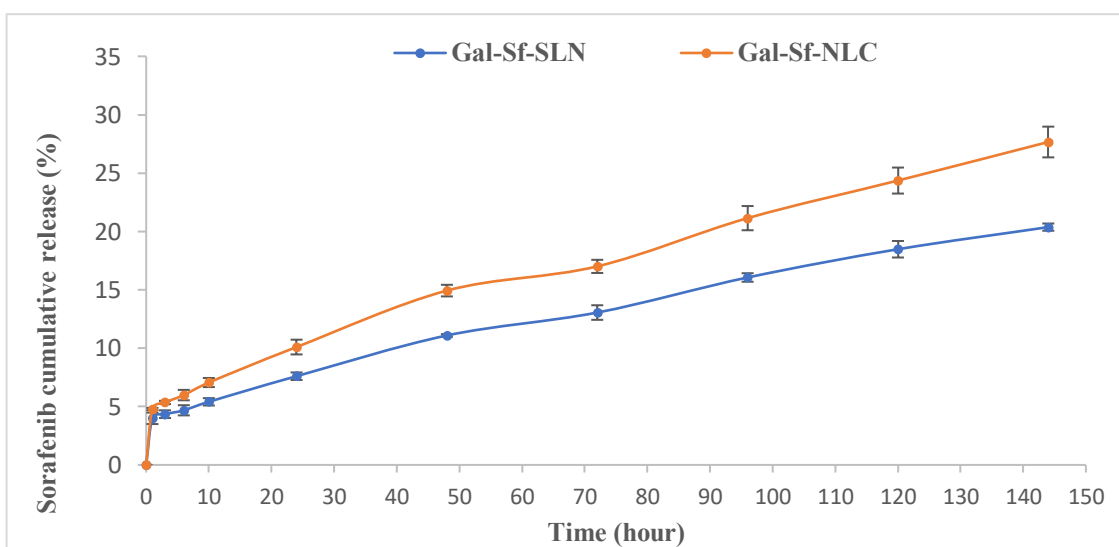


Figure 3.19: *In-vitro* Sorafenib release profiles from Gal-Sf-SLN and Gal-Sf-NLC using 1% Tween 80 in PBS at pH 7.4 as release medium and kept under shaking at 100 rpm at 37° C.

The difference ( $f_1$ ) and similarity ( $f_2$ ) factors were calculated for further mathematical comparison between different Sf release profiles. From Table 3.10, the Sf release profile from the solution was significantly different ( $f_1 > 15$  and  $f_2 < 50$ ) from those from Gal-Sf-SLN and Gal-Sf-NLC. However, drug release profiles from both Gal-Sf-SLN and Gal-Sf-NLC showed a high level of similarity (70.44%).

Table 3.10: Difference factors ( $f_1$ ) and Similarity factors ( $f_2$ ) of the release profiles of Sf solution, Gal-Sf-SLN, and Gal-Sf-NLC.

Comparison parameter	Formulation		
	Sf solution	Gal-Sf-SLN	Gal-Sf-NLC
Difference factor ( $f_1$ )	87.3		
		31.7	
	83.3		83.3
Similarity factor ( $f_2$ )	6.9		
		70.44	
	7.9		7.9

Furthermore, the mathematical modelling of the *in-vitro* release data (Table 3.11) revealed that the release of Sf from the solution followed first-order release kinetics with  $R^2$  value of 0.9878, implying that Sf release is proportional to the amount of Sf remaining in the dialysis bag that diminishes over time. While the release data of both Gal-Sf-SLN and Gal-Sf-NLC followed Korsmeyer-Peppas release kinetic model with  $R^2$  values of 0.9800 and 0.9826, respectively, and  $n$  values very close to 0.5 implying a fickian model of drug release where the drug release is mainly governed by drug diffusion through lipid matrix after the initial burst release.

Table 3.11: *In-vitro* drug release kinetic models of Sf solution, Gal-Sf-SLN and Gal-Sf-NLC.

Model	Equation	$R^2$ of different formulations		
		Sf solution	Gal-Sf-SLN	Gal-Sf-NLC
Zero-order	$f = k_0.t$	0.6078	0.7897	0.8159
First-order	$f = 1 - \exp(-kt)$	<b>0.9878</b>	0.8164	0.8484
Higuchi	$f = k_H . t^{0.5}$	0.352	0.9780	0.9821
Korsmeyer-Peppas	$f = k_{kp} . t^n$	0.977 $n = 1.002$	<b>0.9800</b> <b><math>n = 0.463</math></b>	<b>0.9826</b> <b><math>n = 0.482</math></b>
Hixon-Crowell	$f = [1 - (1 - k_{HC} . t)^3]$	0.2887	0.8079	0.8384

### 3.3.11. *In-vitro* cytotoxicity

As a proof of concept, the cytotoxicity studies of the optimised SLN and NLC were carried out to investigate the effect of drug encapsulation and the surface galactosylation on the cytotoxic efficiency of Sf on HepG 2 cells after incubation for 48 h. From Figure 3.20, the Sf solution exhibited remarkable cytotoxicity with  $IC_{50}$  of  $2.378 \pm 0.33 \mu\text{g/mL}$ . At the same time, both Sf-loaded SLN and NLC showed a lower cytotoxicity with  $IC_{50}$  values of  $7.49 \pm 0.93$  and  $6.46 \pm 0.75 \mu\text{g/mL}$ , respectively. This could be attributed to the prolonged drug release character from these lipid-based nanoparticles, as demonstrated in the drug release section, besides the lipid's slow degradation rate after cellular uptake<sup>394</sup>. On the other hand, galactosylated lipid nanoparticles exhibited a slight insignificant ( $p > 0.05$ ) decrease in  $IC_{50}$  values to  $6.14 \pm 0.89$  and  $5.172 \pm 0.53 \mu\text{g/mL}$  for Gal-Sf-SLN and Gal-Sf-NLC, respectively, compared to the unmodified counterparts. This could be explained by the low surface exposure of the galactosylated lipid due to the use of an insufficient amount of Gal-SA and low conjugation efficiency. Additionally, it was noteworthy that the blank lipid nanoparticles displayed remarkable cytotoxicity even though lipid nanoparticles are considered relatively safe nanodelivery systems compared to other nanocarriers such as polymeric nanoparticles<sup>154,179</sup>.

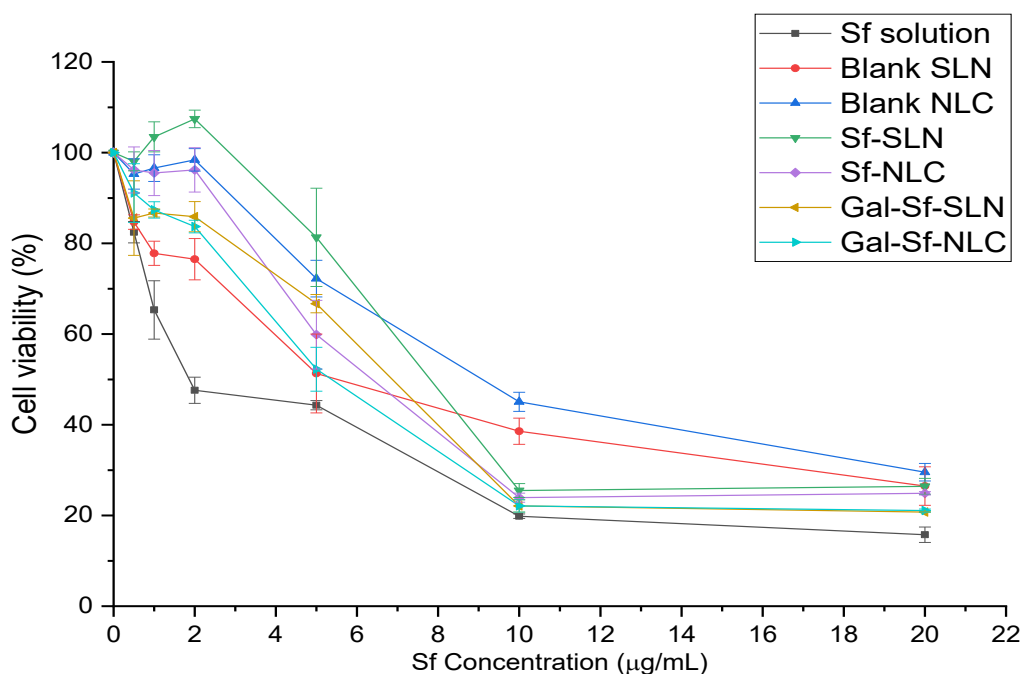


Figure 3.20: Cell viability plot of HepG 2 cells after incubation for 48 h at 37°C with free Sf solution, blank and Sf-loaded SLN and NLC, and their galactosylated counterparts (both blank formulations were diluted similarly to the Sf-loaded counterparts).

To investigate the source of cytotoxicity of the blank lipid nanoparticles, Blank SLN comprised of Precirol® ATO 5 and stabilised with different stabilisers (namely, Tween 80 (T80), Poloxamer 188 (P188), and Poloxamer 407 (P407)) at lipid: surfactant ratio of 5:2 and incubated with HepG2 cells in concentrations up to 1250 µg/ml lipid (up to 500 µg/mL of surfactant) for 48 h. Surprisingly, Precirol® ATO 5-based SLN showed high cytotoxicity over the investigated concentrations with all tested surfactants, as depicted in Figure 3.21a, with IC<sub>50</sub> values (281.3 ± 23.8 µg/mL, 320 ± 21.2 µg/mL, and 380.7 ± 20.3 µg/mL of lipid concentration for blank Precirol SLN with T80, P144, and P407, respectively).

It is well reported that the most possible source of cytotoxicity of lipid nanoparticles are the surfactants<sup>175,180–182</sup>. However, there are some discrepancies about whether the surfactants' cytotoxicity is ascribed to the free or the bound portion on the nanoparticles. To examine that, the cytotoxicity of free surfactant solutions was tested on HepG 2 cells for 48 h. From Figure 3.21b, both P188 and P407 demonstrated 100% cell viability with concentrations up to 1.2 mg/mL, while Tween 80 solution exhibited considerable cytotoxicity with IC<sub>50</sub> of 621.7 ± 29.3 µg/mL. Nevertheless, all tested surfactants did not show significant cytotoxicity (cell viability > 80%) up to 500 µg/mL, suggesting that the cytotoxicity of blank Precirol® ATO 5 SLN originated from the nanoparticles themselves. Schöler N. *et al.* reported the same finding<sup>182</sup>, as it was found that SLN stabilised by different stabilisers (P188, P407, T80, Solutol® HS15) showed higher cytotoxicity on peritoneal macrophages compared to free stabiliser solutions<sup>182</sup>.

To verify the role of the lipid nature in the cytotoxicity of SLN, the cytotoxicity of blank Compritol® 888 ATO-based SLN using different stabilisers, in the same manner as blank Precirol® ATO 5-based SLN, was examined. As shown in Figure 3.21c, blank lipid nanoparticles stabilised with P188 and P407 were completely safe over the screened concentrations up to 1250 µg/mL lipid concentration, while T80-stabilised nanoparticles exhibited lower cellular viability (76.6 ± 6.6 %) at the highest concentration (1250 µg/mL). The relative high cytotoxicity of T80 compared to P188 and P407 was previously reported by Müller *et al.* when Compritol® 888 ATO based stabilised with different stabilisers were tested for their cytotoxicity on Polymorphonuclear leukocytes (PMN)<sup>48</sup>. This signifies that the cytotoxicity of blank Precirol® ATO 888 was partially attributed to the Precirol® ATO 888 solid lipid itself.

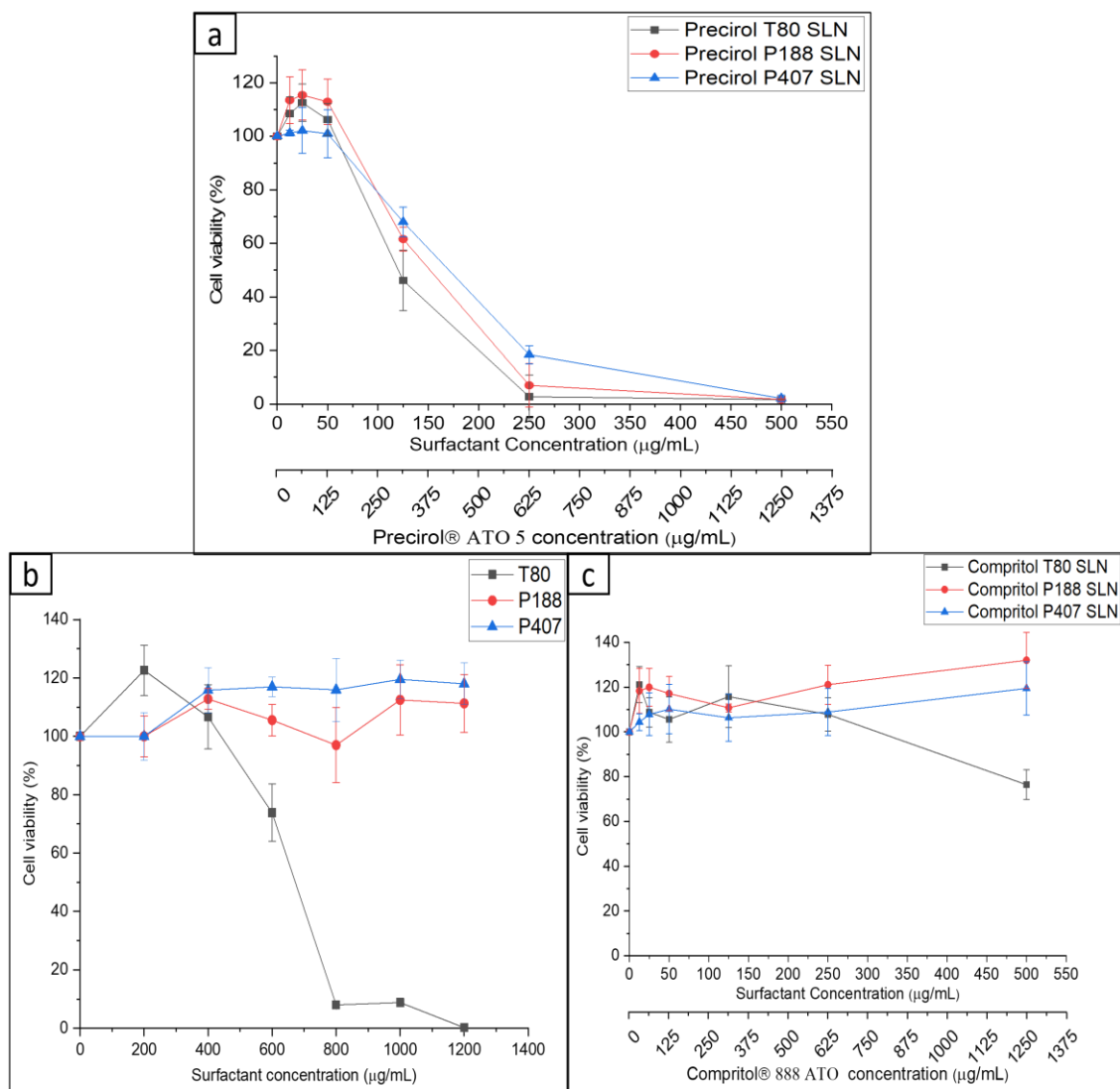


Figure 3.21: Cytotoxicity profiles of (a) blank Precirol® ATO 5-based SLN using different surfactants, (b) free surfactant solutions, and (c) blank Compritol® 888 ATO-based SLN using different surfactants after incubation with HepG2 cells for 48 h.

By screening the literature, the only reported study that investigated the cytotoxicity of a blank Precirol ATO 5 based SLN, stabilised with Cremophor RH 40 in lipid to surfactant ratio of 3:2.5, on HepG2 cell after incubation for 48 h showed that SLN were safe up to 0.6 mg/mL with  $IC_{50}$  of 3.1 mg/mL<sup>394</sup>. This finding suggests that the cytotoxicity in our current study could be attributed to impurities in Precirol® ATO 5.

### 3.4. Conclusion

The synthesis of a galactosylated stearylamine as a liver-targeting ligand was successfully achieved by direct amidation reaction and confirmed by both FTIR and <sup>1</sup>H-NMR. During the preparation of SLN and NLC, it was found that using high solid lipid concentrations and insufficient surfactant may lead to the gelation of the lipid dispersion. In addition, surfactant type and concentration were found to have a significant impact not only on the particle size and size distribution of the lipid nanoparticles but also on the drug loading. It was revealed that increasing Tween 80 concentration led to increasing the drug loading till a certain limit, above which increasing surfactant concentration seems to increase drug partitioning into the aqueous medium, negatively affecting the drug loading.

Moreover, incorporating Sf solubilisers, such as Gelucire® 48/16 and Transcutol® P that demonstrated high miscibility with Precirol® ATO 5, led to a remarkable enhancement in the drug loading into lipid nanoparticles compared to SLN compared to SLN or NLC that encompasses Peceol™ oil. This could comprise a promising strategy to augment drug loading in lipid nanoparticles.

The galactosylated SLN and NLC were successfully prepared by incorporating the galactosylated conjugate into the lipid matrix during preparation. Both galactosylated SLN and NLC showed a nanosized (< 150 nm) with narrow size distribution (< 0.25) spherically shaped particles. FTIR analysis of freeze-dried systems showed no change compared to physical mixtures. Moreover, the DSC study confirmed the complete incorporation of Sf in the lipid matrix. Galactosylated systems showed a very sustained release profile compared to drug solutions.

By assessing the cellular cytotoxicity on HepG2 cells, blank lipid systems showed significant cytotoxicity levels, which masked the effect of nanoformulation and galactosylation on Sf cytotoxicity. The cytotoxicity of the blank lipid systems could be attributed to the presence of impurities in the solid lipid. From this finding, it is very crucial to consider the safety of the blank nanocarriers during the design and formulation of delivery systems, especially in case of low drug loading.



## **Chapter 4**

*Preparation and in-vitro appraisal of galactosylated Sorafenib-loaded lipid nanocapsules with lipiodol oil core as a liver-targeted theranostic agent*

#### 4.1.Introduction

Lipid nanocapsules (LNC) have evolved as a promising nanodelivery system for encapsulating hydrophobic drugs since being initially introduced by Heurtault et al.<sup>202</sup>. As mentioned in Chapter 1 (section 1.5.2.) LNC have a distinctive structure with an oil core (typically medium chain triglycerides ‘MCT’) surrounded by a rigid shell of phospholipids stabilised by a hydrophilic non-ionic surfactant<sup>203</sup>. LNC demonstrate attractive potential for drug delivery due to their appealing traits, such as improved physical stability, encapsulation of hydrophobic drugs, controlling drug release, and prolonged blood circulation due to their pegylated surface. Since most anticancer agents are hydrophobic, several agents have been successfully encapsulated into LNC, such as paclitaxel<sup>216,227</sup>, docetaxel<sup>405</sup>, cisplatin<sup>214</sup>, curcumin<sup>406</sup> and etoposide<sup>221,228</sup>.

Lipiodol oil is an oil-based radio-opaque contrast agent that functions as a drug delivery platform due to its radio-opacity and preferential tumour accumulation relative to surrounding liver tissues<sup>54,407</sup>. In addition, It has been employed as a vehicle for delivering different anticancer agents, including oxaliplatin<sup>54</sup>, and doxorubicin<sup>55,408,409</sup>. From that, the use of Lipiodol oil as a contrasting vehicle of the nanodelivery systems would impart a diagnostic functionality to these systems allowing the detection and the tracking of the accumulation of the delivered cytotoxic agent dose.

Although active targeting of nanodelivery systems has attracted significant attention for the selective delivery of anticancer agents, minimising their side effects on healthy tissues<sup>102</sup>, limited studies have investigated the active targeting of LNC<sup>224,241,410–413</sup>. For the selective delivery of anticancer agents to liver cancer tissues, different active targeting ligands have been studied. From this, targeting ASGP receptors via galactosylated nanodelivery systems showed encouraging outcomes<sup>107</sup>.

This study aims to formulate and characterise Sf-loaded LNC using lipiodol oil as a core with the surface grafting of the LNC with galactosylated TPGS using the post-insertion method to serve as a liver-targeted theranostic agent for hepatocellular carcinoma (HCC) (Figure 4.1).

The objectives of this chapter:

- To synthesise and characterise a lactobionic acid and TPGS conjugate to function as liver targeting ligand (Gal-TPGS).
- To fabricate of Sf-loaded lipid nanocapsules (Sf-LNC) and explore the impact of different formulation parameters of their physicochemical properties.
- To assess the post-insertion of Gal-TPGS into Sf-LNC on physical properties of LNC.
- To Appraise the colloidal stability of Gal-Sf-LNC during short-term storage and under physiological conditions.
- To examine the targeting efficiency, cytotoxicity, and cellular uptake of the developed Gal-Sf-LNC on HepG2 cells.

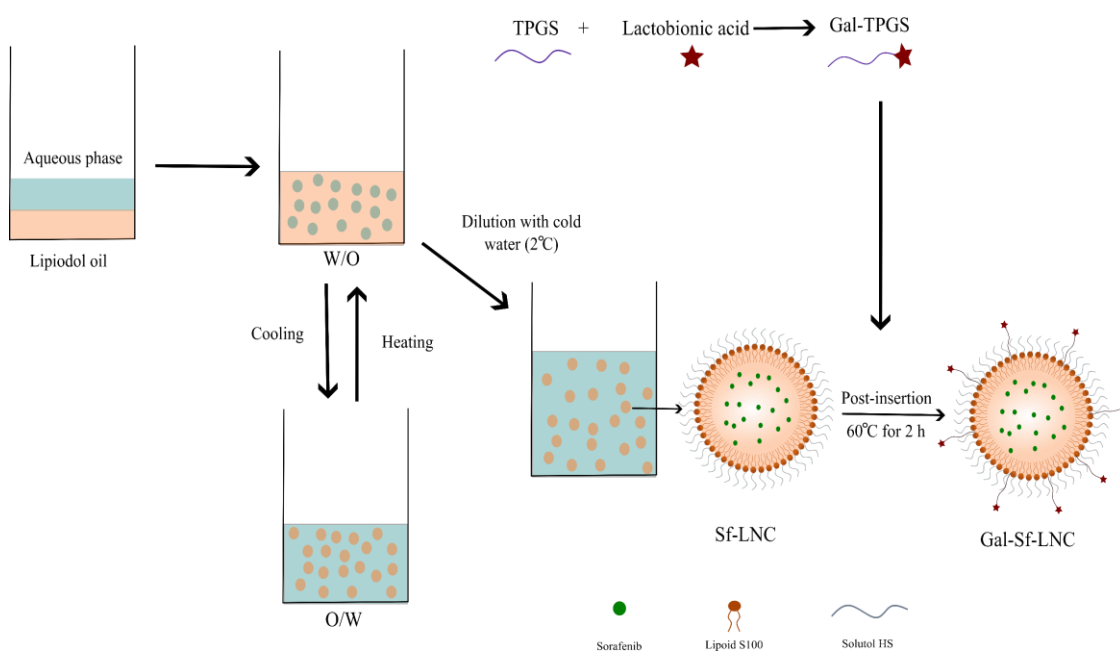


Figure 4.1: Schematic abstract for the preparation of galactosylated Sf-loaded lipid nanocapsules (Gal-Sf-LNC)

## 4.2. Materials and methods

### 4.2.1. Materials

Solutol® HS (Kolliphor® HS15) and Lipoid S 100 were gifted from BASF (Ludwigshafen, Germany) and Lipoid GmbH (Germany), respectively. Labrafac® WL 1349 and Transcutol® P were kindly provided by Gattefosse (France). Lipiodol® oil was purchased from Guerbet (UK). Sorafenib was obtained from LC Labs (USA). Ricinus communis agglutinin, RCA120, was purchased from 2BScientific (UK). Sodium chloride, Tween 80, lactobionic acid, D- $\alpha$ -Tocopherol polyethylene glycol 1000 succinate (TPGS), Acetone, Triethylamine (TEA), dimethyl sulfoxide (DMSO), deuterated dimethyl sulfoxide (DMSO-d<sub>6</sub>), ethylenediamine (EDA), 1,1'-Carbonyldiimidazole (CDI), N-hydroxysuccinimide (NHS), 1-Ethyl-3-(3-dimethylaminopropyl) carbodiimide (EDC), trypsin-EDTA solution, RPMI 1640 Medium, fetal bovine serum (FBS), phosphate buffer saline (PBS), Hanks' Balanced Salt Solution (HBSS), 1% non-essential amino acids (NEAA), 1% penicillin–streptomycin solution, phosphotungstic acid (PTA), trifluoroacetic acid (TFA), and Coumarin-6 (C6), HPLC grade acetonitrile were purchased from (Sigma Aldrich, UK).

### 4.2.2. Preparation of Sf-loaded lipid nanocapsules (Sf-LNC)

Lipid nanocapsules formulations were prepared using the phase inversion temperature (PIT) method first reported by Heurtault et al.<sup>201,202</sup>. Initially, a mixture of Sf (40 mg), Lipiodol oil® (20% w/w), Lipoid® S100 (2.8% w/w), Kolliphor® HS15 (20% w/w), Milli-Q water (55.5% w/w), and NaCl (1.68% w/w) was heated up to 90 °C under magnetic stirring and then cooled to 60 °C. This heating-cooling cycle was repeated three times. During the last temperature decrease, at the phase inversion temperature (~75° C), an irreversible shock was induced by dilution with 7.5 g of pure cold Milli-Q water (~2° C). Finally, LNC were kept under magnetic stirring at 400 rpm for 5 min. The LNC dispersions were filtered through 0.22  $\mu$ m syringe filters (Fisherbrand, UK) to remove any unloaded drug and stored at 4°C. All given percentages were relative to the initial dispersion weight. Blank LNC (B-LNC) were formulated similarly but without Sf

addition. The effect of oil composition (Table 4.1) and oil: Solutol HS ratio on particle size and drug entrapment efficiency was studied.

Table 4.1: Different oil compositions of LNC.

<b>Formulation</b>	<b>Labrafac® WL 1349</b> (% w/w)	<b>Lipiodol oil</b> (% w/w)	<b>Transcutol® P</b> (% w/w)
Sf-LNC 1	20	-	-
Sf-LNC 2	10	10	-
Sf-LNC 3	-	20	-
SF-LNC 4	-	20	5

#### 4.2.3. Characterisation of lipid nanocapsules (LNC)

The average particle size (P.S.), size distribution (PDI) and Zeta potential (Z.P.) of all formulations were measured using (Zetasizer Nano, Malvern Instruments, Malvern, UK) using the same procedures detailed in Chapter 2 (2.3.2.1.). TEM was used to analyse the morphologies of LNC formulations according to the procedures described in Chapter 2 (section 2.3.3.1.). Drug loading was quantified using the previously reported HPLC method in Chapter 3 (section 3.2.4.). 10 µL of filtered LNC was dissolved in 990 µL of acetonitrile and filtered using a 0.22 µm syringe filter. 20 µL of the solution was injected into the HPLC system. Sf loading was calculated and expressed in mg of Sf/g of LNC dispersion, while entrapment efficiency (%) was calculated using Eq. (3.1.) in Chapter 3 (section 3.2.9.).

#### 4.2.4. Synthesis of galactosylated TPGS (Gal-TPGS)

Galactosylation of TPGS was carried out as previously reported with slight modifications<sup>414</sup>. Briefly, 500 mg (0.33 mmol) TPGS was dissolved with 267 mg CDI (1.64 mmol) in 5 mL dioxane and left under stirring at 37°C overnight to form the imidazole carbamate intermediate (TPGS-CDI). Then, dioxane was removed by a rotary evaporator at 60° C. The residue was dissolved in 2 mL of DMSO with 0.1 ml (1.5 mmol) of ethylenediamine (EDA) and left under stirring for another 24 h. Afterwards, the

reaction solution was dialysed using a dialysis membrane 1000 Da MWCO (Spectrum Laboratories Inc., USA) against DMSO for 24 hr to remove excess EDA and CDI. In the meantime, 358 mg (1 mmol) lactobionic acid (LA), 173 mg (1.5 mmol) NHS, and 233 mg (1.5 mmol) EDC were dissolved in 2 mL of DMSO and left under stirring for 4 h for carboxylic acid activation. Next, the dialysis bag content was mixed with the activated lactobionic acid. The reaction was left under stirring for 48 h, followed by dialysis (MWCO = 1000 Da) against Milli-Q water for 48 h. The final product was then freeze-dried for 24 h. The detailed scheme of chemical synthesis is detailed in Figure 4.2.

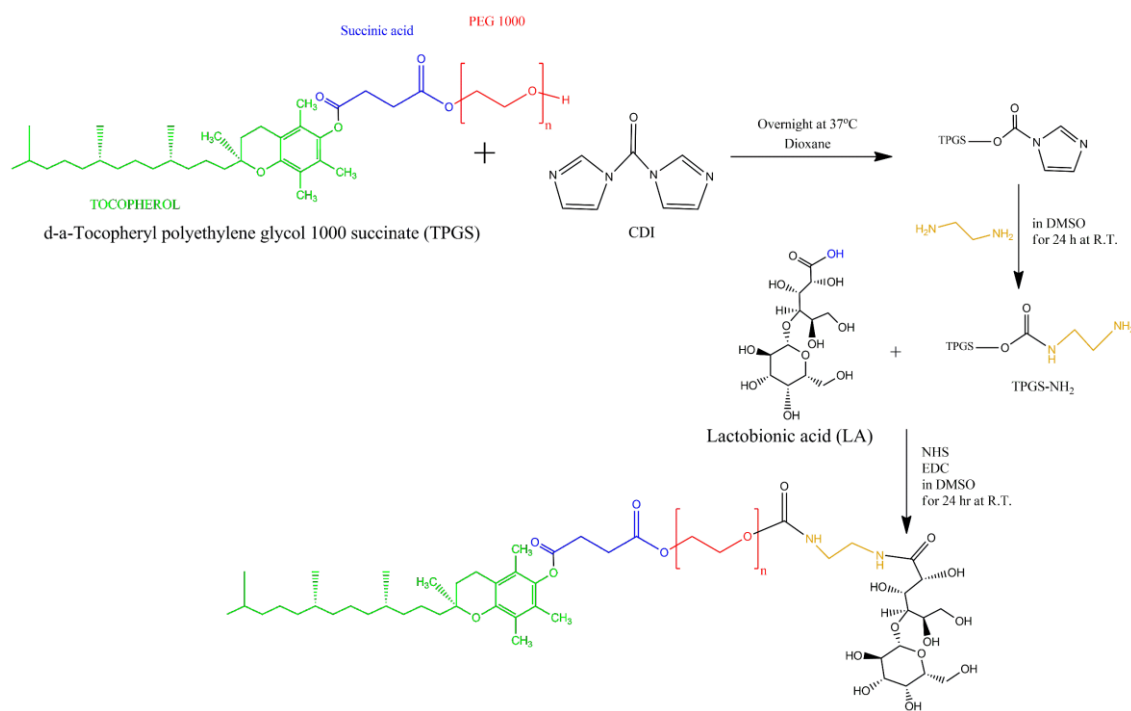


Figure 4.2: The chemical scheme of the synthesis of Gal-TPGS.

#### 4.2.5. Characterisation of Gal-TPGS

Different analytical methods, including ATR-FTIR spectroscopy, <sup>1</sup>H-NMR spectroscopy, and MALDI-TOF spectroscopy were used to verify the conjugation between TPGS and Lactobionic acid (LA). ATR-FTIR measurements were done as detailed in Chapter 2 (section 2.3.2.6.), while <sup>1</sup>H-NMR spectra were acquired after dissolving samples in DMSO-d<sub>6</sub> and analysed using 500 MHz spectrometer (Bruker Avance DRX 500, UK). For MALDI-TOF measurement, samples (TPGS, LA, and Gal-TPGS) were dissolved in a solvent mixture (1:1 acetonitrile: Milli-Q water + 0.1% TFA) at 1 mg/mL, and 1 μL

was spotted twice onto sample spot of a clean MALDI sample plate. Samples were examined using linear positive ionisation detection mode on a MALDI-TOF (AXIMA performance, Shimadzu, UK). TGA analysis was carried out as described in Chapter 2 (section 2.3.2.4.). The conjugation efficiency was determined by quantifying galactose content in the conjugation product using the phenol/sulfuric acid assay method<sup>362</sup>, As previously detailed in Chapter 3 (section 3.3.1.).

#### **4.2.6. Post-insertion of Gal-TPGS into Sf-LNC**

For surface grafting of LNC, post-insertion was adopted as previously reported<sup>412</sup>. Sf-LNC dispersion was incubated with Gal-TPGS micellar dispersion (20 mol.% of Solutol® HS content in LNC) at 60°C for 2 h. The mixture was vortexed every 15 min, followed by quenching in an ice bath for 1 min. Subsequently, the Gal-LNC dispersion was dialysed overnight using a dialysis membrane (50 KDa MWCO, spectrum laboratories, Inc., UK). The surface modification of LNC was verified by monitoring particle size and zeta potential using DLS, as mentioned in the previous section.

#### **4.2.7. Galactose surface accessibility (lectin-induced agglutination assay)**

Lectin agglutination assay has been carried out to confirm the surface exposure and accessibility of galactose moieties on the surface of the galactosylated LNC according to the previously reported method<sup>350</sup>. In a 96-well flat-bottom microwell plate (Hellma, UK), 100 µL of Sf-LNC or Gal-Sf-LNC dispersions (2 mg/mL final Gal-TPGS content in Gal-Sf-LNC) were mixed with 100 µL of Ricinus communis agglutinin, RCA120 (1.0 mg/mL in HBSS, pH 7.4). The turbidity was then determined by measuring the absorbance at max of 450 nm using a POLARstar® microplate reader (BMG LABTECH, UK) for 20 minutes (2 min intervals) to track the lectin-induced agglutination. After 20 min, 100 µL of free galactose (10 mg/mL) was added, followed by absorbance measurement to confirm the reversibility of the agglutination. PBS was used with micellar dispersions as a control (without RCA120). All the samples were done in triplicate.

#### **4.2.8. Short-term shelf physical stability of Sf-LNC and Gal-Sf-LNC**

The colloidal stability of Sf-LNC and Gal-Sf-LNC was evaluated over one week, two weeks and one month intervals, at 4° C. The particle size distribution and zeta potential were measured as previously described after the filtration of samples using 0.45 µm syringe filters (Fisherbrand, UK). The Sf entrapment efficiency (EE%) was also evaluated using the HPLC method to ensure the drug payload's stability. Additionally, a water-soluble starch solution (1%) was used to detect any iodine leakage from the lipiodol oil core of LNC. All samples were measured in triplicate.

#### **4.2.9. Colloidal stability of Sf-LNC and Gal-LNC in physiological blood condition**

The colloidal stability was further investigated under physiological blood conditions<sup>415</sup>. Both Sf-LNC and Gal-Sf-LNC were diluted 10 times using PBS at pH 7.4 containing 5.4% BSA (mimicking serum albumin concentration in a healthy person) and incubated at 37°C for 72 h. Consequently, particle size, size distribution and zeta potential were monitored using DLS as previously outlined<sup>415,416</sup>.

#### **4.2.10. *In-vitro* drug release study**

The sorafenib release profile was investigated using the dialysis bag method. Briefly, 2 mL of Sf-LNC, Gal-Sf-LNC and free sorafenib solution in PEG 400 (with equivalent sorafenib content of 100 µg) were put in a dialysis tube (Snakeskin™, M.W.C.O =10 KDa, regenerated cellulose, Sigma, UK). The bag was immersed in 40 ml of 1% Tween 80 in PBS at pH 7.4 as a release medium (Sf solubility in release mediums was 72.3 ± 5 µg/mL) and incubated in a shaking incubator at 37°C with a shaking rate of 100 rpm. At predetermined intervals (0.5, 1, 2, 4, 8, 10, 24, 48, 72, 96, 120 hrs), samples of 0.5 mL were taken and replaced with 0.5 mL of fresh release medium. Released samples were filtered with a 0.22 µm syringe filter (fisherbrand, UK) and analysed by injecting 20 µL into the HPLC system as previously described. The experiments were done in triplicate. Data were fitted to different drug release models. Besides, the mean dissolution (MDT), the difference (*f*1) and similarity (*f*2) factors were calculated (as detailed in Chapter 3 section 3.3.10).

#### **4.2.11. *In-vitro* cellular study**

##### **4.2.11.1. Cellular cytotoxicity on HepG2 cells**

Cellular cytotoxicity experiments were conducted using the MTS assay technique to determine the impact of sorafenib encapsulated into LNC and the galactosylation of LNC on the cytotoxicity efficiency of Sf on HepG2 cells. Briefly, HepG2 cells were seeded at a density of 7,000 cells/well/100  $\mu$ L of the serum-containing RPMI-1640 medium in a 96-well plate and incubated at 37°C for 24 h to allow cell attachment<sup>366</sup>. Afterwards, cells were treated with different formulations (Sf solution in 1% DMSO, Blank LNC, Sf-LNC, Blank Gal-LNC and Gal-Sf-LNC) at Sf concentration ranges from 20 to 0.5  $\mu$ g/mL. All formulations were sterilised by filtration using a 0.45  $\mu$ m sterile syringe filter (Minisart, Sartorius, UK). After 48 h of incubation, the medium was replaced with a fresh one, 10  $\mu$ l of MTS reagent was added to each well and cells were further incubated in a dark incubator for another 3 h. The absorbance was measured by a microplate reader (CLARIOstar, BMG LABTECH, Germany) at wavelength 490 nm. Cell viability was calculated according to Eq. (3.4) in Chapter 3 (section 3.2.13).

For the competitive inhibition test, another set of cells was preincubated with free galactose (10 mg/mL) for 1 h before the treatment with Gal-Sf-LNC<sup>417</sup>. All experiments were carried out in triplicate.

##### **4.2.11.2. Cellular uptake study using an inverted Fluorescence microscope**

To investigate the cellular uptake of LNC formulations by HepG2 cells (ASGP receptors positive), coumarin-6 (C6) was used as a lipophilic fluorescent probe and loaded into both galactosylated and non-galactosylated LNC (with final concentration of 40  $\mu$ g/mL of formula) instead of Sorafenib. The cellular uptake was visualised using a fluorescent microscope.

Firstly, HepG2 cells were grown in 12-well culture plates at a density of  $5 \times 10^5$  cells/well for 24 h using serum-containing RPMI-1640 media. Then, the medium was discarded and replaced with fresh media containing different test samples (namely, C6-loaded LNC, C6-loaded Gal-LNC, and C6-loaded Gal-LNC with free galactose (10 mg/mL) containing

a final coumarin-6 concentration of 0.2 µg/mL), and cells were incubated for further 4 h. Afterwards, cells were rinsed three times with cold PBS and fixed with 4% paraformaldehyde (PFA), PFA was dissolved in PBS and pH was adjusted to the range of 6.9 to 7.4, for 15 minutes. The cells were then washed three times with PBS before being counterstained with DAPI (1 mL/well of 1 µg/mL DAPI in PBS) for 15 minutes. Then cells were rinsed with PBS three times. After that, 300 µL/well of PBS was added, and the cells were analysed under fluorescence microscope (Zeiss Axiovert 200M, Germany). The green channel was excited at 485 nm to detect coumarin 6, while the blue channel was excited at 430 nm for DAPI.

#### **4.2.11.3. Cellular uptake study using flow cytometer**

The uptake of LNC by cells has been quantified using a flow cytometer (Beckman Coulter CytoFlex, USA). First, HepG2 cells ( $5 \times 10^5$  cells/well) were seeded in 12-well culture plates and grown in serum-containing RPMI-1640 media at 37°C for 24 hours. Subsequently, the media were discarded, and new media with different formulations (C6-loaded LNC, C6-loaded Gal-LNC, and C6-loaded Gal-LNC with free galactose (10 mg/mL)) were added at a final C6 concentration of 0.2 µg/mL. After 4 hours of incubation, the medium was discarded, and the cells were washed three times with PBS. Trypsinisation of the cells was carried out by a 3-minute incubation with 300 µL/well of trypsin-EDTA. The trypsin was inactivated by adding 700 µL of complete culture medium to each well. The cell suspension was then placed in Eppendorf tubes and centrifuged at 400 RCF for 5 minutes. After the media were discarded, the cell pellets were disaggregated and resuspended in 300 µL of sterile 1% bovine serum albumin solution by vortexing for 3 minutes. The cell suspension was transferred into a flow cytometer column, and fluorescence intensity was measured using flow cytometer. The run was adjusted to count 10,000 events in the second assigned gate (FSC-H vs FSC-Width). Data were collected and analysed using CytExpert software (v2.3, Beckman Coulter, USA).

### 4.3. Results and discussion

#### 4.3.1. Preparation and characterisation of Sf-loaded Lipid nanocapsules (LNC)

In order to study the effect of using lipiodol oil as the main core oil of LNC to serve as a contrasting agent beside being the main vehicle matrix, the effect of using different oil compositions (Table 4.1) on the particle size and drug loading of Sf-loaded LNC formulations was investigated. As shown in Table 4.2, using Labrafac® WL 1349, the typical oil component in LNC, as reported by Heurtault et al.<sup>201,202</sup>, formed Sf-LNC with P.S. of  $41.2 \pm 1.4$  nm with a very narrow particle size distribution ( $0.04 \pm 0.02$ ). This data comes in line with the reported values<sup>202</sup>. However, increasing lipiodol oil amount in the oil core showed a statistically significant ( $p < 0.05$ ) incremental reduction in the particle size of Sf-LNC, giving P.S. of  $28.6 \pm 1.3$  nm with maintaining the narrow particle size distribution ( $PDI = 0.02 \pm 0.00$ ) upon complete replacement of Labrafac® WL 1349 with lipiodol oil. On the other hand, changing the oil composition had no impact on the entrapment efficiency of Sf; this could be attributed to the slight difference in Sf solubilities in both Labrafac® WL 1349 and lipiodol® oil, as reported in Chapter 3 (section 3.3.3.).

Nevertheless, the use of 5% w/w Transcutol®P (in Sf-LNC 4) exhibited a slight but statistically significant ( $p < 0.05$ ) increase in the entrapment efficiency of Sf with no effect on both P.S. and PDI. This could be ascribed to the high solubility of Sf in Transcutol®P ( $162.2 \pm 2.8$  mg/mL). Changing oil composition had no effect on Z.P. values, which is explained by considering the structure of LNC in which the oil represents the internal core surrounded by a corona structure composed of lipophilic surfactant (lipoid S 100) and hydrophilic one (Solutol® HS). Besides, the presence of a relatively high NaCl concentration in LNC dispersion could mask any changes in the zeta potential values that could happen due to the change in the composition.

Table 4.2: The effect of variable oil composition on P.S., PDI, ZP and drug load of Sf-LNC.

<b>Formulation</b>	<b>P.S. ± SD</b> (nm)	<b>PDI ± SD</b>	<b>Z.P. ± SD</b> (mV)	<b>EE% ± SD</b> (%)	<b>Drug load</b> (mg/g)
Sf-LNC 1	41.2 ± 1.4	0.04 ± 0.02	- 2.1 ± 1.13	88.2 ± 1.5	2.8 ± 0.05
Sf-LNC 2	34.6 ± 1.1	0.057 ± 0.03	- 3.4 ± 1.77	88.4 ± 1.9	2.8 ± 0.06
Sf-LNC 3	28.6 ± 1.3	0.02 ± 0.00	-1.92 ± 1.3	89.6 ± 0.5	2.8 ± 0.02
Sf-LNC 4	28.2 ± 1.4	0.02 ± 0.01	- 1.96 ± 1.3	95.7 ± 2.1	3.1 ± 0.07

Furthermore, to minimise Solutol HS content in LNC, the impact of using different oil: Solutol HS ratios on Sf-LNC particle size, size distribution, ZP, and drug loading was investigated. For this experiment, the composition of Sf-LNC 4 was used by changing the oil: Solutol® HS ratios. From Table 4.3, decreasing Solutol® HS ratios resulted in a significant ( $p < 0.05$ ) incremental increase in P.S. of Sf-LNC with a limited influence on particle size distribution (PDI). Using an oil: Solutol HS ratio of 1:0.4, the phase inversion of the dispersion was not achieved during the heating cycles suggesting that the amount of Solutol® HS is insufficient to undergo a phase inversion and stabilise the formed w/o emulsion at the raised temperature<sup>205</sup>. This observation agrees with the reported study by Heurtault et al., where it was found that the size of the formed LNC depends on the concentration of hydrophilic surfactant<sup>202</sup>.

On the other hand, decreasing Solutol® ratios led to a significant ( $p < 0.05$ ) drop in Sf loading. It is possible that the incorporation of PEG in the structure of Solutol® HS, given that Sf is reported to be soluble in PEG 400<sup>418</sup>, is responsible for this substantial impact. This observation underlines that Solutol® HS not only has a crucial role in forming LNC but also affects drug loading.

Table 4.3: The effect of lipiodol oil: Solutol® HS ratio on P.S., PDI, ZP and drug load of Sf-LNC.

<b>Oil: Solutol® HS ratio</b>	<b>P.S. ± SD (nm)</b>	<b>PDI ± SD</b>	<b>Z.P. ± SD (mV)</b>	<b>EE% ± SD (%)</b>	<b>Drug load (mg/g)</b>
1:1	28.2 ± 1.4	0.02 ± 0.01	- 1.96 ± 1.3	95.7 ± 2.1	3.1 ± 0.07
1:0.8	36.7 ± 1.2	0.092 ± 0.01	- 3.4 ± 1	78.8 ± 2.4	2.6 ± 0.08
1:0.6	41.1 ± 1.2	0.094 ± 0.01	- 3.4 ± 1	31.5 ± 3.7	1 ± 0.12
1: 0.4	No clear phase inversion				

According to this experiment's results, formulation Sf-LNC 4 was chosen for further investigations.

#### 4.3.2. Characterisation of Gal-TPGS

Galactosylation of different delivery systems has been intensively reported during the last few years as a promising strategy for liver-targeted delivery of anticancer agents relying on the overexpression of ASGP receptors on cancerous hepatocytes<sup>107</sup>, as discussed in Chapter 1 (section 1.3.). In this study, lactobionic acid was conjugated to TPGS through a two-step chemical pathway. The same chemical approach has been employed to functionalised TPGS with targeting ligands such as folic acid<sup>251</sup> and Glycyrrhetic acid<sup>324</sup>. Different analytical methods were used to verify the synthesis of Gal-TPGS conjugate. It is worth mentioning that slight modification was introduced to the procedures; in the typical reported method, TPGS-CDI was purified from excess CDI and EDA via precipitation using cold ether followed by filtration<sup>414</sup>. However, by trying that, no sensible precipitate was recovered after filtration. Alternatively, the purification step was carried out using the dialysis method.

##### 4.3.2.1.ATR-FTIR

ATR-FTIR first confirmed the synthesis of Gal-TPGS. As shown in Figure 4.3, TPGS showed its characteristic band at 1736 cm<sup>-1</sup> attributed to C=O, bands at 1244 cm<sup>-1</sup> and 1107 cm<sup>-1</sup> for (C-O-C) with overlapping bands at 2870 cm<sup>-1</sup> ascribed to (-CH)<sup>419,420</sup>. On the other hand, LA demonstrated a broad band around 3339 cm<sup>-1</sup> for its OH groups and a

band at  $1738\text{ cm}^{-1}$  for the carbonyl group of the carboxylic acid (C=O). However, for the synthesised conjugate Gal-TPGS, the presence of the broad band around  $3339\text{ cm}^{-1}$  related to OH groups of LA and the appearance of new distinctive bands at  $1649\text{ cm}^{-1}$  and  $1560\text{ cm}^{-1}$  attributed to the newly formed amide bonds (N-H)<sup>369</sup> confirms the successful formation of Gal-TPGS conjugate. This finding comes in line with previously reported data<sup>421</sup>.

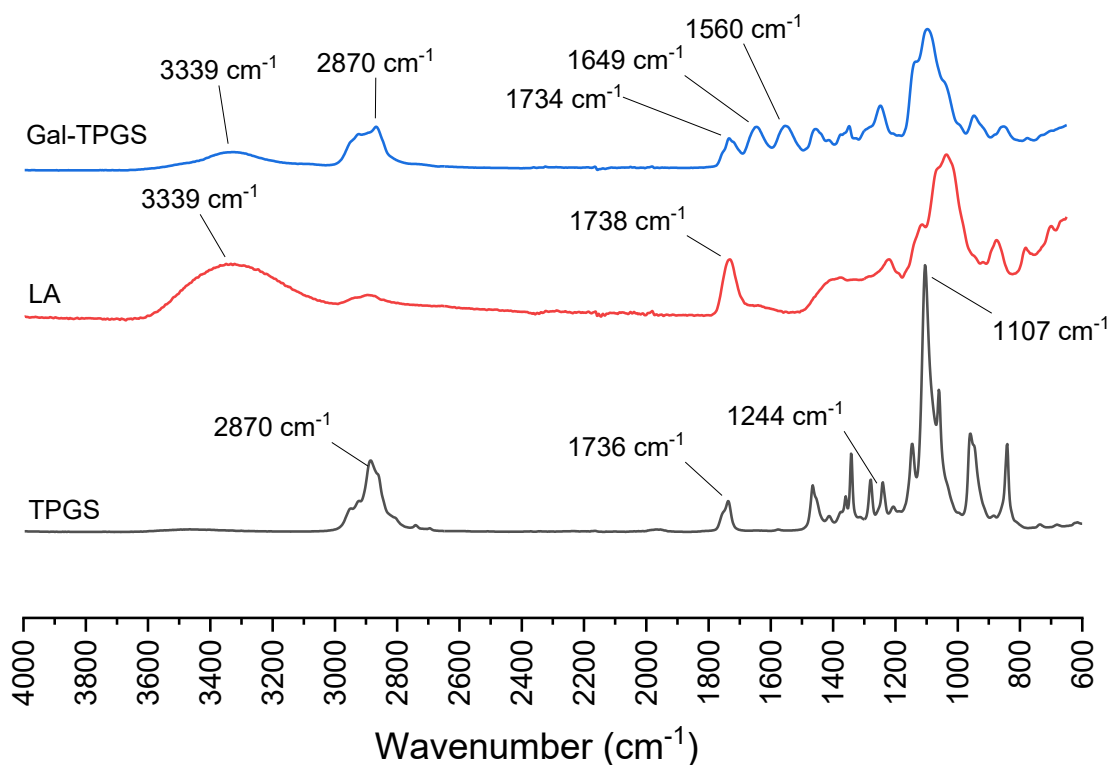


Figure 4.3: FTIR spectra of TPGS, LA, and Gal-TPGS.

#### 4.3.2.2. $^1\text{H-NMR}$

To confirm the structure of the synthesised Gal-TPGS,  $^1\text{H-NMR}$  was carried out. From the Gal-TPGS spectrum disclosed in Figure 4.4a, new proton signals around 3.6 to 4.65 ppm have appeared compared to the TPGS spectrum (Figure 4.4b).

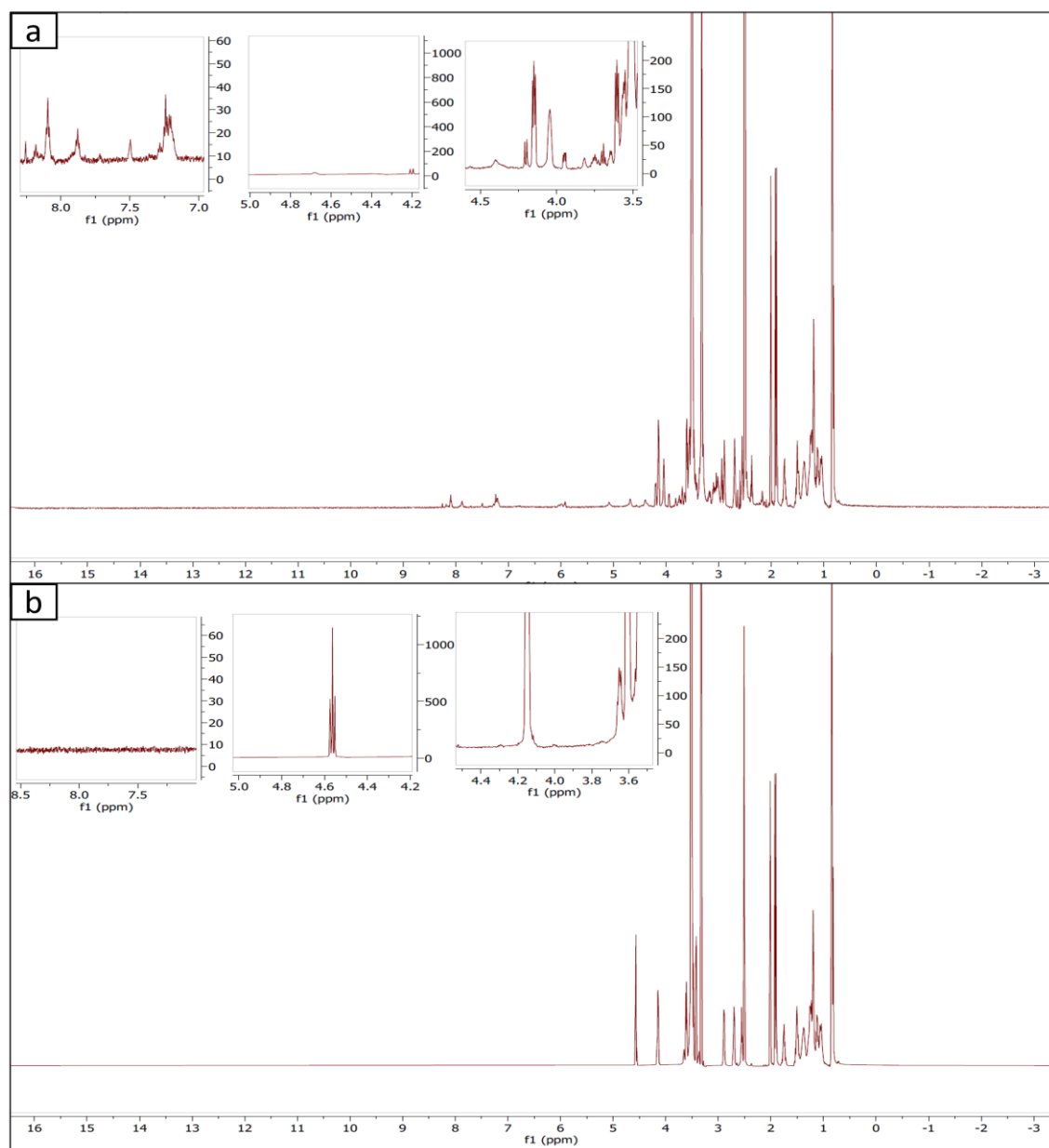


Figure 4.4:  $^1\text{H}$ -NMR spectra of Gal-TPGS (a) and TPGS (b) dissolved in  $\text{DMSO-d}_6$ .

The peak at 4.04 is attributed to the C1 proton of the pyran ring, while the peaks in the range of 3.6-3.9 ppm correspond to the protons of the hydroxyl groups and the pyran ring of the sugar moiety of LA. Furthermore, the newly formed peak in the Gal-TPGS spectrum at 7.34 ppm, coupled with the disappearance of the proton peak of the terminal hydroxyl group in the TPGS spectrum at 4.56 ppm, indicates the formation of an amide bond between TPGS and LA.

In addition to these characteristic peaks, the peaks around 0.7–1.7 ppm are assigned to the -CH<sub>3</sub>- and -CH<sub>2</sub>- moieties of the TPGS, and the peak at 3.50 ppm is attributed to the -CH<sub>2</sub>- protons of the polyethylene oxide region of the TPGS. The peaks at 3.30 ppm and 2.50 ppm belong to H<sub>2</sub>O and DMSO, respectively. Altogether, these results confirm the successful conjugation of LA to TPGS<sup>421</sup>.

#### 4.3.2.3.MALDI-TOF

Gal-TPGS was further characterised using MALDI-TOF. As depicted in Figure 4.5, LA exhibited a molecular ion peak at 323 g/mol (Figure 4.5a), which is lower than the labelled molecular weight from the manufacturer (358.3 g/mol). Similarly, the most abundant mass peak of TPGS was observed at 1477 g/mol (Figure 4.5b), while the labelled mass was 1513 g/mol. This deviation could be attributed to machine calibration<sup>422</sup>. In the case of the Gal-TPGS mass spectrum (Figure 4.5c), the main parental TPGS peak was shifted to a higher molecular weight (1817 g/mol). This significant shift in masses confirms the formation of Gal-TPGS<sup>298,422</sup>.

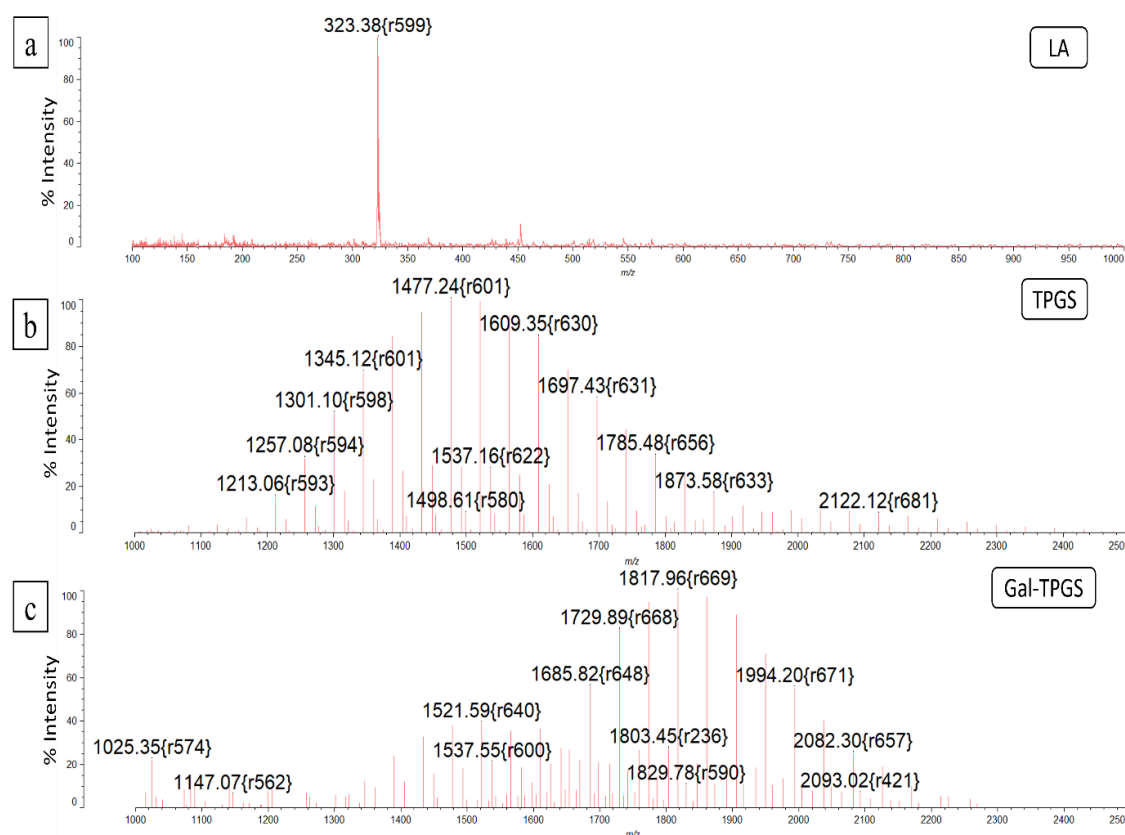


Figure 4.5: MALDI-TOF mass spectra of LA (a) and TPGS (b), and Gal-TPGS (c).

#### 4.3.2.4.TGA

TGA of the synthesised Gal-TPGS was conducted to investigate its thermal stability. Figure 4.6 demonstrates the typical thermal decomposition profile of TPGS with a one-step degradation process at a temperature range ( $\sim 350 - 430^\circ\text{C}$ )<sup>423</sup>. However, Gal-TPGS exhibited two-step degradation<sup>299,303,424</sup>. Each degradation step is attributed to one segment of the synthesised conjugate. The first degradation step started at a temperature of  $190^\circ\text{C}$  assigned to the lactobionic acid segment, while the second step, which begins at around  $358^\circ\text{C}$ , is related to the TPGS segment. The same finding was reported by Tao, W. *et al.* after conjugating TPGS to PLGA to prepare docetaxel-loaded polymeric nanoparticles for breast cancer treatment. PLGA-TPGS conjugate showed a two-step degradation profile in which the first step ( $\sim 250-350^\circ\text{C}$ ) was attributed to PLGA while the second step ( $\sim 350 - 430^\circ\text{C}$ ) was ascribed to TPGS<sup>423</sup>.

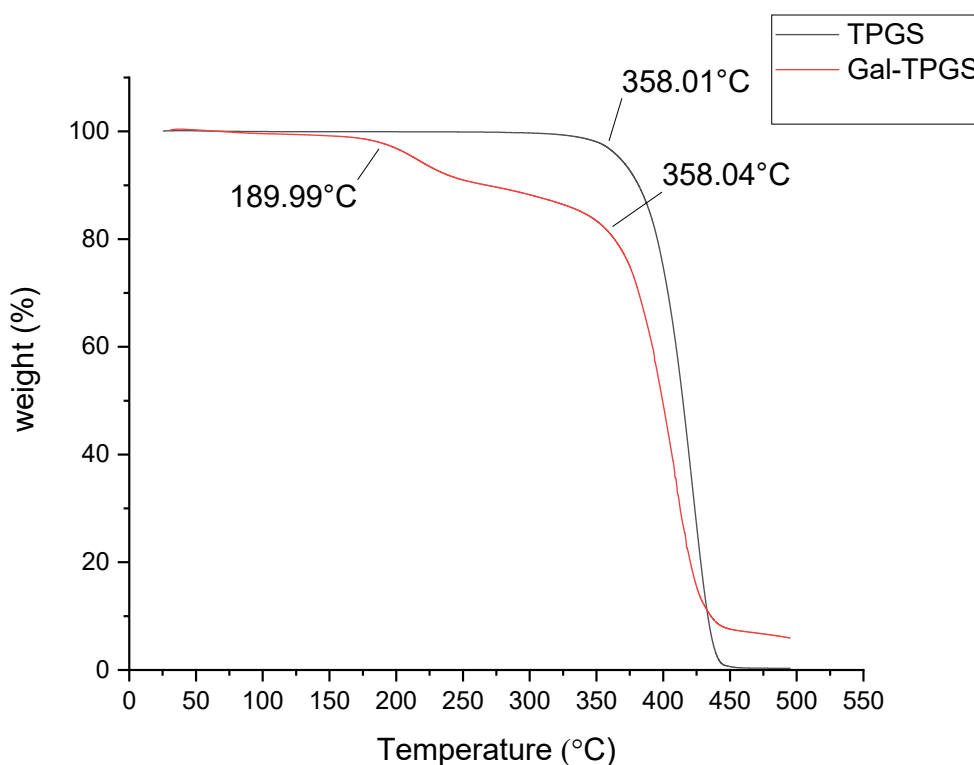


Figure 4.6: TGA curves of TPGS and Gal-TPGS (heating from  $25^\circ\text{C}$  to  $500^\circ\text{C}$  at a heating rate of  $20^\circ\text{C}/\text{min}$ )

### 4.3.3. Conjugation efficiency of Gal-TPGS

The phenol/sulfuric acid colourimetric assay method has been conducted to quantify the conjugation efficiency, as detailed in Chapter 3 (section 3.2.3.). Conjugation efficiency (number of conjugated TPGS moles to the total number of moles) calculated was  $74.6 \pm 5.2\%$ , giving galactose content of  $7.6 \pm 0.2\%$ .

It is noteworthy that an attempt for conjugation of DSPE-PEG<sub>2000</sub>-NH<sub>2</sub> with lactobionic acid (LA) was carried out using EDC/NHS amidation reaction. Briefly, 35.8 mg (0.1 mmol) lactobionic acid (LA), 17.3 mg (0.15 mmol) NHS, and 23.3 mg (0.15 mmol) EDC were dissolved in 2 mL of DMSO and left under stirring for 2 h for activation of carboxylic acid. Afterwards, 40 mg (0.014 mmol) of DSPE-PEG<sub>2000</sub>-NH<sub>2</sub> was added, and the reaction was continued for 48 h. The reaction solution was then dialysed using a dialysis membrane 1000 Da MWCO (Spectrum Laboratories Inc., USA) against Milli-Q water for 48 h, followed by freeze-drying.

The amidation product was characterised using FITR. As shown in Figure 4.7, the characteristic bands of DSPE-PEG<sub>2000</sub>-NH<sub>2</sub> were N-C=O ( $1740\text{ cm}^{-1}$ ), -CH<sub>2</sub> ( $2889\text{ cm}^{-1}$ ), -CH<sub>3</sub> ( $1342\text{ cm}^{-1}$ ), and O-CH<sub>2</sub> ( $1105\text{ cm}^{-1}$ ). LA exhibited its distinctive band at -C=O ( $1740\text{ cm}^{-1}$ ) and a broad band of OH groups ( $3354\text{ cm}^{-1}$ ). For the conjugation product, the presence of amide bands at  $1740\text{ cm}^{-1}$  and  $1649\text{ cm}^{-1}$  beside the characteristic broad band of OH groups of LA at  $3369\text{ cm}^{-1}$  asserts the successful formation of DSPE-PEG<sub>2000</sub>-Gal conjugate.

Despite the successful chemical conjugation, the recovery of the conjugate after freeze-drying was very low (17.5% w/w). Thus, TPGS was considered a readily available, inexpensive surrogate for DSPE-PEG<sub>2000</sub>-NH<sub>2</sub>. Especially, variable moieties of different chemical natures have been reported to be successfully inserted into LNC, such as Pluronic® F108<sup>411</sup>, lipochitosan (LC), and lipodextran (LD)<sup>412</sup>.

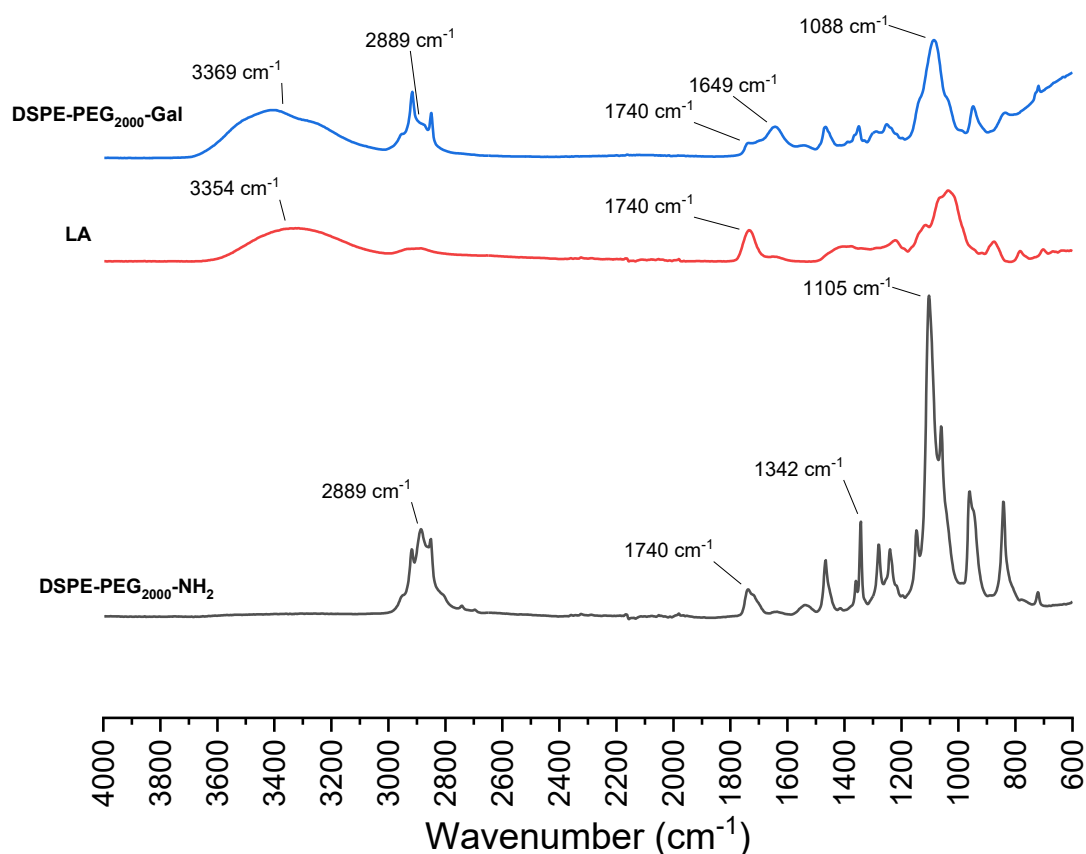


Figure 4.7: FTIR spectra of DSPE-PEG2000-NH<sub>2</sub>, LA, and DSPE-PEG2000-Gal.

#### 4.3.4. Post-insertion of Gal-TPGS into LNC and Sf-LNC

Post-insertion approach was first reported by Ulster et al.<sup>425</sup> for the pegylation of preformed liposomes to increase their *in-vivo* plasma circulation time through the insertion of methoxypoly(ethylene glycol)<sub>1900</sub>-1,2-distearoyl-sn-glycero-3-phosphoethanolamine (MPEG<sub>1900</sub>-DSPE) into liposomes' surface. Following that, several studies have been conducted to insert different functionalised and pegylated moieties into preformed liposomes<sup>425-431</sup>. Principally, post-insertion of pegylated phospholipids (mostly DSPE-mPEG<sub>2000</sub>) is achieved by the incubation of the preformed liposomal dispersion with a micellar dispersion of the pegylated phospholipid at a temperature above the phase transition temperature of the liposomes' phospholipid for a certain time (ideally, 60 min according to ulster et al.<sup>425</sup> after which the insertion efficiency was found to be plateaued) to ensure complete insertion.

Similarly, Post-insertion has been employed for surface grafting of lipid nanocapsules but to a lesser extent<sup>412,432</sup> For instance, Béduneau, A. *et al.* prepared immunonanocapsules conjugated with OX26 monoclonal antibodies (OX26 MAb) and Fab' fragments for targeting the transferrin receptors (TfRs) that are highly expressed on the cerebral endothelium<sup>410</sup>. Firstly, DSPE-PEG2000-Maleimide was inserted into the surface of LNC, followed by the conjugation of both targeting moieties that were conjugated to OX26 Mab and Fab' fragments. After *in-vivo* animal studies, the brain concentrations of Fab'-immunonanocapsules and OX26-immunonanocapsules were 1.5 and 2-fold, respectively, higher than non-targeted nanocapsules<sup>433</sup>.

As depicted in Table 4.4, the effect of the post-insertion procedure on Sf-LNC was first assessed by the incubation of Sf-LNC at 60°C for 2 h without Gal-TPGS. Sf-LNC (heat treated) did not show any significant ( $p > 0.05$ ) change in its colloidal properties or drug EE%. However, Sf-LNC incubated with Gal-TPGS (referred to as Gal-Sf-LNC) showed a limited insignificant ( $p > 0.05$ ) increase in P.S but a remarkable ( $p < 0.05$ ) increase in PDI, yet unimodal distribution, with a significant ( $p < 0.05$ ) increase in the Z.P. to a positive value ( $8.56 \pm 1.6$  mV). The unimodal size distribution of Gal-Sf-LNC with the inflection in the ZP of the surface suggests the successful insertion of Gal-TPGS in the structure of Sf-LNC. Although it was reported that post-insertion of DSPE-PEG<sub>2000</sub> into LNC was accompanied by a slight increase in particle size ( $\sim 9$  nm)<sup>434</sup>, the insertion of Gal-TPGS did not show a significant ( $p > 0.05$ ) increase in P.S. This could be attributed to the different length of PEG moiety in TPGS (PEG content = 1000 g/mol  $\simeq$  23 PEG units<sup>206</sup>) compared to DSPE-PEG<sub>2000</sub> (PEG content = 2000 g/mol  $\simeq$  45 PEG units<sup>435</sup>) that may affect the spatial conformation of PEG arm rendering it more folded (mushroom brush intermediate or mushroom-like conformation) rather than the extended PEG chain (brush-like conformation)<sup>413,436</sup>. Different possible spatial conformations of PEG arms at the surface of LNC are shown in Figure 4.8. The galactose exposure at the surface of Gal-Sf-LNC was further investigated using a lectin-induced agglutination assay, as discussed in the next section.

Table 4.4: The effect of post-insertion of Gal-TPGS into LNC on P.S., PDI, ZP and EE% of Sf-LNC.

<b>Formulation</b>	<b>P.S. <math>\pm</math> SD (nm)</b>	<b>PDI <math>\pm</math> SD</b>	<b>Z.P. <math>\pm</math> SD (mV)</b>	<b>EE% <math>\pm</math> SD (%)</b>
Gal-TPGS micelles (2%)	5.7 $\pm$ 2.2	0.323 $\pm$ 0.01	18.4 $\pm$ 1.5	--
Sf-LNC (heat-treated)	27.2 $\pm$ 1.5	0.048 $\pm$ 0.01	- 1.21 $\pm$ 0.7	95.6 $\pm$ 1.8
Gal-LNC (20%mol)	29.3 $\pm$ 1.1	0.192 $\pm$ 0.01	8.56 $\pm$ 1.6	95.6 $\pm$ 1.9

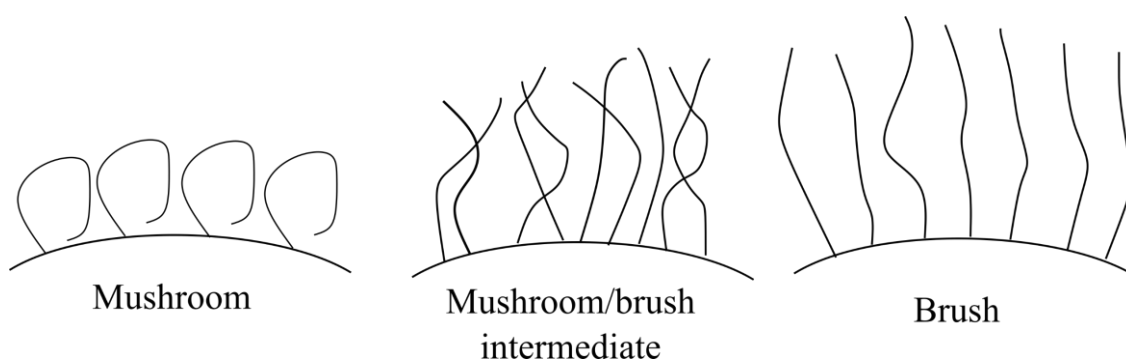


Figure 4.8: Schematic representation of the different spatial conformation of PEG arms at the surface of lipid nanocapsules.

The morphology of both Sf-LNC and Gal-Sf-LNC was inspected using TEM. As demonstrated in Figure 4.9, both Sf-LNC showed a spherical core-shell structure. In which the dark core is comprised of lipiodol oil with high electron density due to iodine content with a less dense shell of PEG corona of Solutol® HS. The particle size distributions were comparable to those measured by DLS.

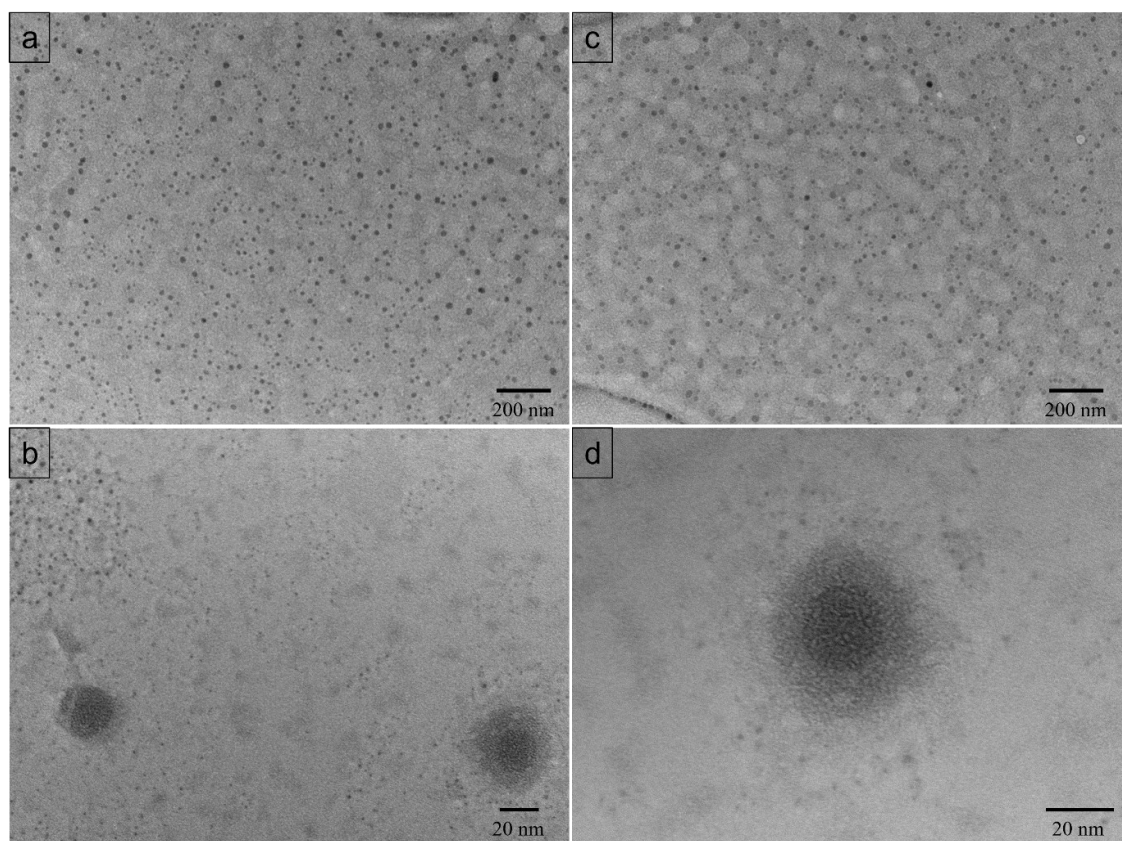


Figure 4.9: TEM images of Sf-LNC (a and b) and Gal-Sf-LNC (c and d).

#### 4.3.5. Galactose surface accessibility (lectin-induced agglutination assay)

The surface exposure of the galactose moieties on the surface of LNC and their selectivity in binding to ASGP receptors was investigated. Lectin-induced agglutination test<sup>351,353,437</sup> was employed based on the fact that lectin from *Ricinus communis* (RCA120) has a very selective affinity to bind to D-galactose and N-acetyl galactosamine<sup>346</sup>. As elicited in Figure 4.10, Gal-Sf-LNC exhibited an increase in turbidity compared to unmodified LNC, indicating an interaction between surface galactose moieties of Gal-Sf-LNC with RCA120. Furthermore, after adding free galactose solution, the turbidity of galactosylated LNC dropped, suggesting that the interaction between lectin and Gal-Sf-LNC was reversible and could be competitively inhibited by free galactose<sup>349</sup>. Despite that, the magnitude of agglutination is considered limited compared to previously reported studies<sup>349,351,353</sup>. This could be attributed to the folded spatial conformation of Gal-TPGS (mushroom brush intermediate or mushroom-like conformation), as discussed in the previous section.

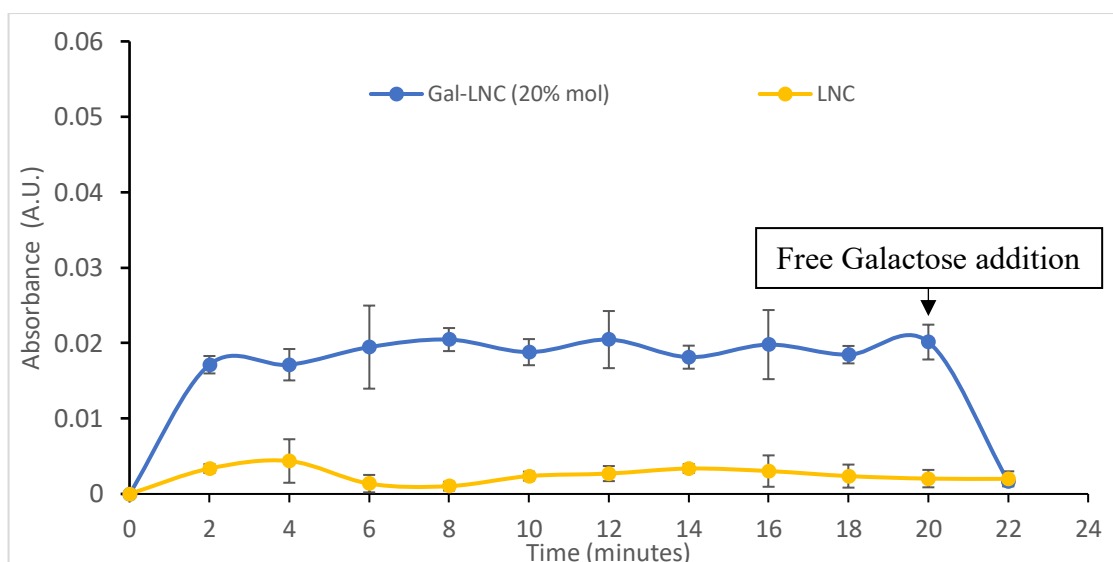


Figure 4.10: RCA120-induced agglutination of Sf-LNC and Gal-Sf-LNC. 100  $\mu$ L of LNC dispersions were incubated with 100  $\mu$ L of RCA120 (1 mg/mL) for 20 min with continuous absorbance measurement at 450 nm at 2 min intervals. The reversibility of agglutination was verified by adding free D-galactose (10 mg/mL) at the 20<sup>th</sup> min.

#### 4.3.6. Short-term shelf physical stability of Sf-LNC and Gal-Sf-LNC

The physical stability of Sf-loaded LNC was assessed for 1 month by storing them at 4°C. As depicted in Figure 4.11, both Sf-loaded LNC (galactosylated and unmodified) were physically stable for at least 1 month of storage with no substantial change in the mean particle size or PDI being observed. Moreover, there was not any visual precipitation of the drug noticed. This was confirmed by measuring the EE% of Sf that showed no statistical difference ( $P < 0.05$ ), and EE% was preserved around 95.5%. Furthermore, due to the iodinated nature of lipiodol oil, samples were inspected for any colour change that indicates the leakage of iodine from the internal oil core of LNC. No colour change was noticed, and this observation was confirmed by adding a few drops of 1% water-soluble starch solution to LNC dispersions without exhibiting any colour change. The physical stability of LNC is well-reported in different studies<sup>222,285,438–441</sup>. This stability is mainly ascribed to the pegylated structure of the surface of LNC due to the presence of Solutol® HS. These PEG arms confer a corona structure to LNC that stabilise them sterically<sup>203,438</sup>.

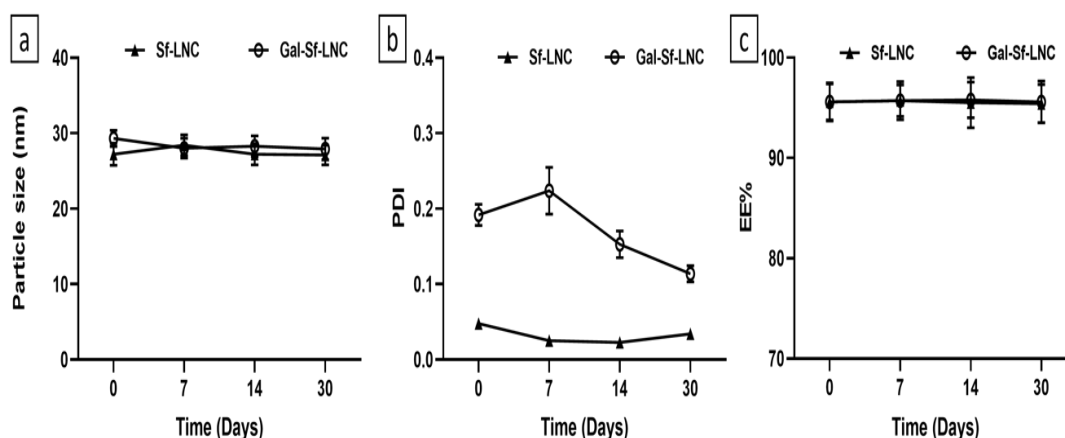


Figure 4.11: The effect of short-term storage of Sf-LNC and Gal-Sf-LNC at 4° C for one month on particle size (a), size distribution PDI (b), and EE% (C).

#### 4.3.7. Colloidal stability of Sf-LNC and Gal-Sf-LNC in physiological blood conditions

*In-vivo* colloidal stability of nanoparticles after administration is a key parameter to maintain nanocarrier integrity and payload. Thus, lipid nanocapsules' (LNC's) stability was investigated in PBS at pH 7.4 containing a physiologically relevant protein concentration (5.4% BSA) at 37° C for 72 h, mimicking conditions after intravenous administration. As depicted in Figure 4.12, 5.4% BSA in PBS colloidal solution showed multiple size distribution peaks in DLS measurements, with the main peak around 9 nm<sup>442</sup>. This could be attributed to the fact that BSA represents a complex cocktail of polydisperse proteins of different sizes, as previously reported<sup>443</sup>. After incubation of both LNC formulations with BSA, the particle size distribution of LNC showed a bimodal size distribution owing to the presence of a BSA peak around 9 nm, dramatically affecting the PDI measurement. Thus, the measurement of each individual peak (based on intensity) was considered. Figure 4.12 b and c revealed a noticeable increase in particle size of the main peak of both LNC dispersions with a value of almost 9 nm. This could be attributed to the adsorption of BSA on the surface of LNC. It is well reported that the presence of plasma or serum proteins may substantially alter the surface characteristics of many nanoparticles due to the formation of an adsorbed protein corona around nanoparticles<sup>230,443–445</sup>. Nevertheless, the effect of protein on the particle size of LNC was minimal, and LNC successfully retained their nanosized range, which is vital for passive accumulation in cancer tissues<sup>446,447</sup>. Besides, the overexpression of ASGP receptors on hepatocytes, with their

high affinity towards galactose-bearing biomolecules, is expected to overcome this limited protein adsorption<sup>107,110</sup>.

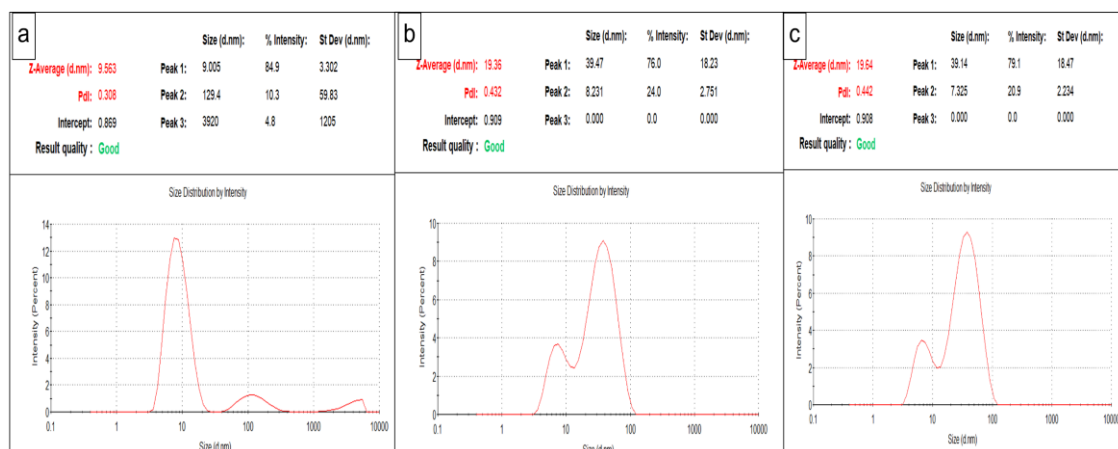


Figure 4.12: DLS reports of 5.4% BSA in PBS at pH 7.4 (a), Sf-LNC in 5.4% BSA in PBS at pH 7.4 (b), and Gal-Sf-LNC in 5.4% BSA in PBS at pH 7.4 (c) after incubation for 72 h at 37° C.

#### 4.3.8. *In-vitro* drug release study

An *in-vitro* drug release study was conducted to investigate the impact of encapsulation of Sf into LNC on sustaining the drug release throughout blood circulation. As depicted in Figure 4.13, Sf-solution exhibited rapid drug release that reached 100% after almost 20 h confirming the dialysability of Sf. In comparison, both Sf-LNC and Gal-Sf-LNC showed a sustained release that reached  $6.5 \pm 0.3\%$  and  $5.3 \pm 1.7\%$  after 120 h, respectively. Furthermore, the mean dissolution time (MDT) of both Sf-LNC and Gal-Sf-LNC was approximately 10 times higher than that of the Sf solution indicating a strong sustained drug release effect of LNC (Table 4.5). For further comparison between release profiles, the difference ( $f_1$ ) and Similarity ( $f_2$ ) factors of release profiles were calculated. From Table 4.6, according to FDA regulatory guidelines for comparing drug release profiles<sup>341–343</sup>, Sf release profiles from both Sf-LNC and Gal-Sf-LNC demonstrated high similarity ( $f_1 < 15$  and  $f_2 > 50$ ). In contrast, the Sf release profile from the Sf solution was statistically different ( $f_1 > 15$  and  $f_2 < 50$ ) from both profiles from Sf-LNC and Gal-Sf-LNC. Conclusively, the encapsulation of Sf into LNC exhibited a strong sustained release effect which, in turn, prolongs the drug effect and retains Sf into LNC for enough time to allow passive and active accumulation of Sf-loaded LNC in liver cancer tissues.

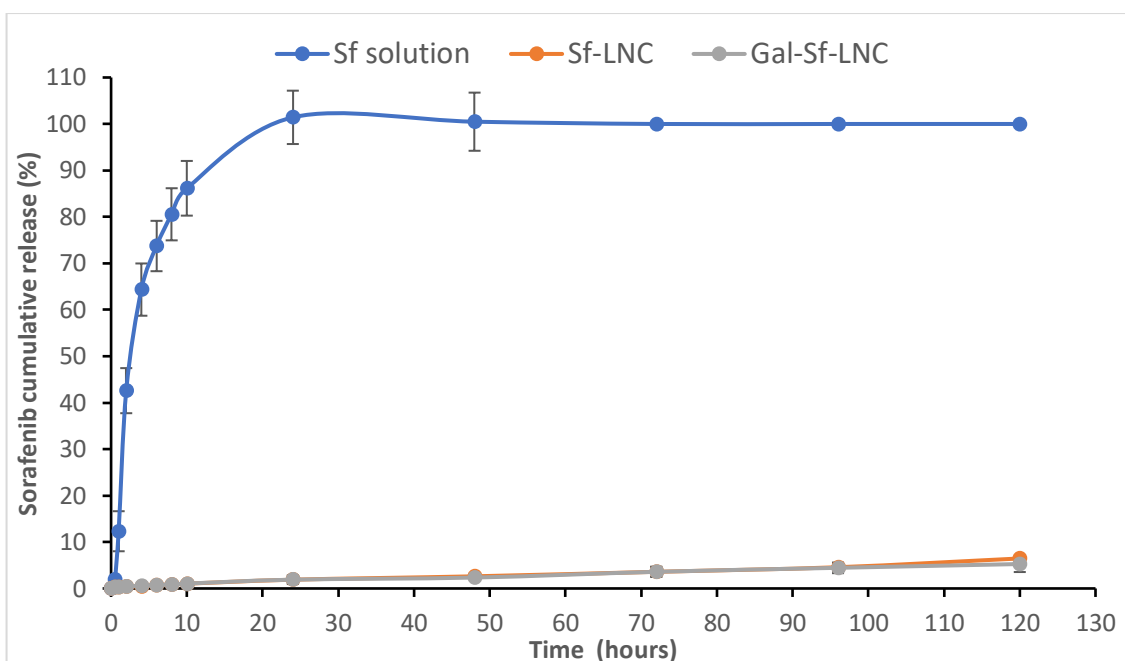


Figure 4.13: *In-vitro* Sf release profiles from Sf solution, Sf-LNC and Gal-Sf-LNC into PBS at pH 7.4 containing 1% tween 80 under shaking at 100 rpm for 5 days.

Table 4.5: Mean dissolution time (MDT) of Sf solution, Sf-LNC, and Gal-Sf-LNC.

Formulation	MDT (h)
Sf solution	4.6 ± 3.5
Sf-LNC	41.1 ± 3.8
Gal-Sf-LNC	41 ± 2.9

Table 4.6: Difference ( $f_1$ ) and similarity factors ( $f_2$ ) of Sf release profiles from Sf solution, Sf-LNC and Gal-Sf-LNC.

Comparison parameter	Formulation		
	Sf solution	Sf-LNC	Gal-Sf-LNC
Difference factor ( $f_1$ )	97.3		
		7.7	
	97.5		97.5
Similarity factor ( $f_2$ )	6.5		
		98.8	
	6.4		6.4

### 4.3.9. *In-vitro* cellular studies

#### 4.3.9.1. Cellular cytotoxicity

The proliferation inhibition potency of galactosylated and non-galactosylated Sf-LNC was verified on HepG2 cells compared to free Sf solution after cell treatment for 48 h. As depicted in Figure 4.14, all tested Sf formulations showed concentration-dependent cytotoxicity. However, Sf-solution exhibited higher cytotoxicity on HepG2 cells, more profound at low concentrations, compared to Sf-loaded LNC. This difference could be attributed to the moderate release rate of Sf from LNC after being taken up by the cells, thus reducing toxicity<sup>448</sup>. On the other hand, Gal-Sf-LNC showed higher cytotoxicity than all other tested samples at high concentrations (> 5  $\mu\text{g/mL}$ ). This could be attributed to the galactosylation of LNC, which is expected to enhance cellular uptake via receptor-mediated endocytosis. Additionally, it was remarkable that the cytotoxicity of Gal-Sf-LNC was lowered in the presence of free galactose, suggesting that free galactose competitively inhibited cellular uptake of Gal-Sf-LNC, reducing its cytotoxic effect on the cells.

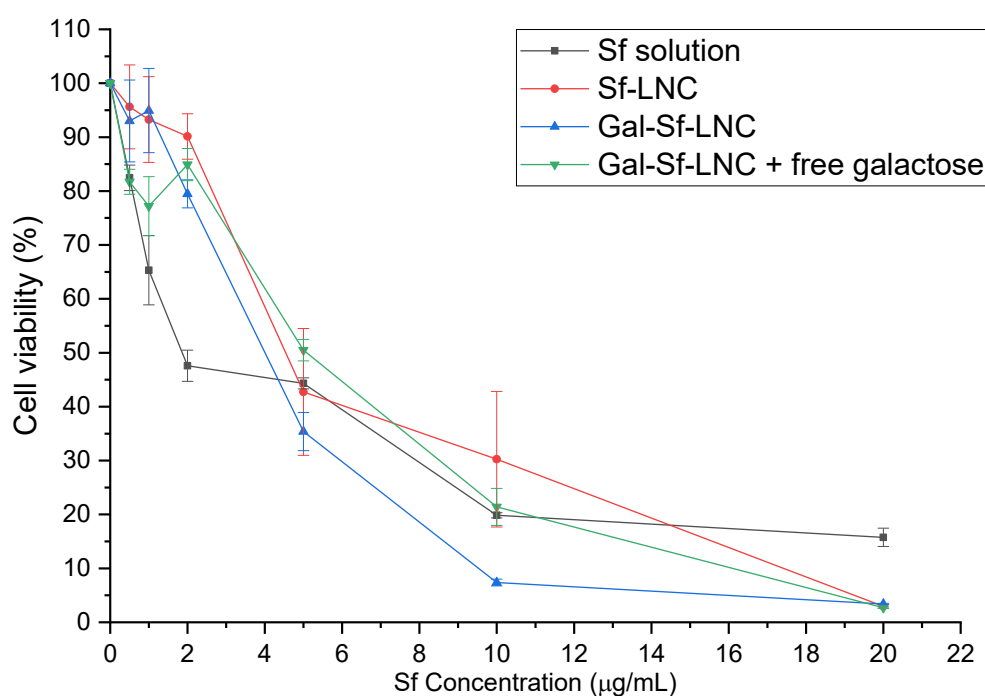


Figure 4.14: Cell viability plot of HepG2 cells after incubation for 48 h at 37° C with free Sf solution, Sf-LNC, Gal-Sf-LNC and Gal-Sf-LNC in the presence of free galactose (10 mg/mL).

By calculating IC<sub>50</sub> (Table 4.7), the Sf solution had IC<sub>50</sub> of 2.38 ± 0.33 µg/mL, which agrees with the previously reported data for the same incubation time in HepG2 cells<sup>449</sup>. Moreover, Gal-Sf-LNC showed IC<sub>50</sub> of 3.71 ± 0.24 µg/mL, which is significantly (p < 0.05) lower than that of unmodified Sf-LNC (4.99 ± 0.65 µg/mL), asserting the role of galactosylation in enhancing the cellular cytotoxicity of LNC. On the other hand, the presence of free galactose with Gal-Sf-LNC increased its IC<sub>50</sub> to 4.4 ± 0.71 µg/mL. However, this increase was not statistically significant (p > 0.05) due to the limitations in the precision of cytotoxicity studies<sup>450,451</sup>. It is noteworthy that the cytotoxicity studies were primarily applied to free solutions of the tested compounds. Hence, the use of drug-loaded nanoparticles makes the assay more complicated as it is expected to deal with different drug states (free-released drug, surface adsorbed drug and drug released upon nanoparticles uptake and digestion by the cells).

Table 4.7: IC<sub>50</sub> values of Sf solution, Sf-LNC, Gal-Sf-LNC, and Gal-Sf-LNC in the presence of free galactose on HepG2 cells after incubation for 48 h.

	Sf solution	Sf-LNC	Gal-Sf-LNC	Gal-Sf-LNC + free galactose
IC <sub>50</sub> (µg/mL)	2.38 ± 0.33	4.99 ± 0.65	3.71 ± 0.24	4.4 ± 0.71

Furthermore, the impact of the replacement of Labrafac® WL 1349 oil with lipiodol oil on the cellular cytotoxicity of LNC was investigated. From Figure 4.15, lipiodol oil LNC showed a comparable cytotoxicity profile to that of standard Labrafac® WL 1349 oil LNC suggesting the aptness of lipiodol oil for incorporation into LNC. Remarkably, both blank LNC (containing Labrafac® WL 1349 or lipiodol oil) showed some cytotoxicity on HepG2 cells at high concentrations of LNC. The same observation was reported with different cell lines such as HepG2<sup>452</sup>, HaCat<sup>206</sup>, MCF-7<sup>453</sup>, MDA-MB-231<sup>453</sup>, MDA-MB-468<sup>453</sup>, and Rat 9L glioma cells<sup>222</sup>. Maupas, C. et al. studied the impact of using different non-ionic hydrophilic surfactants on the cytotoxicity of LNC on HaCat cells<sup>206</sup>. In the study, Solutol as the ‘standard’ hydrophilic surfactant was replaced with different non-ionic surfactants (namely, Cremphor EL, Simulsol 4000, TPGS, Tween 20, and Tween80). Using different surfactants resulted in slight changes in LNC particle sizes

(~50 nm) but did not change the feasibility domain for LNC formation. The cytotoxicity of LNC on HaCat cells was “highly” surfactant dependent (TPGS > Solutol HS > Tween 20 > Tween 80 > Cremphor EL > Simulsol 4000). In contrast, the cytotoxicity of LNC was found to be slightly higher than that of the corresponding pure surfactants<sup>206</sup>.

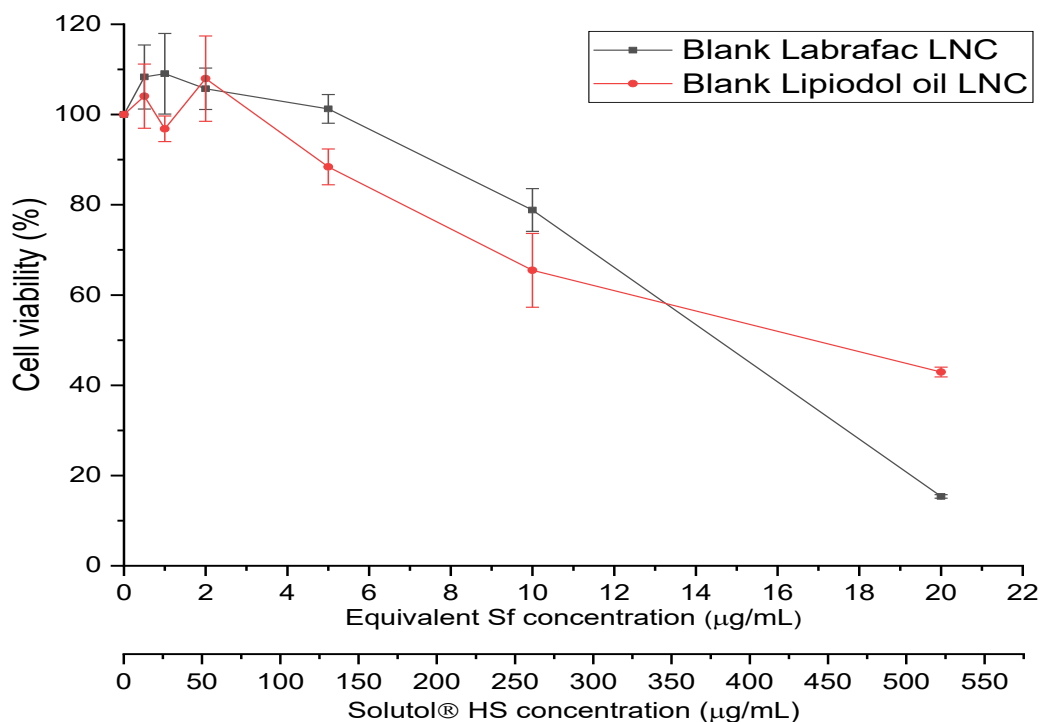


Figure 4.15: Cytotoxicity profiles of blank Labrafac® WL 1349 LNC (standard LNC) and lipiodol oil LNC (the blank LNC were diluted in the same manner as Sf-loaded LNC).

#### 4.3.9.2. Cellular uptake assessment by fluorescence microscope

Fluorescence microscopy is routinely used to study the cellular uptake of several nanodelivery systems. In this experiment, the formulated LNC were loaded with C6 as a fluorescent probe and incubated with HepG2 cells for 4 h before being washed and counterstained by DAPI for nuclei staining. After inspection under an inverted fluorescence microscope, galactosylated LNC (C6-Gal-LNC) exhibited a profound increase in the fluorescence intensity compared to non-galactosylated LNC (C6-LNC), suggesting the involvement of lectin receptor-mediated active cellular uptake due to the presence of galactose moieties on LNC’s surface (Figure 4.16).

On the other hand, incubation of free galactose with C6-Gal-LNC resulted in preferential binding of galactose to lectin receptors, saturating them and preventing galactosylated LNC from entering the cell through lectin receptor-mediated endocytosis. Consequently, reduced cellular uptake following the addition of galactose and, in the case of non-galactosylated LNC (C6-LNC), asserted that lectin receptor-mediated endocytosis of galactosylated LNC facilitates enhanced uptake and cytotoxic activity. This observation comes in accordance with the previously reported data with galactosylated liposomes for selective liver delivery of a norcantharimide derivative, where galactosylated liposomes exhibited time-dependent enhanced cellular uptake compared to unmodified liposomes<sup>454</sup>.

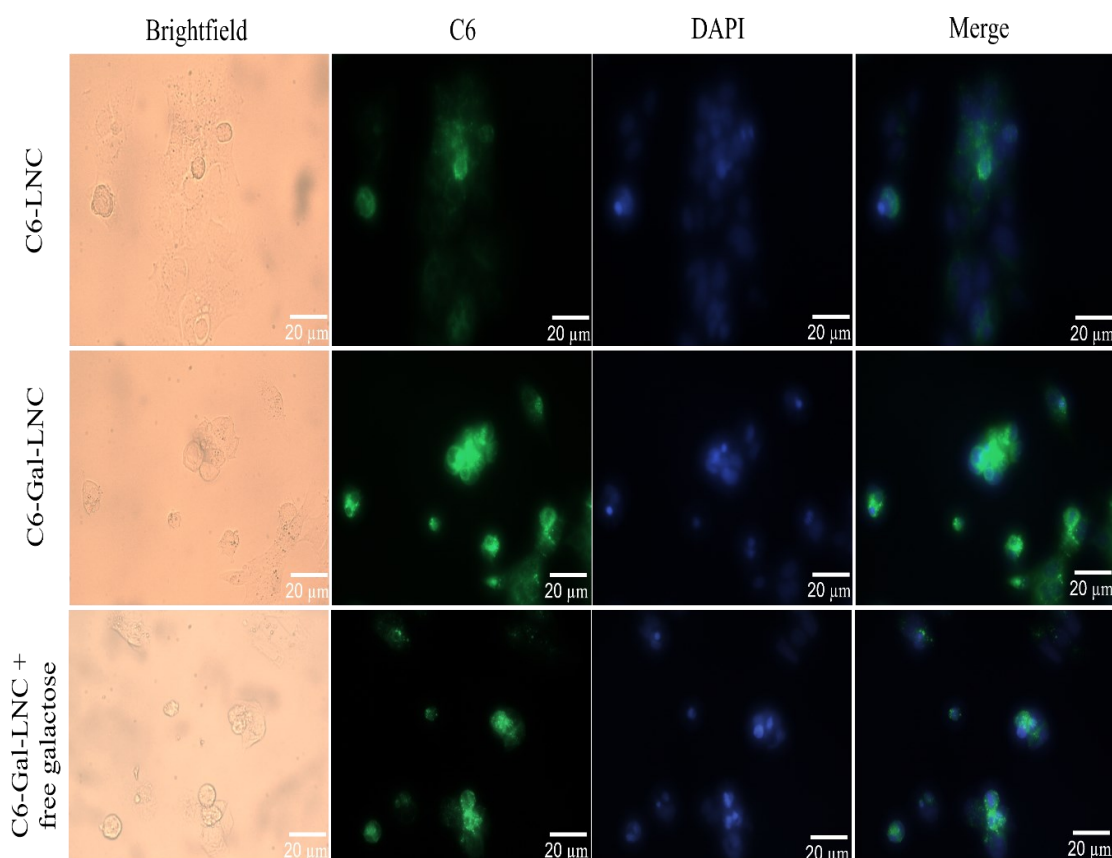


Figure 4.16: Fluorescence microscope images using 40X objective lens of HepG2 cells after incubation for 4 h with different C6-loaded LNC at 37° C.

### 4.3.9.3. Cellular uptake study using a flow cytometer

A flow cytometer has been employed to quantify the fluorescence intensity for a quantitative comparison of HepG2 cellular uptake of different LNC formulations. The proper cell population was first gated based on FSC and SSC, as previously described in Chapter 2 (section 2.3.6.2.). Figure 4.17a shows the overlaid histogram of green fluorescence from HepG 2 cells after incubation for 4 h with different treatments. C6-Gal-LNC showed a marginal but statistically significant ( $p < 0.05$ ) increase in the fluorescence intensity (expressed as GeoMean of fluorescence intensity Figure 4.17b) compared to non-conjugated C6-LNC meanwhile, the fluorescence intensity of C6-Gal-LNC in the presence of free galactose was not significantly ( $p > 0.05$ ) different from non-galactosylated C6-LNC. These findings agree with the previous observation from the fluorescence microscope suggesting the pivotal role of galactose surface grafting in the enhancement of HepG2 cellular uptake through lectin receptor-mediated endocytosis.

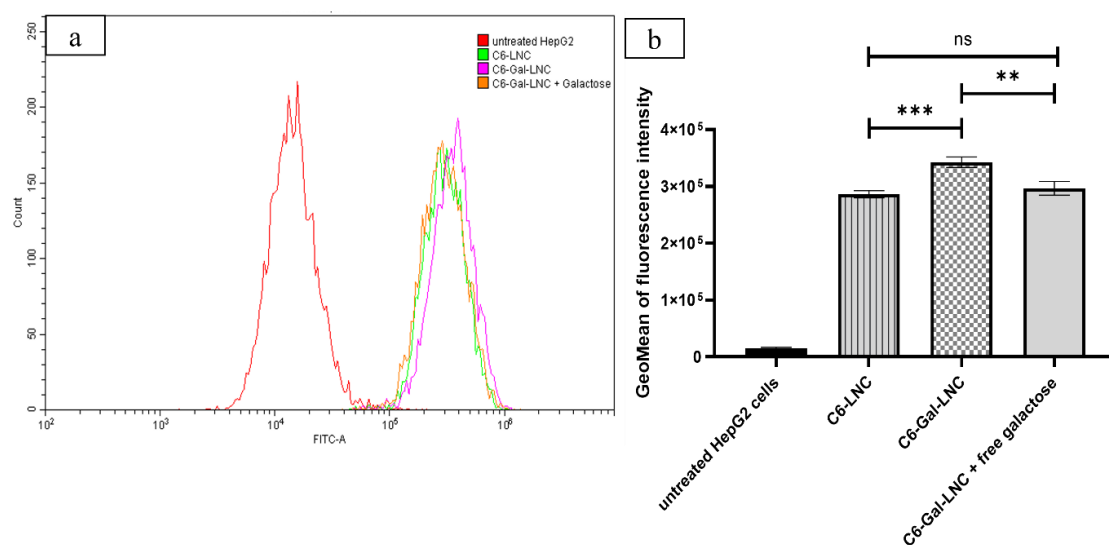


Figure 4.17: Histogram overlay (a) and GeoMean fluorescence intensities (b) of HepG2 cells after incubation for 4 h at 37°C with different LNC formulations containing C6 at a concentration of 0.2 µg/mL. \*\* ( $P < 0.01$ ), \*\*\* ( $P < 0.001$ ), and ns ( $P \geq 0.05$ ). Error bars represent the standard deviation and  $n=3$ .

#### **4.4. Conclusion**

In summary, Galactosylated Sf-loaded LNC using lipiodol oil as an oil core were successfully developed in this study via the phase inversion temperature method followed by the post-insertion of Gal-TPGS into the preformed Sf-LNC. Sf was efficiently loaded into LNC with an EE% higher than 95%. Labrafac® WL 1349 replacement with lipiodol oil resulted in a slight decrease in particle size with no significant impact on PDI, ZP or drug EE%. Additionally, Solutol HS content has shown to be inversely proportional with LNC particle size but directly proportional with Sf drug loading.

Galactosylation of TPGS was carried out satisfactorily and validated by FTIR, H-NMR, and MALDI-TOF. The galactosylation of LNC was done using post-insertion. Sf-LNC and Gal-Sf-LNC revealed good physical stability upon storage over one month. Moreover, they showed a minimal increase in particle size upon incubation under physiological blood conditions (5.4% BSA at pH 7.4) due to albumin adsorption. Both Sf-LNC demonstrated very sustained release profiles of Sf compared to free Sf solution. This allows more time for LNC to circulate and preferentially accumulate in tumour tissues due to the leaky vasculature. Although the surface exposure of galactose was limited when assessed by the lectin-induced agglutination test, Gal-Sf-LNC showed enhanced cytotoxicity and cellular uptake compared to unmodified Sf-LNC. Moreover, the galactose-mediated cellular uptake was further confirmed by the competitive inhibition study using free galactose.

Based on these findings, the study provides a better understanding of the impact of different formulation parameters on the physical properties of LNC. Moreover, it offers a novel galactosylated LNC platform that can efficiently deliver both Sf and Lipiodol oil to liver cancer cells acting as a theranostic agent.



## **Chapter 5**

***Soluplus® and Soluplus®/TPGS mixed micelles for oral administration  
of Sorafenib***

## 5.1. Introduction

Polymeric micelles are a type of nanoparticles that has been extensively researched for their potential use in drug delivery. These micelles are composed of a hydrophobic core surrounded by a shell of hydrophilic polymeric material. The hydrophobic core allows the micelles to encapsulate hydrophobic drugs, while the hydrophilic shell allows them to remain stable in aqueous solutions and target specific cells or tissues. Polymeric micelles as drug delivery systems have a plethora of advantages, such as enhancing drug solubility, stability, and dissolution rate, promoting intestinal drug permeation and oral bioavailability<sup>244–248,261,455</sup>. Moreover, the surface of the micelles can be functionalised with specific ligands, allowing them to target specific cells, tissues or cellular transport mechanisms<sup>456</sup>.

However, some challenges face using polymeric micelles for drug delivery, such as achieving the appropriate size and stability while maintaining the desired level of drug release. Moreover, selecting the suitable polymer and the proper preparation method is crucial for successful drug delivery<sup>457</sup>. To overcome these drawbacks, the mixed micelles approach using polymeric micelles composed of two or more different polymers has been adopted<sup>261</sup>.

The use of mixed polymeric micelles can provide several advantages over single-component polymeric micelles, such as improved stability due to the presence of multiple types of interactions between the different polymers, enhanced drug loading, tailored drug release by adjusting the properties of the different polymers, such as their hydrophobicity, hydrophilicity, and degradation rate. Mixed polymeric micelles have been used in preclinical and clinical studies to deliver anticancer drugs, gene therapy, and other drugs, showing promising results in terms of stability, drug loading and selectivity of delivery<sup>272</sup>.

Soluplus® is an amphiphilic copolymer commonly used as a solubiliser in pharmaceutical formulations. It has been widely used to enhance drug solubility, stability, and bioavailability<sup>258,260,291</sup>. It can form polymeric micelles in aqueous solutions through self-assembly. It has been used to prepare polymeric micelles to deliver hydrophobic drugs, such as anticancer drugs and imaging agents<sup>259,260,290</sup>.

TPGS (d- $\alpha$ -tocopheryl polyethylene glycol succinate) is a type of amphiphilic copolymer that is commonly used as a solubiliser and surfactant in pharmaceutical formulations<sup>292,293</sup>. It was also used as a component in polymeric micelles for drug delivery. Incorporating TPGS into the micelle can improve the micelle's stability and drug-loading capacity of the micelle<sup>265,458</sup>.

In our study, Soluplus® and TPGS were employed as single (SM) and mixed (MM) micelles to encapsulate Sf and assess its impact on solubility, stability, dissolution rate and intestinal permeation.

The objectives of this chapter are:

- To develop and optimise single Soluplus® micelles and mixed Soluplus®/TPGS micelles for the enhancement of Sf solubility and dissolution rate.
- To characterise the physicochemical properties of the Sf-loaded single and mixed micelles.
- To examine the colloidal stability of both single and mixed micelles under short-term storage conditions and gastrointestinal physiological conditions.
- To study the impact of using single and mixed micelles on Sf solubility and release kinetics under gastrointestinal physiological conditions.
- To evaluate the *in-vitro* cellular transport study of single and mixed micelles using Caco-2 cell line.

## **5.2. Materials and methods**

### **5.2.1. Materials**

Soluplus® (polyvinyl caprolactam–polyvinyl acetate–polyethylene glycol graft copolymer) was obtained from BASF (Redditch, UK). D- $\alpha$ Tocopherol polyethylene glycol 1000 succinate (TPGS, Mwt ~1513 g/mol), Sorafenib was obtained from LC Labs (USA). Phosphate buffer saline tablets (PBS), dimethyl sulfoxide (DMSO), ethylenediamine (EDA), trypsin-EDTA solution, Dulbecco's modified eagle medium (DMEM Medium), fetal bovine serum (FBS), phosphate buffer saline (PBS), Hanks' Balanced Salt Solution (HBSS), 1% non-essential amino acids (NEAA), 1% penicillin–streptomycin solution, Tween-80, and phosphotungstic acid (PTA) were purchased from (Sigma-Aldrich, UK). Tetrazolium compound [3- (4,5-dimethylthiazol-2-yl)-5-(3-carboxymethoxyphenyl)-2-(4-sulfo- phenyl)-2H-tetrazolium], inner salt (MTS) was purchased from Promega Ltd (UK). All solvents: acetone, HPLC grade methanol and acetonitrile were purchased from Sigma-Aldrich (UK).

### **5.2.2. Preparation of sorafenib loaded Soluplus® micelles (Sf-SM) and Soluplus®/TPGS mixed micelles (MM)**

The preparation of sorafenib-loaded Soluplus® single micelles (Sf-SM) and Soluplus®/TPGS mixed micelles (Sf-MM) was carried out by a simple solvent evaporation method. Briefly, mixtures of Soluplus® and TPGS at different ratios (50:0, 45:5, 40:10, 30:20, and 0:50 w/w) and 10 mg of Sf were co-dissolved in 1 mL of acetone to form the organic phase. The organic phase was then dripped into 4 mL of Milli-Q water at a rate of 1 mL/min under stirring at 300 rpm and left till complete evaporation of acetone for 6 h. The resultant micellar dispersions were then filtered using a 1  $\mu$ m syringe filter (glass filter, Kinesis scientific, UK) to remove any untrapped drug and topped up to 5 mL with Milli-Q water so that the total polymeric concentration in dispersion is 1%.

### 5.2.3. Characterisation and optimisation of Sf-SM and Sf-MM

The particle size, size distribution (PDI), and zeta-potential (Z.P.) of Sf-SM and Sf-MM were measured using dynamic light scattering (DLS) via Zetasizer Nano (Malvern Instruments Ltd., Malvern, UK) following the procedures detailed in Chapter 2 (section 2.3.2.1.).

### 5.2.4. Drug loading (DL%) and encapsulation efficiency (EE%)

Drug loading (DL%) and encapsulation efficiency (EE%) were evaluated through a direct assay method. Briefly, 50  $\mu\text{L}$  of the formulations were diluted 20 times in acetonitrile to dissolve the ingredients and analyse Sf content using a high-performance liquid chromatography (HPLC) system, as mentioned in Chapter 3 (section 3.2.4.). The EE% and DL% were calculated using equations (3.1) and (3.2), respectively, as mentioned in Chapter 3 (section 3.2.9.). Solubility factors ( $f_s$ ) were also determined to assess the solubilisation capacities of different micellar dispersions. Solubility factors ( $f_s$ ) were calculated according to the following equation:

$$f_s = \frac{S_a}{S_w} \quad \text{Eq. (5.1)}$$

Where  $S_a$  is the apparent solubility of Sf in each micellar system, and  $S_w$  is the intrinsic solubility of the drug in MilliQ water (1.7  $\mu\text{g}/\text{mL}$ )<sup>459</sup>.

### 5.2.5. Critical micelles concentration determination

The CMCs of Blank SM and MMs were determined by the iodine ultraviolet-visible (UV-Vis) spectroscopy method, as previously reported<sup>326</sup>. Firstly, 0.2 g of potassium iodide (KI) and 0.1 g of iodine ( $\text{I}_2$ ) were dissolved in 10 mL Milli-Q water to prepare KI/ $\text{I}_2$  standard solution. Afterwards, 10  $\mu\text{L}$  of KI/ $\text{I}_2$  standard solution was added to different micellar formulations with polymer concentrations varying from 0.24 to 1000  $\mu\text{g}/\text{mL}$ . The mixtures were incubated at room temperature ( $\sim 25^\circ\text{C}$ ) in a dark place for 12 h. The UV absorbance value was measured by a microplate reader (CLARIOstar, BMG LABTECH, UK) at wavelength 366 nm. All measurements were performed in triplicate.

The CMC value was assigned by the concentration of the polymers where there was a dramatic increase in the UV absorbance. The obtained experimental values were further compared to the theoretically calculated ones using the following equation<sup>460</sup>:

$$\frac{1}{CMC} = \frac{X_{Soluplus}}{CMC_{Soluplus}} + \frac{X_{TPGS}}{CMC_{TPGS}} \quad \text{Eq. (5.2)}$$

where  $X_{Soluplus}$  and  $X_{TPGS}$  are the molar fractions of Soluplus® and TPGS are calculated by the ratio between the number of moles of the component to the total number of moles of both polymers in the mixture. Whereas  $CMC_{Soluplus}$  and  $CMC_{TPGS}$  are the CMC values of Soluplus® and TPGS (CMC of Soluplus® and TPGS single micelles, respectively).

#### **5.2.6. Morphology of micelles using transmission electron microscopy (TEM)**

TEM was used to examine the morphology of the produced micelles following the procedures mentioned in Chapter 2 (section 2.3.3.1.).

#### **5.2.7. Short-term storage physical stability**

To investigate the physical and drug-loading stability of Sf-MM and Gal-Sf-MM, the samples were transferred into glass vials sealed with plastic caps and stored at 4° C for 14 days. At the predetermined times (0, 3, 7, and 14 days), the particle size, size distribution (PDI), zeta potential, and EE% were assessed using DLS and HPLC<sup>461</sup>.

#### **5.2.8. Solid state characterisation**

For solid-state characterisation, all optimised micellar dispersions were frozen with liquid nitrogen and then placed into freeze-dryer (VirTis® Wizard 2.0, SP SCIENTIFIC, USA) under a vacuum for 24 h. The lyophilised samples were placed in a silica gel desiccator at room temperature (~ 25°C) until the analysis.

### **5.2.8.1. Attenuated total reflection-Fourier transform infrared (ATR-FTIR)**

The Attenuated total reflection-Fourier transform infrared (ATR-FTIR) spectra of raw materials, physical mixtures, and blank and Sf-loaded micelles were obtained using FTIR spectrophotometer as mentioned in Chapter 2 (section 2.3.2.6.).

### **5.2.8.2. Differential scanning calorimetry (DSC)**

DSC was used to investigate the effect of formulation and sorafenib encapsulation on the thermal behaviour of the components. DSC was done for raw materials, physical mixtures, freeze-dried blank and Sf-loaded micelles. Samples were tested over a temperature range from 25 to 230 °C at a heating rate of 10 °C/min. All other conditions followed the described procedures in Chapter 2 (section 2.3.2.3.)

### **5.2.8.3. Powder X-Ray Diffraction (PXRD)**

The X-ray powder diffraction patterns of raw materials, physical mixtures, and blank and Sf-loaded micelles were acquired as detailed in Chapter 2 (section 2.3.2.5.) to examine the effect of nanoformulation on their crystallinity.

### **5.2.9. Physical stability in simulated gastric fluid (SGF) and simulated intestinal fluid (SIF)**

The colloidal stability of Sf-SM and Sf-MM was assessed after 10 times dilution with simulated gastric fluid (pH at 1.2) and simulated intestinal fluid (pH at 6.8) without enzymes. SGF and SIF were made according to United States Pharmacopeia USP, 2002. For the gastric fluid, 2 g of NaCl and 7 mL of HCl were dissolved in 1 litre of MilliQ water. The intestinal fluid comprised of 6.805 g of  $\text{KH}_2\text{PO}_4$  and 0.896 g of NaOH per litre of deionised water. Micellar dispersions were incubated at 37 °C for 2 h in the gastric fluid (SGF) and 24 h in the intestinal fluid (SIF). The samples were then analysed before and after incubation looking for any alternation in particle size. The experiments were carried out in triplicate<sup>331,460</sup>.

### **5.2.10. *In-vitro* drug release study**

The *in-vitro* dissolution behaviour of Sf-SM and Sf-MM was studied using the dialysis membrane method<sup>460</sup>. One millilitre of the sample (Sf suspension, Sf-SM and Sf-MM) with Sf concentration of 1 mg/mL was added into the dialysis membrane bags with a molecular mass cut-off of 10 KDa (SnakeSkin™ Dialysis tubing, UK). The bags were placed into 200 mL of release medium at 37 °C under stirring at 100 rpm using a shaking incubator (IKA®-Werke GmbH & Co. KG, Germany). Two sets of experiments were carried out; one used SGF as a release medium, and the release study was conducted for 2 h. The other set used SIF as a release medium for 72 h. both media contained 1% Tween to ensure sink conditions. At predetermined intervals, 0.5 mL of each release medium was withdrawn and replaced with an equal volume of fresh medium. The Sf concentration in the samples was assayed by the HPLC analysis method. The experiments were carried out in triplicate. Release profiles of different samples were expressed in terms of the percentage of Sf released plotted against time ( $n = 3$ )<sup>460</sup>. Moreover, the release profiles in SIF were compared by fitting them into different release kinetic models, and the dissolution efficiency (DE) parameter was calculated as mentioned in Chapter 2 (section 2.3.4.).

### **5.2.11. *In-vitro* cellular studies on Caco-2**

As an early stage of investigation of biocompatibility and intestinal permeation of micellar systems, both cellular viability and cellular transport studies were carried out on Caco-2 cells (mimicking the lining epithelial cells of the small intestine).

#### **5.2.11.1. Cell viability studies**

To assess the cellular cytotoxicity of micellar systems on intestinal cells, Caco-2 cells from (Sigma-Aldrich, UK) with passage numbers from 8 to 12, were cultivated in DMEM at 37 °C in a 5% CO<sub>2</sub> atmosphere and at a relative humidity of 95%, supplemented with 1% non-essential amino acids (NEAA), 1% L-glutamine, 100 U/mL penicillin and 100 mg/mL streptomycin. Then 100 µL of cell suspension were seeded in 96-well plates at  $5 \times 10^5$  cells/well density. After 24h, the medium was discarded, and the cells were incubated with Blank SM and MM at various total polymer concentrations ranging from

(2000 to 25 µg/mL). After different incubation times (6 h, 24 h and 48 h), the medium was removed and replaced with fresh medium containing 10 µL of MTS Reagent (CellTiter 96® AQueous Solution, Promega UK Ltd) and incubated for 3 h. Afterwards, the absorbance was measured at 490 nm using a CLARIOstar OPTIMA plate reader (BMG LABTECH, UK). Each treatment was performed in triplicate, and readings were taken as averages of three measurements per well<sup>266,462</sup>. The inhibition of the cell growth was calculated by Eq. (3.4) mentioned in Chapter 3 (section 3.2.13).

### 5.2.11.2. Cellular transport studies

A cellular transport study was carried out to investigate the impact of micelles on the intestinal permeation of Sf. For that, Caco-2 cells (with a high passage number of 68) were seeded in a 12-well Millicell® Trans-well insert (Merck Millipore Ltd, Ireland) with 0.4 µm PCF, 12 mm diameter at a density of 10<sup>5</sup> cell/well and incubated at 37° C, 95% relative humidity, 5% CO<sub>2</sub>. The culture medium was replaced every other day, and cells were allowed to differentiate before experiments. After 21 days post-seeding, the cells were well differentiated with TEER values greater than 600 Ω/cm<sup>2</sup> using EVOM (World Precision Instruments, UK).

Before the transport assays, the differentiated cell monolayers were washed three times with blank HBSS (pH 7.4, 37°C) and then incubated in HBSS at 37° C for 30 min. Then, pure sorafenib, Sf-SM, and Sf-MM (at Sf concentration 50 µg/mL) dispersed in HBSS were added to the apical (AP) (0.4 mL) or basolateral (BL) (1.2 mL) side, respectively. 4% BSA was dissolved in HBSS and used as receiving medium to ensure the sink condition. At predetermined intervals 1, 2, 3, and 4 h, the whole receiving medium was withdrawn and replaced with a fresh prewarmed medium. The transport study was conducted under shaking at 100 rpm (IKA i300 shaking incubator). Sf in the samples was measured by the HPLC method mentioned earlier after extraction of Sf (using acetonitrile in the ratio of 1:2 sample to acetonitrile). All the experiments were done in triplicate. The permeability of Sf was calculated using Eq. (5.3):

$$P_{app} = \frac{V}{S \times C} \times \frac{dC}{dt} \quad \text{Eq. (5.3)}$$

Where V is the volume of the receiver (1.2 mL or 0.4 mL for influx and efflux, respectively), S is the surface area of the cell monolayer (1.12 cm<sup>2</sup>), C is the initial concentration (50 µg/mL), dC/dt is the rate of concentration change in the receiver side (slope of the linear region of the curve of cumulative Sf concentration in the receiving medium against time, µg.mL<sup>-1</sup>.S<sup>-1</sup>)<sup>463</sup>.

Moreover, the efflux ratio was calculated using Eq. (5.3) to assess P-gp efflux inhibition.

$$Efflux\ ratio = \frac{P_{app\ (BL-AP)}}{P_{app\ (AP-BL)}} \quad Eq. (5.4)$$

At the end of transport assays, TEER values were measured again to ensure the integrity of Caco-2 cells monolayers after exposure to tested samples.

## 5.3. Results and discussion

### 5.3.1. Preparation and characterisation of Sf-SM and Sf-MM

One of the most appealing advantages of polymeric micelles is the ease of preparation. In the literature, there are different methods for preparing polymeric micelles, such as thin film hydration, solvent evaporation, dialysis, and emulsification methods<sup>247</sup>. From these, the solvent evaporation method was chosen due to its simplicity and the relative quickness of the process<sup>247,261</sup>. Different Soluplus®: TPGS ratios have been screened to study the impact of the incorporation of TPGS in the micelles structure on the colloidal properties, such as particle size (P.S.), size distribution (PDI), zeta potential (Z.P.) and drug loading. As depicted in Table 5.1, all Soluplus® containing micelles showed P.S. around 95 nm with no particular trend, while single TPGS micelles had P.S. of 17.9 ± 3.3 nm. All tested micelles showed a monodispersed distribution (PDI <0.22)<sup>310</sup>. Moreover, the zeta potential of all micelles was negative, with an increase in the negative values with increasing Soluplus® content (Figure 5.1). The ease of assembly is attributed to the good amphiphilic properties of both materials<sup>457</sup>.

Table 5.1: Particle size analysis and drug loading of Sf-loaded micelles with different compositions

<b>Soluplus®:</b> <b>TPGS</b> <b>ratio</b> (mg: mg)	<b>P.S ± SD</b> (nm)	<b>PDI ± SD</b>	<b>Z.P. ± SD</b> (mV)	<b>EE%</b>	<b>LC%</b>
<b>50: 0</b>	99.6 ± 3.2	0.185 ± 0.028	-17.7 ± 1.2	97.5 ± 0.5	16.3 ± 0.1
<b>45: 5</b>	94.9 ± 4.9	0.111 ± 0.019	-17.7 ± 2	95.8 ± 0.6	16.1 ± 0.1
<b>40: 10</b>	91.6 ± 2.5	0.096 ± 0.025	-14 ± 1.3	94.2 ± 0.9	15.9 ± 0.1
<b>30: 20</b>	98.1 ± 4.7	0.169 ± 0.026	-13.3 ± 1.2	82.2 ± 1.2	14.1 ± 0.2
<b>0: 50</b>	17.9 ± 3.3	0.219 ± 0.051	-11.3 ± 2.6	7 ± 0.4	1.4 ± 0.1

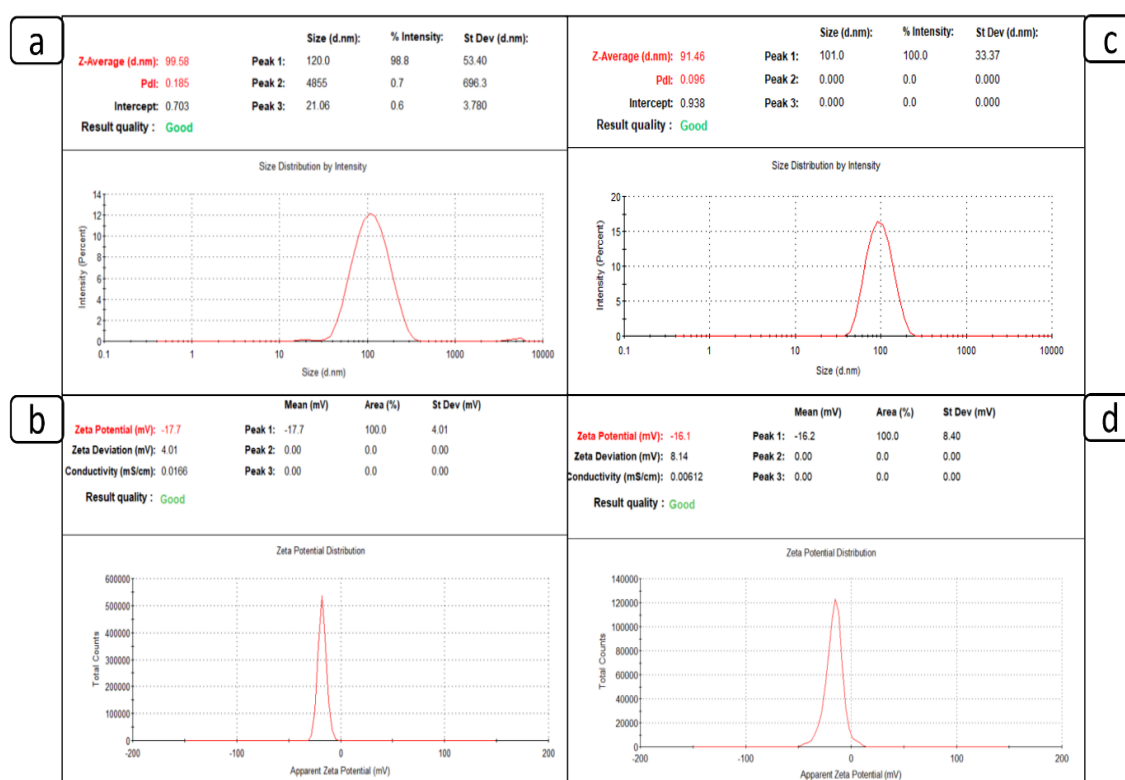


Figure 5.1: DLS reports of particle size and Zeta potential of Sf-SM (a and b), and Sf-MM (c and d)

As shown in Figure 5.2, the micelles comprised of pure Soluplus® (Sf-SM) demonstrated the highest apparent solubility  $S_a$  ( $1.9492 \pm 0.009$  mg/mL). In contrast, pure TPGS micelles exhibited the lowest  $S_a$  ( $0.139 \pm 0.0076$  mg/mL) at the same concentration. The low solubilising capacity of pure TPGS could be attributed to its small lipophilic portion

compared to Soluplus®. The copolymer's lipophilic portion constitutes the micelle's core which acts as a microenvironment for the encapsulation and accommodation of hydrophobic molecules via hydrophobic-hydrophobic interactions<sup>455</sup>. Additionally, for emphasising the solubilising effect of the micelles, solubility factor ( $f_s$ ), which correlates the apparent solubility to the intrinsic solubility of Sf in Milli-Q water, was used to compare different micelles. From Table 5.2., Soluplus® single micelles (Sf-SM) markedly improved the solubility of Sf ( $1147 \pm 5$  times) with a slight gradual decrease in  $f_s$  with decreasing Soluplus® portion till it reached the lowest value with pure TPGS micelles ( $82 \pm 4$  times).

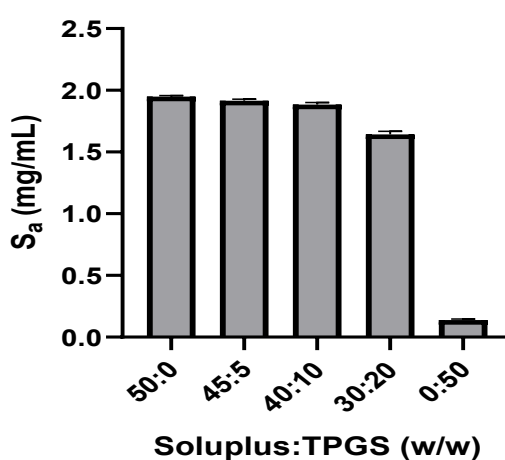


Figure 5.2: Sf apparent solubility ( $S_a$ ) in single and mixed micelles comprised of Soluplus® and/or TPGS in MilliQ water at 25°C. (n = 3)

Table 5.2: Sf apparent solubility ( $S_a$ ) and solubility factors ( $f_s$ ) for single and mixed micellar dispersions in MilliQ water at 25° C. (n = 3)

Soluplus®: TPGS (w/w)	$S_a$ (mg/mL)	$f_s$
50:0	$1.9492 \pm 0.009$	$1147 \pm 5$
45:5	$1.9156 \pm 0.0118$	$1127 \pm 6$
40:10	$1.88336 \pm 0.0184$	$1108 \pm 11$
30:20	$1.6434 \pm 0.024$	$967 \pm 14$
0:50	$0.139 \pm 0.0076$	$82 \pm 4$

### 5.3.2. Critical micelles concentration determination

The CMC is one of the most essential features for evaluating the stability of various micellar systems<sup>245</sup>. The lower CMC, the easier they are assembled, and the more stable they are. It is a vital parameter since micelles are subjected to a variety of environmental changes, including changes in pH and ionic strength, exposure to various fluids containing numerous proteins and cells, and significant dilution after oral administration or intravenous injection. As mentioned in Chapter 2 (section 2.3.2.9.), CMC could be determined using different methods from which the UV-Vis spectroscopy method was adopted (Figure 5.3). From Table 5.3, Soluplus® single micelles exhibited the lowest experimental CMC ( $65.9 \pm 9.6 \mu\text{g/mL}$ ), while CMC values gradually increased with increasing TPGS ratio. This is ascribed to the relatively high TPGS CMC value ( $447.6 \pm 13.7 \mu\text{g/mL}$ ). This observation is consistent with the previously reported data<sup>265</sup>.

Remarkably, all experimental CMC values showed a negative deviation from the theoretical values calculated by Eq. (5.2) using the CMC values of both Soluplus® (Soluplus® single micelles) and TPGS (TPGS single micelles). It was reported that the negative deviation of the experimental CMC values from the theoretically calculated ones might indicate a favourable mixing and compatibility between components in mixed micelles<sup>265,464</sup>. This implies good stability of the formed mixed micelles. It is worth mentioning that using different methods for determining CMC may result in some deviations. For instance, the CMC value was estimated for Soluplus® micelles at 25°C to be 800  $\mu\text{g/mL}$  using the isothermal titration calorimetry method (ITC)<sup>465</sup>. However, another study reported the CMC of Soluplus®/TPGS (at molar ratio 6:1) mixed micelles at 16  $\mu\text{g/mL}$ <sup>326</sup>. Besides, the mathematical fitting during the calculation may be a source of variation. Nevertheless, our CMC values suggest that the micellar system will retain its integrity upon dilution after oral administration since CMC values are less than 135  $\mu\text{g/mL}$ , as previously recommended for orally administered micelles<sup>244</sup>.

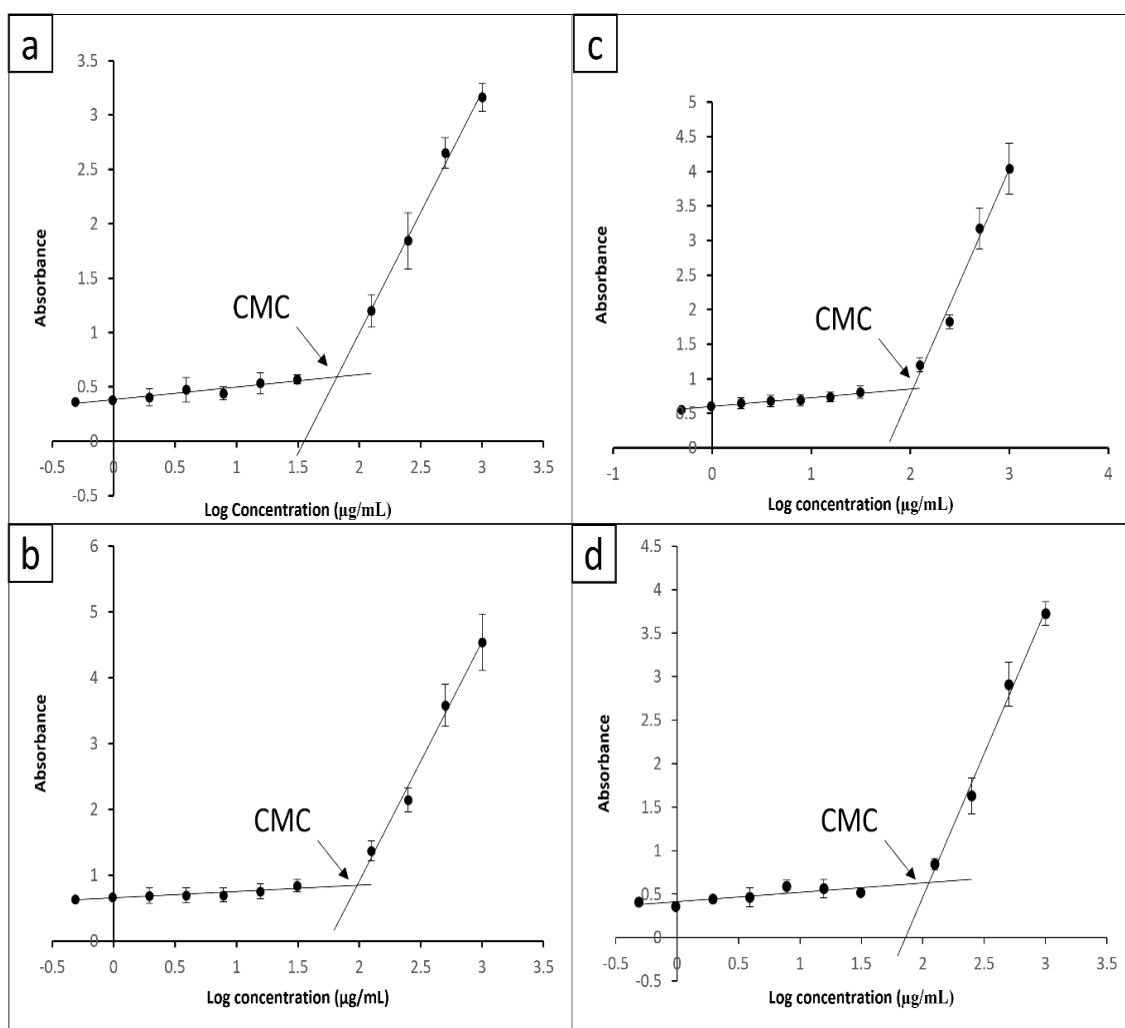


Figure 5.3: The measurement of CMC of Soluplus® single micelles (a) and Soluplus®/TPGS mixed micelles at different ratios 45:5 (b), 40:10 (c), and 30:20 (d) using the iodine UV-Vis spectroscopy method.

Table 5.3: Theoretical and Experimental critical micellar concentration of micelles with different Soluplus®: TPGS ratios.

Soluplus:TPGS (mg/mg)	Theoretical CMC values (µg/mL)	Experimental CMC values (µg/mL)
50: 0	--	65.9 ± 9.6
45: 5	279.9	95.7 ± 3.4
40: 10	349	106.9 ± 2.9
30: 20	403.5	112.4 ± 6.7
0: 50	--	447.6 ± 13.7

Based on the previous data, two micellar formulations were selected with Soluplus® only, and a Soluplus®/TPGS ratio of 40:10 were chosen to represent Soluplus single micelles (SM) and Soluplus®/TPGS mixed micelles (MM), respectively. Although, the incorporation of TPGS in the micelles resulted in a decrease in drug loading and increase in CMC, the MM formulation was kept to study the effect of TPGS incorporation on drug release and cellular transport. Further investigations were carried out to study the differences and the significance of using single and mixed micelles on Sf dissolution and permeation rates.

### 5.3.3. Morphology of micelles using transmission electron microscopy (TEM)

TEM was carried out to confirm the size and shape of Sf-SM and Sf-MM. As shown in Figure 5.4, both Sf-SM and Sf-MM presented an almost spherical shape with particle size ranges around 90 nm, which agrees with the size measurements from DLS (Table 5.1).

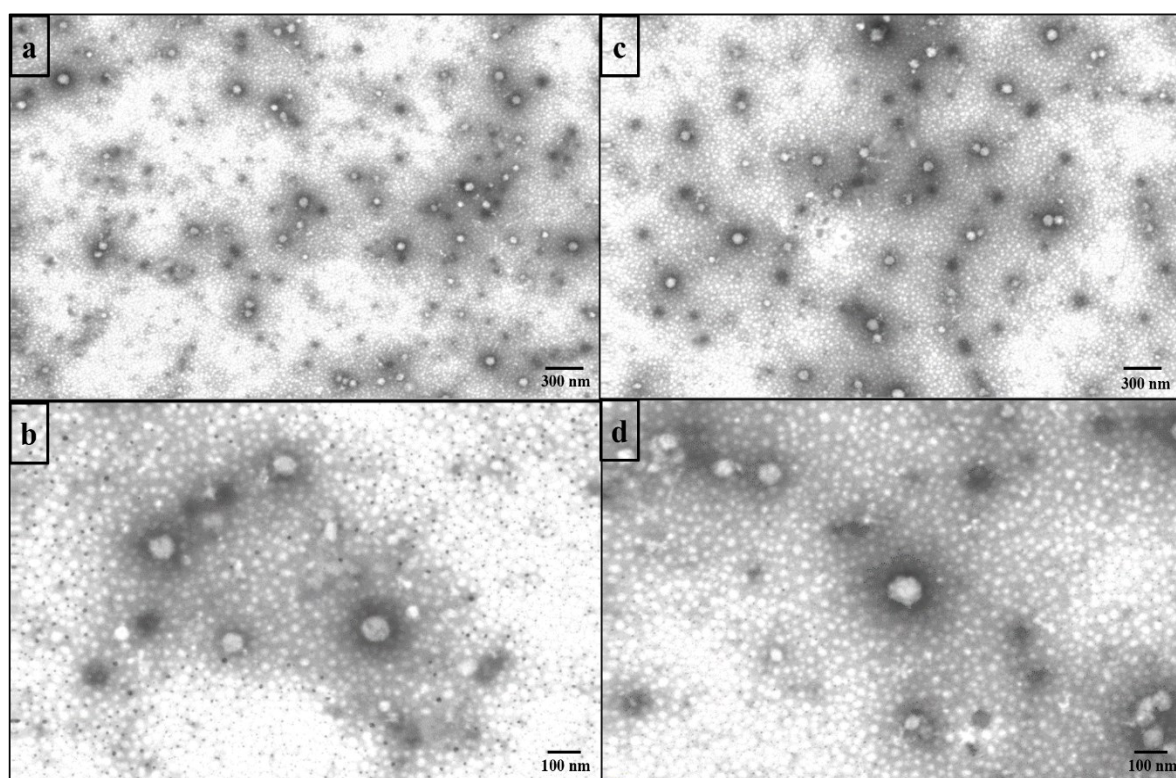


Figure 5.4: TEM images of Sf-SM (a and b) and Sf-MM (c and d) at different scales

### 5.3.4. Short-term physical stability of Sf-SM and Sf-MM

The physical short-term storage stability of micellar systems was monitored for 14 days at refrigerated conditions (4°C) to ensure the integrity and stability of the drug payload of the systems during optimisation and characterisation time. Physical parameters such as P.S., PDI and Z.P. were evaluated using DLS, while EE% was determined using HPLC. Besides, samples were inspected for any visual drug precipitation. As shown in Figure 5.5a and b, both Sf-SM and Sf-MM were stable, retaining their physical integrity with no detectable drug precipitation that was confirmed by EE% monitoring (Figure 5.5c). Micellar stability could be attributed to the large hydrophobic portion (poly Vinyl caprolactam/vinyl acetate) of Soluplus® that imparts a low CMC<sup>258,260</sup> in addition to the presence of PEG hydrophilic tail in both Soluplus® and TPGS that contributes in the physical stabilisation of the micelles through steric stabilisation<sup>244,245,455</sup>.

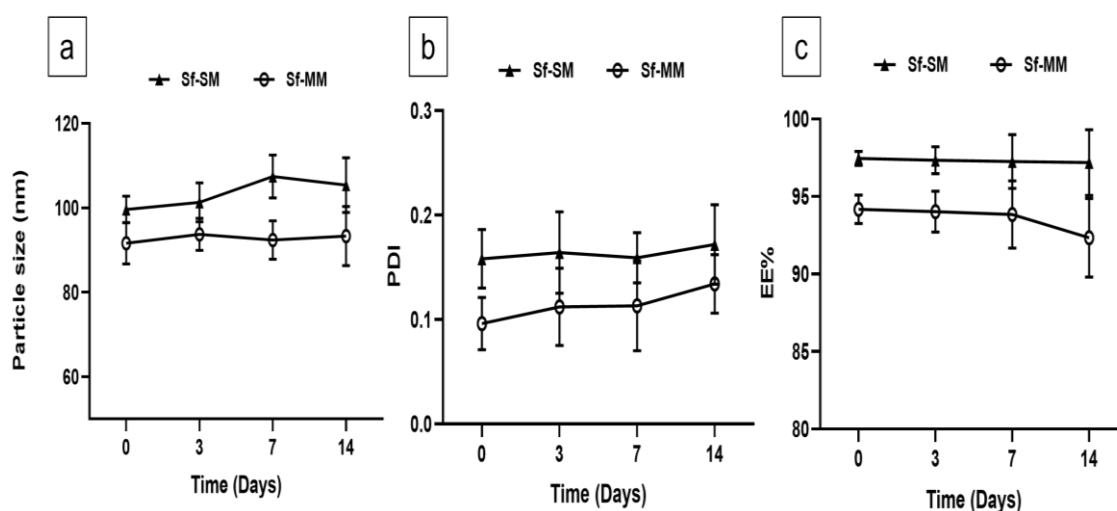


Figure 5.5: Short-term physical stability, of (a)P.S., (b)PDI and (c) EE%, for Sf-SM and Sf-MM at 4°C for 14 days

### 5.3.5. Solid state characterisation

#### 5.3.5.1. Attenuated total reflection-Fourier transform infrared (ATR-FTIR)

ATR-FTIR was carried out to check for any chemical changes in micellar systems' components for both single (Sf-SM) (Figure 5.6a) and mixed micelles (Sf-MM) (Figure 5.6b). Soluplus® spectrum displayed bands at 3449 cm<sup>-1</sup> (O-H stretching), 2928 cm<sup>-1</sup>

(aromatic C-H stretching),  $1736\text{ cm}^{-1}$ ,  $1630\text{ cm}^{-1}$  (C=O stretching), and  $1476\text{ cm}^{-1}$  (C-O-C stretching)<sup>466</sup>.while TPGS showed (-CH) overlapping bands at  $2891\text{ cm}^{-1}$ , (C=O) carbonyl band at  $1739.7\text{ cm}^{-1}$  and (C-O) ester bands at  $1107$  and  $1244\text{ cm}^{-1}$ <sup>419,420</sup>. The Sf spectrum demonstrated the two characteristic bands at  $3298\text{ cm}^{-1}$  and  $3337\text{ cm}^{-1}$  due to the N-H stretching of amide. The detected band at  $3074\text{ cm}^{-1}$  is related to the C-H stretching band, and the band at  $1705\text{ cm}^{-1}$  is for the amide C=O group<sup>389</sup>. In both micellar formulations, there was no detectable change or chemical shift in the characteristic peaks of the ingredients confirming the chemical stability and compatibility of micellar formulations.

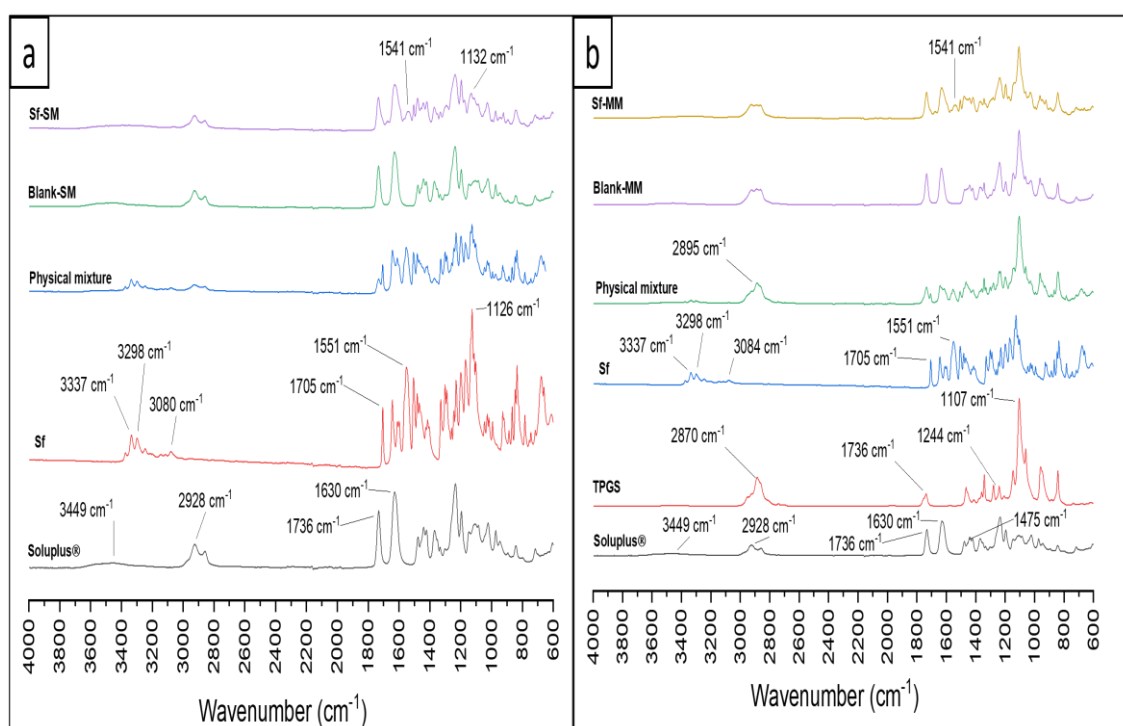


Figure 5.6: FTIR absorbance spectra of Sf-SM (a) and Sf-MM (b) with their raw materials, physical mixtures, and blank micelles

### 5.3.5.2. Differential scanning calorimetry (DSC)

DSC for both freeze-dried formulations was done to investigate the thermal behaviour of the ingredients, especially the Sf loaded in the nanoformulation. As depicted in Figure 5.7a and b, Sf displayed a large sharp endothermic melting peak <sup>TM</sup> at  $209^{\circ}\text{C}$ , confirming the crystalline structure of crude Sf powder. On the other hand, the Soluplus® thermogram showed a typical broad glass transition peak ( $T_g$ ) at  $73^{\circ}\text{C}$  as previously

reported<sup>331,467</sup>. While TPGS had a sharp endothermic melting peak ( $T_m$ ) at 35.5° C<sup>331</sup>. Interestingly, the thermograms of the physical mixtures of both formulations demonstrated a massive decrease in Sf melting peak (completely disappearing in MM). This could be ascribed to the dissolution of Sf in the melted polymeric material during the heating cycle, which implies good drug-polymer solubility. Good drug-polymer affinity can explain the high solubilisation capacity of the micellar systems, as the hydrophobic core of the micelles can accommodate large amounts of the drug. In the case of freeze-dried micellar systems, the Sf peak has completely disappeared which suggests the complete molecular dispersion of the drug in the hydrophobic core of the micelles. Besides, there was a significant downward shift in the ( $T_m$ ) and ( $T_g$ ) of both TPGS and Soluplus®, respectively, due to the nanosize of the polymeric micelles. According to Gibbs–Thomposon effect<sup>468</sup>, decreasing particle size leads to depression in both melting and glass transition temperatures.

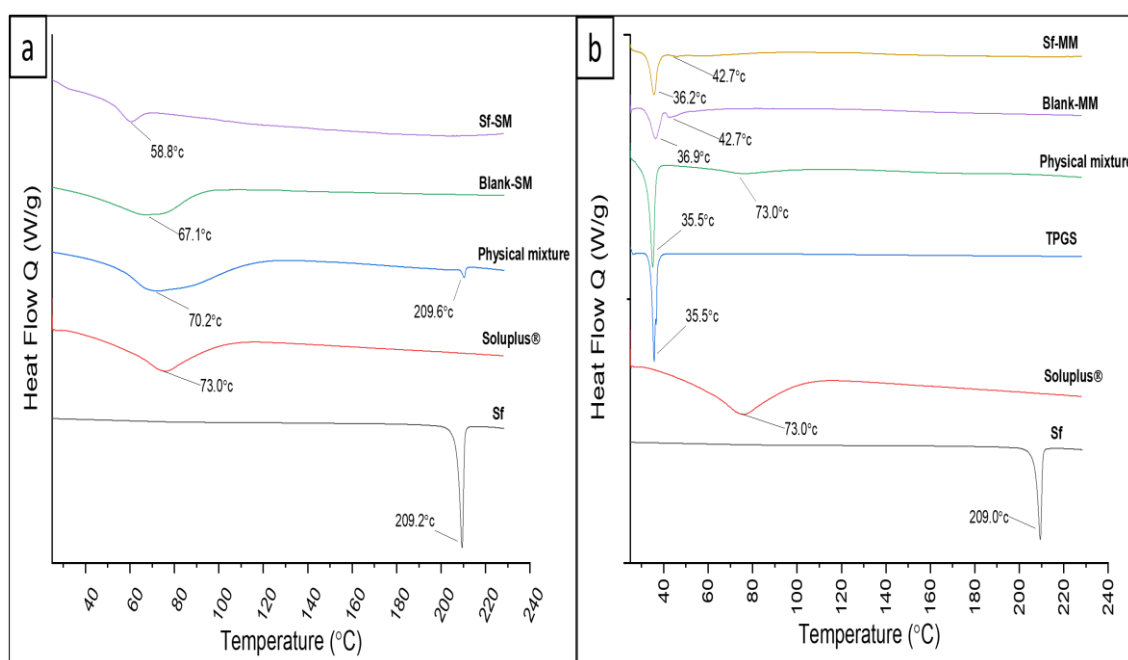


Figure 5.7: DSC thermogram of Sf-SM (a) and Sf-MM (b) with their raw materials, physical mixtures, and blank micelles

### 5.3.5.3. Powder X-Ray Diffraction (PXRD)

PXRD was carried out to further investigate the internal structure of the micellar systems. Figure 5.8a and b show that the Soluplus® diffraction pattern had no 2θ peaks, which

denotes its amorphous structure<sup>331,469</sup>. On the other hand, TPGS exhibited two distinctive  $2\theta$  peaks at  $19.2^\circ$  and  $23.4^\circ$ <sup>470</sup>. The crystalline structure of Sf powder was endorsed by various sharp diffraction  $2\theta$  peaks (such as peaks at  $11.3^\circ$ ,  $18.5^\circ$ , and  $24.7^\circ$ ). The physical mixture of components of both single micelles and mixed micelles showed all the corresponding distinctive peaks of both Sf and TPGS. In contrast, the freeze-dried micelle samples showed only the peaks of TPGS (with a lowering in the extent due to size reduction). The disappearance of Sf peaks confirms the encapsulation of the drug into micelles core in a molecular state. These results are consistent with DSC findings.

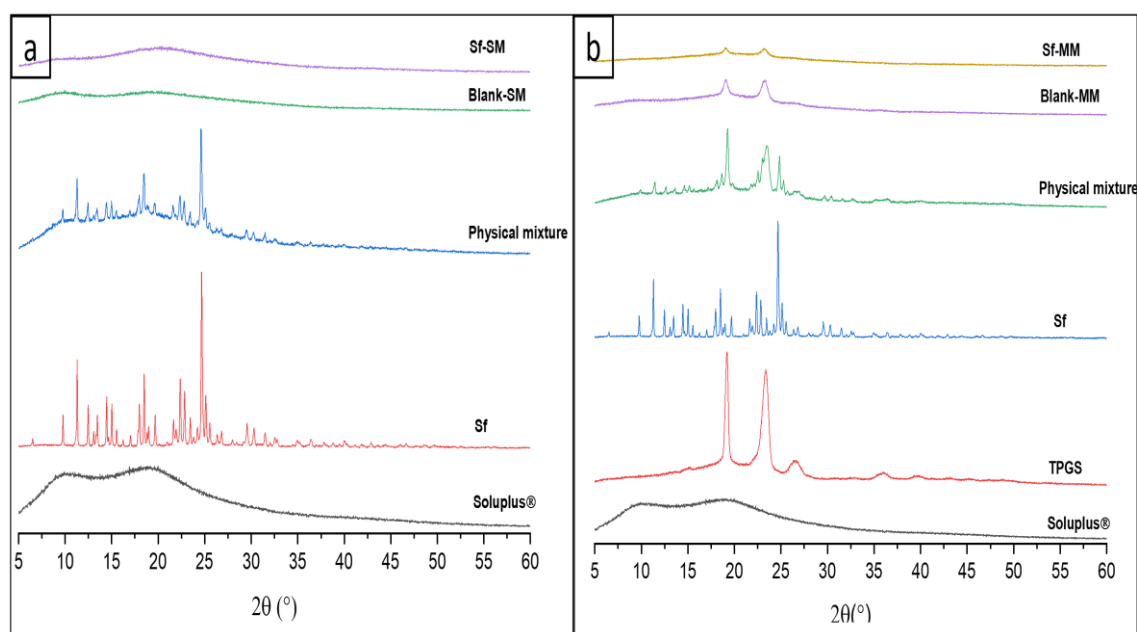


Figure 5.8:PXRD patterns of Sf-SM (a) and Sf-MM (b) with their raw materials, physical mixtures, and blank micelles

### 5.3.6. Physical stability in simulated gastric fluid (SGF) and simulated intestinal fluid (SIF)

It is well-known that the harsh environment of the gastrointestinal tract is the major challenge for oral drug administration. Gastrointestinal fluids could cause micelles to dissociate, resulting in the release of the encapsulated drug. Furthermore, retaining the nanosize of the micelles is a key factor in gastrointestinal absorption as it was reported that particle diameter less than 200 nm is beneficial for intestinal permeation, besides its role in boosting dissolution rate<sup>271,471,472</sup>. Although the presence of digestive enzymes (such as pepsin and pancreatin), the bile salts (such as Sodium taurocholate) and lecithin

would make simulated fluids more biorelevant, monitoring polymeric micelles particle size would be difficult due to the micelle formation of bile salts and lecithin. Hence, SGF and SIF (without enzymes) were chosen for monitoring the stability. The average hydrodynamic diameter of both Sf-SM and Sf-MM was comparable to that measured before incubation under both conditions (Table 5.4 and 5.5), implying that both micellar systems maintained their integrity and the loaded drug. That may be ascribed to the protective effect of PEG on the surface of the micelles against pH variations and ionic strength<sup>415,460</sup>. Notably, the zeta potential was dramatically lowered for both micellar systems in SIF, and it was even inflected to positive values in SGF. This may be explained by the effect of electrolytes and pH change (especially in SGF, which may affect the ionisation state of the components). Despite that, micellar systems showed good physical stability in both SGF and SIF, which implies that micellar systems rely on steric stability (due to PEG tails) rather than an electrostatic one. The stability of micelles in the gastrointestinal environment coincides with the minimal release of Sf, as revealed by the *in-vitro* release study discussed in the next section. These findings come in agreement with the previously reported data<sup>331,415</sup>.

Table 5.4: The colloidal stability of Sf-SM in SGF over 2 h and SIF for 6 h at 37° C.

<b>SGF (without enzymes)</b>			
<b>Time</b>	<b>P.S ± SD (nm)</b>	<b>PDI ± SD</b>	<b>Z.P. ± SD (mV)</b>
0 time	95.59 ± 1.04	0.148 ± 0.013	2.62 ± 1.8
2 h	98.12 ± 1.72	0.169 ± 0.026	3.28 ± 2.6
<b>SIF (without enzymes)</b>			
0 time	96.32 ± 1.9	0.151 ± 0.008	-5.19 ± 2.7
6 h	95.99 ± 1.8	0.130 ± 0.033	-3.53 ± 1.9

Table 5.5: The colloidal stability of Sf-MM in SGF over 2 h and SIF for 6 h at 37° C.

<b>SGF (without enzymes)</b>			
<b>Time</b>	<b>P.S ± SD (nm)</b>	<b>PDI ± SD (nm)</b>	<b>Z.P. ± SD (mV)</b>
0 time	97.43 ± 2.8	0.175 ± 0.008	1.13 ± 1
2 h	95.68 ± 3.4	0.164 ± 0.014	1.46 ± 0.9
<b>SIF (without enzymes)</b>			
0 time	88.9 ± 3.5	0.091 ± 0.01	-2.33 ± 0.24
6 h	87.94 ± 2.9	0.093 ± 0.012	-3.26 ± 0.35

### 5.3.7. *In-vitro* drug release study

Drug dissolution in the gastrointestinal fluids is considered a key step in the overall absorption process of orally administered drugs. Since Sf is classified as a class II drug in the biopharmaceutical classification system (with poor aqueous solubility and high permeability)<sup>125,127</sup>, the Sf dissolution step is considered the rate-determining step in its overall oral absorption process<sup>127</sup>. Thus, enhancing Sf aqueous solubility is expected to profoundly impact its oral bioavailability (oral bioavailability of Sf tablets was reported to be 38-45% relative to oral Sf solution<sup>125,130</sup>). Furthermore, Sf is only marketed as oral tablets (Nexavar®) with relatively high doses (200 mg/tablet), which mostly results in gastrointestinal side effects<sup>473</sup>. Accordingly, encapsulation of Sf into micelles for oral administration is anticipated to enhance its bioavailability lowering the required oral dose and, consequently, its side effects<sup>291</sup>. To investigate that, an *in-vitro* release study was carried out in both SGF and SIF without enzymes as a release medium to mimic both gastric and intestinal environments, respectively. 1% Tween 80 was dissolved in release media to maintain the sink condition. In SGF (Figure 5.9), both Sf-SM and Sf-MM showed limited but enhanced release rates ( $5.35 \pm 0.23\%$  and  $6.3 \pm 0.39\%$  after 2 h) compared to Sf suspension ( $0.59 \pm 0.07\%$ ). It was remarkable that Sf-MM has a slightly but significantly ( $p < 0.05$ ) higher released amount after 2 h than Sf-SM ( $P < 0.05$ ). Likewise, the drug release rates of Sf from both Sf-SM and Sf-MM in SIF were substantially higher than Sf-suspension (Figure 5.10). Sf-SM and Sf-MM released 36.35

$\pm 1\%$  and  $47.36 \pm 3.39\%$ , respectively, compared to only  $1.45 \pm 0.09\%$  from Sf suspension after 72 h.

For further study of the influence of micellar systems on the dissolution rate of Sf in SIF, the dissolution efficiency (DE%) parameter was calculated according to equation (2.11) in Chapter 2 (section 2.3.4.). As depicted in Figure 5.11, Sf-MM showed the highest DE% with  $0.324 \pm 0.005\%$ , while Sf-SM exhibited a lower DE% with  $0.235 \pm 0.026\%$ . This could be explained by the stronger hydrophobic interaction between Sf and the inner core of single Soluplus® micelles compared to Soluplus®/TPGS mixed micelles' core. On the other hand, the DE% value of Sf suspension was extremely low ( $0.012 \pm 0.001\%$ ), asserting the role of micelle formation in boosting the dissolution rate of Sf.

Furthermore, Sf release data from different formulations were fitted into different release mechanism models, and the best fit was chosen based on the coefficient of determination (COD)<sup>340,474</sup>. From Table 5.6, both micellar formulations and Sf suspension best fit the Korsmeyer-Peppas model. However, due to the limited cumulated amount of Sf released, fitting of Sf suspension may not be very reliable, and more data points may be needed for more precise fitting. For both micellar systems, the release exponent parameter value (n) between 0.5 and 1, which indicates that the drug release is anomalous where different mechanisms could be involved (diffusion, dissolution, and micelles disaggregation).

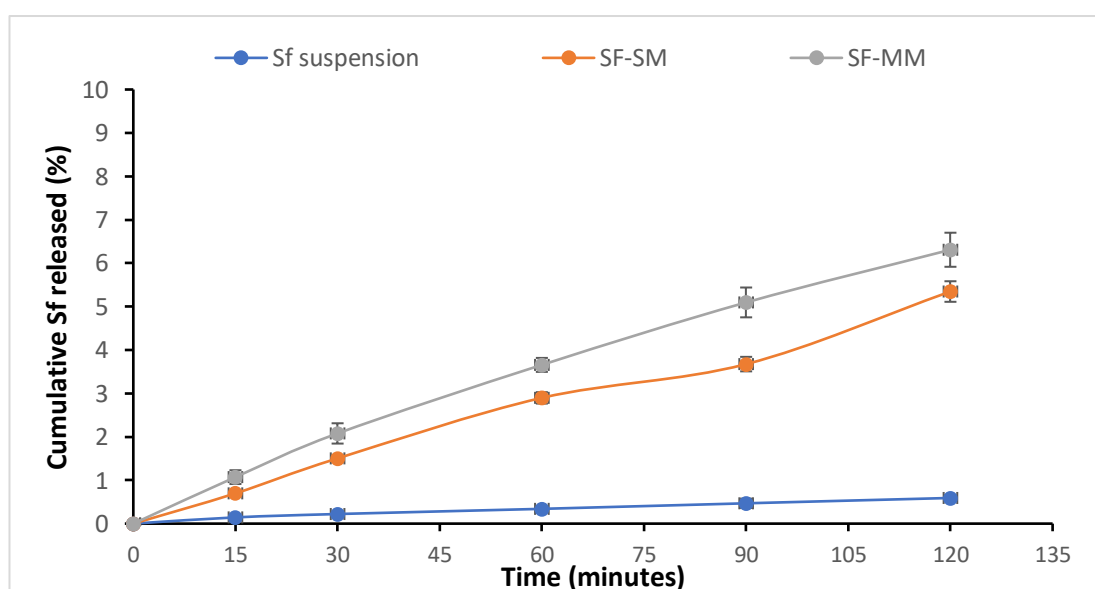


Figure 5.9: Cumulative Sf release from Sf-suspension, Sf-SM and Sf-MM in SGF over 2 h at 37° C under shaking at 100 rpm using the dialysis bag method.

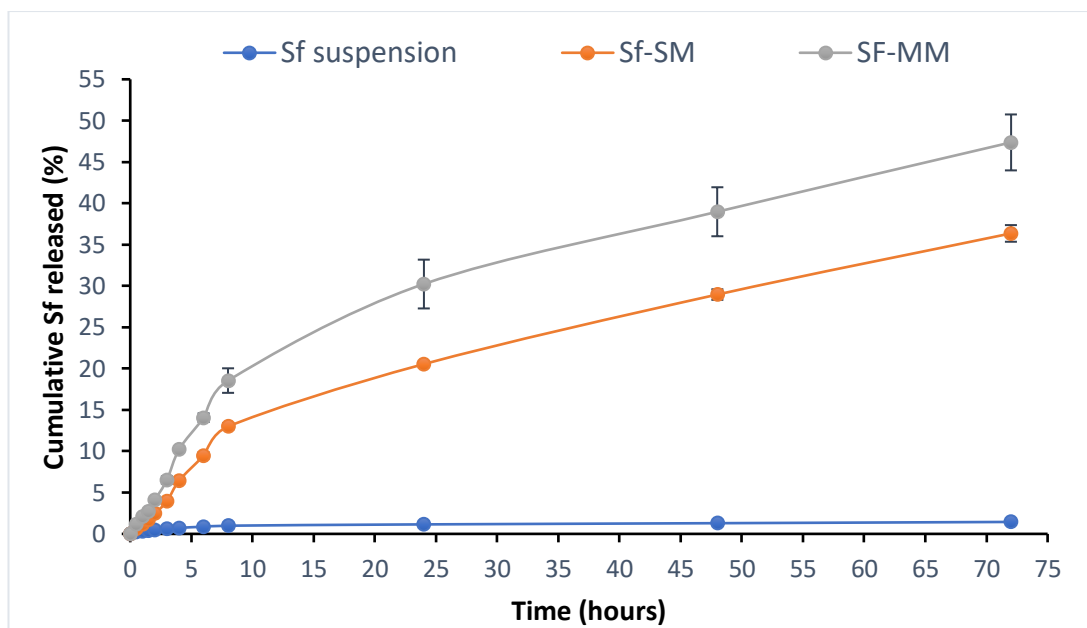


Figure 5.10: Cumulative Sf release from Sf-suspension, Sf-SM and Sf-MM in SIF over 72 h at 37° C under shaking at 100 rpm using the dialysis bag method.

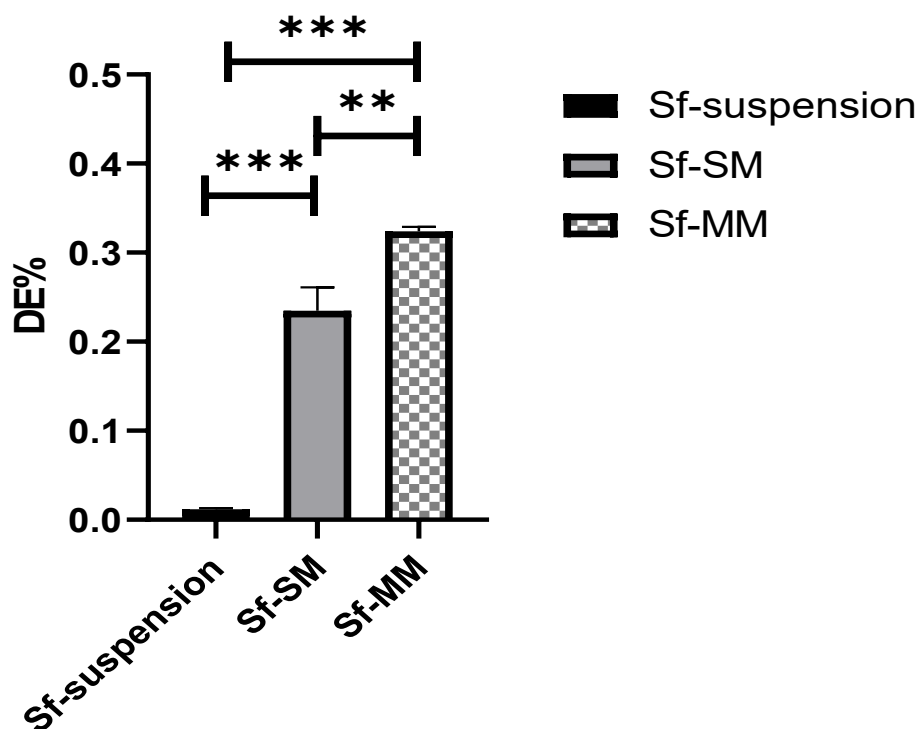


Figure 5.11: Dissolution efficiency (DE%) values of Sf-suspension, Sf-SM and Sf-MM. \*P < 0.05, \*\*P < 0.01, \*\*\*P < 0.001, and ns = not significant (P > 0.05)

Table 5.6: *In-vitro* drug release kinetic models of Sf-suspension, Sf-SM and Sf-MM

Model	Equation	R <sup>2</sup> of different formulations		
		Sf suspension	Sf-SM	Sf-MM
<b>Zero-order</b>	$f = k_0.t$	-0.1747	0.8733	0.8116
<b>First-order</b>	$f = 1 - \exp(-kt)$	-0.1694	0.9139	0.8860
<b>Higuchi</b>	$f = k_H . t^{0.5}$	0.7135	0.9663	0.9721
<b>Korsmeyer-Peppas</b>	$f = k_{kp} . t^n$	<b>0.9461</b> n = 0.293	<b>0.9831</b> n = 0.601	<b>0.9771</b> n = 0.550
<b>Hixon-Crowell</b>	$f = [1 - (1 - k_{HC} . t)^3]$	-0.1712	0.9014	0.8632

### 5.3.8. *In-vitro* cellular studies on Caco-2 cells

#### 5.3.8.1. Cellular viability study

Cellular viability studies of blank micelles (SM and MM) on Caco-2 cells as a model for intestinal epithelial cells have been done to appraise the cellular biocompatibility of the delivery system on the intestinal lining cells<sup>357</sup>. For that, different micelle concentrations ranging from 25µg/ml to 2 mg/ml (total polymer concentration) were tested on Caco-2 cells for different incubation times (6 h, 24 h and 48 h). As shown in Figure 5.12-5.14, blank Soluplus® micelles did not exhibit any cytotoxicity on Caco-2 cells for all tested concentrations and overall incubation times. Furthermore, Soluplus® was previously reported safe when tested on murine macrophage RAW 264.7 cells<sup>321</sup> and different breast cancer cells<sup>253</sup>. On the other hand, MM has shown concentration and time-dependent cytotoxicity. A similar observation has been reported previously<sup>253,327,328,475</sup>. This could be attributed to the presence of TPGS, as it has been proved that TPGS has a selective cytotoxicity towards cancer cell lines<sup>256,257,475,476</sup>. This anticancer activity was reported to be due to its apoptosis-inducing properties through generating reactive oxygen species (ROS)<sup>301</sup>. ROS damage cell DNA, proteins, and fatty acids, eventually resulting in apoptotic cell death. Since normal cells are more resistant to oxidative stress, TPGS is selectively cytotoxic to cancerous cells such as DOX-resistant KB cells<sup>301</sup>, MCF-7 and MDA-MB 231 human breast cancer cell lines<sup>296</sup>, Hepatocellular carcinoma cells (HepG2, Hep3B and Huh7)<sup>256</sup>, the human H460 and A549 lung cancer cell lines<sup>257</sup> but not normal cells.

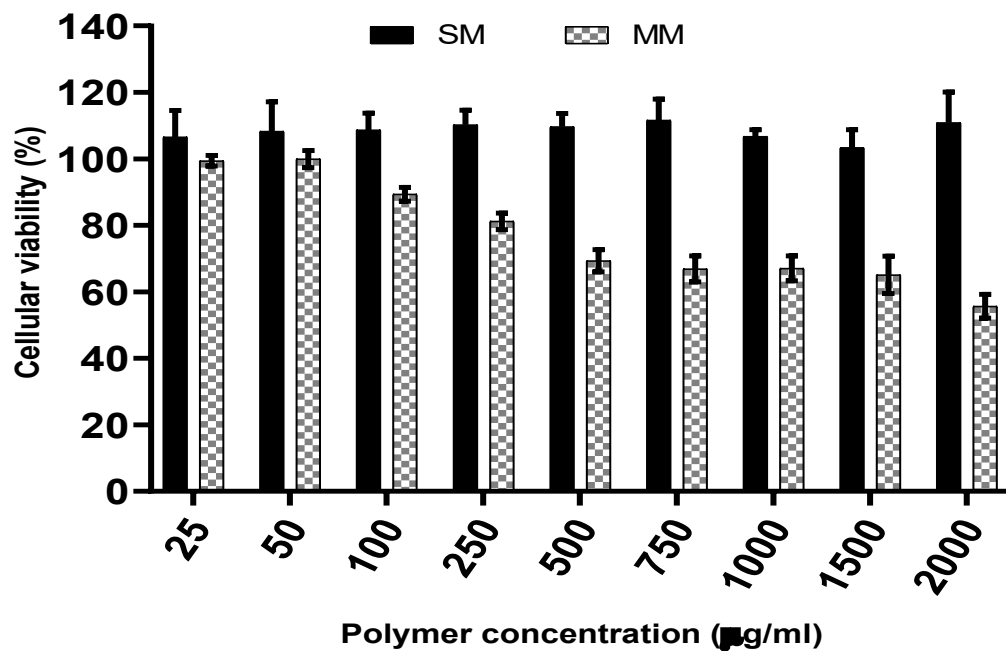


Figure 5.12: Cytotoxicity of Blank SM and MM on Caco-2 cells after incubation for 6 h

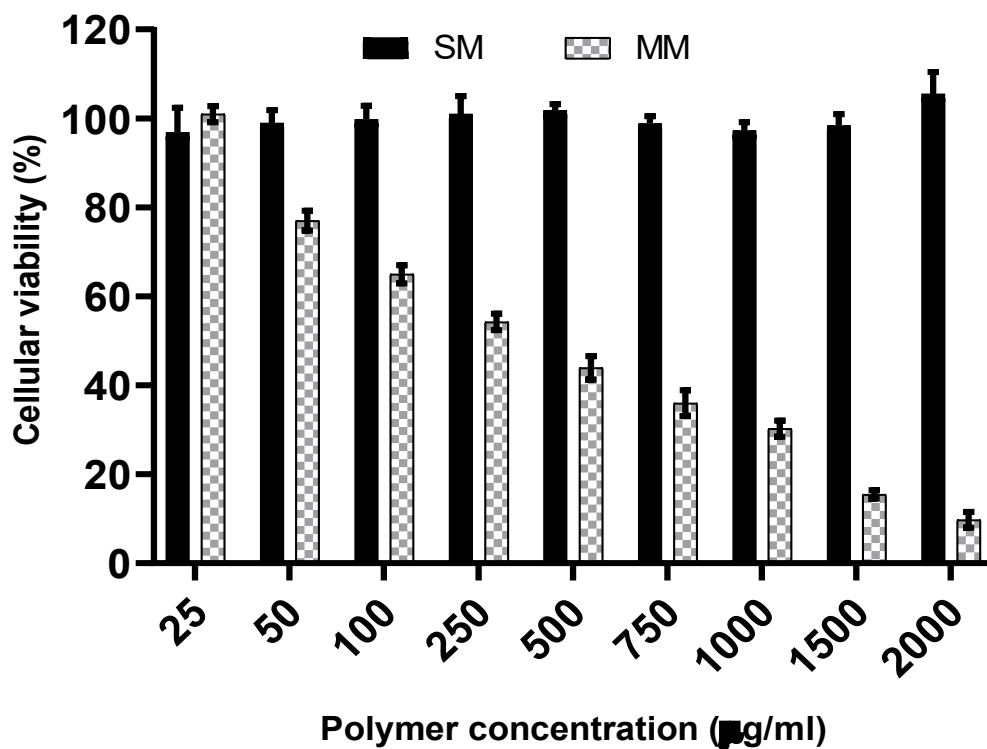


Figure 5.13: Cytotoxicity of Blank SM and MM on Caco-2 cells after incubation for 24 h

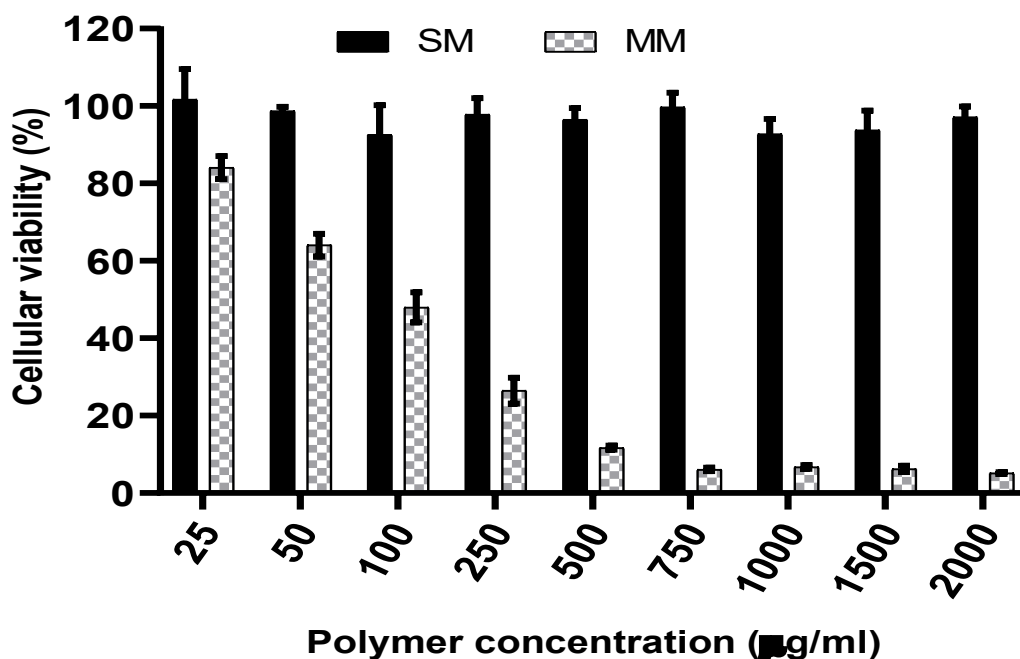


Figure 5.14: Cytotoxicity of Blank SM and MM on Caco-2 cells after incubation for 48 h

### 5.3.8.2. Cellular transport study

To assess the impact of the enhancement of Sf dissolution rate on its intestinal permeation through the intestinal epithelial barrier, a cell transport study using a Caco-2 cell monolayer was employed<sup>266,415</sup>. Before the experiment, the cytotoxicity of blank formulations was assessed for 6 hrs to ensure that both micellar dispersions were safe (cell viability > 80%)<sup>415</sup> for 6 h (Figure 5.12). Besides, TEER values were monitored before and after the experiment to ensure the integrity of the cell monolayer. The limit of quantification (LOQ) of the HPLC-UV method was calculated (LOQ = 0.0308 µg/mL) to ensure the capability of HPLC-UV to detect the expected permeated amounts of Sf. As shown in Figure 5.15 and Table 5.7, Sf-SM exhibited a significantly ( $p < 0.05$ ) higher  $P_{app}$  than the Sf-suspension. This could be ascribed to the effect of Soluplus® in enhancing Sf's dissolution rate and permeation. Moreover, the presence of TPGS in Sf-MM boosted the  $P_{app}$  as TPGS improves not only the Sf dissolution rate but also its permeation through the intestinal epithelium, augmenting the effect of Soluplus® as previously reported<sup>260,415,460,477</sup>. In addition, the BL-AP permeability was measured to investigate the impact of Soluplus® and TPGS on P-gp efflux inhibition of Sf.

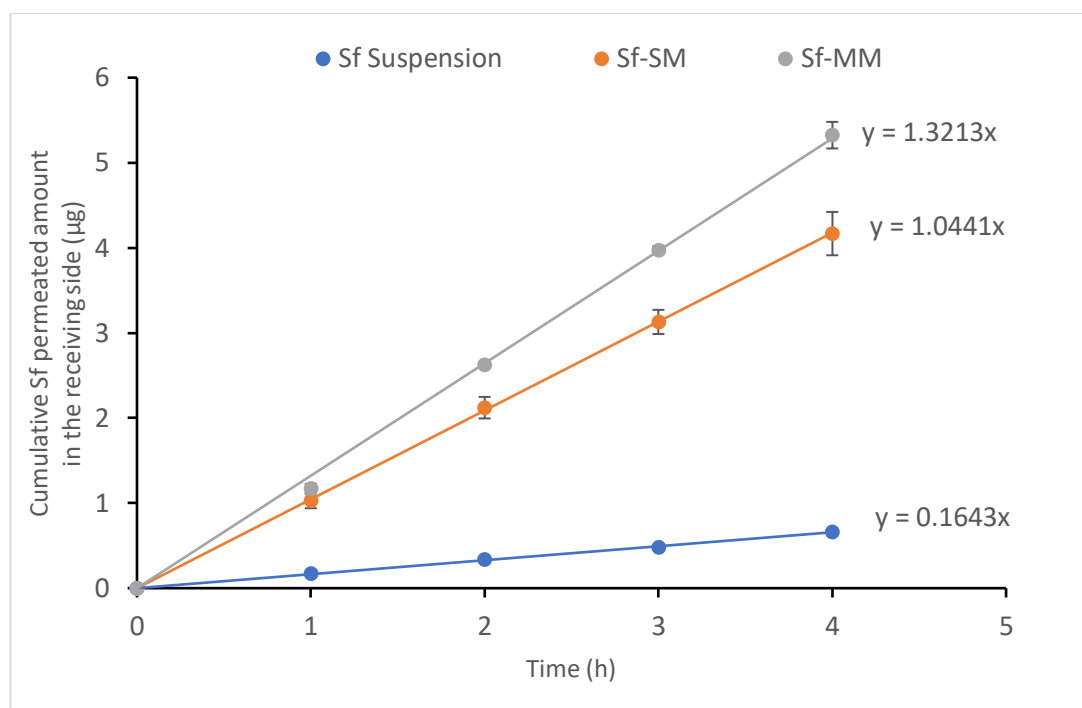


Figure 5.15: Time-dependent Caco-2 cell influx (AP-BL) of Sf from Sf-suspension, Sf-SM, and Sf-MM over 4 h

Table 5.7: Apparent Permeability values and Efflux ratio of Sf suspension, Sf-SM and Sf-MM (n=3).

Formulations	$P_{app}$ (AP-BL) $\times 10^{-7}$ (cm/s)	$P_{app}$ (BL-AP) $\times 10^{-7}$ (cm/s)	Efflux ratio
Sf-suspension	$8.15 \pm 0.6858$	$3.886 \pm 1.211$	$0.477 \pm 0.119$
Sf-SM	$51.791 \pm 2.833$	$24.578 \pm 0.1681$	$0.475 \pm 0.022$
Sf-MM	$65.541 \pm 3.083$	$15.986 \pm 4.056$	$0.244 \pm 0.053$

As demonstrated in Figure 5.16, both Sf-SM and Sf-MM showed higher efflux rates than the Sf suspension, which could be attributed to the enhanced dissolution rate of Sf from the micellar dispersion into the basolateral compartment, allowing more free drug molecules to be transported to the apical compartment. Nevertheless, the efflux ratios (Table 5.7) reveal that Sf-MM exhibited a slight but significant inhibition of P-gp efflux pumps compared to other tested samples ( $p < 0.05$ ). This could be explained by the inhibitory effect of TPGS on P-gp pumps<sup>305,478</sup>. However, the magnitude of the impact was not very profound because Sf is considered a weak P-gp substrate<sup>479</sup>.

Convincingly, the encapsulation of Sf into single and mixed micelles is anticipated to promote intestinal absorption by enhancing its dissolution rate and permeation with additional P-gp inhibition effect by TPGS in the case of Sf-MM.

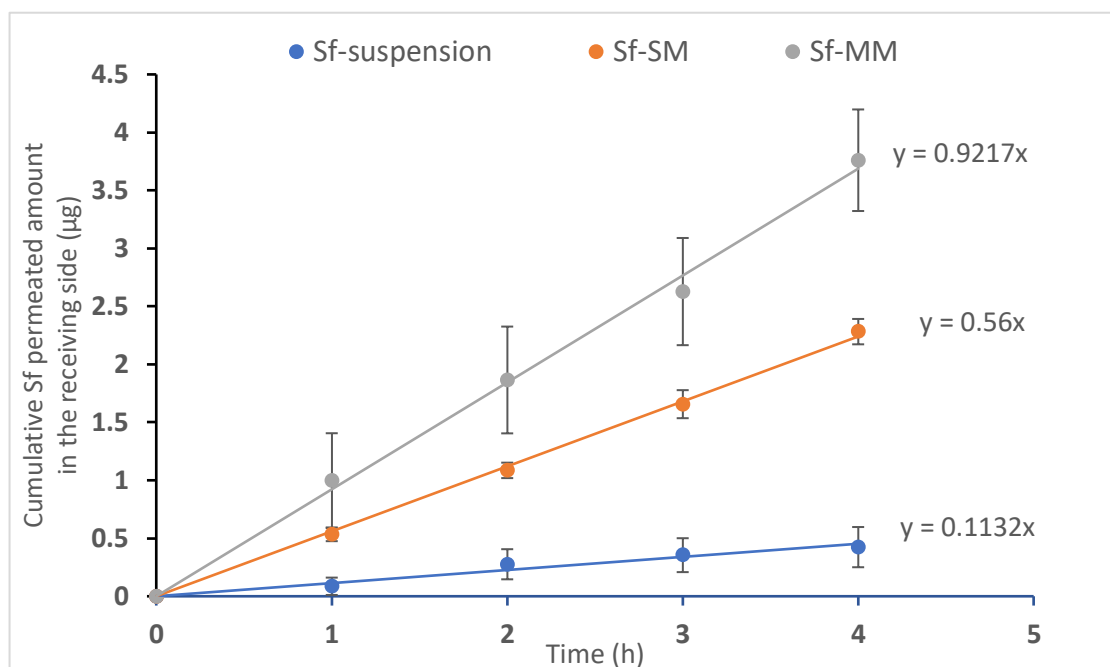


Figure 5.16: Time-dependent Caco-2 cell efflux (BL-AP) of sf from Sf-suspension, Sf-SM, and Sf-MM over 4 h

#### 5.4. Conclusion

During recent years, polymeric micelles for oral administration have attracted significant attention as a promising delivery system for poorly soluble drugs (especially those of class II in BCS) due to a plethora of merits such as enhancing drug solubility, permeability and stability in addition to their biocompatibility<sup>244</sup>. Recently, the employment of mixed micelles was addressed to allow more optimisation and overcome any drawbacks of using a single micelle system<sup>261</sup>.

In this Chapter, the impact of using both single (Soluplus®) and mixed micellar systems (based on Soluplus® and TPGS) on the physicochemical properties of the micellar dispersion and the influence on Sf dissolution and intestinal permeation was investigated.

Soluplus® single micelles demonstrated highly effective Sf solubilisation capacity, while increasing the TPGS ratio in the mixed micelles resulted in an incremental reduction in

Sf solubilisation with no significant ( $p > 0.05$ ) effect on particle size and size distribution of micelles. Likewise, increasing the TPGS ratio led to a corresponding increase in the CMC value of the mixed micelles. This may raise a stability issue upon dilution in biological fluids.

On the other hand, both the single and mixed micelle (Sf-SM and Sf-MM) system's ingredients showed high chemical and physical compatibility with good stability in both SGF and SIF, suggesting that micelles integrity will be maintained after oral ingestion. *In-vitro* Sf dissolution studies in SGF and SIF, Sf-SM and Sf-MM showed improved dissolution rates compared to Sf suspension. Besides, it was remarkable that despite that Sf-SM having a higher solubilisation capacity, Sf-MM exhibited a higher dissolution rate, suggesting that the dissolution rate could be tailored by changing the Soluplus®/TPGS ratio.

At the cellular level, SM showed a good safety profile on Caco-2 cells, while MM showed concentration and time-dependent cytotoxicity due to the presence of TPGS. Following the same pattern of dissolution rates, Sf-SM and Sf-MM demonstrated significantly ( $p < 0.05$ ) higher apparent permeability across the Caco-2 monolayer than Sf suspension. Moreover, by comparing the efflux ratios of Sf from different formulations, it was significant that Sf-MM had a modest efflux inhibition property due to the presence of TPGS.

In conclusion, polymeric micelles based on Soluplus® and TPGS may be considered a promising approach to improve Sf solubility, dissolution rate, and intestinal permeation, which is expected to enhance its oral bioavailability.



## **Chapter 6**

*Preparation and characterisation of galactosylated TPGS/Soluplus®  
mixed micelles for liver-targeted delivery of Sorafenib*

## 6.1.Introduction

Polymeric micelles (PMs) have been intensively studied for the delivery of hydrophobic anticancer agents due to their distinctive properties of high encapsulation efficiency of hydrophobic agents owing to the amphiphilic character<sup>248</sup>. The nanosize (typically 20-200 nm) of PMs allows for the preferential passive accumulation of anticancer agents in tumour tissues through the leaky vasculature (what is known as enhanced permeation and retention phenomenon (EPR))<sup>247,248</sup>. Polymers, such as Soluplus®, containing PEG as the hydrophilic moiety can provide extended blood circulation and more time for anticancer agent accumulation. Besides, some polymers can counteract multidrug resistance (MDR) through P-gp inhibition<sup>248,249,259</sup>. Currently, several polymeric micellar formulations for anticancer therapy delivery are under clinical investigations<sup>272</sup>, of which Genexol®-PM (Paclitaxel loaded PEG-PLA polymeric micelles) has been marketed for the treatment of breast cancer and Eligard® (leuprolide acetate loaded PLGA polymeric nanoparticles) have been granted FDA approvals for prostate cancer and showing very promising clinical proficiency<sup>249,442</sup>.

Furthermore, functionalisation of polymeric micelles, such as galactosylation, is regarded a potential strategy to enhance the accumulation of drugs in the tumor site, reducing the exposure of healthy tissues to the drugs and minimising their side effects. TPGS was reported to be functionalised by coupling with different targeting ligands (such as folic acid<sup>480,481</sup>, glycyrrhetic acid<sup>304</sup> and Lactobionic acid<sup>414,482</sup>) for targeted delivery of anticancer agents to different cancer types showing promising results in the preclinical studies. Beside its functionalisation, TPGS demonstrated a P-glycoprotein (P-gp) inhibitory effect that counteract the multidrug resistance (MDR) of cancer cells<sup>478,483,484</sup>. Additionally, TPGS has been shown an *in-vitro* and *in-vivo* cytotoxic action on many cancer cell lines via inducing cellular apoptosis<sup>256,257</sup>.

This study investigates the potentials of galactosylated-TPGS/Soluplus® mixed micelles for the targeted delivery of Sf to hepatocellular carcinoma (HCC) cells.

The objectives of this chapter are:

- To develop galactosylated Soluplus/TPGS mixed micelles for liver-targeted intravenous delivery of Sf.
- To characterise the physicochemical properties of galactosylated Sf-loaded mixed micelles (Gal-MM).
- To evaluate the colloidal stability of Gal-Sf-MM during short-term storage and under administration and physiological conditions and studying Sf release kinetics from Gal-Sf-MM.
- To appraise the targeting efficiency, cytotoxicity, and cellular uptake of the developed Gal-Sf-MM on HepG2 cells.

## **6.2. Materials and methods**

### **6.2.1. Materials**

Soluplus®, polyvinyl caprolactam–polyvinyl acetate–polyethylene glycol graft copolymer, was obtained from BASF (Redditch, UK). Sorafenib was obtained from LC Labs (USA). Ricinus communis agglutinin, RCA120, was purchased from 2BScientific (UK). D- $\alpha$ -Tocopherol polyethylene glycol 1000 succinate (TPGS, Mwt ~1513 g/mol), phosphate buffer saline tablets (PBS), Tween-80, phosphotungstic acid (PTA), Bovine serum albumin (BSA), coumarin-6 (C6), Triethylamine (TEA), ethylenediamine (EDA), 1,1'-Carbonyldiimidazole (CDI), N-hydroxysuccinimide (NHS), 1-Ethyl-3-(3-dimethylaminopropyl) carbodiimide (EDC), trypsin-EDTA solution, RPMI 1640 Medium, fetal bovine serum (FBS), Hanks' Balanced Salt Solution (HBSS), 1% non-essential amino acids (NEAA), 1% penicillin–streptomycin solution, trifluoroacetic acid (TFA), and 4',6-diamidino-2-phenylindole (DAPI) were all purchased from (Sigma-Aldrich, UK). Tetrazolium compound [3-(4,5-dimethylthiazol-2-yl)-5-(3-carboxymethoxyphenyl)-2-(4-sulfo-phenyl)-2H-tetrazolium], inner salt (MTS) was purchased from Promega Ltd (UK). All solvents, such as acetone, DMSO, deuterated DMSO-D<sub>6</sub>, HPLC grade methanol and acetonitrile were purchased from Sigma-Aldrich (UK).

### **6.2.2. Synthesis of Gal-TPGS**

Synthesis of Gal-TPGS has been achieved as previously reported in Chapter 4 (section 4.2.4.)

### **6.2.3. Characterisation and determination of conjugation efficiency of Gal-TPGS**

Gal-TPGS has been characterised using FTIR, <sup>1</sup>H-NMR and MALDI-TOF. Furthermore, the conjugation efficiency has been quantified using the phenol/sulfuric acid assay method, as mentioned in Chapter 4 (section 4.2.5.)

#### **6.2.4. Preparation of galactosylated Sf-loaded TPGS/Soluplus® mixed micelles (Gal-Sf-MM)**

Gal-Sf-MM were prepared by the solvent evaporation method using Soluplus®: TPGS weight ratio of 40:10, as previously detailed in Chapter 5 (section 5.2.2.) using Gal-TPGS instead of TPGS during the preparation procedures. The blank mixed micelles (MM) were prepared in the same manner without Sf.

#### **6.2.5. Particle size and Zeta potential**

The particle size, size distribution (PDI), and zeta-potential (Z.P.) of Sf-MM and Gal-Sf-MM were measured using dynamic light scattering (DLS) via Zetasizer Nano (Malvern Instruments Ltd., Malvern, UK) following the procedures detailed in Chapter 2 (section 2.3.2.1.).

#### **6.2.6. Encapsulation efficiency (EE%) and loading capacity (LC%)**

Encapsulation efficiency (EE%) and loading capacity (LC%) of sorafenib (SF) into micelles were measured through the direct assay method following the same procedures described in Chapter 5 (section 5.2.4.).

#### **6.2.7. Short-term storage physical stability**

To investigate the physical and drug-loading stability of Sf-MM and Gal-Sf-MM, the samples were transferred into glass vials sealed with plastic caps and stored at 4 °C over 14 days. At the predetermined times (0, 3, 7, and 14 days) the particle size, polydispersity index (PDI), zeta potential, and EE% were assessed using DLS and HPLC<sup>461</sup>.

#### **6.2.8. Micellar colloidal stability under administration and physiological blood condition**

To investigate the physical stability of Sf-MM and Gal-Sf-MM under administration conditions (in 0.9% NaCl and 5% Dextrose for 30 min at 25° C) and physiological blood condition (5.4% BSA in PBS at 7.4 for 72 h at 37° C), samples were 10 times diluted in the corresponding media for the assigned time<sup>461</sup>. Consequently, particle size, polydispersity index and zeta potential were monitored using DLS as previously outlined.

### **6.2.9. Micelles morphology using transmission electron microscopy (TEM)**

TEM was used to inspect the morphology of the produced micelles following the steps mentioned in Chapter 2 (section 2.3.3.1.).

### **6.2.10. Critical micellar concentration (CMC) measurement**

Iodine UV-Vis spectroscopy method was used to determine the CMC of MM and Gal-MM in MilliQ water following the procedures detailed in Chapter 5 (section 5.2.5.).

### **6.2.11. Solid state characterisation**

For further investigation of the prepared mixed micelles in the solid state, micellar dispersions were freeze-dried using VirTis® Wizard 2.0 freeze dryer (SP SCIENTIFIC, USA). After preparation, samples were frozen using liquid nitrogen and then freeze-dried at -80 °C under vacuum for 24 hr.

#### **6.2.11.1. Attenuated total reflection-Fourier transform infrared (ATR-FTIR)**

The Attenuated total reflection-Fourier transform infrared (ATR-FTIR) spectra of raw materials, physical mixtures, and Gal-Sf-MM were acquired using FTIR spectrophotometer as mentioned in Chapter 2 (section 2.3.2.6.).

#### **6.2.11.2. Differential scanning calorimetry (DSC)**

DSC was used to investigate the effect of formulation and sorafenib encapsulation on the thermal behaviour of the components following the same conditions mentioned in Chapter 2 (section 2.3.2.3.).

#### **6.2.11.3. Powder X-Ray Diffraction (PXRD)**

The X-ray powder diffraction patterns was acquired to further investigate the impact of formulation on the crystallinity of the components under the same conditions stated in Chapter 2 (section 2.3.2.5.).

#### **6.2.12. Drug release study**

Sorafenib release profiles were investigated using the dialysis bag method following the same procedures detailed in Chapter 4 (section 4.2.10.).

#### **6.2.13. Surface accessibility (lectin-induced agglutination assay)**

To verify the surface exposure/accessibility of galactose moieties on the surface of Gal-MM, the lectin agglutination test was carried out as previously detailed in Chapter 4 (section 4.2.7.)

#### **6.2.14. *In-vitro* cellular studies**

For *in-vitro* cellular studies, HepG2 cells were used as *in-vitro* model of liver cancer.

##### **6.2.14.1. *In-vitro* Cellular cytotoxicity**

Cellular cytotoxicity studies were carried out to investigate the effect of sorafenib encapsulation and the galactosylation of mixed micelles on cytotoxicity efficiency of Sf on HepG2 cells using the MTS assay method. All the conditions and procedure steps were followed as detailed in Chapter 4 (section 4.2.11.1.).

##### **6.2.14.2. Cellular uptake using an inverted fluorescence microscope**

In this study, coumarin-6 (C6) was used as a lipophilic fluorescent probe and loaded into both galactosylated and non-galactosylated mixed micelles formulations instead of Sorafenib with a final C6 concentration of 100 µg/mL of formula to investigate the cellular uptake of these formulations on HepG2 cells (ASGP positive). All the conditions and steps were followed as mentioned in Chapter 4 (section 4.2.11.2.). However, the cells were treated with different tested formulations at a final C6 concentration of 0.5 µg/mL.

### 6.2.14.3. Cellular uptake study using flow cytometer

A flow cytometer (Beckman Coulter CytoFlex, USA) was used to quantify the cellular uptake of the C6-labelled mixed micelles applying all the conditions and the steps detailed in Chapter 4 (section 4.2.11.3.). However, cells were incubated with different tested sampled at a final C6 concentration of 0.5  $\mu\text{g/mL}$ .

## 6.3. Results and discussion

### 6.3.1. Synthesis and characterisation of Gal-TPGS

The synthesis of Gal-TPGS was done as previously discussed in Chapter 4 (section 4.2.4.). Firstly, the terminal hydroxyl group of PEG of TPGS was reacted with carbonyldiimidazole (CDI) to form intermediate carbamate to be reacted afterwards with an excess amount of ethylenediamine (EDA) imparting a terminal amine to TPGS molecule. The amine-terminated TPGS was then coupled with lactobionic acid through direct amidation reaction in the Presence of 1-Ethyl-3-(3-dimethylaminopropyl) carbodiimide (EDC) and N-hydroxysuccinimide (NHS)<sup>414</sup>. The product was purified by intensive dialysis against MilliQ water and characterised by FTIR, <sup>1</sup>H-NMR and MALDI-TOF (Chapter 4, section 4.3.2.). Furthermore, the conjugation efficiency was quantified using Phenol/sulfuric acid assay<sup>362</sup>. Conjugation efficiency (number of conjugated TPGS moles to total number of moles) was  $74.6 \pm 5.2\%$ , giving galactose content of  $7.6 \pm 0.2\%$ .

### 6.3.2. Preparation and characterisation of Sf-MM and Gal-Sf-MM

The preparation of TPGS/Soluplus<sup>®</sup> mixed micelles was done using the solvent evaporation method as previously reported<sup>461</sup>. Firstly, different Soluplus<sup>®</sup>: TPGS ratios have been screened and characterised in terms of particle size, LC% and CMC (Chapter 5, section 5.3.1.). Since all screened ratios exhibited acceptable colloidal properties (Particle size, PDI and Zeta potential), as shown in Table 6.1, the ratio of 40:10 w/w (Soluplus<sup>®</sup>: TPGS) was chosen based on LC% ( $15.9 \pm 0.1\%$ ) and its CMC ( $106.9 \pm 2.9 \mu\text{g/mL}$ ), which is low enough to produce stable micelles and still contains considerable TPGS content for good liver targeting. As shown in Table 6.1, all formulated micelles showed nanosized micelles with narrow size distribution that are key features for the *in-*

*vivo* application of parenteral colloidal systems. The particle size of nanodelivery systems has a particular importance in the treatment of cancer as nanosized delivery systems below 200 nm are well known to passively accumulate in cancerous tissues due to the enhanced permeation and retention phenomenon (EPR)<sup>81,234,447</sup>.

Since the formation of polymeric micelles is a dynamic process, the encapsulation of Sorafenib into micelles increased micellar size for both non-galactosylated and galactosylated counterpart systems (Figure 6.1 and 6.2). Moreover, despite the fact that the use of Gal-TPGS instead of TPGS did not affect the particle size, it showed a slight increase in the polydispersity index (PDI) which may be due to the change in the hydrophilic/lipophilic balance between TPGS and Gal-TPGS that imparted some heterogeneity in the assembly process of Gal-MM. Additionally, using Gal-TPGS has resulted in a change in the zeta potential from negative values, in the case of MM and Sf-MM, into positive values in the case of Gal-MM and Gal-Sf-MM., indicating that TPGS has been chemically modified. The same observation was reported by Tsend-Ayush, A. et al. during the preparation of lactobionic acid-conjugated TPGS for the delivery of Etoposide to HCC cells<sup>421</sup>.

Furthermore, both Sf-MM and Gal-Sf-MM showed high LC% of  $15.9 \pm 0.1\%$  and  $15.5 \pm 0.5\%$ , respectively. In this case, the apparent solubility of Sf in water has been tremendously improved by 1110 and 1080 times, respectively, compared to the intrinsic solubility of Sf ( $\sim 1.7 \mu\text{g/mL}$ <sup>459</sup>). The same observation was reported by Riedel, J. *et al.* after encapsulation of Paclitaxel (PTX) into TPGS/Soluplus mixed micelles as the solubility of PTX was enhanced by more than 6000 fold compared to intrinsic PTX solubility in water<sup>461</sup>.

Table 6.1: Particle size, polydispersity index (PDI) and Zeta potential of blank and Sf loaded MM and Gal-MM.

<b>Formulation</b>	<b>P.S. <math>\pm</math> SD (nm)</b>	<b>PDI <math>\pm</math> SD</b>	<b>Z.P. <math>\pm</math> SD (mV)</b>	<b>EE <math>\pm</math> SD (%)</b>	<b>LC <math>\pm</math> SD (%)</b>
<b>Blank MM</b>	$69.2 \pm 1.6$	$0.103 \pm 0.030$	$- 15.6 \pm 2.2$	--	--
<b>Blank Gal-MM</b>	$71.1 \pm 1.5$	$0.127 \pm 0.015$	$5.2 \pm 2.4$	--	--
<b>Sf-MM</b>	$91.6 \pm 2.5$	$0.096 \pm 0.025$	$-14 \pm 1.3$	$94.2 \pm 0.9$	$15.9 \pm 0.1$
<b>Gal-Sf-MM</b>	$91.4 \pm 0.9$	$0.142 \pm 0.008$	$1.6 \pm 2.9$	$91.9 \pm 3.6$	$15.5 \pm 0.5$

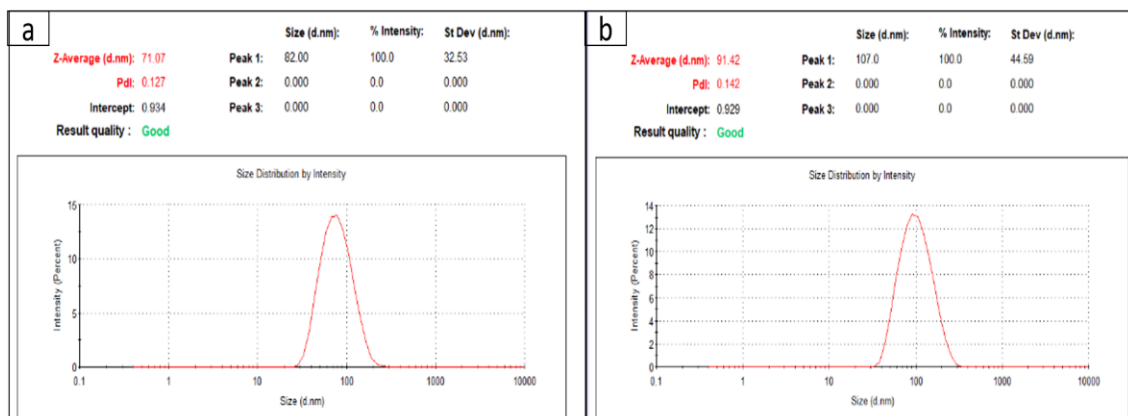


Figure 6.1: DLS reports of the particle size of Blank Gal-MM (a) Gal-Sf-MM (b).

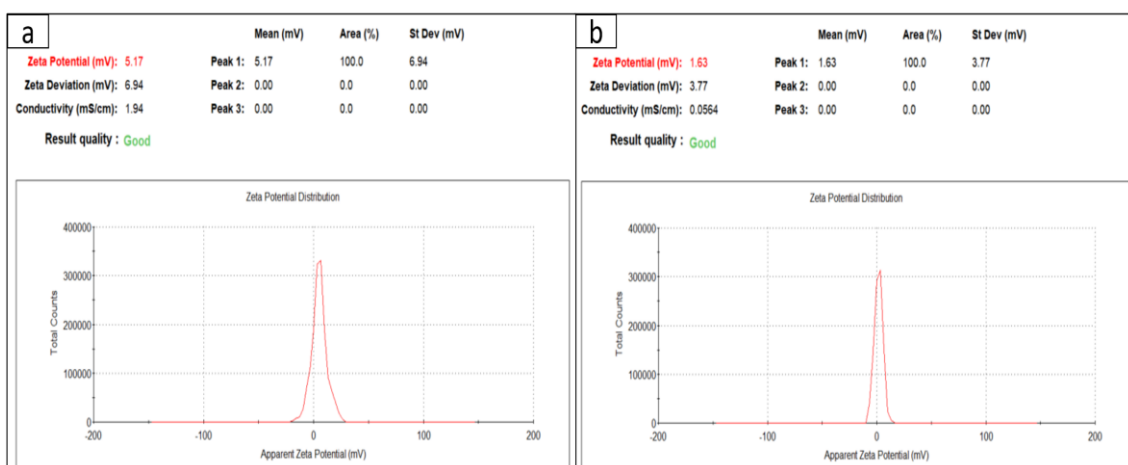


Figure 6.2: DLS reports of the Zeta Potential of Blank Gal-MM (a) and Gal-Sf-MM (b).

### 6.3.3. Morphology using transmission electron microscopy (TEM)

TEM was used to visualise the formulated micelles. As depicted in Figure 6.3, all micelles revealed a spherical shape in the particle size range around 100 nm with no significant difference in both shape and particle size between MM and Gal-MM.

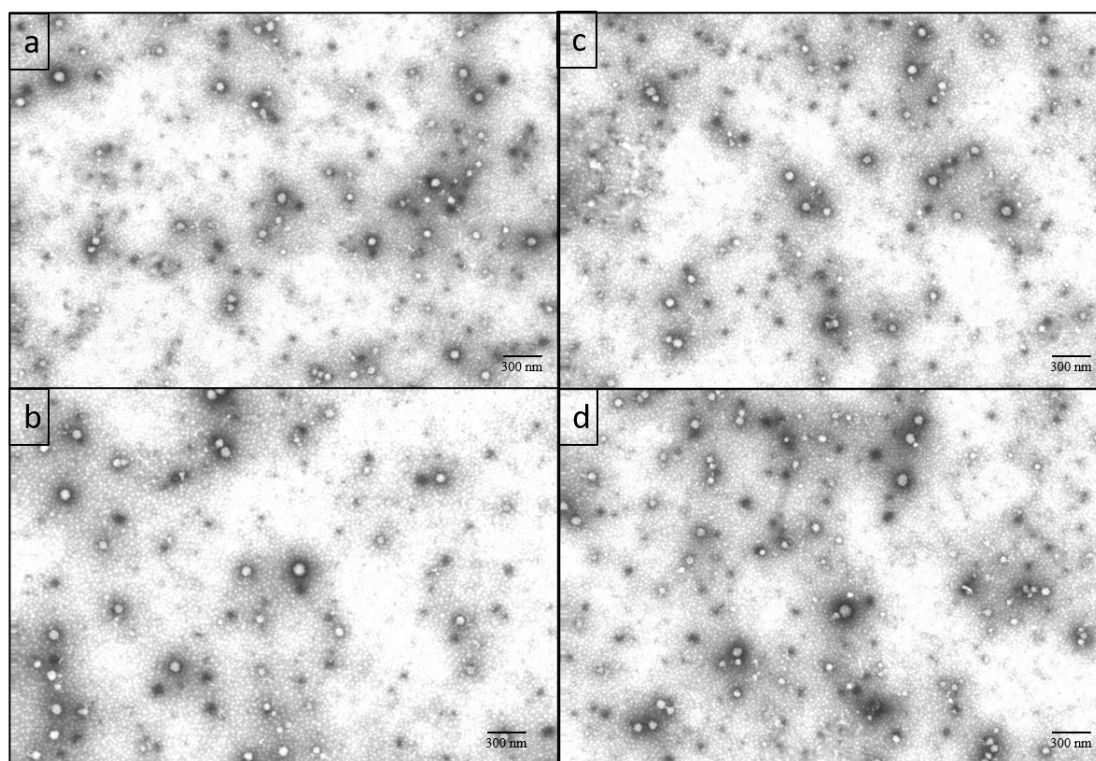


Figure 6.3: TEM images of (a) blank MM, (b) Sf-MM, (c) blank Gal-MM, and (d) Gal-Sf-MM.

#### 6.3.4. Short-term stability of Sf-MM and Gal-Sf-MM

The short-term stability study of Sf-MM and Gal-Sf-MM was done to ensure the colloidal stability and the drug loading during the study time when stored at 4° C for up to 14 days. As depicted in Figure 6.4, both Sf-MM and Gal-Sf-MM did not show any significant ( $p > 0.05$ ) difference in both particle size and polydispersity index. Moreover, both micellar systems did not exhibit any sign of drug precipitation or aggregation, which was confirmed by assessing the entrapment efficiency that remained unchanged during storage time. This asserts the high solubilising capacity of Soluplus® and TPGS for Sf to withstand the effect of storage under lowered temperature<sup>485</sup>. This micellar stability is attributed to the compatibility between Soluplus® and TPGS and the low CMC of the formed micelles<sup>290,293</sup>.

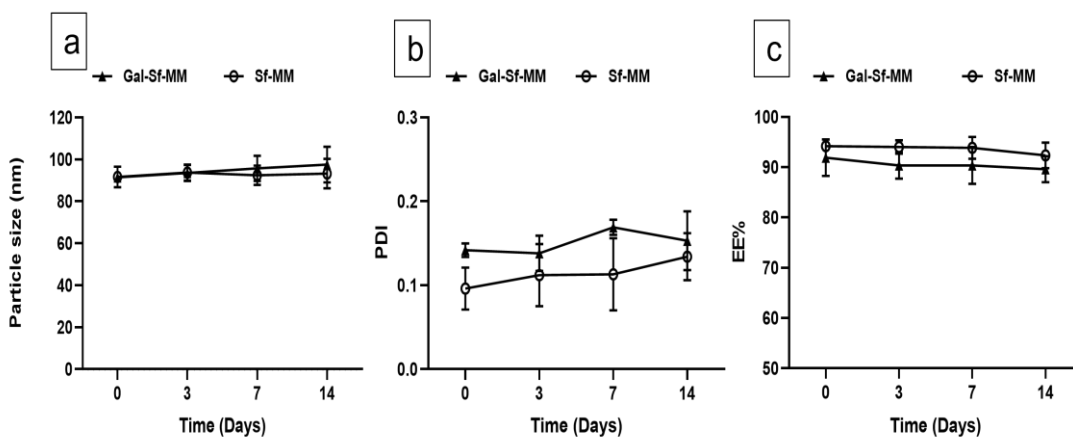


Figure 6.4: The effect of short-term storage of Sf-MM and Gal-Sf-MM at 4°C for 14 days on particle size (a), polydispersity index, PDI (b), and EE% (C).

### 6.3.5. Colloidal stability in administration and physiological conditions

Colloidal stability of micellar systems under administration conditions is essential to ensure the safety and accuracy of drug cargo. Moreover, Upon intravenous injection, micelles encounter a variety of environmental changes, including considerable dilution, exposure to pH and salt fluctuations, and interaction with various proteins and cells<sup>457,486</sup>. Therefore, particle size, polydispersity index and zeta potential were monitored for any change under tested conditions. For administration conditions, both 0.9% NaCl and 5% dextrose were used as they are the most common diluents for intravenous administration. Micellar dispersions were diluted 10 times and incubated for 30 min at 25° C. Results revealed no substantial change in both particle size and polydispersity index of the incubated samples compared to initial values before dispersion in the tested media (Table 6.1) and at zero time after dispersion in the tested media (Table 6.2 and 6.3), regardless of the dilution medium. However, in the case of 0.9% NaCl, the zeta potential of Sf-MM has been diminished to almost neutrality due to the presence of NaCl electrolytes that neutralised surface charge (Table 6.2) with no profound impact on Gal-Sf-MM due to low Zeta potential values. Despite these low zeta potential values, micelles retained their colloidal size, suggesting that micelles are primarily sterically stabilised. On the other hand, the 5% dextrose solution did not exhibit a remarkable effect on the zeta potential of both micellar systems (Table 6.3).

Table 6.2: Particle size (PS), polydispersity index (PDI), and zeta potential (ZP) of Sf-MM and Gal-Sf-MM before and after incubation in 0.9% NaCl at 25°C for 30 min (n=3).

	Zero time			30 min		
	P.S. $\pm$ SD (nm)	PDI $\pm$ SD	ZP $\pm$ SD (mV)	P.S. $\pm$ SD (nm)	PDI $\pm$ SD	ZP $\pm$ SD (mV)
Sf-MM	108.1 $\pm$ 1.7	0.262 $\pm$ 0.013	-1.7 $\pm$ 0.9	85.2 $\pm$ 1.1	0.154 $\pm$ 0.019	-2.1 $\pm$ 1.8
Gal-Sf-MM	87.2 $\pm$ 5	0.227 $\pm$ 0.021	2.3 $\pm$ 1.6	74.1 $\pm$ 1.3	0.062 $\pm$ 0.019	1.5 $\pm$ 0.5

Table 6.3: Particle size (PS), polydispersity index (PDI), and zeta potential (ZP) of Sf-MM and Gal-Sf-MM before and after incubation in 5% dextrose at 25°C for 30 min (n=3).

	Zero time			30 min		
	P.S. $\pm$ SD (nm)	PDI $\pm$ SD	ZP $\pm$ SD (mV)	P.S. $\pm$ SD (nm)	PDI $\pm$ SD	ZP $\pm$ SD (mV)
Sf-MM	91.2 $\pm$ 2.8	0.122 $\pm$ 0.004	-10.2 $\pm$ 1.1	89.9 $\pm$ 1.1	0.129 $\pm$ 0.008	-14.6 $\pm$ 0.9
Gal-Sf-MM	85.5 $\pm$ 1.2	0.138 $\pm$ 0.043	1.5 $\pm$ 2.6	89.3 $\pm$ 2.8	0.075 $\pm$ 0.038	1.6 $\pm$ 1.7

Furthermore, as a trial to investigate the micellar behaviour upon intravenous administration, micelles were incubated in 5.4% BSA in PBS at pH 7.4 (mimicking serum physiological environment) for 72 h at 37° C. BSA solution exhibited its main peak around 9 nm (Figure 6.5a) due to the formation of colloidal solution<sup>442</sup>. On the other hand, Both Sf-MM and Gal-Sf-MM revealed bimodal size distribution with a peak at 9 nm representing BSA and another peak at 117.1  $\pm$  0.8 and 100.1  $\pm$  2.3 nm, respectively, representing the micelles (Figure 6.5b and c). This slight but significant ( $p < 0.05$ ) increase in particle size could be attributed to the adsorption of BSA macromolecules on the surface of polymeric micelles<sup>230,443-445</sup>. Nevertheless, the protein adsorption was considerably low which could be ascribed to the shielding effect of PEG units in the structure of both TPGS and Soluplus®<sup>487,488</sup>. This confirms the colloidal stability of micellar systems under physiological serum conditions for 72 h. This finding comes in agreement with previously reported data<sup>415</sup>.

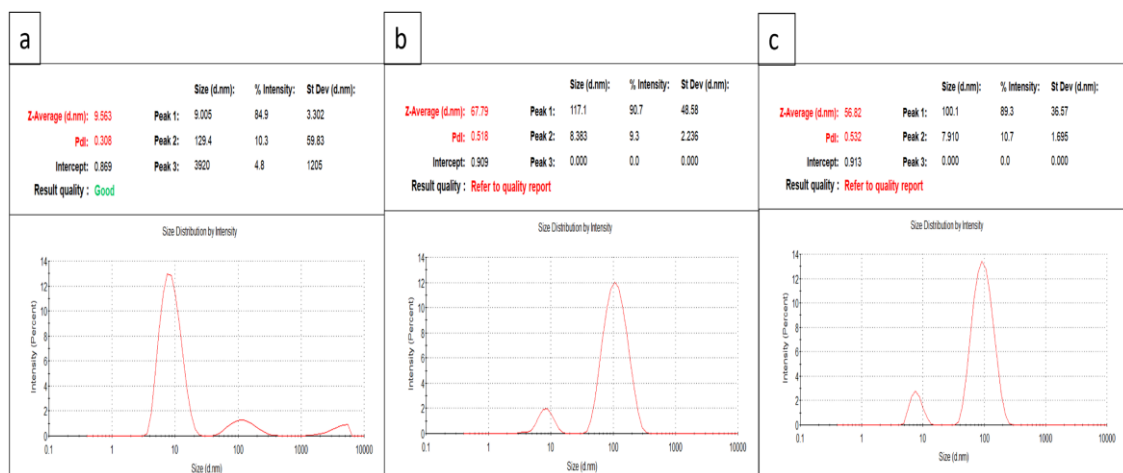


Figure 6.5: DLS reports of 5.4%BSA in PBS at 7.4 (a), Sf-MM in 5.4% BSA in PBS at 7.4 (b), and Gal-Sf-MM in 5.4% BSA in PBS at 7.4 (c) after incubation for 72 h at 37° C.

### 6.3.6. Solid-state characterisation

#### 6.3.6.1. Attenuated total reflection-Fourier transform infrared (ATR-FTIR)

Fourier transform infrared spectroscopy (FTIR) spectra of Soluplus®, Gal-TPGS, Sf, physical mixture of (Soluplus, Gal-TPGS, and Sf at 4:1:1 ratio), Blank-Gal-MM, and Gal-Sf-MM are shown in Figure 6.6.6. Soluplus® spectrum exhibited bands at  $3448.6\text{ cm}^{-1}$  (O-H stretching),  $2927.8\text{ cm}^{-1}$  (aromatic C-H stretching),  $1736\text{ cm}^{-1}$ ,  $1630\text{ cm}^{-1}$  (C=O stretching), and  $1476\text{ cm}^{-1}$  (C-O-C stretching)<sup>466</sup>. Gal-TPGS showed its characteristic bands at  $3377\text{ cm}^{-1}$  (OH of lactobionic acid) and  $1713\text{ cm}^{-1}$  (C=O of amide bondage) as previously discussed in Chapter 4 (section 4.3.2.1.). The Sf spectrum showed two characteristic bands at  $3298\text{ cm}^{-1}$  and  $3337\text{ cm}^{-1}$  due to the N-H stretching of amide. The observed band at  $3074\text{ cm}^{-1}$  is related to the C-H stretching band with a characteristic band at  $1705\text{ cm}^{-1}$  of the amide C=O group<sup>389</sup>. The physical mix spectrum displayed all the peaks for all components with decreased intensities for Gal-TPGS and SF due to the dilution effect. Besides, the Gal-Sf-MM spectrum was comparable to the physical mix, while Blank-Gal-MM one was missing Sf peaks. Collectively, there was no detectable chemical change in the spectra of the ingredients. The FTIR data interpretation for a non-galactosylated system was previously discussed in Chapter 5 (section 5.3.5.1.).

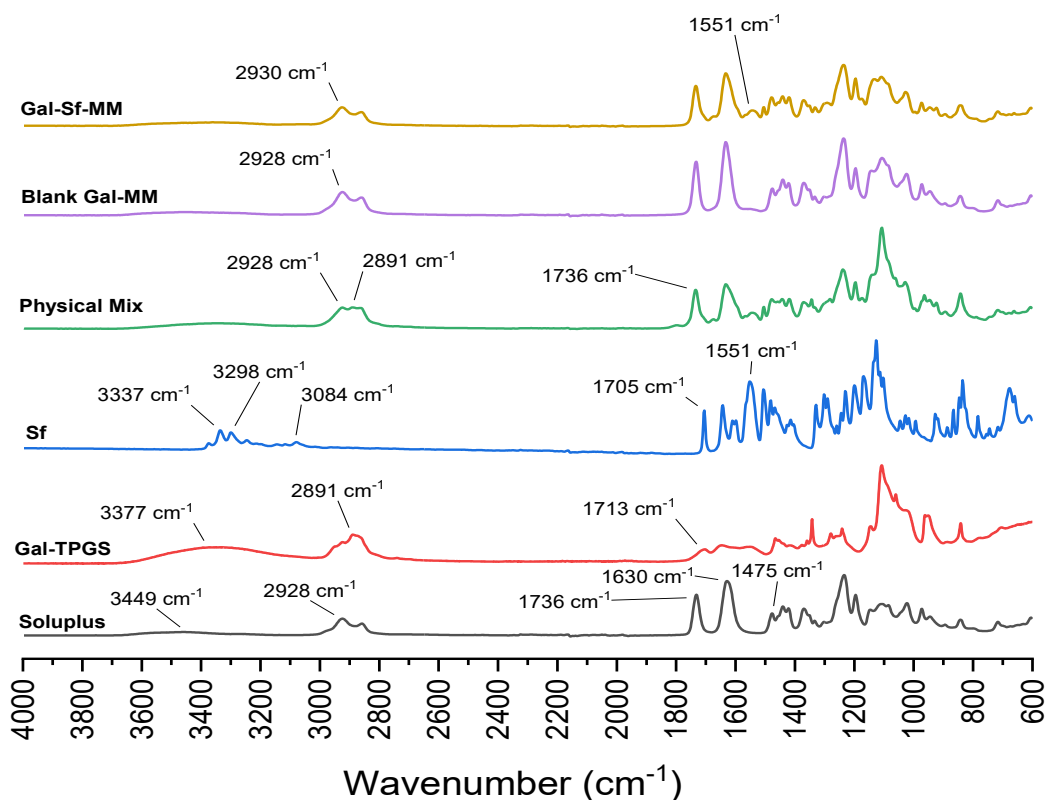


Figure 6.6.6: FTIR spectra of Soluplus®, Gal-TPGS, Sf, Physical mix, Blank-Gal-MM, and Gal-Sf-MM.

### 6.3.6.2. Differential scanning calorimetry (DSC)

Thermal behaviour of different formulations was characterised using the DSC technique. As depicted in Figure 6.7, Sf exhibited its sharp endothermic melting peak at 209° C confirming the crystalline structure of crude Sf powder<sup>392,489</sup>. Furthermore, Soluplus showed a broad  $T_g$  peak at 73° C<sup>331,467</sup>, whereas Gal-TPGS exhibited a sharp melting peak at 35.5° C corresponding mainly to TPGS as previously reported<sup>331</sup>. Interestingly, the physical mix thermogram revealed peaks for both Gal-TPGS and Soluplus but did not show the Sf Peak. This may indicate the high affinity towards the melted polymeric material leading to the complete dissolution of Sf in the melted matrix during the heating cycle which rationalises the high loading capacity of Sf in the micellar system. Consequently, the thermogram of Gal-Sf-MM also did not show Sf melting peak confirming the existence of Sf at a molecular state in the freeze-dried micelles. The same observation was reported by Truong, D. H. *et al.* when Sf-Soluplus solid dispersion was prepared using the spray drying method<sup>127</sup>.

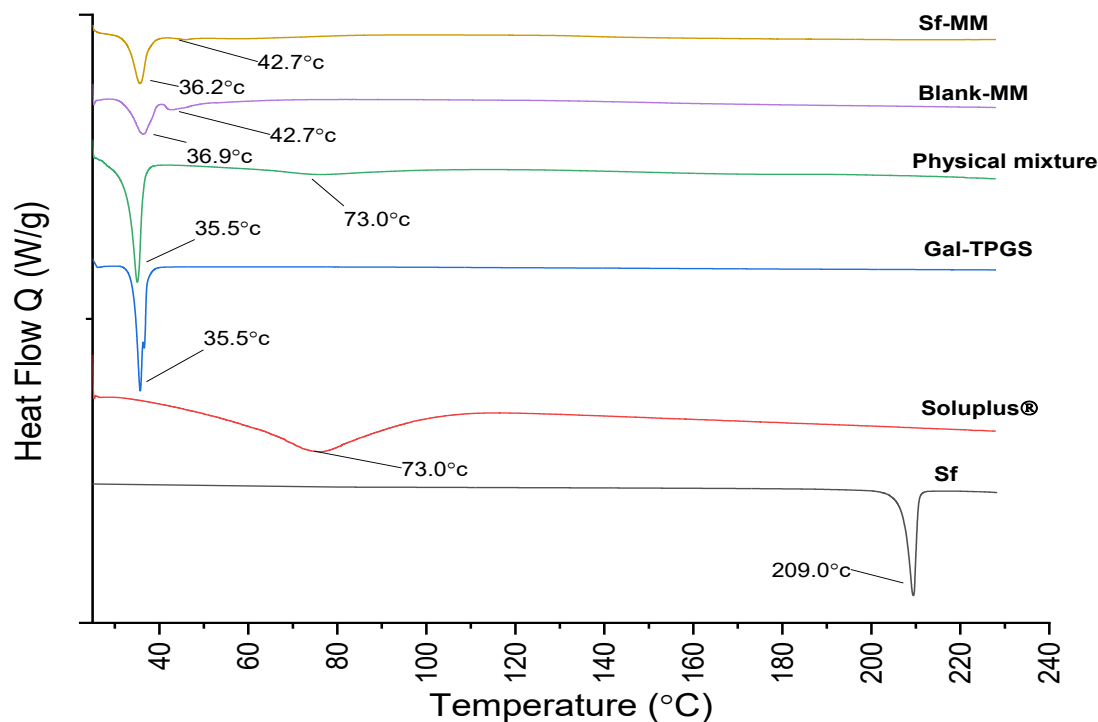


Figure 6.7: Thermograms of Sf, Soluplus, Gal-TPGS, Physical mix, Blank-Gal-MM and Gal-Sf-MM

### 6.3.6.3. Powder X-ray diffraction (PXRD)

For further investigation, the crystallinity of Sf powder, Soluplus, Gal-TPGS, physical mix, blank and Sf-loaded MM were determined via PXRD. From Figure 6.8, the diffraction pattern of Soluplus showed an amorphous structure with no  $2\theta$  peaks<sup>331,469</sup>. However, Gal-TPGS exhibited two distinguishing  $2\theta$  peaks at  $19.2^\circ$  and  $23.4^\circ$ <sup>470</sup>. Sf powder exhibited various characteristic  $2\theta$  peaks at  $11.3^\circ$ ,  $18.5^\circ$ , and  $24.7^\circ$  confirming a highly crystalline structure of Sf. The physical mix diffraction pattern showed the distinctive peaks of both Gal-TPGS and Sf. At the same time, Gal-Sf-MM only revealed Gal-TPGS peaks at lower intensities due to nanoformulation with a complete disappearance of Sf characteristic peaks confirming that Sf is molecularly encapsulated into the micellar structure.

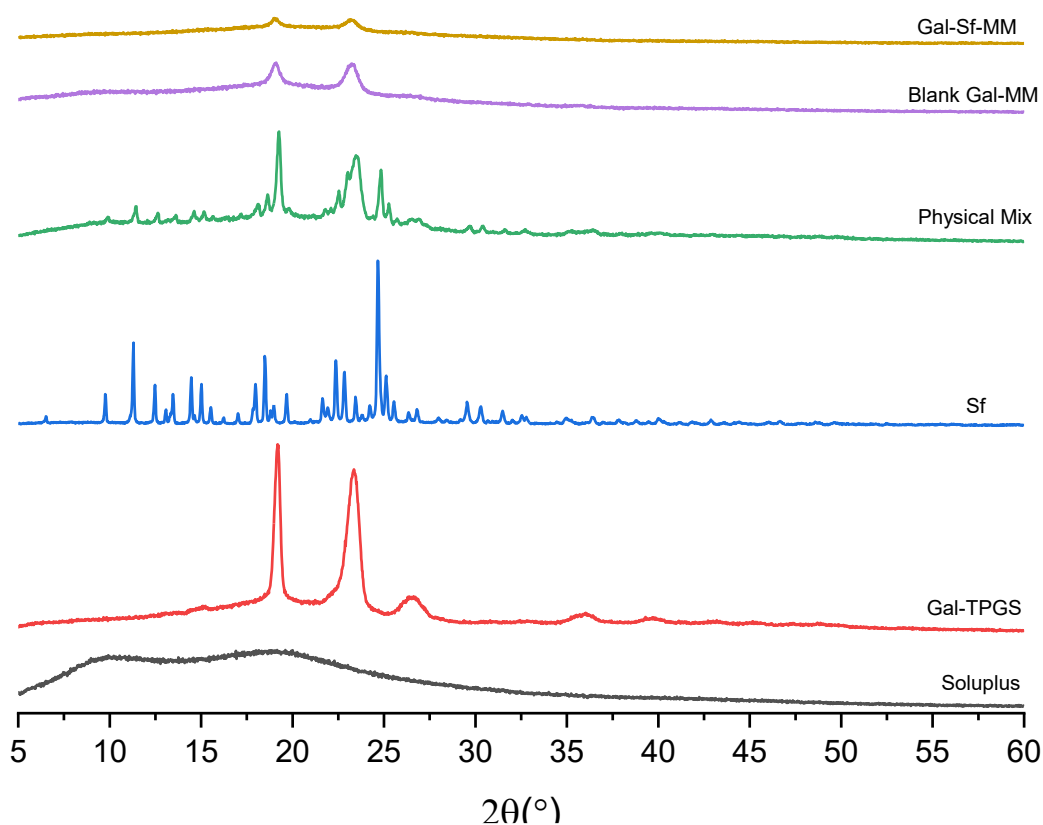


Figure 6.8: PXRD patterns of Soluplus, Gal-TPGS, Sf, physical mixture, Blank and Gal-Sf loaded MM.

### 6.3.7. Critical micellar concentration (CMC) measurement

As aforementioned, CMC is a crucial parameter that determines the physical stability of any micellar system against dilution. Therefore, the CMC of both TPGS/Soluplus mixed micelles and their galactosylated counterpart was determined via the iodine ultraviolet spectrophotometric method<sup>327</sup>. As depicted in Figure 6.9, the CMC of galactosylated TPGS/Soluplus mixed micelles was higher ( $123 \pm 8 \mu\text{g/mL}$ ) than unmodified TPGS/Soluplus mixed micelles ( $106.9 \pm 2.9 \mu\text{g/mL}$ ) at  $25^\circ\text{C}$ . It has been established that the micellar thermodynamic stability is influenced by both of copolymer's hydrophobic block length and the interactions of the hydrophilic block within the micellar corona with the aqueous media<sup>457</sup>. Thus, incorporating hydrophilic moieties (Gal) into the polymer structure increases the copolymer's hydrophilic/hydrophobic balance, resulting in an augmented micellar corona's hydrophilic character, and decreases mixed micelles' propensity towards self-aggregate into polymeric micelles<sup>490</sup>. The same results have been reported previously by Moretton et al<sup>442</sup> after glycosylation of Soluplus® with glucose

using a microwave-assisted ring-opening reaction of  $\delta$ -gluconolactone. It was found that the CMC of glycopolymer has been increased from 22  $\mu\text{g/mL}$  to 151  $\mu\text{g/mL}$  after glycosylation of Soluplus®.

It is worth mentioning that CMC of methoxy-poly(ethylene glycol)-block-poly(D, L-lactide) (mPEG- PDLA) polymer (the former polymer of the marketed product Genexol® PM) loaded with docetaxel was determined to be 44  $\mu\text{g/mL}$ <sup>491</sup> suggesting that the obtained CMC of MM and Gal-MM are within the acceptable range for clinical application.

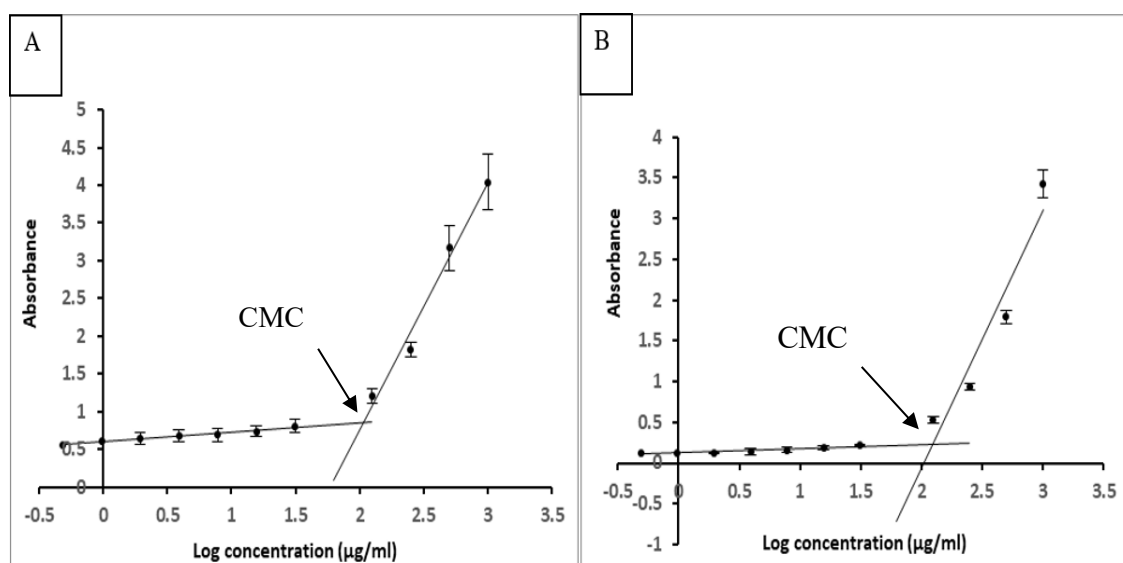


Figure 6.9: Determination of critical micelle concentration (CMC) of MM (A) and Gal-MM(B) using iodine UV-Vis spectroscopy method.

### 6.3.8. *In-vitro* dissolution in PBS at pH 7.4

From Figure 6.10, Sf solution reached 100% drug release after almost 20 h, while both Sf-MM and Gal-Sf-MM only released  $69.1 \pm 8\%$  and  $68.6 \pm 3.3\%$  h, respectively, after 120 h. Moreover, Both Sf-MM and Gal-Sf-MM showed mean dissolution time (MDT) of  $38.1 \pm 4.1$  h and  $39.6 \pm 0.8$  h, respectively, which is 10 times higher than the Sf solution ( $4.6 \pm 3.5$  h), which asserts that encapsulation of Sf into micellar system confers a sustained release pattern for Sf.

For a comprehensive comparison between Sf release profiles, both difference factor ( $f_1$ ) and similarity factor ( $f_2$ ) were calculated using the equations mentioned in Chapter 2 (section 2.3.4.). From Table 6.4, both Sf release profiles from Sf-MM and Gal-Sf-MM

showed high similarity ( $F1 < 15$  and  $F2 > 50$ ). In contrast, the release profile of Sf solution was different (dissimilar) to both Sf-MM and Gal-Sf-MM release profiles ( $F1 > 15$  and  $F2 < 50$ ).

Furthermore, by comparing the obtained drug release profiles with different kinetic models, Sf solution release followed first-order kinetics, where drug release merely depends on the remaining drug concentration in the dialysis bag (Table 6.5). At the same time, both Sf-MM and Gal-Sf-MM best fitted with the Korsmeyer-Peppas model with  $n$  values between 0.5 and 1, which indicates an anomalous transport of drug molecules and by that drug release is governed by different mechanisms (such as dissolution, diffusion, or/and micellar disaggregation).

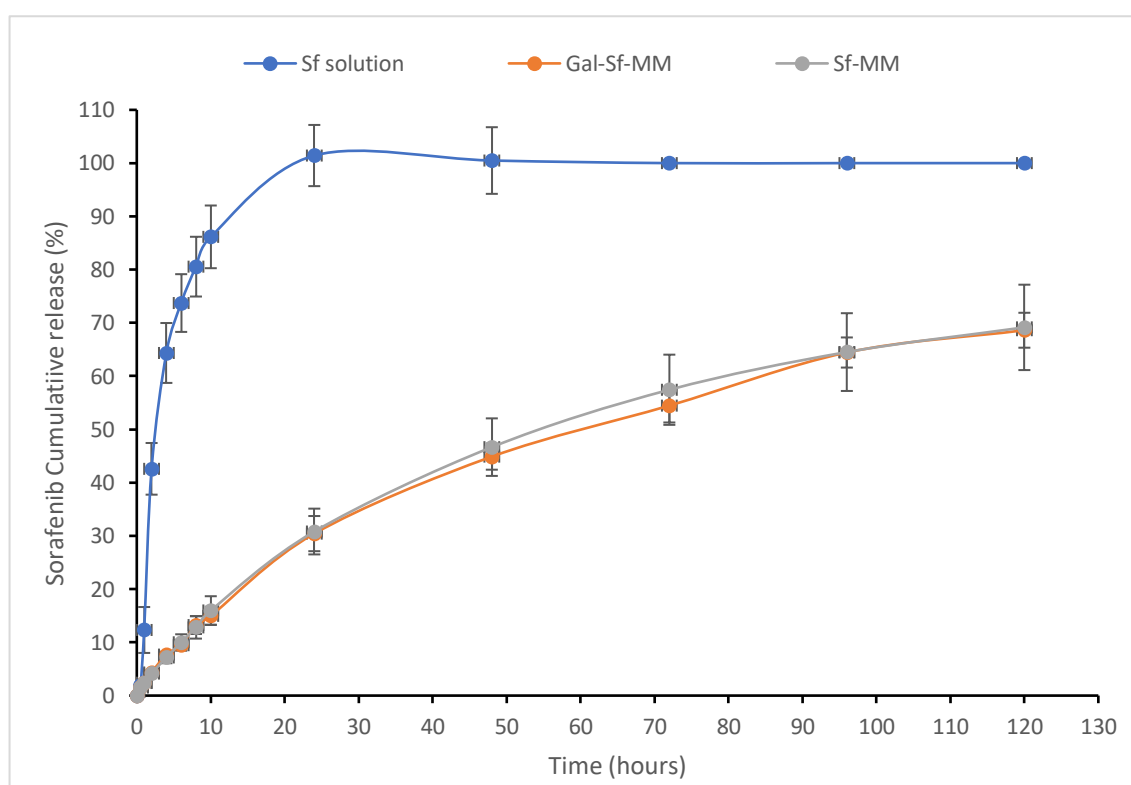


Figure 6.10: *In-vitro* sorafenib release profiles of Sf solution, Sf-MM, and Gal-Sf-MM in PBS at pH 7.4 containing 1% tween 80 at 37° C under shaking at 100 rpm for 5 days.

Table 6.4: Difference factors ( $f_1$ ) and Similarity factors ( $f_2$ ) of the release profiles of Sf solution, Sf-MM, and Gal-Sf-MM.

Comparison parameter	formulation		
	Sf solution	Sf-MM	Gal-Sf-MM
Difference factor ( $f_1$ )	62.6		
		2.67	
	63.3		63.3
Similarity factor ( $f_2$ )	15.8		
		91.9	
	15.6		15.6

Table 6.5: *In-vitro* drug release kinetic models of Sf solution, Sf-MM and Gal-Sf-MM.

Model	Equation	$R^2$ of different formulations		
		Sf solution	Sf-MM	Gal-Sf-MM
<b>Zero-order</b>	$f = k_0 \cdot t$	- 0.6078	0.849	0.9027
<b>First-order</b>	$f = 1 - \exp(-kt)$	0.9878	0.9795	0.9897
<b>Higuchi</b>	$f = k_H \cdot t^{0.5}$	0.352	0.9776	0.9794
<b>Korsmeyer-Peppas</b>	$f = k_{kp} \cdot t^n$	0.977 $n = 1.002$	<b>0.9901</b> $n = 0.598$	<b>0.9929</b> $n = 0.603$
<b>Hixon-Crowell</b>	$f = [1 - (1 - k_{HC} \cdot t)^3]$	0.2887	0.9605	0.9624

### 6.3.9. Surface accessibility (lectin-induced agglutination)

Surface exposure of the galactosylated moiety of mixed micelles and their selective binding capability to ASGP receptors was evaluated through the lectin agglutination test. As depicted in Figure 6.11, Gal-Sf-MM showed an increment in the turbidity after adding RCA<sub>120</sub> compared to the non-galactosylated counterpart. Moreover, the agglutination was reversed upon the addition of free galactose, asserting the agglutination's specificity towards the galactose moiety. However, it was remarkable that the magnitude of the change in the absorbance was limited (maximum absorbance was 0.03). That could be due to using a low concentration of micelles, or the nanosize of the micelles was not large enough to induce a detectable change in the turbidity, especially RCA<sub>120</sub> can only bind to

two molecules of sugar. The same findings were previously reported with a maximum absorbance values around 0.1 and 0.04 UV absorbance units<sup>437,492</sup> which is regarded as a limitation of this assay. Therefore, some reports proposed using DLS or TEM to confirm the agglutination<sup>442</sup>.

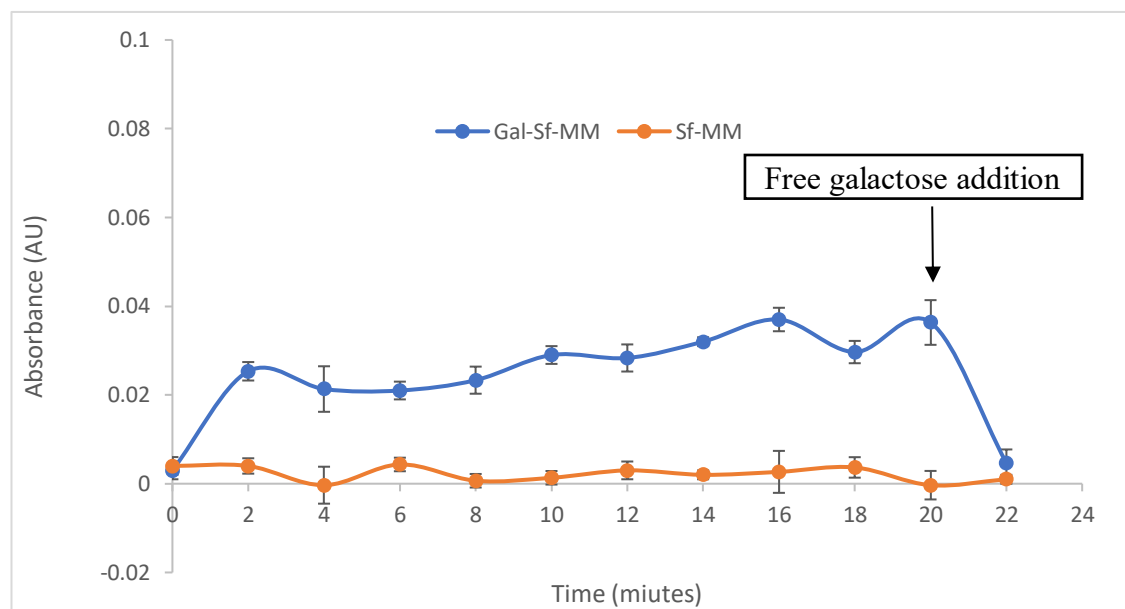


Figure 6.11: RCA<sub>120</sub> induced agglutination of Sf-MM and Gal-Sf-MM when 100  $\mu$ L of micellar dispersion (10 mg/mL) was incubated with 100  $\mu$ L of RCA<sub>120</sub> (1 mg/mL) for 20 min with continuous measurement of the absorbance at 450 nm at 2 min intervals. The reversibility of agglutination was verified by adding free D-galactose (10 mg/mL) at the 20<sup>th</sup> min.

### 6.3.10. *In-vitro* cellular studies

#### 6.3.10.1. *In-vitro* cellular cytotoxicity

MTS assay was carried out to investigate the effect of Sf encapsulation into micelles and galactosylation of the mixed micelles on the cytotoxicity of sorafenib on HepG2 cells after incubation for 48 h. As shown in Figure 6.12 and Table 6.6, Gal-Sf-MM showed enhanced cytotoxicity with a 1.4 times decrease in IC<sub>50</sub> ( $3.57 \pm 0.5 \mu\text{g/mL}$ ) compared to untargeted Sf-MM (IC<sub>50</sub> =  $5.07 \pm 0.56 \mu\text{g/mL}$ ). This could be ascribed to the enhanced cellular uptake of Gal-Sf-MM through ASGP receptor-mediated active endocytosis. Additionally, when cells were incubated with Gal-Sf-MM and free galactose (10 mg/mL), the cytotoxicity decreased (IC<sub>50</sub> =  $4.87 \pm 0.56 \mu\text{g/mL}$ ) compared to the incubation with Gal-Sf-MM without Galactose. This may be owing to the ability of free galactose to

competitively bind to ASGPR and saturate them, inhibiting the active process of cellular endocytosis<sup>107</sup>.

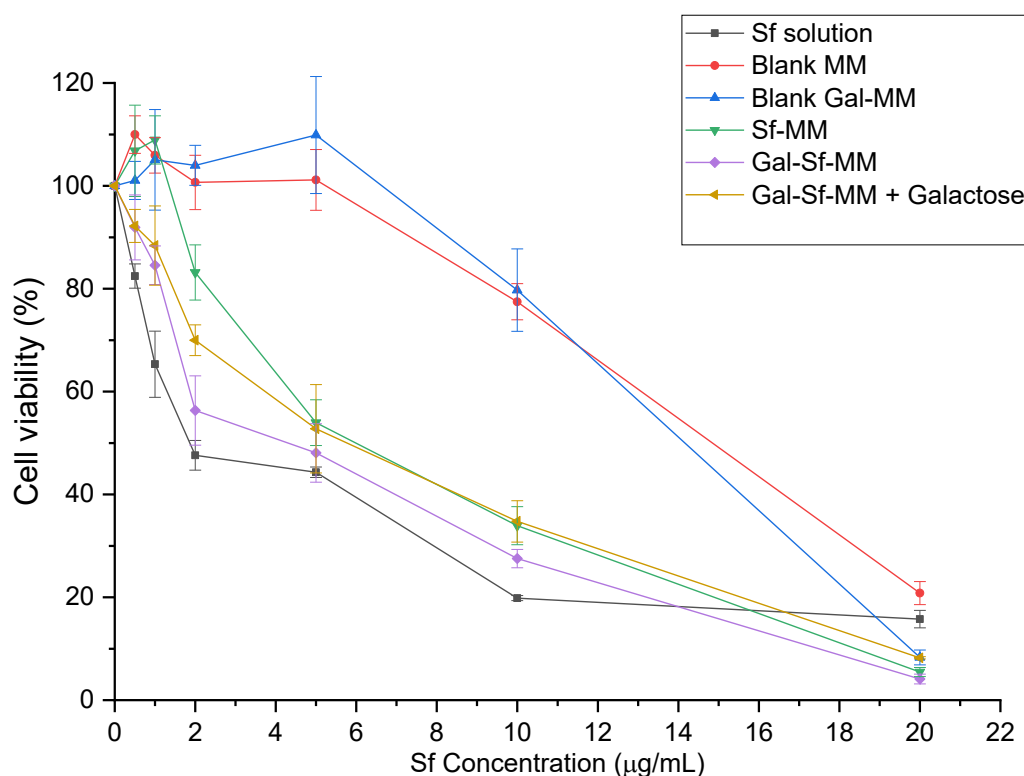


Figure 6.12: Cell viability plot of HepG2 cells after incubation for 48 h at 37° C with free Sf solution, Blank MM, blank Gal-MM, Sf-MM, Gal-Sf-MM and Gal-Sf-MM in the presence of free galactose (10 mg/mL). (both blank formulations were diluted similarly to the Sf-loaded counterparts)

Table 6.6: IC<sub>50</sub> values of different Sf formulations after incubation with HepG2 cells for 48 h

Formula	Sf solution	Sf-MM	Gal-Sf-MM	Gal-Sf-MM + Galactose
IC <sub>50</sub> (µg/mL)	2.38 ± 0.33	5.07 ± 0.56	3.57 ± 0.5	4.87 ± 0.56

Interestingly, free Sf solution demonstrated higher cytotoxicity (IC<sub>50</sub> = 2.38 ± 0.33 µg/mL) than all the Sf-loaded micellar formulations. This could be explained by the fact that sf is encapsulated inside a micellar system and needs more time to be digested by the cells compared to the free Sf molecules. Similar findings were observed by Bernabeu, E. *et al*<sup>265</sup> when Paclitaxel (PTX) loaded Soluplus micelles showed lower cytotoxicity than

free PTX solution. Nevertheless, SF encapsulation into micelles enables the intravenous administration of Sf where all marketed Sf products are orally administered with low oral bioavailability (relative bioavailability of 38-49% compared to oral solution)<sup>125,130</sup>. Besides, Sf encapsulation into nanosized formulations is expected to exhibit passive preferential accumulation to cancerous tissues due to enhanced permeation and retention phenomenon (EPR) beside the active targeting of ASGPR mediated endocytosis. This all is anticipated to lower the side effects of Sf on normal tissues.

Remarkably, blank micelles also exhibited significant cytotoxicity at high concentrations (> 10 µg/mL). Since Soluplus® is reported to be safe on different cell types<sup>265</sup>, the cytotoxicity of the mixed micelles could be attributed to the cytotoxic and pro-apoptotic activity of TPGS against cancer cells through the generation of reactive oxygen species<sup>265,328,442,458,461</sup>.

#### **6.3.10.2. Cellular uptake using an inverted fluorescence microscope**

To study the impact of the micelles galactosylation on their uptake into HepG2 cells, the uptaken C6-labeled micelles into the cells after 4 h incubation with cells were inspected using a fluorescence microscope. The results are depicted in Figure 6.13 and 6.14. Comparing to their non-galactosylated counterparts, C6-Gal-MM (middle row) showed a notably higher fluorescence, suggesting that the galactosylation of micelles increased their cellular uptake into HepG2 cells through receptor-mediated endocytosis. To further clarify the effect of galactose ligand on the receptor-mediated cellular uptake, the uptake of C6-Gal-MM was compared in the presence and absence of free galactose as a competitive inhibitor for ASGPR. As shown in Figure 6.13 and 6.14 (lower row), the fluorescence intensity was noticeably reduced in the presence of free galactose compared to the same formula in the absence of free galactose, indicating that galactosylated TPGS plays a significant role in ASGPR recognition and the uptake by HepG2 cells<sup>414</sup>.

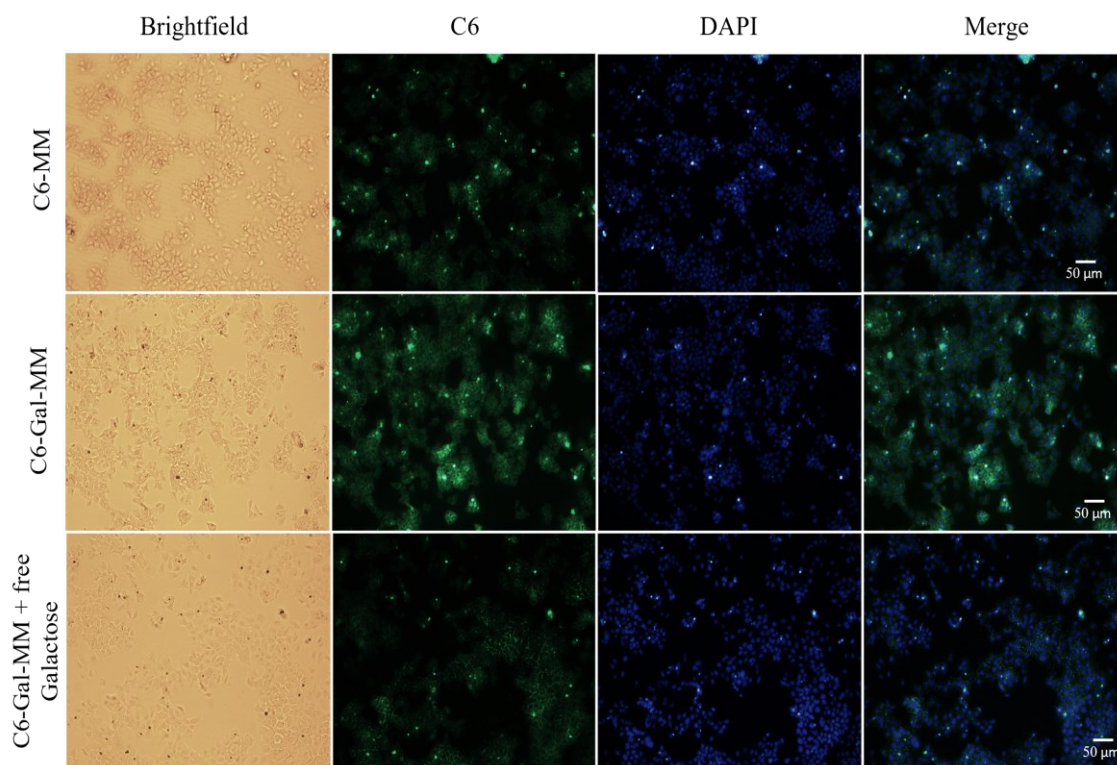


Figure 6.13: Fluorescence microscope images using 10X objective lens of HepG2 cells after incubation for 4 h with different C6-loaded mixed micelles at 37°C.

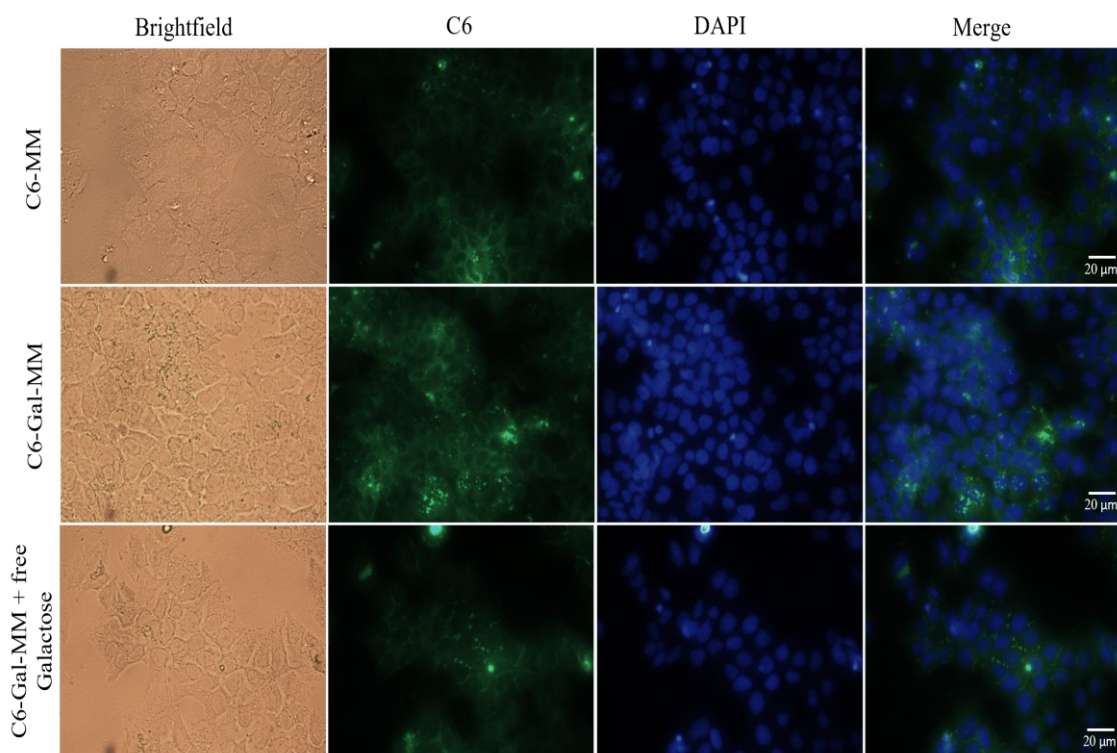


Figure 6.14: Fluorescence microscope images using 40X objective lens of HepG2 cells after incubation for 4 h with different C6-loaded mixed micelles at 37° C.

### 6.3.10.3. Cellular uptake study using flow cytometer

For further quantitative investigation of the effect of galactosylation on the cellular uptake of micelles by HepG2 cells via ASGPR-mediated endocytosis, a flow cytometer was used to measure the fluorescence intensity of uptaken micelles. The green fluorescence intensity was measured from 10,000 events (HepG2 cells) in gate (P2) using the FTIC-A channel. As depicted in Figure 6.15, HepG2 cells treated with C6-Gal-MM have shown 1.43 times higher cellular uptake than their non-galactosylated counterpart, suggesting that galactosylation has contributed to a receptor-mediated cellular uptake. Furthermore, the presence of free galactose has significantly ( $p < 0.05$ ) reduced the cellular uptake, which confirms that the cellular uptake of Gal-MM was enhanced through ASGP receptor-mediated endocytosis. This data agrees with the cytotoxicity study findings in the previous section, confirming that the enhancement of the cytotoxicity of Gal-Sf-MM is ascribed to the enhancement of cellular uptake due to ASGP receptors mediated endocytosis<sup>107,417,493</sup>. The same cellular uptake pattern was noticed by Feng, L. *et al.*<sup>494</sup> when tested galactosylated micelles composed of pH-responsive methoxyl poly(ethylene glycol)-b-poly( $\beta$ -amino ester) (MPEG-PBAE) for the targeted delivery of doxorubicin (DOX) to hepatoma cells (HepG2 cells). It was found that galactosylated micelles showed higher cellular uptake after incubation with HepG2 cells for 4 h compared to non galactosylated counterpart. Moreover, the preincubation of cells with galactose resulted in a lower cellular uptake while preincubation with glucose has almost no effect on the endocytosis of the targeted micelles<sup>494</sup>.

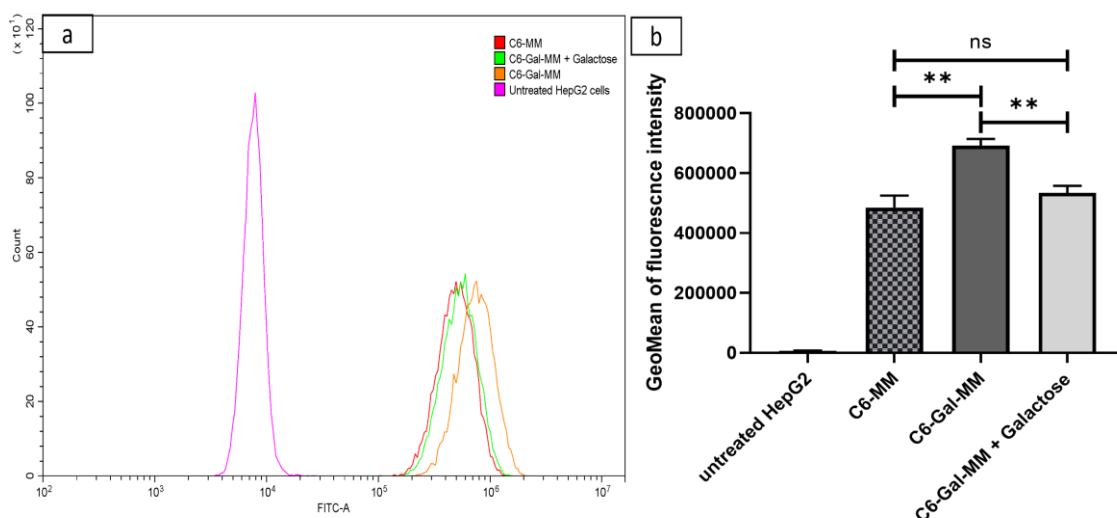


Figure 6.15: Histogram of the green fluorescent events using Fluorescein isothiocyanate channel (FITC-A) detecting cells that have uptaken C6-loaded micelles (a), and GeoMean fluorescence intensities of HepG2 cells after incubation for 4 h at 37° C with different C6-loaded micelles formulations at a concentration of 0.5 µg/mL (b). \*\* (P < 0.01), and ns (P > 0.05). Error bars represent the standard deviation and n=3.

#### 6.4. Conclusion

Galactosylated TPGS/Soluplus polymeric mixed micelles were successfully synthesised by solvent evaporation method producing nanoparticles within 100 nm particle size and narrow size distribution ( $> 0.2$ ). Moreover, mixed micelles showed very good loading capacity ( $15.85 \pm 0.13\%$  and  $15.52 \pm 0.52\%$  for Sf-MM and Gal-Sf-MM, respectively), enabling the easy intravenous administration of Sf that is commercially available only in the form of oral tablets (NEXAVAR®). Thus, nanoformulation of Sf into micelles is expected to lower the required dose lessening the side effects and the cost of manufacturing.

By characterising the produced micellar systems, both systems (Sf-MM and Gal-Sf-MM) showed a spherical shape under TEM and with no significant change in FTIR spectra of micelles compared to pure ingredients with a complete encapsulation of Sf into the micellar core at a molecular level as demonstrated in both DSC and PXRD. Both MM systems also showed remarkable colloidal stability under administration conditions (with 10-time dilution in 0.9% NaCl and 5% Dextrose). Moreover, they retained their nanosize

when incubated at 5.4% BSA in PBS (mimicking serum biological condition after IV administration).

Both micellar systems (Sf-MM and Gal-Sf-MM) showed a sustained drug release pattern compared to the drug solution, which may allow reducing the dosing rate of the drug. Although the lectin agglutination assay exhibited some agglutination with Gal-Sf-MM confirming the surface exposure of galactose moieties on the surface of micelles, the magnitude of the increase in the turbidity was limited. This limitation may be attributed to the nanosize of the micelles that are not large enough to induce a detectable increase in turbidity and the use of relatively low concentrations of the micellar system.

At the cellular level, Gal-Sf-MM showed enhanced cytotoxicity on HepG2 cells compared to Sf-MM. While Gal-Sf-MM cytotoxicity was undermined in the presence of free galactose, suggesting the involvement of the surface galactose moieties in the active cellular uptake process. Likewise, C6-Gal-MM showed enhanced cellular uptake compared to C6-MM determined by both fluorescence microscope and flow cytometer.

Conclusively, Gal-TPGS/Soluplus mixed micelle has shown to be a promising strategy for liver-targeted delivery of sorafenib through intravenous administration.



## **Chapter 7**

*Conclusion and future outlook*

## **7.1. General conclusions**

The presented study investigates the influence of the development of different galactosylated nanoformulations on the solubility, anticancer efficiency and liver targeting of Sorafenib (Sf) for treating hepatocellular carcinoma (HCC). Different nanodelivery systems were successfully developed, including SLN, NLC, LNC, and PMs. They showed promising results in enhancing drug solubility and anticancer activity with improved cellular tumour targeting due to the employed targeting strategy.

### **7.1.1. Impact of formulation parameters on the properties of SLN and NLC**

As discussed in Chapter 3, SLN and NLC comprise promising platforms for delivering hydrophobic anticancer agents such as sorafenib. During the preliminary screening, it was found that using high solid lipid concentrations (5% w/v) and insufficient surfactant may lead to the gelation of the lipid dispersion. Moreover, the type and concentration of the surfactant were shown to have a substantial effect not only on the particle size and size distribution of the lipid nanoparticles but also on the drug loading. It was observed that an increase in Tween 80 concentration led to an increase in drug loading up to a certain limit, after which increasing surfactant concentration appears to promote drug partitioning into the aqueous medium, resulting in a decrease in drug loading. In addition, due to the limited solubility of Sf in liquid oils, the incorporation of Peceol<sup>TM</sup> oil into the lipid matrix has shown a limited impact on drug loading compared to the incorporation of lipid miscible solubilisers such as Transcutol® P and Gelucire® 48/16 that exhibited good drug entrapment efficiencies (86.2%, and 93.4%, respectively)

Furthermore, to examine the impact of drug encapsulation into the lipid matrix on sustaining the drug release, drug solution should be considered as a control in the experiment design. Due to low drug solubility in an aqueous buffer, different solvent systems were screened, from which PEG 400 allowed 100% drug release after 20 h. In contrast, other tested solvents did not reach that level due to solvent diffusion and subsequent drug precipitation. Both SLN and NLC showed a prolonged drug release compared to the drug solution.

The *in-vitro* assessment of formulation cytotoxicity on HepG2 cells revealed that the blank SLN and LNC had remarkable cytotoxicity that could be ascribed to the solid lipid, suggesting the presence of impurities. Thus, further investigations are needed to eliminate the source of cytotoxicity.

### **7.1.2. Formulation of Gal-Sf-LNC using lipiodol® oil core**

In Chapter 4, an investigational study was carried out to develop liver-targeted LNC with lipiodol oil core to function as a theranostic agent for HCC. This study found that Solutol® HS content had a profound impact on particle size and drug loading of the LNC. In contrast, replacing MCT (Labrafac® WL 1349) with lipiodol® oil showed a minimal effect on the particle size of LNC with no significant ( $p > 0.05$ ) impact on Sf loading. In addition, the galactosylation of TPGS was successfully synthesised and post-inserted into the preformulated LNC to function as a liver-targeting ligand. Furthermore, the encapsulation of Sf into LNC has demonstrated a means to sustain drug release compared to the free drug solution. From the *in-vitro* cellular studies on HepG2 cells, galactosylated LNC revealed a superior cytotoxic and cellular uptake efficiency compared to untargeted LNC suggesting a key role of ASGPR receptor-mediated endocytosis in the cellular uptake process. Conclusively, this chapter offers a novel galactosylated LNC platform that can efficiently deliver both Sf and Lipiodol oil to liver cancer cells acting as a theranostic agent.

### **7.1.3. Development of single and mixed polymeric micelles to oral delivery of Sf**

Chapter 5 focused on developing sf-loaded polymeric micelles to enhance Sf solubility and dissolution rate for oral administration. In this chapter, the impact of using both single (Soluplus®) and mixed micellar systems (based on Soluplus® and TPGS) on the physicochemical properties of the micellar dispersion and the influence on Sf dissolution and intestinal permeation was investigated. It was found that Soluplus® single micelles had a highly effective Sf solubilisation capacity ( $1.949 \pm 0.009$  mg/mL), while increasing the TPGS ratio in the mixed micelles led to an incremental reduction in Sf solubilisation capacity with no significant effect ( $p > 0.05$ ) on particle size and size distribution of micelles. In addition, both single (SM) and mixed (MM) micelles demonstrated good

stability in SGF and SIF, while both micellar systems showed a significantly ( $p < 0.05$ ) higher dissolution efficiency than Sf suspension.

The in-vitro cellular studies on Caco-2 cells showed that blank SM has a good safety profile on Caco-2 cells, while MM displayed a concentration and time-dependent cytotoxicity due to the presence of TPGS. Furthermore, Sf-SM and Sf-MM demonstrated a significantly ( $p < 0.05$ ) higher apparent permeability across the Caco-2 monolayer than Sf suspension. At the same time, Sf-MM had a modest efflux inhibition property due to the presence of TPGS. Decisively, Soluplus-based single and mixed micelles offer a potential approach to enhance Sf solubility, dissolution rate and intestinal permeation, which is anticipated to be translated into improved oral bioavailability.

#### **7.1.4. Preparation of Galactosylated mixed micelles for liver-targeted delivery of Sf (Gal-Sf-MM)**

As discussed in Chapter 6, Gal-Sf-MM was successfully prepared by a solvent evaporation method using the previously synthesised Gal-TPGS as a targeting ligand and producing nanoparticles with particle sizes around 100 nm and narrow size of distribution ( $> 0.2$ ), having a very high Sf loading capacity ( $> 15.5\%$ ). Gal-Sf-MM displayed a sustained drug release pattern compared to the drug solution. Furthermore, the micellar system showed excellent colloidal stability in both administration (in 0.9% NaCl and 5% dextrose) and physiological conditions (5.4% BSA in PBS at 7.4 ), confirming its suitability for its application. At the cellular level, Gal-Sf-MM displayed enhanced cytotoxicity ( $IC_{50} = 3.57 \pm 0.5 \mu\text{g/mL}$ ) on HepG2 cells compared to its untargeted counterpart ( $IC_{50} = 5.07 \pm 0.56 \mu\text{g/mL}$ ). While Gal-Sf-MM cytotoxicity was undermined in the presence of free galactose ( $IC_{50} = 4.87 \pm 0.56 \mu\text{g/mL}$ ), suggesting the involvement of the surface galactose moieties in the active cellular uptake process. Similarly, C6-Gal-MM showed enhanced cellular uptake (1.43 times) compared to C6-MM examined by both fluorescence microscope and flow cytometer.

Overall, the overall study provides insights into the potential of employing different nanodelivery systems for addressing the Sf low solubility issue, offering potential

candidate nanodelivery systems for enhancing the therapeutic outcomes and clinical application of Sf.

## **7.2.Future outlook**

The presented studies presented different nanodrug delivery systems candidates for Sf, showing promising *in-vitro* results. However, the cellular studies of the galactosylated Sf-loaded SLN and NLC were interrupted due to the COVID-19 lockdown that limited the lab capacities and the transportation between universities to conduct different characterisation techniques. Thus, the following experiments could be needed to evaluate further the biological efficiency of the targeted nanodelivery systems and the contrasting potency of the lipiodol® oil loaded LNC.

### **7.2.1. *In-vitro* cell cellular cytotoxicity studies for SLN and NLC**

As described in chapter 3, blank Precirol® ATO 5-based SLN showed considerable cytotoxicity of HepG2 cells that was most probably attributed to impurities in Precirol® solid lipid since Precirol was reported to be safe on HepG2 cells up to 3.1 mg/mL. Therefore, further cytotoxicity cellular studies using different solid lipid batches could be needed to determine and eliminate the source of cytotoxicity.

### **7.2.2. Further *in-vitro* cellular studies**

Further *in-vitro* cellular studies on HepG2 cells, such as apoptosis assay using annexin V-FITC/propidium iodide method<sup>495</sup>, cycle analysis<sup>495</sup>, and western blot, could be conducted to confirm the efficiency of nanoformulation to induce apoptosis and inhibit the cell growth tumour cells.

### **7.2.3. *In-vitro* and *In-vivo* assessment of the contrasting potency of Gal-Sf-LNC containing lipiodol® oil core**

These experiments could provide proof of concept data about the applicability of the lipiodol oil containing LNC (in Chapter 4) as a contrasting agent. For *in-vitro* investigation, HepG2 cells could be incubated with the Gal-Sf-LNC containing lipiodol® oil for a certain time, followed by the fixation of the cells with 4% formaldehyde. Afterwards, cells could be suspended in 1% agarose gel and visualised using a micro-CT machine<sup>59</sup>. On the other hand, the *in-vivo* assessment using model animals, mostly male BALB/c nude mice, could be carried out by injecting LNC into the model animals, and serial CT images could be taken over different time intervals to monitor the biodistribution and accumulation of the administered dose over the time<sup>63,496</sup>.

### **7.2.4. *Ex-vivo* intestinal permeation study of oral polymeric single and mixed micelles (Sf-SM and Sf-MM)**

From Chapter 5, both Sf-SM and Sf-MM demonstrated a remarkable enhancement in Sf solubility and dissolution efficiency that was reflected on its cellular transport using an *in-vitro* Caco-2 cell model. The investigation of the micellar systems efficiency to enhance the intestinal permeation using *ex-vivo* non-everted sac technique could be a reasonable step. The micellar dispersions could be injected into excised rat intestines via a blunt syringe and tied from both sides, forming a sac. Then, a drug permeation study in ringer solution under sink conditions could be conducted<sup>497</sup>.

### **7.2.5. *In-vivo* animal studies**

As a final preclinical testing stage, successful nanoformulations could be tested for their *in-vivo* efficiency on animal models, such as HepG2 xenograft BALB/c nude mice model, studying the pharmacokinetics, biodistribution, antitumour activity and immunohistochemical analysis to detect the nuclear proliferative markers and apoptosis-related proteins<sup>398</sup>.



## References

1. Rumgay, H. *et al.* Global burden of primary liver cancer in 2020 and predictions to 2040. *J. Hepatol.* **77**, 1598–1606 (2022).
2. Yang, C. *et al.* Evolving therapeutic landscape of advanced hepatocellular carcinoma. *Nat. Rev. Gastroenterol. Hepatol.* (2022) doi:10.1038/s41575-022-00704-9.
3. Llovet, J. M. *et al.* Hepatocellular carcinoma. *Nat. Rev. Dis. Prim.* **7**, (2021).
4. Rahib, L. *et al.* Projecting cancer incidence and deaths to 2030: The unexpected burden of thyroid, liver, and pancreas cancers in the united states. *Cancer Res.* **74**, 2913–2921 (2014).
5. Jemal, A. *et al.* Annual Report to the Nation on the Status of Cancer, 1975-2014, Featuring Survival. *J. Natl. Cancer Inst.* **109**, 1–22 (2017).
6. Chen, S. *et al.* Estimates and Projections of the Global Economic Cost of 29 Cancers in 204 Countries and Territories From 2020 to 2050. *JAMA Oncol.* 1–9 (2023) doi:10.1001/jamaoncol.2022.7826.
7. Aly, A., Ronnebaum, S., Patel, D., Doleh, Y. & Benavente, F. Epidemiologic, humanistic and economic burden of hepatocellular carcinoma in the USA: a systematic literature review. *Hepatic Oncol.* **7**, (2020).
8. Trinchet, J. C. *et al.* Complications and competing risks of death in compensated viral cirrhosis (ANRS CO12 CirVir prospective cohort). *Hepatology* **62**, 737–750 (2015).
9. Singal, A. G., Lampertico, P. & Nahon, P. Epidemiology and surveillance for hepatocellular carcinoma: New trends. *J. Hepatol.* **72**, 250–261 (2020).
10. Akinyemiju, T. *et al.* The Burden of Primary Liver Cancer and Underlying Etiologies From 1990 to 2015 at the Global, Regional, and National Level: Results From the Global Burden of Disease Study 2015. *JAMA Oncol.* **3**, 1683–1691 (2017).
11. Kanwal, F. *et al.* Risk of Hepatocellular Cancer in HCV Patients Treated With Direct-Acting Antiviral Agents. *Gastroenterology* **153**, 996-1005.e1 (2017).
12. Jain, M. K. *et al.* Evaluation of a Multifaceted Intervention to Reduce Health Disparities in Hepatitis C Screening: A Pre-Post Analysis. *Hepatology* **70**, 40–50

- (2019).
13. Park, J. W. *et al.* Global patterns of hepatocellular carcinoma management from diagnosis to death: The BRIDGE Study. *Liver Int.* **35**, 2155–2166 (2015).
  14. Tillman, H. L. & Choi, S. S. Risk for hepatocellular carcinoma in patients with alcoholic cirrhosis. *Ann. Intern. Med.* **157**, (2012).
  15. Lin, C. W. *et al.* Heavy alcohol consumption increases the incidence of hepatocellular carcinoma in hepatitis B virus-related cirrhosis. *J. Hepatol.* **58**, 730–735 (2013).
  16. Younossi, Z. M. *et al.* Association of nonalcoholic fatty liver disease (NAFLD) with hepatocellular carcinoma (HCC) in the United States from 2004 to 2009. *Hepatology* **62**, 1723–1730 (2015).
  17. Li, X. *et al.* Diabetes mellitus increases the risk of hepatocellular carcinoma in treatment-naïve chronic hepatitis C patients in China. *Med. (United States)* **96**, (2017).
  18. Yang, J. D. *et al.* A global view of hepatocellular carcinoma: trends, risk, prevention and management. *Nat. Rev. Gastroenterol. Hepatol.* **16**, 589–604 (2019).
  19. Kew, M. C. Aflatoxins as a cause of hepatocellular carcinoma. *J. Gastrointest. Liver Dis.* **22**, 305–310 (2013).
  20. Gouas, D., Shi, H. & Hainaut, P. The aflatoxin-induced TP53 mutation at codon 249 (R249S): Biomarker of exposure, early detection and target for therapy. *Cancer Lett.* **286**, 29–37 (2009).
  21. Kew, M. C. Synergistic interaction between aflatoxin B1 and hepatitis B virus in hepatocarcinogenesis. *Liver Int.* **23**, 405–409 (2003).
  22. Stern, M. C. *et al.* Hepatitis B, aflatoxin B1, and p53 codon 249 mutation in hepatocellular carcinomas from Guangxi, People’s Republic of China, and a meta-analysis of existing studies. *Cancer Epidemiol. Biomarkers Prev.* **10**, 617–625 (2001).
  23. Forner, A., Reig, M. & Bruix, J. Hepatocellular carcinoma. *Lancet* **391**, 1301–1314 (2018).

24. McGlynn, K. A., Petrick, J. L. & El-Serag, H. B. Epidemiology of Hepatocellular Carcinoma. *Hepatology* **73**, 4–13 (2021).
25. Bertuccio, P. *et al.* Global trends and predictions in hepatocellular carcinoma mortality. *J. Hepatol.* **67**, 302–309 (2017).
26. Kanwal, F. *et al.* Trends in the Burden of Nonalcoholic Fatty Liver Disease in a United States Cohort of Veterans. *Clin. Gastroenterol. Hepatol.* **14**, 301-308.e2 (2016).
27. Cancer Today. [https://gco.iarc.fr/today/online-analysis-map?v=2020&mode=population&mode\\_population=continents&population=900&populations=900&key=asr&sex=0&cancer=11&type=0&statistic=5&prevalence=0&population\\_group=0&ages\\_group%5B%5D=0&ages\\_group%5B%5D=17&nb\\_items=10&gr](https://gco.iarc.fr/today/online-analysis-map?v=2020&mode=population&mode_population=continents&population=900&populations=900&key=asr&sex=0&cancer=11&type=0&statistic=5&prevalence=0&population_group=0&ages_group%5B%5D=0&ages_group%5B%5D=17&nb_items=10&gr).
28. Farazi, P. A. & DePinho, R. A. Hepatocellular carcinoma pathogenesis: From genes to environment. *Nat. Rev. Cancer* **6**, 674–687 (2006).
29. Block, T. M., Mehta, A. S., Fimmel, C. J. & Jordan, R. Molecular viral oncology of hepatocellular carcinoma. *Oncogene* **22**, 5093–5107 (2003).
30. McClain, C. J., Hill, D. B., Song, Z., Deaciuc, I. & Barve, S. Monocyte activation in alcoholic liver disease. *Alcohol* **27**, 53–61 (2002).
31. Hoek, J. B. & Pastorino, J. G. Ethanol, oxidative stress, and cytokine-induced liver cell injury. *Alcohol* **27**, 63–68 (2002).
32. Tarocchi, M. & Galli, A. Oxidative Stress as a Mechanism for Hepatocellular Carcinoma. in *Liver Pathophysiology: Therapies and Antioxidants* 279–287 (Elsevier Inc., 2017). doi:10.1016/B978-0-12-804274-8.00021-7.
33. Bressac, B. *et al.* p53 mutation in hepatocellular carcinoma after aflatoxin exposure. *Lancet* **338**, 1356–1359 (1991).
34. Reig, M. *et al.* BCLC strategy for prognosis prediction and treatment recommendation: The 2022 update. *J. Hepatol.* **76**, 681–693 (2022).
35. Breen, D. J. & Lencioni, R. Image-guided ablation of primary liver and renal tumours. *Nat. Rev. Clin. Oncol.* **12**, 175–186 (2015).

36. Cucchetti, A. *et al.* Cost-effectiveness of hepatic resection versus percutaneous radiofrequency ablation for early hepatocellular carcinoma. *J. Hepatol.* **59**, 300–307 (2013).
37. Zhou, X. Da *et al.* Experience of 1000 patients who underwent hepatectomy for small hepatocellular carcinoma. *Cancer* **91**, 1479–1486 (2001).
38. Hammad, A. Y. *et al.* Palliative interventions for hepatocellular carcinoma patients: Analysis of the National Cancer Database. *Ann. Palliat. Med.* **6**, 26–35 (2017).
39. Sapisochin, G. & Bruix, J. Liver transplantation for hepatocellular carcinoma: Outcomes and novel surgical approaches. *Nat. Rev. Gastroenterol. Hepatol.* **14**, 203–217 (2017).
40. Mazzaferro, V. *et al.* Predicting survival after liver transplantation in patients with hepatocellular carcinoma beyond the Milan criteria: a retrospective, exploratory analysis. *Lancet Oncol.* **10**, 35–43 (2009).
41. Mazzaferro, V. *et al.* Liver Transplantation for the Treatment of Small Hepatocellular Carcinomas in Patients with Cirrhosis. *N. Engl. J. Med.* **334**, 693–700 (1996).
42. Idée, J. M. & Guiu, B. Use of Lipiodol as a drug-delivery system for transcatheter arterial chemoembolization of hepatocellular carcinoma: A review. *Crit. Rev. Oncol. Hematol.* **88**, 530–549 (2013).
43. Raoul, J. L. *et al.* Updated use of TACE for hepatocellular carcinoma treatment: How and when to use it based on clinical evidence. *Cancer Treat. Rev.* **72**, 28–36 (2019).
44. Bonnemain, B. & Guerbet, M. Histoire du Lipiodol (1901-1994) ou Comment un médicament peut évoluer avec son temps. *Rev. Hist. Pharm. (Paris)*. **83**, 159–170 (1995).
45. Ahnfelt, E. *et al.* Lipiodol-based emulsions used for transarterial chemoembolization and drug delivery: Effects of composition on stability and product quality. *J. Drug Deliv. Sci. Technol.* **53**, 101143 (2019).
46. Kim, H. *et al.* Effects of iodinated fatty acid ester on human hepatocellular

- carcinoma cells. *Yonsei Med. J.* **32**, 16 (1991).
47. R.E., H. *et al.* Biodistribution of Lipiodol following hepatic arterial injection. *Br. J. Surg.* **79**, 952–954 (1992).
  48. Iwai, K., Maeda, H. & Konno, T. Use of oily contrast medium for selective drug targeting to tumor: enhanced therapeutic effect and X-ray image. *Cancer Res.* **44**, 2115–2121 (1984).
  49. de Baere, T. *et al.* Treatment of Liver Tumors with Lipiodol TACE: Technical Recommendations from Experts Opinion. *Cardiovasc. Intervent. Radiol.* **39**, 334–343 (2016).
  50. Konno, T. Targeting cancer chemotherapeutic agents by use of lipiodol contrast medium. *Cancer* **66**, 1897–1903 (1990).
  51. Liapi, E. & Geschwind, J. F. H. Transcatheter Arterial chemoembolization for liver cancer: Is it time to distinguish conventional from drug-eluting chemoembolization? *Cardiovasc. Intervent. Radiol.* **34**, 37–49 (2011).
  52. Najmi Varzaneh, F. *et al.* Prediction of post-TACE necrosis of hepatocellular carcinoma using volumetric enhancement on MRI and volumetric oil deposition on CT, with pathological correlation. *Eur. Radiol.* **28**, 3032–3040 (2018).
  53. Deschamps, F. *et al.* Stabilization Improves Theranostic Properties of Lipiodol®-Based Emulsion During Liver Trans-arterial Chemo-embolization in a VX2 Rabbit Model. *Cardiovasc. Intervent. Radiol.* **40**, 907–913 (2017).
  54. Deschamps, F. *et al.* Pickering-Emulsion for Liver Trans-Arterial Chemo-Embolization with Oxaliplatin. *Cardiovasc. Intervent. Radiol.* **41**, 781–788 (2018).
  55. Yi, S. W. *et al.* Stable lipiodolized emulsions for hepatoma targeting and treatment by transcatheter arterial chemoembolization. *J. Control. Release* **50**, 135–143 (1998).
  56. Barbier, C. E., Heindryckx, F. & Lennernäs, H. Limitations and possibilities of transarterial chemotherapeutic treatment of hepatocellular carcinoma. *Int. J. Mol. Sci.* **22**, (2021).
  57. Liu, J. *et al.* Polymersome-stabilized doxorubicin-lipiodol emulsions for high-

- efficacy chemoembolization therapy. *J. Control. Release* **350**, 122–131 (2022).
58. Hino, T., Kawashima, Y. & Shimabayashi, S. Basic study for stabilization of w/o/w emulsion and its application to transcatheter arterial embolization therapy. *Adv. Drug Deliv. Rev.* **45**, 27–45 (2000).
  59. Le Kim, T. H. *et al.* Lipiodol nanoemulsions stabilized with polyglycerol-polycaprolactone block copolymers for theranostic applications. *Biomater. Res.* **21**, 1–10 (2017).
  60. Chen, S. C. *et al.* Preparation and Characterization of Hyaluronic Acid-Polycaprolactone Copolymer Micelles for the Drug Delivery of Radioactive Iodine-131 Labeled Lipiodol. *Biomed Res. Int.* **2017**, (2017).
  61. Bae, K. H., Lee, Y. & Park, T. G. Oil-encapsulating PEO-PPO-PEO/PEG shell cross-linked nanocapsules for target-specific delivery of paclitaxel. *Biomacromolecules* **8**, 650–656 (2007).
  62. Ho Kong, W. *et al.* Nanoparticulate carrier containing water-insoluble iodinated oil as a multifunctional contrast agent for computed tomography imaging. *Biomaterials* **28**, 5555–5561 (2007).
  63. Oh, K. S. *et al.* Blood-pool multifunctional nanoparticles formed by temperature-induced phase transition for cancer-targeting therapy and molecular imaging. *Int. J. Pharm.* **437**, 192–202 (2012).
  64. Oh, M. H., Kim, J. S., Lee, J. Y., Park, T. G. & Nam, Y. S. Radio-opaque theranostic nanoemulsions with synergistic anti-cancer activity of paclitaxel and Bcl-2 siRNA. *RSC Adv.* **3**, 14642–14651 (2013).
  65. Llovet, J. M., Montal, R., Sia, D. & Finn, R. S. Molecular therapies and precision medicine for hepatocellular carcinoma. *Nat. Rev. Clin. Oncol.* **15**, 599–616 (2018).
  66. Lohitesh, K., Chowdhury, R. & Mukherjee, S. Resistance a major hindrance to chemotherapy in hepatocellular carcinoma: An insight. *Cancer Cell Int.* **18**, 1–15 (2018).
  67. Blum, H. E. & Spangenberg, H. C. Hepatocellular carcinoma: An update. *Arch. Iran. Med.* **10**, 361–371 (2007).

68. Llovet, J. M. *et al.* Sorafenib in Advanced Hepatocellular Carcinoma. *N. Engl. J. Med.* **359**, 378–390 (2008).
69. Chen, S., Cao, Q., Wen, W. & Wang, H. Targeted therapy for hepatocellular carcinoma: Challenges and opportunities. *Cancer Lett.* **460**, 1–9 (2019).
70. Bruix, J. *et al.* Regorafenib for patients with hepatocellular carcinoma who progressed on sorafenib treatment (RESORCE): a randomised, double-blind, placebo-controlled, phase 3 trial. *Lancet* **389**, 56–66 (2017).
71. Kudo, M. *et al.* Lenvatinib versus sorafenib in first-line treatment of patients with unresectable hepatocellular carcinoma: a randomised phase 3 non-inferiority trial. *Lancet* **391**, 1163–1173 (2018).
72. Wilhelm, S. M. *et al.* Preclinical overview of sorafenib, a multikinase inhibitor that targets both Raf and VEGF and PDGF receptor tyrosine kinase signaling. *Mol. Cancer Ther.* **7**, 3129–3140 (2008).
73. Li, L. & Wang, H. Heterogeneity of liver cancer and personalized therapy. *Cancer Lett.* **379**, 191–197 (2016).
74. Bertrand, N., Wu, J., Xu, X., Kamaly, N. & Farokhzad, O. C. Cancer nanotechnology: The impact of passive and active targeting in the era of modern cancer biology. *Adv. Drug Deliv. Rev.* **66**, 2–25 (2014).
75. Kuncic, Z. Cancer nanomedicine: Challenges and opportunities. *Med. J. Aust.* **203**, 204-205.e1 (2015).
76. Sutradhar, K. B. & Amin, M. L. Nanotechnology in Cancer Drug Delivery and Selective Targeting. *ISRN Nanotechnol.* **2014**, 1–12 (2014).
77. Xie, J. *et al.* Nanotechnology for the delivery of phytochemicals in cancer therapy. *Biotechnol. Adv.* **34**, 343–353 (2016).
78. Zhao, Z., Ukidve, A., Krishnan, V. & Mitragotri, S. Effect of physicochemical and surface properties on in vivo fate of drug nanocarriers. *Adv. Drug Deliv. Rev.* **143**, 3–21 (2019).
79. Gustafson, H. H., Holt-Casper, D., Grainger, D. W. & Ghandehari, H. Nanoparticle uptake: The phagocyte problem. *Nano Today* **10**, 487–510 (2015).

80. Donahue, N. D., Acar, H. & Wilhelm, S. Concepts of nanoparticle cellular uptake, intracellular trafficking, and kinetics in nanomedicine. *Adv. Drug Deliv. Rev.* **143**, 68–96 (2019).
81. Golombek, S. K. *et al.* Tumor targeting via EPR: Strategies to enhance patient responses. *Adv. Drug Deliv. Rev.* **130**, 17–38 (2018).
82. Ojha, T. *et al.* Pharmacological and physical vessel modulation strategies to improve EPR-mediated drug targeting to tumors. *Adv. Drug Deliv. Rev.* **119**, 44–60 (2017).
83. Hare, J. I. *et al.* Challenges and strategies in anti-cancer nanomedicine development: An industry perspective. *Adv. Drug Deliv. Rev.* **108**, 25–38 (2017).
84. Kim, Y., Lin, Q., Glazer, P. & Yun, Z. Hypoxic Tumor Microenvironment and Cancer Cell Differentiation. *Curr. Mol. Med.* **9**, 425–434 (2009).
85. Kato, Y. *et al.* Acidic extracellular microenvironment and cancer. *Cancer Cell Int.* **13**, 1–8 (2013).
86. Li, Z., Tan, S., Li, S., Shen, Q. & Wang, K. Cancer drug delivery in the nano era: An overview and perspectives (Review). *Oncol. Rep.* **38**, 611–624 (2017).
87. Shi, J., Kantoff, P. W., Wooster, R. & Farokhzad, O. C. Cancer nanomedicine: Progress, challenges and opportunities. *Nat. Rev. Cancer* **17**, 20–37 (2017).
88. Martinelli, C., Pucci, C. & Ciofani, G. Nanostructured carriers as innovative tools for cancer diagnosis and therapy. *APL Bioeng.* **3**, (2019).
89. Haute, D. Van & Berlin, J. M. Challenges in realizing selectivity for nanoparticle biodistribution and clearance: Lessons from gold nanoparticles. *Ther. Deliv.* **8**, 763–774 (2017).
90. Zhou, Y. & Dai, Z. New Strategies in the Design of Nanomedicines to Oppose Uptake by the Mononuclear Phagocyte System and Enhance Cancer Therapeutic Efficacy. *Chem. - An Asian J.* **13**, 3333–3340 (2018).
91. Bakrania, A., Zheng, G. & Bhat, M. Nanomedicine in hepatocellular carcinoma: A new frontier in targeted cancer treatment. *Pharmaceutics* **14**, 1–25 (2022).
92. Lu, J., Wang, J. & Ling, D. Surface Engineering of Nanoparticles for Targeted

- Delivery to Hepatocellular Carcinoma. *Small* **14**, (2018).
93. Khawar, I. A., Kim, J. H. & Kuh, H. J. Improving drug delivery to solid tumors: Priming the tumor microenvironment. *J. Control. Release* **201**, 78–89 (2015).
  94. Liu, J., Chen, Q., Feng, L. & Liu, Z. Nanomedicine for tumor microenvironment modulation and cancer treatment enhancement. *Nano Today* **21**, 55–73 (2018).
  95. Yang, S. *et al.* Drug delivery strategy in hepatocellular carcinoma therapy. *Cell Commun. Signal.* **20**, 1–14 (2022).
  96. Sun, Y. *et al.* Cancer nanotechnology: Enhancing tumor cell response to chemotherapy for hepatocellular carcinoma therapy. *Asian J. Pharm. Sci.* **14**, 581–594 (2019).
  97. Li, M. *et al.* Ligand-based targeted therapy: A novel strategy for hepatocellular carcinoma. *Int. J. Nanomedicine* **11**, 5645–5669 (2016).
  98. Nakamura, Y., Mochida, A., Choyke, P. L. & Kobayashi, H. Nanodrug Delivery: Is the Enhanced Permeability and Retention Effect Sufficient for Curing Cancer? *Bioconjug. Chem.* **27**, 2225–2238 (2016).
  99. Peer, D. *et al.* Nanocarriers as an emerging platform for cancer therapy. *Nat. Nanotechnol.* **2**, 751–760 (2007).
  100. Wilhelm, S. *et al.* Analysis of nanoparticle delivery to tumours. *Nat. Rev. Mater.* **1**, 16014 (2016).
  101. Chi, X. *et al.* Recent advances of nanomedicines for liver cancer therapy. *J. Mater. Chem. B* **8**, 3747–3771 (2020).
  102. Rosenblum, D., Joshi, N., Tao, W., Karp, J. M. & Peer, D. Progress and challenges towards targeted delivery of cancer therapeutics. *Nat. Commun.* **9**, (2018).
  103. Bertrand, N., Wu, J., Xu, X., Kamaly, N. & Farokhzad, O. C. Cancer nanotechnology: The impact of passive and active targeting in the era of modern cancer biology. *Adv. Drug Deliv. Rev.* **66**, 2–25 (2014).
  104. Varshosaz, J. & Farzan, M. Nanoparticles for targeted delivery of therapeutics and small interfering RNAs in hepatocellular carcinoma. *World J. Gastroenterol.*

- 21, 12022–12041 (2015).
105. Lu, J., Wang, J. & Ling, D. Surface Engineering of Nanoparticles for Targeted Delivery to Hepatocellular Carcinoma. *Small* **14**, 1–25 (2018).
  106. Kumar, V. *et al.* Current status and future directions of hepatocellular carcinoma-targeted nanoparticles and nanomedicine. *Expert Opin. Drug Deliv.* **18**, 673–694 (2021).
  107. D’Souza, A. A. & Devarajan, P. V. Asialoglycoprotein receptor mediated hepatocyte targeting - Strategies and applications. *J. Control. Release* **203**, 126–139 (2015).
  108. Das, S., Kudale, P., Dandekar, P. & Devarajan, P. V. Asialoglycoprotein Receptor and Targeting Strategies. in *AAPS Advances in the Pharmaceutical Sciences Series* vol. 39 353–381 (2019).
  109. Trerè, D. *et al.* The asialoglycoprotein receptor in human hepatocellular carcinomas: its expression on proliferating cells. *Br. J. Cancer* **81**, 404–408 (1999).
  110. Li, Y., Huang, G., Diakur, J. & Wiebe, L. Targeted Delivery of Macromolecular Drugs: Asialoglycoprotein Receptor (ASGPR) Expression by Selected Hepatoma Cell Lines used in Antiviral Drug Development. *Curr. Drug Deliv.* **5**, 299–302 (2008).
  111. Managit, C., Kawakami, S., Yamashita, F. & Hashida, M. Effect of galactose density on asialoglycoprotein receptor-mediated uptake of galactosylated liposomes. *J. Pharm. Sci.* **94**, 2266–2275 (2005).
  112. Warriar, D. U. *et al.* Novel derivatives of arabinogalactan, pullulan & lactobionic acid for targeting asialoglycoprotein receptor: Biomolecular interaction, synthesis & evaluation. *Int. J. Biol. Macromol.* **207**, 683–699 (2022).
  113. Thao, L. Q. *et al.* Doxorubicin and paclitaxel co-bound lactosylated albumin nanoparticles having targetability to hepatocellular carcinoma. *Colloids Surfaces B Biointerfaces* **152**, 183–191 (2017).
  114. Shen, Z. *et al.* A galactosamine-mediated drug delivery carrier for targeted liver cancer therapy. *Pharmacol. Res.* **64**, 410–419 (2011).

115. Wang, S. *et al.* Sustained liver targeting and improved antiproliferative effect of doxorubicin liposomes modified with galactosylated lipid and PEG-lipid. *AAPS PharmSciTech* **11**, 870–877 (2010).
116. Wang, S. N. *et al.* Synthesis of a novel galactosylated lipid and its application to the hepatocyte-selective targeting of liposomal doxorubicin. *Eur. J. Pharm. Biopharm.* **62**, 32–38 (2006).
117. Sonoke, S., Ueda, T., Fujiwara, K., Kuwabara, K. & Yano, J. Galactose-modified cationic liposomes as a liver-targeting delivery system for small interfering RNA. *Biol. Pharm. Bull.* **34**, 1338–1342 (2011).
118. Varshosaz, J., Hassanzadeh, F., Sadeghi, H. & Khadem, M. Galactosylated nanostructured lipid carriers for delivery of 5-FU to hepatocellular carcinoma. *J. Liposome Res.* **22**, 224–236 (2012).
119. Xu, Z. *et al.* The performance of docetaxel-loaded solid lipid nanoparticles targeted to hepatocellular carcinoma. *Biomaterials* **30**, 226–232 (2009).
120. Ganguly, S. *et al.* Apigenin-loaded galactose tailored PLGA nanoparticles: A possible strategy for liver targeting to treat hepatocellular carcinoma. *Colloids Surfaces B Biointerfaces* **204**, 111778 (2021).
121. Liang, H. F. *et al.* Paclitaxel-loaded poly( $\gamma$ -glutamic acid)-poly(lactide) nanoparticles as a targeted drug delivery system against cultured HepG2 cells. *Bioconj. Chem.* **17**, 291–299 (2006).
122. Laquintana, V. *et al.* Targeting human liver cancer cells with lactobionic acid-G(4)-PAMAM-FITC sorafenib loaded dendrimers. *Int. J. Pharm.* **528**, 485–497 (2017).
123. U.S. Food and Drug Administration. *FDA Nexavar (sorafenib) Approval Letter*. [http://www.accessdata.fda.gov/drugsatfda\\_docs/applletter/2007/021923s004,s005,s006,s007.pdf](http://www.accessdata.fda.gov/drugsatfda_docs/applletter/2007/021923s004,s005,s006,s007.pdf) (2007).
124. U.S. Food and Drug Administration. *FDA approval letter for use of sorafenib in advanced renal cancer*. [http://www.accessdata.fda.gov/drugsatfda\\_docs/applletter/2005/021923ltr.pdf](http://www.accessdata.fda.gov/drugsatfda_docs/applletter/2005/021923ltr.pdf) (2009).

125. Liu, C. *et al.* Improving Oral Bioavailability of Sorafenib by Optimizing the ‘spring’ and ‘parachute’ Based on Molecular Interaction Mechanisms. *Mol. Pharm.* **13**, 599–608 (2016).
126. FDA. *sorafenib FDA profile*.  
[https://www.accessdata.fda.gov/drugsatfda\\_docs/label/2010/021923s008s0091bl.pdf](https://www.accessdata.fda.gov/drugsatfda_docs/label/2010/021923s008s0091bl.pdf) (2010).
127. Truong, D. H. *et al.* Preparation and characterization of solid dispersion using a novel amphiphilic copolymer to enhance dissolution and oral bioavailability of sorafenib. *Powder Technol.* **283**, 260–265 (2015).
128. Tunki, L. *et al.* Modulating the site-specific oral delivery of sorafenib using sugar-grafted nanoparticles for hepatocellular carcinoma treatment. *Eur. J. Pharm. Sci.* **137**, 104978 (2019).
129. Zhang, Z. *et al.* The use of lipid-coated nanodiamond to improve bioavailability and efficacy of sorafenib in resisting metastasis of gastric cancer. *Biomaterials* **35**, 4565–4572 (2014).
130. Keating, G. M. & Santoro, A. Sorafenib A Review of its Use in Advanced Hepatocellular Carcinoma. *Drugs* **69**, 223–240 (2009).
131. Kong, F. H. *et al.* Current status of sorafenib nanoparticle delivery systems in the treatment of hepatocellular carcinoma. *Theranostics* **11**, 5464–5490 (2021).
132. Chen, F. *et al.* Recent advances of sorafenib nanoformulations for cancer therapy: Smart nanosystem and combination therapy. *Asian J. Pharm. Sci.* **16**, 318–336 (2021).
133. Xiao, Y. *et al.* Sorafenib and gadolinium co-loaded liposomes for drug delivery and MRI-guided HCC treatment. *Colloids Surfaces B Biointerfaces* **141**, 83–92 (2016).
134. Zheng, N. *et al.* Co-delivery of sorafenib and metapristone encapsulated by CXCR4-targeted PLGA-PEG nanoparticles overcomes hepatocellular carcinoma resistance to sorafenib. *J. Exp. Clin. Cancer Res.* **38**, 1–18 (2019).
135. Gao, W. *et al.* Preparation and evaluation of folate-decorated human serum albumin nanoparticles for the targeted delivery of sorafenib to enhance

- antihepatocarcinoma efficacy. *J. Drug Deliv. Sci. Technol.* **54**, 101349 (2019).
136. Sun, W. *et al.* Codelivery of sorafenib and GPC3 siRNA with PEI-modified liposomes for hepatoma therapy. *Biomater. Sci.* **5**, 2468–2479 (2017).
137. Mo, L. *et al.* PEGylated hyaluronic acid-coated liposome for enhanced in vivo efficacy of sorafenib via active tumor cell targeting and prolonged systemic exposure. *Nanomedicine Nanotechnology, Biol. Med.* **14**, 557–567 (2018).
138. Wang, H. *et al.* Improved Oral Bioavailability and Liver Targeting of Sorafenib Solid Lipid Nanoparticles in Rats. *AAPS PharmSciTech* **19**, 761–768 (2018).
139. Zhang, H., Zhang, F. M. & Yan, S. J. Preparation, in vitro release, and pharmacokinetics in rabbits of lyophilized injection of sorafenib solid lipid nanoparticles. *Int. J. Nanomedicine* **7**, 2901–2910 (2012).
140. Grillone, A. *et al.* Active Targeting of Sorafenib: Preparation, Characterization, and In Vitro Testing of Drug-Loaded Magnetic Solid Lipid Nanoparticles. *Adv. Healthc. Mater.* **4**, 1681–1690 (2015).
141. Babos, G., Biró, E., Meiczinger, M. & Feczko, T. Dual drug delivery of sorafenib and doxorubicin from PLGA and PEG-PLGA polymeric nanoparticles. *Polymers (Basel)*. **10**, 1–12 (2018).
142. Gao, D. Y. *et al.* CXCR4-targeted lipid-coated PLGA nanoparticles deliver sorafenib and overcome acquired drug resistance in liver cancer. *Biomaterials* **67**, 194–203 (2015).
143. Dayani, L., Dehghani, M., Aghaei, M., Taymouri, S. & Taheri, A. Preparation and evaluation of targeted albumin lipid nanoparticles with lactobionic acid for targeted drug delivery of sorafenib in hepatocellular carcinoma. *J. Drug Deliv. Sci. Technol.* **69**, 103142 (2022).
144. Zhang, J. Y. *et al.* Preparation of the albumin nanoparticle system loaded with both paclitaxel and sorafenib and its evaluation in-vitro and in-vivo. *J. Microencapsul.* **28**, 528–536 (2011).
145. Müller, R. H., Radtke, M. & Wissing, S. A. Solid lipid nanoparticles (SLN) and nanostructured lipid carriers (NLC) in cosmetic and dermatological preparations. *Adv. Drug Deliv. Rev.* **54**, 131–155 (2002).

146. Campos, J. R. *et al.* Solid lipid nanoparticles (SLN): Prediction of toxicity, metabolism, fate and physicochemical properties. prediction of toxicity, metabolism, fate and physicochemical properties. in *Nanopharmaceuticals: Volume 1: Expectations and Realities of Multifunctional Drug Delivery Systems* 1–15 (Elsevier, 2020). doi:10.1016/B978-0-12-817778-5.00001-4.
147. Javed, S., Mangla, B., Almoshari, Y., Sultan, M. H. & Ahsan, W. Nanostructured lipid carrier system: A compendium of their formulation development approaches, optimization strategies by quality by design, and recent applications in drug delivery. *Nanotechnol. Rev.* **11**, 1744–1777 (2022).
148. Müller, R. H., Radtke, M. & Wissing, S. A. Nanostructured lipid matrices for improved microencapsulation of drugs. *Int. J. Pharm.* **242**, 121–128 (2002).
149. Khatak, S. & Dureja, H. Structural Composition of Solid Lipid Nanoparticles for Invasive and Noninvasive Drug Delivery. *Curr. Nanomater.* **2**, 129–153 (2018).
150. Garg, J., Pathania, K., Sah, S. P. & Pawar, S. V. Nanostructured lipid carriers: a promising drug carrier for targeting brain tumours. *Futur. J. Pharm. Sci.* **8**, (2022).
151. Geszke-Moritz, M. & Moritz, M. Solid lipid nanoparticles as attractive drug vehicles: Composition, properties and therapeutic strategies. *Mater. Sci. Eng. C* **68**, 982–994 (2016).
152. Jaiswal, P., Gidwani, B. & Vyas, A. Nanostructured lipid carriers and their current application in targeted drug delivery. *Artif. Cells, Nanomedicine Biotechnol.* **44**, 27–40 (2016).
153. Apostolou, M., Assi, S., Fatokun, A. A. & Khan, I. The Effects of Solid and Liquid Lipids on the Physicochemical Properties of Nanostructured Lipid Carriers. *J. Pharm. Sci.* **110**, 2859–2872 (2021).
154. Mehnert, W. & Mäder, K. Solid lipid nanoparticles: Production, characterization and applications. *Adv. Drug Deliv. Rev.* **64**, 83–101 (2012).
155. Nobari Azar, F. A., Pezeshki, A., Ghanbarzadeh, B., Hamishehkar, H. & Mohammadi, M. Nanostructured lipid carriers: Promising delivery systems for encapsulation of food ingredients. *J. Agric. Food Res.* **2**, 100084 (2020).

156. Nasirizadeh, S. & Malaekheh-Nikouei, B. Solid lipid nanoparticles and nanostructured lipid carriers in oral cancer drug delivery. *J. Drug Deliv. Sci. Technol.* **55**, 101458 (2020).
157. Borges, A., de Freitas, V., Mateus, N., Fernandes, I. & Oliveira, J. Solid Lipid Nanoparticles as Carriers of Natural Phenolic Compounds. *Antioxidants* **9**, 998 (2020).
158. Duong, V. A., Nguyen, T. T. L. & Maeng, H. J. Preparation of solid lipid nanoparticles and nanostructured lipid carriers for drug delivery and the effects of preparation parameters of solvent injection method. *Molecules* **25**, 1–36 (2020).
159. Akbari, J. *et al.* Solid lipid nanoparticles and nanostructured lipid carriers: a review of the methods of manufacture and routes of administration. *Pharm. Dev. Technol.* **27**, 525–544 (2022).
160. Fonte, P., Nogueira, T., Gehm, C., Ferreira, D. & Sarmiento, B. Chitosan-coated solid lipid nanoparticles enhance the oral absorption of insulin. *Drug Deliv. Transl. Res.* **1**, 299–308 (2011).
161. Ansari, M. J. *et al.* Enhanced oral bioavailability of insulin-loaded solid lipid nanoparticles: pharmacokinetic bioavailability of insulin-loaded solid lipid nanoparticles in diabetic rats. *Drug Deliv.* **7544**, 1–8 (2015).
162. Gallarate, M., Trotta, M., Battaglia, L. & Chirio, D. Preparation of solid lipid nanoparticles from W/O/W emulsions: Preliminary studies on insulin encapsulation. *J. Microencapsul.* **26**, 394–402 (2009).
163. Subramaniam, B., Siddik, Z. H. & Nagoor, N. H. Optimization of nanostructured lipid carriers: understanding the types, designs, and parameters in the process of formulations. *J. Nanoparticle Res.* **22**, 141 (2020).
164. Lippacher, A., Müller, R. . & Mäder, K. Semisolid SLN<sup>TM</sup> dispersions for topical application: influence of formulation and production parameters on viscoelastic properties. *Eur. J. Pharm. Biopharm.* **53**, 155–160 (2002).
165. Siddiqui, A., Alayoubi, A., El-Malah, Y. & Nazzal, S. Modeling the effect of sonication parameters on size and dispersion temperature of solid lipid nanoparticles (SLNs) by response surface methodology (RSM). *Pharm. Dev.*

- Technol.* **19**, 342–346 (2014).
166. Tran, T. H. *et al.* Formulation and Optimization of Raloxifene-Loaded Solid Lipid Nanoparticles to Enhance Oral Bioavailability. *J. Nanosci. Nanotechnol.* **14**, 4820–4831 (2014).
  167. Mehnert, W. Solid lipid nanoparticles Production, characterization and applications. *Adv. Drug Deliv. Rev.* **47**, 165–196 (2001).
  168. Varshosaz, J., Sadeghi, H., Andalib, S. & Hassanzadeh, F. Optimization of LDL targeted nanostructured lipid carriers of 5-FU by a full factorial design. *Adv. Biomed. Res.* **1**, 45 (2012).
  169. Soleimanian, Y., Goli, S. A. H., Varshosaz, J. & Maestrelli, F. Propolis wax nanostructured lipid carrier for delivery of  $\beta$  sitosterol: Effect of formulation variables on physicochemical properties. *Food Chem.* **260**, 97–105 (2018).
  170. Zhang, W. *et al.* Design, characterization, and in vitro cellular inhibition and uptake of optimized genistein-loaded NLC for the prevention of posterior capsular opacification using response surface methodology. *Int. J. Pharm.* **454**, 354–366 (2013).
  171. Negi, L. M., Jaggi, M. & Talegaonkar, S. A logical approach to optimize the nanostructured lipid carrier system of irinotecan: efficient hybrid design methodology. *Nanotechnology* **24**, 015104 (2013).
  172. Müller, R. H., Mäder, K. & Gohla, S. Solid lipid nanoparticles (SLN) for controlled drug delivery - A review of the state of the art. *Eur. J. Pharm. Biopharm.* **50**, 161–177 (2000).
  173. Freitas, C. and R. H. M. Stability determination of solid lipid nanoparticles (SLN TM) in aqueous dispersion after addition of electrolyte. *J. Microencapsul.* **16**, 59–71 (1999).
  174. Westesen, K. & Siekmann, B. Investigation of the gel formation of phospholipid-stabilized solid lipid nanoparticles. *Int. J. Pharm.* **151**, 35–45 (1997).
  175. Doktorovová, S., Kovačević, A. B., Garcia, M. L. & Souto, E. B. Preclinical safety of solid lipid nanoparticles and nanostructured lipid carriers: Current evidence from in vitro and in vivo evaluation. *Eur. J. Pharm. Biopharm.* **108**,

235–252 (2016).

176. Fröhlich, E. The role of surface charge in cellular uptake and cytotoxicity of medical nanoparticles. *Int. J. Nanomedicine* 5577 (2012)  
doi:10.2147/IJN.S36111.
177. Silva, A. *et al.* Soft Cationic Nanoparticles for Drug Delivery: Production and Cytotoxicity of Solid Lipid Nanoparticles (SLNs). *Appl. Sci.* **9**, 4438 (2019).
178. Heydenreich, A. Preparation and purification of cationic solid lipid nanospheres—effects on particle size, physical stability and cell toxicity. *Int. J. Pharm.* **254**, 83–87 (2003).
179. Müller, R. Cytotoxicity of magnetite-loaded polylactide, polylactide/glycolide particles and solid lipid nanoparticles. *Int. J. Pharm.* **138**, 85–94 (1996).
180. Müller, R. H., Rühl, D., Runge, S., Schulze-Forster, K. & Mehnert, W. Cytotoxicity of solid lipid nanoparticles as a function of the lipid matrix and the surfactant. *Pharm. Res.* **14**, 458–462 (1997).
181. Dal Pizzol, C. *et al.* Influence of surfactant and lipid type on the physicochemical properties and biocompatibility of solid lipid nanoparticles. *Int. J. Environ. Res. Public Health* **11**, 8581–8596 (2014).
182. Schöler, N. *et al.* Surfactant, but not the size of solid lipid nanoparticles (SLN) influences viability and cytokine production of macrophages. *Int. J. Pharm.* **221**, 57–67 (2001).
183. Doktorovova, S., Souto, E. B. & Silva, A. M. Nanotoxicology applied to solid lipid nanoparticles and nanostructured lipid carriers – A systematic review of in vitro data. *Eur. J. Pharm. Biopharm.* **87**, 1–18 (2014).
184. How, C. W., Rasedee, A. & Abbasalipourkabir, R. Characterization and cytotoxicity of nanostructured lipid carriers formulated with olive oil, hydrogenated palm oil, and polysorbate 80. *IEEE Trans. Nanobioscience* **12**, 72–78 (2013).
185. Joshi, M. D. & Müller, R. H. Lipid nanoparticles for parenteral delivery of actives. *Eur. J. Pharm. Biopharm.* **71**, 161–172 (2009).
186. Weber, S., Zimmer, A. & Pardeike, J. Solid Lipid Nanoparticles (SLN) and

- Nanostructured Lipid Carriers (NLC) for pulmonary application: A review of the state of the art. *Eur. J. Pharm. Biopharm.* **86**, 7–22 (2014).
187. Li, R., Eun, J. S. & Lee, M. K. Pharmacokinetics and biodistribution of paclitaxel loaded in pegylated solid lipid nanoparticles after intravenous administration. *Arch. Pharm. Res.* **34**, 331–337 (2011).
  188. Yuan, H. *et al.* Cellular uptake of solid lipid nanoparticles and cytotoxicity of encapsulated paclitaxel in A549 cancer cells. *Int. J. Pharm.* **348**, 137–145 (2008).
  189. Lee, M. K., Lim, S. J. & Kim, C. K. Preparation, characterization and in vitro cytotoxicity of paclitaxel-loaded sterically stabilized solid lipid nanoparticles. *Biomaterials* **28**, 2137–2146 (2007).
  190. Müller, R. H., Maaßen, S., Weyhers, H. & Mehnert, W. Phagocytic uptake and cytotoxicity of solid lipid nanoparticles (SLN) sterically stabilized with poloxamine 908 and poloxamer 407. *J. Drug Target.* **4**, 161–170 (1996).
  191. Sarmiento, B. *et al.* Effect of chitosan coating in overcoming the phagocytosis of insulin loaded solid lipid nanoparticles by mononuclear phagocyte system. *Carbohydr. Polym.* **84**, 919–925 (2011).
  192. Talluri, S. V., Kuppusamy, G., Karri, V. V. S. R., Tummala, S. & Madhunapantula, S. R. V. Lipid-based nanocarriers for breast cancer treatment – comprehensive review. *Drug Deliv.* **23**, 1291–1305 (2016).
  193. Fontana, G., Maniscalco, L., Schillaci, D., Cavallaro, G. & Giammona, G. Solid lipid nanoparticles containing tamoxifen characterization and in vitro antitumoral activity. *Drug Deliv. J. Deliv. Target. Ther. Agents* **12**, 385–392 (2005).
  194. Yuan, Q. *et al.* Docetaxel-loaded solid lipid nanoparticles suppress breast cancer cells growth with reduced myelosuppression toxicity. *Int. J. Nanomedicine* **9**, 4829–4846 (2014).
  195. Wang, Y. *et al.* Lung cancer combination therapy: co-delivery of paclitaxel and doxorubicin by nanostructured lipid carriers for synergistic effect. *Drug Deliv.* **23**, 1398–1403 (2016).
  196. Mussi, S. V. & Torchilin, V. P. Recent trends in the use of lipidic nanoparticles as pharmaceutical carriers for cancer therapy and diagnostics. *J. Mater. Chem. B*

- 1, 5201–5209 (2013).
197. Bukhari, S. I. *et al.* Recent progress in lipid nanoparticles for cancer theranostics: Opportunity and challenges. *Pharmaceutics* **13**, (2021).
  198. Bae, K. H., Lee, J. Y., Lee, S. H., Park, T. G. & Nam, Y. S. Optically traceable solid lipid nanoparticles loaded with sirna and paclitaxel for synergistic chemotherapy with in situ imaging. *Adv. Healthc. Mater.* **2**, 576–584 (2013).
  199. Madan, J. *et al.* Poly (ethylene)-glycol conjugated solid lipid nanoparticles of noscapine improve biological half-life, brain delivery and efficacy in glioblastoma cells. *Nanomedicine Nanotechnology, Biol. Med.* **9**, 492–503 (2013).
  200. Yassemi, A., Kashanian, S. & Zhaleh, H. Folic acid receptor-targeted solid lipid nanoparticles to enhance cytotoxicity of letrozole through induction of caspase-3 dependent-apoptosis for breast cancer treatment. *Pharm. Dev. Technol.* **25**, 397–407 (2020).
  201. Heurtault, B., Saulnier, P., Pech, B., Proust, J. E. & Benoit, J. P. A novel phase inversion-based process for the preparation of lipid nanocarriers. *Pharm. Res.* **19**, 875–880 (2002).
  202. Saulnier, P., Benoit, J., Proust, J., Richard, J. & Etypharm, S. A. LIPID NANOCAPSULES, PREPARATION PROCESS AND USE AS MEDICINE. vol. 2 (1996).
  203. Huynh, N. T., Passirani, C., Saulnier, P. & Benoit, J. P. Lipid nanocapsules: A new platform for nanomedicine. *Int. J. Pharm.* **379**, 201–209 (2009).
  204. Jintapattanakit, A. Preparation of nanoemulsions by phase inversion temperature (PIT) method. *Pharm. Sci. Asia* **45**, 1–12 (2018).
  205. Heurtault, B. *et al.* The influence of lipid nanocapsule composition on their size distribution. *Eur. J. Pharm. Sci.* **18**, 55–61 (2003).
  206. Maupas, C., Moulari, B., Béduneau, A., Lamprecht, A. & Pellequer, Y. Surfactant dependent toxicity of lipid nanocapsules in HaCaT cells. *Int. J. Pharm.* **411**, 136–141 (2011).
  207. Anton, N., Gayet, P., Benoit, J. P. & Saulnier, P. Nano-emulsions and

- nanocapsules by the PIT method: An investigation on the role of the temperature cycling on the emulsion phase inversion. *Int. J. Pharm.* **344**, 44–52 (2007).
208. Rao, J. & McClements, D. J. Stabilization of phase inversion temperature nanoemulsions by surfactant displacement. *J. Agric. Food Chem.* **58**, 7059–7066 (2010).
209. Manconi, M. *et al.* Viscoelastic properties of concentrated dispersions in water of soy lecithin. *Colloids Surfaces A Physicochem. Eng. Asp.* **222**, 141–145 (2003).
210. Vonarbourg, A., Saulnier, P., Passirani, C. & Benoit, J. P. Electrokinetic properties of noncharged lipid nanocapsules: Influence of the dipolar distribution at the interface. *Electrophoresis* **26**, 2066–2075 (2005).
211. Shinoda, K. & Saito, H. The Stability of O/W type emulsions as functions of temperature and the HLB of emulsifiers: The emulsification by PIT-method. *J. Colloid Interface Sci.* **30**, 258–263 (1969).
212. Dulieu, C. & Bazile, D. Influence of lipid nanocapsules composition on their aptness to freeze-drying. *Pharm. Res.* **22**, 285–292 (2005).
213. Tadros, T., Izquierdo, P., Esquena, J. & Solans, C. Formation and stability of nano-emulsions. *Adv. Colloid Interface Sci.* **108–109**, 303–318 (2004).
214. Zhai, Q. *et al.* Preparation and Optimization Lipid Nanocapsules to Enhance the Antitumor Efficacy of Cisplatin in Hepatocellular Carcinoma HepG2 Cells. *AAPS PharmSciTech* **19**, 2048–2057 (2018).
215. Idlas, P., Lepeltier, E., Jaouen, G. & Passirani, C. Ferrocifen loaded lipid nanocapsules: A promising anticancer medication against multidrug resistant tumors. *Cancers (Basel)*. **13**, 1–23 (2021).
216. Groo, A. C. *et al.* In vivo evaluation of paclitaxel-loaded lipid nanocapsules after intravenous and oral administration on resistant tumor. *Nanomedicine* **10**, 589–601 (2015).
217. Morille, M. *et al.* Long-circulating DNA lipid nanocapsules as new vector for passive tumor targeting. *Biomaterials* **31**, 321–329 (2010).
218. Ding, B. *et al.* Preparation and evaluation of folate-modified lipid nanocapsules for quercetin delivery. *J. Drug Target.* **22**, 67–75 (2014).

219. Clavreul, A. *et al.* Development and characterization of sorafenib-loaded lipid nanocapsules for the treatment of glioblastoma. *Drug Deliv.* **25**, 1756–1765 (2018).
220. Clavreul, A. *et al.* Targeting and treatment of glioblastomas with human mesenchymal stem cells carrying ferrociphenol lipid nanocapsules. *Int. J. Nanomedicine* **10**, 1259–1271 (2015).
221. Lamprecht, A. & Benoit, J. P. Etoposide nanocarriers suppress glioma cell growth by intracellular drug delivery and simultaneous P-glycoprotein inhibition. *J. Control. Release* **112**, 208–213 (2006).
222. Lollo, G. *et al.* In vitro anti-cancer activity and pharmacokinetic evaluation of curcumin-loaded lipid nanocapsules. *Mater. Sci. Eng. C* **91**, 859–867 (2018).
223. Waghray, D. & Zhang, Q. Inhibit or Evade Multidrug Resistance P-Glycoprotein in Cancer Treatment. *J. Med. Chem.* **61**, 5108–5121 (2018).
224. Hirsjärvi, S., Belloche, C., Hindré, F., Garcion, E. & Benoit, J. P. Tumour targeting of lipid nanocapsules grafted with cRGD peptides. *Eur. J. Pharm. Biopharm.* **87**, 152–159 (2014).
225. Cornaire, G. *et al.* Impact of excipients on the absorption of P-glycoprotein substrates in vitro and in vivo. *Int. J. Pharm.* **278**, 119–131 (2004).
226. Gurjar, R. *et al.* Inhibitory Effects of Commonly Used Excipients on P-Glycoprotein in Vitro. *Mol. Pharm.* **15**, 4835–4842 (2018).
227. Peltier, S., Oger, J. M., Lagarce, F., Couet, W. & Benoît, J. P. Enhanced oral paclitaxel bioavailability after administration of paclitaxel-loaded lipid nanocapsules. *Pharm. Res.* **23**, 1243–1250 (2006).
228. Saliou, B. *et al.* Development and in vitro evaluation of a novel lipid nanocapsule formulation of etoposide. *Eur. J. Pharm. Sci.* **50**, 172–180 (2013).
229. Hoshyar, N., Gray, S., Han, H. & Bao, G. The effect of nanoparticle size on in vivo pharmacokinetics and cellular interaction. *Nanomedicine* **11**, 673–692 (2016).
230. Xiao, Q. *et al.* The effects of protein corona on in vivo fate of nanocarriers. *Adv. Drug Deliv. Rev.* **186**, 114356 (2022).

231. Vonarbourg, A. *et al.* Evaluation of pegylated lipid nanocapsules versus complement system activation and macrophage uptake. *J. Biomed. Mater. Res. Part A* **78A**, 620–628 (2006).
232. Béduneau, A. *et al.* Pegylated nanocapsules produced by an organic solvent-free method: Evaluation of their stealth properties. *Pharm. Res.* **23**, 2190–2199 (2006).
233. Hoarau, D., Delmas, P., David, S., Roux, E. & Leroux, J. C. Novel long-circulating lipid nanocapsules. *Pharm. Res.* **21**, 1783–1789 (2004).
234. Maeda, H., Nakamura, H. & Fang, J. The EPR effect for macromolecular drug delivery to solid tumors: Improvement of tumor uptake, lowering of systemic toxicity, and distinct tumor imaging in vivo. *Adv. Drug Deliv. Rev.* **65**, 71–79 (2013).
235. Khalid, M. N., Simard, P., Hoarau, D., Dragomir, A. & Leroux, J. C. Long circulating poly(ethylene glycol)-decorated lipid nanocapsules deliver docetaxel to solid tumors. *Pharm. Res.* **23**, 752–758 (2006).
236. Resnier, P. *et al.* Model Affitin and PEG modifications onto siRNA lipid nanocapsules: Cell uptake and: In vivo biodistribution improvements. *RSC Adv.* **9**, 27264–27278 (2019).
237. Huynh, N. T. *et al.* Treatment of 9L gliosarcoma in rats by ferrociphenol-loaded lipid nanocapsules based on a passive targeting strategy via the EPR effect. *Pharm. Res.* **28**, 3189–3198 (2011).
238. Resnier, P. *et al.* Efficient in vitro gene therapy with PEG siRNA lipid nanocapsules for passive targeting strategy in melanoma. *Biotechnol. J.* **9**, 1389–1401 (2014).
239. Vyas, D., Patel, M. & Wairkar, S. Strategies for active tumor targeting-an update. *Eur. J. Pharmacol.* **915**, 174512 (2022).
240. Karim, R. *et al.* Enhanced and preferential internalization of lipid nanocapsules into human glioblastoma cells: Effect of a surface-functionalizing NFL peptide. *Nanoscale* **10**, 13485–13501 (2018).
241. Balzeau, J. *et al.* The effect of functionalizing lipid nanocapsules with NFL-

- TBS.40-63 peptide on their uptake by glioblastoma cells. *Biomaterials* **34**, 3381–3389 (2013).
242. Lu, Y. & Park, K. Polymeric micelles and alternative nanonized delivery vehicles for poorly soluble drugs. *Int. J. Pharm.* **453**, 198–214 (2013).
243. Torchilin, V. P. Micellar nanocarriers: Pharmaceutical perspectives. *Pharm. Res.* **24**, 1–16 (2007).
244. Gaucher, G., Satturwar, P., Jones, M. C., Furtos, A. & Leroux, J. C. Polymeric micelles for oral drug delivery. *Eur. J. Pharm. Biopharm.* **76**, 147–158 (2010).
245. Ghezzi, M. *et al.* Polymeric micelles in drug delivery: An insight of the techniques for their characterization and assessment in biorelevant conditions. *J. Control. Release* **332**, 312–336 (2021).
246. Upponi, J. R. *et al.* Polymeric micelles: Theranostic co-delivery system for poorly water-soluble drugs and contrast agents. *Biomaterials* **170**, 26–36 (2018).
247. Kore, G., Kolate, A., Nej, A. & Misra, A. Polymeric micelle as multifunctional pharmaceutical carriers. *J. Nanosci. Nanotechnol.* **14**, 288–307 (2014).
248. Zhang, Y., Huang, Y. & Li, S. Polymeric micelles: Nanocarriers for cancer-targeted drug delivery. *AAPS PharmSciTech* **15**, 862–871 (2014).
249. Oerlemans, C. *et al.* Polymeric micelles in anticancer therapy: Targeting, imaging and triggered release. *Pharm. Res.* **27**, 2569–2589 (2010).
250. Sun, M. *et al.* TPGS-functionalized and ortho ester-crosslinked dextran nanogels for enhanced cytotoxicity on multidrug resistant tumor cells. *Carbohydr. Polym.* **198**, 142–154 (2018).
251. Pawar, A., Patel, R., Arulmozhi, S. & Bothiraja, C. D- $\alpha$ -Tocopheryl polyethylene glycol 1000 succinate conjugated folic acid nanomicelles: Towards enhanced bioavailability, stability, safety, prolonged drug release and synergized anticancer effect of plumbagin. *RSC Adv.* **6**, 78106–78121 (2016).
252. Hao, J. *et al.* Folic acid-functionalized drug delivery platform of resveratrol based on pluronic 127/D- $\alpha$ -tocopheryl polyethylene glycol 1000 succinate mixed micelles. *Int. J. Nanomedicine* **12**, 2279–2292 (2017).

253. Bernabeu, E. *et al.* Novel Soluplus® —TPGS mixed micelles for encapsulation of paclitaxel with enhanced in vitro cytotoxicity on breast and ovarian cancer cell lines. *Colloids Surfaces B Biointerfaces* **140**, 403–411 (2016).
254. Liu, T. *et al.* Mechanisms of TPGS and its derivatives inhibiting P-glycoprotein efflux pump and application for reversing multidrug resistance in hepatocellular carcinoma. *Polym. Chem.* **9**, 1827–1839 (2018).
255. Tan, S. *et al.* Recent developments ind-a-tocopheryl polyethylene glycol-succinate-based nanomedicine for cancer therapy. *Drug Deliv.* **24**, 1831–1842 (2017).
256. Chen, Y. *et al.* TPGS-1000 exhibits potent anticancer activity for hepatocellular carcinoma in vitro and in vivo. *Aging (Albany, NY)*. **12**, 1624–1642 (2020).
257. Youk, H. J. *et al.* Enhanced anticancer efficacy of  $\alpha$ -tocopheryl succinate by conjugation with polyethylene glycol. *J. Control. Release* **107**, 43–52 (2005).
258. Zeng, Y. C. *et al.* Soluplus micelles for improving the oral bioavailability of scopoletin and their hypouricemic effect in vivo. *Acta Pharmacol. Sin.* **38**, 424–433 (2017).
259. Jin, X., Zhou, B., Xue, L. & San, W. Soluplus® micelles as a potential drug delivery system for reversal of resistant tumor. *Biomed. Pharmacother.* **69**, 388–395 (2015).
260. Linn, M. *et al.* Soluplus® as an effective absorption enhancer of poorly soluble drugs in vitro and in vivo. *Eur. J. Pharm. Sci.* **45**, 336–343 (2012).
261. Cagel, M. *et al.* Polymeric mixed micelles as nanomedicines: Achievements and perspectives. *Eur. J. Pharm. Biopharm.* **113**, 211–228 (2017).
262. Kim, S., Shi, Y., Kim, J. Y., Park, K. & Cheng, J. X. Overcoming the barriers in micellar drug delivery: Loading efficiency, in vivo stability, and micelle-cell interaction. *Expert Opin. Drug Deliv.* **7**, 49–62 (2010).
263. Ishida, O., Maruyama, K., Sasaki, K. & Iwatsuru, M. Size-dependent extravasation and interstitial localization of polyethyleneglycol liposomes in solid tumor-bearing mice. *Int. J. Pharm.* **190**, 49–56 (1999).
264. Primard, C. *et al.* Traffic of poly(lactic acid) nanoparticulate vaccine vehicle

- from intestinal mucus to sub-epithelial immune competent cells. *Biomaterials* **31**, 6060–6068 (2010).
265. Bernabeu, E. *et al.* Novel Soluplus®-TPGS mixed micelles for encapsulation of paclitaxel with enhanced in vitro cytotoxicity on breast and ovarian cancer cell lines. *Colloids Surfaces B Biointerfaces* **140**, 403–411 (2016).
266. Hou, J. *et al.* Improved oral bioavailability and anticancer efficacy on breast cancer of paclitaxel via Novel Soluplus®—Solutol® HS15 binary mixed micelles system. *Int. J. Pharm.* **512**, 186–193 (2016).
267. Jose, S. *et al.* Transferrin-conjugated Docetaxel-PLGA nanoparticles for tumor targeting: Influence on MCF-7 cell cycle. *Polymers (Basel)*. **11**, (2019).
268. El-Hammadi, M. M., Delgado, Á. V., Melguizo, C., Prados, J. C. & Arias, J. L. Folic acid-decorated and PEGylated PLGA nanoparticles for improving the antitumour activity of 5-fluorouracil. *Int. J. Pharm.* **516**, 61–70 (2017).
269. Kesharwani, S. S., Kaur, S., Tummala, H. & Sangamwar, A. T. Multifunctional approaches utilizing polymeric micelles to circumvent multidrug resistant tumors. *Colloids Surfaces B Biointerfaces* **173**, 581–590 (2019).
270. Zhang, J. *et al.* Systematic evaluation of multifunctional paclitaxel-loaded polymeric mixed micelles as a potential anticancer remedy to overcome multidrug resistance. *Acta Biomater.* **50**, 381–395 (2017).
271. Espuelas, S., Agüeros, M., Esparza, I. & Irache, J. M. Nanoparticles for the Oral Administration of Cancer Therapies. in *Vasa* (ed. Prokop, A.) vol. 5 487–509 (Springer Netherlands, 2011).
272. Cabral, H. & Kataoka, K. Progress of drug-loaded polymeric micelles into clinical studies. *J. Control. Release* **190**, 465–476 (2014).
273. Clavreul, A. *et al.* Development and characterization of sorafenib-loaded lipid nanocapsules for the treatment of glioblastoma. *Drug Deliv.* **25**, 1756–1765 (2018).
274. Shah, H., Jain, A., Laghate, G. & Prabhudesai, D. *Handbook of Pharmaceutical Excipients – 7th Edition. Pharmaceutical press* vol. 18 (Elsevier, 2009).
275. Gattefosse'. *Geleol Mono and Diglycerides Nf.* (2010).

276. Rizwanullah, M., Ahmad, J. & Amin, S. Nanostructured Lipid Carriers: A Novel Platform for Chemotherapeutics. *Curr. Drug Deliv.* **13**, 4–26 (2016).
277. Precirol ATO 5. *Gattefosse'* (2012).
278. Mehnert, W. & Mäder, K. Solid lipid nanoparticles: Production, characterization and applications. *Adv. Drug Deliv. Rev.* **64**, 83–101 (2012).
279. Aburahma, M. H. & Badr-Eldin, S. M. Compritol 888 ATO: a multifunctional lipid excipient in drug delivery systems and nanopharmaceuticals. *Expert Opin. Drug Deliv.* **11**, 1865–1883 (2014).
280. *Oral Drug Delivery With Lipid Excipients. Gattefossé* (2020).
281. Panigrahi, K. C. *et al.* Gelucire: A versatile polymer for modified release drug delivery system. *Futur. J. Pharm. Sci.* **4**, 102–108 (2018).
282. Kasongo, K. W., Pardeike, J., Müller, R. H. & Walker, R. B. Selection and characterization of suitable lipid excipients for use in the manufacture of didanosine-loaded solid lipid nanoparticles and nanostructured lipid carriers. *J. Pharm. Sci.* **100**, 5185–5196 (2011).
283. El-Sheridy, N. A., Ramadan, A. A., Eid, A. A. & El-Khordagui, L. K. Itraconazole lipid nanocapsules gel for dermatological applications: In vitro characteristics and treatment of induced cutaneous candidiasis. *Colloids Surfaces B Biointerfaces* **181**, 623–631 (2019).
284. Ullio Gamboa, G. V. *et al.* Albendazole-lipid nanocapsules: Optimization, characterization and chemoprophylactic efficacy in mice infected with *Echinococcus granulosus*. *Exp. Parasitol.* **198**, 79–86 (2019).
285. Roger, E., Lagarce, F. & Benoit, J. P. Development and characterization of a novel lipid nanocapsule formulation of Sn38 for oral administration. *Eur. J. Pharm. Biopharm.* **79**, 181–188 (2011).
286. Sharma, T. *et al.* Supersaturated LFCS type III self-emulsifying delivery systems of sorafenib tosylate with improved biopharmaceutical performance: QbD-enabled development and evaluation. *Drug Deliv. Transl. Res.* **10**, 839–861 (2020).
287. BASF. Kolliphor® HS 15. *Basf* 1–5 at

<https://pharmaceutical.basf.com/global/en/drug-formulation/products/kolliphors-15.html> (2020).

288. Hoarau, D., Delmas, P., David, S., Roux, E. & Leroux, J. C. Novel long-circulating lipid nanocapsules. *Pharm. Res.* **21**, 1783–1789 (2004).
289. Lipoid, S. *Lipoid S 100 [Lipoid GmbH]*. (2011).
290. BASF. *Soluplus® Technical Information. BASF, Pharma ingredients & services* (2019).
291. Pignatello, R. *et al.* Soluplus® polymeric nanomicelles improve solubility of BCS-class II drugs. *Drug Deliv. Transl. Res.* (2022) doi:10.1007/s13346-022-01182-x.
292. Guo, Y., Luo, J., Tan, S., Otieno, B. O. & Zhang, Z. The applications of Vitamin E TPGS in drug delivery. *Eur. J. Pharm. Sci.* **49**, 175–186 (2013).
293. Zhang, Z., Tan, S. & Feng, S. S. Vitamin E TPGS as a molecular biomaterial for drug delivery. *Biomaterials* **33**, 4889–4906 (2012).
294. Muthu, M. S., Avinash Kulkarni, S., Liu, Y. & Feng, S. S. Development of docetaxel-loaded vitamin e TPGS micelles: Formulation optimization, effects on brain cancer cells and biodistribution in rats. *Nanomedicine* **7**, 353–364 (2012).
295. Meng, X. *et al.* Pluronic F127 and D- $\alpha$ -Tocopheryl Polyethylene Glycol Succinate (TPGS) Mixed Micelles for Targeting Drug Delivery across The Blood Brain Barrier. *Sci. Rep.* **7**, 1–12 (2017).
296. Bernabeu, E. *et al.* Paclitaxel-loaded PCL-TPGS nanoparticles: In vitro and in vivo performance compared with Abraxane®. *Colloids Surfaces B Biointerfaces* **113**, 43–50 (2014).
297. Ansell, S. M. *et al.* Modulating the therapeutic activity of nanoparticle delivered paclitaxel by manipulating the hydrophobicity of prodrug conjugates. *J. Med. Chem.* **51**, 3288–3296 (2008).
298. Khare, V., Sakarchi, W. Al, Gupta, P. N., Curtis, A. D. M. & Hoskins, C. Synthesis and characterization of TPGS-gemcitabine prodrug micelles for pancreatic cancer therapy. *RSC Adv.* **6**, 60126–60137 (2016).

299. Jiang, T. *et al.* Doxorubicin Encapsulated in TPGS-Modified 2D-Nanodisks Overcomes Multidrug Resistance. *Chem. - A Eur. J.* **26**, 2470–2477 (2020).
300. Mi, Y., Zhao, J. & Feng, S. S. Targeted co-delivery of docetaxel, cisplatin and herceptin by vitamin E TPGS-cisplatin prodrug nanoparticles for multimodality treatment of cancer. *J. Control. Release* **169**, 185–192 (2013).
301. Zhao, H. & Yung, L. Y. L. Addition of TPGS to folate-conjugated polymer micelles for selective tumor targeting. *J. Biomed. Mater. Res. - Part A* **91**, 505–518 (2009).
302. Cai, Y. *et al.* Glycyrrhetic Acid Mediated Drug Delivery Carriers for Hepatocellular Carcinoma Therapy. *Mol. Pharm.* **13**, 699–709 (2016).
303. Cheng, W. *et al.* TPGS-Functionalized Polydopamine-Modified Mesoporous Silica as Drug Nanocarriers for Enhanced Lung Cancer Chemotherapy against Multidrug Resistance. *Small* **13**, 1–12 (2017).
304. Zhu, X. *et al.* Glycyrrhetic acid-modified TPGS polymeric micelles for hepatocellular carcinoma-targeted therapy. *Int. J. Pharm.* **529**, 451–464 (2017).
305. Yang, C., Wu, T., Qi, Y. & Zhang, Z. Recent advances in the application of vitamin E TPGS for drug delivery. *Theranostics* **8**, 464–485 (2018).
306. Schwartzberg, L. S. & Navari, R. M. Safety of Polysorbate 80 in the Oncology Setting. *Adv. Ther.* **35**, 754–767 (2018).
307. ten Tije, A. J., Verweij, J., Loos, W. J. & Sparreboom, A. Pharmacological Effects of Formulation Vehicles. *Clin. Pharmacokinet.* **42**, 665–685 (2003).
308. Dhand, C. *et al.* Methods and strategies for the synthesis of diverse nanoparticles and their applications: A comprehensive overview. *RSC Adv.* **5**, 105003–105037 (2015).
309. Shaw, R. *Dynamic Light Scattering Training Achieving reliable nano particle sizing (Available from: <http://www.chem.uci.edu/~dmitryf/manuals/Fundamentals/DLS%20concept.pdf>). ATA Scientific; Malvern vol. Accessed 2 [http://www.chem.uci.edu/~dmitryf/manuals/Fundamentals/DLS concept.pdf](http://www.chem.uci.edu/~dmitryf/manuals/Fundamentals/DLS%20concept.pdf) (2014).*

310. Raval, N. *et al.* Importance of physicochemical characterization of nanoparticles in pharmaceutical product development. *Basic Fundamentals of Drug Delivery* (Elsevier Inc., 2018). doi:10.1016/B978-0-12-817909-3.00010-8.
311. Chil-, N. & Kanda, N. *Thermal Analysis of Pharmaceuticals*. (CRC Press, 2006). doi:10.1201/9781420014891.
312. Law, D. & Zhou, D. Solid-State Characterization and Techniques. in *Developing Solid Oral Dosage Forms* 59–84 (Elsevier, 2017). doi:10.1016/B978-0-12-802447-8.00003-0.
313. Bunaciu, A. A., Udriștioiu, E. gabriela & Aboul-Enein, H. Y. X-Ray Diffraction: Instrumentation and Applications. *Crit. Rev. Anal. Chem.* **45**, 289–299 (2015).
314. Titus, D., James Jebaseelan Samuel, E. & Roopan, S. M. Nanoparticle characterization techniques. in *Green Synthesis, Characterization and Applications of Nanoparticles* 303–319 (Elsevier, 2019). doi:10.1016/B978-0-08-102579-6.00012-5.
315. Bunaciu, A. A., Aboul-Enein, H. Y. & Fleschin, S. Application of Fourier Transform Infrared Spectrophotometry in Pharmaceutical Drugs Analysis. *Appl. Spectrosc. Rev.* **45**, 206–219 (2010).
316. Colthup, N. B. Infrared Spectroscopy. in *Encyclopedia of Physical Science and Technology* vol. 24 793–816 (Elsevier, 2003).
317. Tiernan, H., Byrne, B. & Kazarian, S. G. ATR-FTIR spectroscopy and spectroscopic imaging for the analysis of biopharmaceuticals. *Spectrochim. Acta - Part A Mol. Biomol. Spectrosc.* **241**, 118636 (2020).
318. Atta-ur-Rahman. Chemical Shift in <sup>1</sup>H-NMR Spectroscopy. in *Nuclear Magnetic Resonance* vol. 741 1–33 (Springer US, 1986).
319. Pavia, D. L., Lampman, G. M. & Kriz, G. S. Introduction to Spectroscopy fifth edition. in *Thomson Learning, Inc.* 690 (2014).
320. Chary, K. V. R. & Govil, G. Basic Concepts In NMR Spectroscopy. in *NMR in Biological Systems* 1–41 (Springer Netherlands, 2008). doi:10.1007/978-1-4020-6680-1\_1.
321. Grotz, E. *et al.* Pulmonary delivery of rifampicin-loaded soluplus micelles

- against *Mycobacterium tuberculosis*. *J. Drug Deliv. Sci. Technol.* **53**, 101170 (2019).
322. Mi, Y., Liu, Y. & Feng, S. S. Formulation of Docetaxel by folic acid-conjugated D- $\alpha$ -tocopheryl polyethylene glycol succinate 2000 (Vitamin E TPGS2k) micelles for targeted and synergistic chemotherapy. *Biomaterials* **32**, 4058–4066 (2011).
323. Sarika, P. R., James, N. R., Kumar P.R., A. & Raj, D. K. Galactosylated alginate-curcumin micelles for enhanced delivery of curcumin to hepatocytes. *Int. J. Biol. Macromol.* **86**, 1–9 (2016).
324. Zhu, X. *et al.* Glycyrrhetic acid-modified TPGS polymeric micelles for hepatocellular carcinoma-targeted therapy. *Int. J. Pharm.* **529**, 451–464 (2017).
325. Dou, J., Zhang, H., Liu, X., Zhang, M. & Zhai, G. Preparation and evaluation in vitro and in vivo of docetaxel loaded mixed micelles for oral administration. *Colloids Surfaces B Biointerfaces* **114**, 20–27 (2014).
326. Hu, M. *et al.* Improved oral bioavailability and therapeutic efficacy of dabigatran etexilate via Soluplus-TPGS binary mixed micelles system. *Drug Dev. Ind. Pharm.* **43**, 687–697 (2017).
327. Zhao, J. *et al.* Soluplus/TPGS mixed micelles for dioscin delivery in cancer therapy. *Drug Dev. Ind. Pharm.* **43**, 1197–1204 (2017).
328. Ding, Y. *et al.* Development and evaluation of a novel drug delivery: Soluplus®/TPGS mixed micelles loaded with piperine in vitro and in vivo. *Drug Dev. Ind. Pharm.* **44**, 1409–1416 (2018).
329. Wang, Y. *et al.* Dihydroartemisinin and doxorubicin co-loaded Soluplus®-TPGS mixed micelles: formulation characterization, cellular uptake, and pharmacodynamic studies. *Pharm. Dev. Technol.* **24**, 1125–1132 (2019).
330. Patil, S., Ujalambkar, V., Rathore, A., Rojatkar, S. & Pokharkar, V. Galangin loaded galactosylated pluronic F68 polymeric micelles for liver targeting. *Biomed. Pharmacother.* **112**, (2019).
331. Zhou, Y. *et al.* Fast In Vitro Release and In Vivo Absorption of an Anti-Schizophrenic Drug Paliperidone from Its Soluplus®/TPGS Mixed Micelles.

*Pharmaceutics* **14**, (2022).

332. Nandni, D., Vohra, K. K. & Mahajan, R. K. Study of micellar and phase separation behavior of mixed systems of triblock polymers. *J. Colloid Interface Sci.* **338**, 420–427 (2009).
333. Senthil Kumar, P., Grace Pavithra, K. & Naushad, M. *Characterization techniques for nanomaterials. Nanomaterials for Solar Cell Applications* (Elsevier Inc., 2019). doi:10.1016/B978-0-12-813337-8.00004-7.
334. Upright and Inverted Microscopy | Theory and Applications | ibidi. at <https://ibidi.com/content/212-inverted-and-upright-microscopy>.
335. D'Souza, S. A Review of In Vitro Drug Release Test Methods for Nano-Sized Dosage Forms . *Adv. Pharm.* **2014**, 1–12 (2014).
336. Modi, S. & Anderson, B. D. Determination of drug release kinetics from nanoparticles: Overcoming pitfalls of the dynamic dialysis method. *Mol. Pharm.* **10**, 3076–3089 (2013).
337. Costa, P. & Sousa Lobo, J. M. Modeling and comparison of dissolution profiles. *Eur. J. Pharm. Sci.* **13**, 123–133 (2001).
338. Mathematical models of drug release. in *Strategies to Modify the Drug Release from Pharmaceutical Systems* 63–86 (Elsevier, 2015). doi:10.1016/B978-0-08-100092-2.00005-9.
339. Higuchi, T. Rate of release of medicaments from ointment bases containing drugs in suspension. *J. Pharm. Sci.* **50**, 874–875 (1961).
340. Zhang, Y. *et al.* DDSolver: An Add-In Program for Modeling and Comparison of Drug Dissolution Profiles. *AAPS J.* **12**, 263–271 (2010).
341. Tsong, Y., Sathe, P. & Shah, V. P. in Vitro Dissolution Profile Comparison and IVIVR. in *Advances in Experimental Medicine and Biology* vol. 423 31–42 (1997).
342. Shah, V. P. *et al.* fDA Guidance for Industry 1 Dissolution Testing of Immediate Release Solid Oral Dosage Forms. *Dissolution Technol.* **4**, 15–22 (1997).
343. Freitag, G. Guidelines on dissolution profile comparison. *Ther. Innov. Regul. Sci.*

- 35**, 865–874 (2001).
344. Podczeck, F. Comparison of in vitro dissolution profiles by calculating mean dissolution time (MDT) or mean residence time (MRT). *Int. J. Pharm.* **97**, 93–100 (1993).
345. Khan, K. A. The concept of dissolution efficiency. *J. Pharm. Pharmacol.* **27**, 48–49 (2011).
346. Sharon, N. & Lis, H. Lectins. in *Encyclopedia of Biological Chemistry* 701–705 (Elsevier, 2013). doi:10.1016/B978-0-12-378630-2.00217-6.
347. Bettinger, T., Remy, J.-S. & Erbacher, P. Size Reduction of Galactosylated PEI/DNA Complexes Improves Lectin-Mediated Gene Transfer into Hepatocytes. *Bioconjug. Chem.* **10**, 558–561 (1999).
348. Orr, G. A., Rando, R. R. & Bangerter, F. W. Synthetic glycolipids and the lectin-mediated aggregation of liposomes. *J. Biol. Chem.* **254**, 4721–4725 (1979).
349. Nie, H. *et al.* Effect of gal/GalNAc regioisomerism in galactosylated liposomes on asialoglycoprotein receptor-mediated hepatocyte-selective targeting in vivo. *J. Liposome Res.* **31**, 79–89 (2021).
350. Managit, C., Kawakami, S., Yamashita, F. & Hashida, M. Effect of galactose density on asialoglycoprotein receptor-mediated uptake of galactosylated liposomes. *J. Pharm. Sci.* **94**, 2266–2275 (2005).
351. Naicker, K., Ariatti, M. & Singh, M. PEGylated galactosylated cationic liposomes for hepatocytic gene delivery. *Colloids Surfaces B Biointerfaces* **122**, 482–490 (2014).
352. Xue, W. J. *et al.* Asialoglycoprotein receptor-magnetic dual targeting nanoparticles for delivery of RASSF1A to hepatocellular carcinoma. *Sci. Rep.* **6**, 1–13 (2016).
353. Morimoto, K. *et al.* Molecular weight-dependent gene transfection activity of unmodified and galactosylated polyethyleneimine on hepatoma cells and mouse liver. *Mol. Ther.* **7**, 254–261 (2003).
354. Kuete, V., Karaosmanoğlu, O. & Sivas, H. Anticancer Activities of African Medicinal Spices and Vegetables. in *Medicinal Spices and Vegetables from*

- Africa* 271–297 (Elsevier, 2017). doi:10.1016/B978-0-12-809286-6.00010-8.
355. Adan, A., Alizada, G., Kiraz, Y., Baran, Y. & Nalbant, A. Flow cytometry: basic principles and applications. *Crit. Rev. Biotechnol.* **37**, 163–176 (2017).
356. Ibrahim, S. F. & van den Engh, G. Flow Cytometry and Cell Sorting. in *Advances in Biochemical Engineering/Biotechnology* vol. 106 19–39 (2007).
357. Artursson, P., Palm, K. & Luthman, K. Caco-2 monolayers in experimental and theoretical predictions of drug transport. *Adv. Drug Deliv. Rev.* **64**, 280–289 (2012).
358. Chitchumroonchokchai, C. & Failla, M. L. In vitro Approaches for Investigating the Bioaccessibility and Bioavailability of Dietary Nutrients and Bioactive Metabolites. in *Functional Foods and Beverages* 171–199 (John Wiley & Sons, Inc., 2018). doi:10.1002/9781118823309.ch6.
359. Hubatsch, I., Ragnarsson, E. G. E. & Artursson, P. Determination of drug permeability and prediction of drug absorption in Caco-2 monolayers. *Nat. Protoc.* **2**, 2111–2119 (2007).
360. Naseri, N., Valizadeh, H. & Zakeri-Milani, P. Solid lipid nanoparticles and nanostructured lipid carriers: Structure preparation and application. *Adv. Pharm. Bull.* **5**, 305–313 (2015).
361. Daher, S., Massarwa, M., Benson, A. A. & Khoury, T. Current and Future Treatment of Hepatocellular Carcinoma: An Updated Comprehensive Review. *J. Clin. Transl. Hepatol.* **6**, 1–10 (2017).
362. DuBois, M., Gilles, K. A., Hamilton, J. K., Rebers, P. A. & Smith, F. Colorimetric Method for Determination of Sugars and Related Substances. *Anal. Chem.* **28**, 350–356 (1956).
363. Yin, X. *et al.* Ceramide-Fabricated Co-Loaded Liposomes for the Synergistic Treatment of Hepatocellular Carcinoma. *AAPS PharmSciTech* **19**, 2133–2143 (2018).
364. Sun, J. *et al.* Curcumin-loaded solid lipid nanoparticles have prolonged in vitro antitumour activity, cellular uptake and improved in vivo bioavailability. *Colloids Surfaces B Biointerfaces* **111**, 367–375 (2013).

365. Yue, P. F. *et al.* Study on formability of solid nanosuspensions during nanodispersion and solidification: I. Novel role of stabilizer/drug property. *Int. J. Pharm.* **454**, 269–277 (2013).
366. Yang, S. *et al.* In vivo biodistribution, biocompatibility, and efficacy of sorafenib-loaded lipid-based nanosuspensions evaluated experimentally in cancer. *Int. J. Nanomedicine* **11**, 2329–2343 (2016).
367. Wang, W. *et al.* Galactosylated solid lipid nanoparticles with cucurbitacin B improves the liver targetability. *Drug Deliv.* **17**, 114–122 (2010).
368. Abd-Rabou, A. A., Bharali, D. J. & Mousa, S. A. Viramidine-Loaded Galactosylated Nanoparticles Induce Hepatic Cancer Cell Apoptosis and Inhibit Angiogenesis. *Appl. Biochem. Biotechnol.* **190**, 305–324 (2020).
369. Zhang, M. *et al.* Lactosylated gramicidin-based lipid nanoparticles (Lac-GLN) for targeted delivery of anti-miR-155 to hepatocellular carcinoma. *J. Control. Release* **168**, 251–261 (2013).
370. Rodrigues, L. B. O. *et al.* Ion Pair Strategy in Solid Lipid Nanoparticles: a Targeted Approach to Improve Epidermal Targeting with Controlled Adapalene Release, Resulting Reduced Skin Irritation. *Pharm. Res.* **37**, (2020).
371. Das, S., Ng, W. K., Kanaujia, P., Kim, S. & Tan, R. B. H. Formulation design, preparation and physicochemical characterizations of solid lipid nanoparticles containing a hydrophobic drug: Effects of process variables. *Colloids Surfaces B Biointerfaces* **88**, 483–489 (2011).
372. Pandya, N. T., Jani, P., Vanza, J. & Tandel, H. Solid lipid nanoparticles as an efficient drug delivery system of olmesartan medoxomil for the treatment of hypertension. *Colloids Surfaces B Biointerfaces* **165**, 37–44 (2018).
373. Jensen, L. B. *et al.* Corticosteroid solubility and lipid polarity control release from solid lipid nanoparticles. *Int. J. Pharm.* **390**, 53–60 (2010).
374. Bunjes, H. Structural properties of solid lipid based colloidal drug delivery systems. *Curr. Opin. Colloid Interface Sci.* **16**, 405–411 (2011).
375. Yoon, G., Park, J. W. & Yoon, I. S. Solid lipid nanoparticles (SLNs) and nanostructured lipid carriers (NLCs): Recent advances in drug delivery. *J.*

- Pharm. Investig.* **43**, 353–362 (2013).
376. Helgason, T., Awad, T. S., Kristbergsson, K., McClements, D. J. & Weiss, J. Effect of surfactant surface coverage on formation of solid lipid nanoparticles (SLN). *J. Colloid Interface Sci.* **334**, 75–81 (2009).
377. Kovacevic, A., Savic, S., Vuleta, G., Müller, R. H. & Keck, C. M. Polyhydroxy surfactants for the formulation of lipid nanoparticles (SLN and NLC): Effects on size, physical stability and particle matrix structure. *Int. J. Pharm.* **406**, 163–172 (2011).
378. Cirri, M. *et al.* Design, characterization and in vivo evaluation of nanostructured lipid carriers (NLC) as a new drug delivery system for hydrochlorothiazide oral administration in pediatric therapy. *Drug Deliv.* **25**, 1910–1921 (2018).
379. Nnamani, P. O., Hansen, S., Windbergs, M. & Lehr, C. M. Development of artemether-loaded nanostructured lipid carrier (NLC) formulation for topical application. *Int. J. Pharm.* **477**, 208–217 (2014).
380. Kasongo, K. W., Mller, R. H. & Walker, R. B. The use of hot and cold high pressure homogenization to enhance the loading capacity and encapsulation efficiency of nanostructured lipid carriers for the hydrophilic antiretroviral drug, didanosine for potential administration to paediatric patients. *Pharm. Dev. Technol.* **17**, 353–362 (2012).
381. Wa Kasongo, K., Shegokar, R., Müller, R. H. & Walker, R. B. Formulation development and in vitro evaluation of didanosine-loaded nanostructured lipid carriers for the potential treatment of AIDS dementia complex. *Drug Dev. Ind. Pharm.* **37**, 396–407 (2011).
382. Makoni, P. A., Kasongo, K. W. & Walker, R. B. Short term stability testing of efavirenz-loaded solid lipid nanoparticle (SLN) and nanostructured lipid carrier (NLC) dispersions. *Pharmaceutics* **11**, (2019).
383. Mura, P., Maestrelli, F., D’Ambrosio, M., Luceri, C. & Cirri, M. Evaluation and comparison of solid lipid nanoparticles (SLNs) and nanostructured lipid carriers (NLCs) as vectors to develop hydrochlorothiazide effective and safe pediatric oral liquid formulations. *Pharmaceutics* **13**, (2021).

384. Wang, W. *et al.* Galactosylated solid lipid nanoparticles with cucurbitacin B improves the liver targetability. *Drug Deliv.* **17**, 114–122 (2010).
385. Teixeira, M. I. *et al.* Formulation, Characterization, and Cytotoxicity Evaluation of Lactoferrin Functionalized Lipid Nanoparticles for Riluzole Delivery to the Brain. *Pharmaceutics* **14**, (2022).
386. Kumbhar, D. D. & Pokharkar, V. B. Engineering of a nanostructured lipid carrier for the poorly water-soluble drug, bicalutamide: Physicochemical investigations. *Colloids Surfaces A Physicochem. Eng. Asp.* **416**, 32–42 (2013).
387. Vitorino, C. *et al.* QbD-driven development of intranasal lipid nanoparticles for depression treatment. *Eur. J. Pharm. Biopharm.* **153**, 106–120 (2020).
388. Ibrahim, T. M., Abdallah, M. H., El-Megrab, N. A. & El-Nahas, H. M. Upgrading of dissolution and anti-hypertensive effect of Carvedilol via two combined approaches: self-emulsification and liquisolid techniques. *Drug Dev. Ind. Pharm.* **44**, 873–885 (2018).
389. Ruman, U. *et al.* Synthesis and characterization of chitosan-based nanodelivery systems to enhance the anticancer effect of sorafenib drug in hepatocellular carcinoma and colorectal adenocarcinoma cells. *Nanomaterials* **11**, 1–28 (2021).
390. Bunjes, H., Koch, M. H. J. & Westesen, K. Effect of Particle Size on Colloidal Solid Triglycerides. *Langmuir* **16**, 5234–5241 (2000).
391. Botto, C. *et al.* Surfactant effect on the physicochemical characteristics of cationic solid lipid nanoparticles. *Int. J. Pharm.* **516**, 334–341 (2017).
392. Jiang, S. *et al.* Solubility correlation and thermodynamic analysis of sorafenib free base and sorafenib tosylate in monosolvents and binary solvent mixtures. *J. Chem. Eng. Data* **62**, 259–267 (2017).
393. Shinde, U. K., Suryawanshi, D. G. & Amin, P. D. Development of Gelucire® 48/16 and TPGS Mixed Micelles and Its Pellet Formulation by Extrusion Spheronization Technique for Dissolution Rate Enhancement of Curcumin. *AAPS PharmSciTech* **22**, 1–11 (2021).
394. Zhao, X. *et al.* Codelivery of doxorubicin and curcumin with lipid nanoparticles results in improved efficacy of chemotherapy in liver cancer. *Int. J.*

- Nanomedicine* **10**, 257–270 (2014).
395. Suresh, G., Manjunath, K., Venkateswarlu, V. & Satyanarayana, V. Preparation, characterization, and in vitro and in vivo evaluation of lovastatin solid lipid nanoparticles. *AAPS PharmSciTech* **8**, E162–E170 (2007).
396. Trenkenschuh, E. & Friess, W. Freeze-drying of nanoparticles: How to overcome colloidal instability by formulation and process optimization. *Eur. J. Pharm. Biopharm.* **165**, 345–360 (2021).
397. Amis, T. M., Renukuntla, J., Bolla, P. K. & Clark, B. A. Selection of cryoprotectant in lyophilization of progesterone-loaded stearic acid solid lipid nanoparticles. *Pharmaceutics* **12**, 1–15 (2020).
398. Cervello, M. *et al.* Nanoparticles of a polyaspartamide-based brush copolymer for modified release of sorafenib: In vitro and in vivo evaluation. *J. Control. Release* **266**, 47–56 (2017).
399. Chen, J. *et al.* Poly(lactide-co-glycolide) microspheres for MRI-monitored transcatheter delivery of sorafenib to liver tumors. *J. Control. Release* **184**, 10–17 (2014).
400. Zhang, N., Su, Z., Liang, Y. & Yao, Y. pH-Sensitive carboxymethyl chitosan-modified cationic liposomes for sorafenib and siRNA co-delivery. *Int. J. Nanomedicine* 6185 (2015) doi:10.2147/IJN.S90524.
401. Xiao, Y. *et al.* Sorafenib and gadolinium co-loaded liposomes for drug delivery and MRI-guided HCC treatment. *Colloids Surfaces B Biointerfaces* **141**, 83–92 (2016).
402. Kim, D. H. *et al.* Antitumor activity of sorafenib-incorporated nanoparticles of dextran/poly(DL-lactide-co-glycolide) block copolymer. *Nanoscale Res. Lett.* **7**, 1–8 (2012).
403. Wang, C. *et al.* RGD peptide targeted lipid-coated nanoparticles for combinatorial delivery of sorafenib and quercetin against hepatocellular carcinoma. *Drug Dev. Ind. Pharm.* **42**, 1938–1944 (2016).
404. Rainer H. Müller, Karsten MaÈder, S. G. Solid lipid nanoparticles (SLN) for controlled drug delivery - a review of the state of the art. *Eur. J. Pharm.*

- Biopharm.* **50**, 161–177 (2000).
405. Attili-Qadri, S. *et al.* Oral delivery system prolongs blood circulation of docetaxel nanocapsules via lymphatic absorption. *Proc. Natl. Acad. Sci. U. S. A.* **110**, 17498–17503 (2013).
406. Lollo, G. *et al.* In vitro anti-cancer activity and pharmacokinetic evaluation of curcumin-loaded lipid nanocapsules. *Mater. Sci. Eng. C* **91**, 859–867 (2018).
407. Takayasu, K. *et al.* Comparison of CT findings with resected specimens after chemoembolization with iodized oil for hepatocellular carcinoma. *Am. J. Roentgenol.* **175**, 699–704 (2000).
408. Towu, E., Al-Mufti, R., Winslet, M., Quaglia, L. & Losty, P. Uptake of Lipiodol-Cytotoxics Conjugates by Hepatocellular Carcinoma Cells. *J. Pediatr. Surg.* **39**, 203–206 (2004).
409. Lilienberg, E. *et al.* In vivo drug delivery performance of lipiodol-based emulsion or drug-eluting beads in patients with hepatocellular carcinoma. *Mol. Pharm.* **14**, 448–458 (2017).
410. Béduneau, A. *et al.* Design of targeted lipid nanocapsules by conjugation of whole antibodies and antibody Fab' fragments. *Biomaterials* **28**, 4978–4990 (2007).
411. Morille, M., Passirani, C., Letrou-Bonneval, E., Benoit, J. P. & Pitard, B. Galactosylated DNA lipid nanocapsules for efficient hepatocyte targeting. *Int. J. Pharm.* **379**, 293–300 (2009).
412. Hirsjärvi, S. *et al.* Surface modification of lipid nanocapsules with polysaccharides: From physicochemical characteristics to in vivo aspects. *Acta Biomater.* **9**, 6686–6693 (2013).
413. Morille, M., Passirani, C., Letrou-Bonneval, E., Benoit, J. P. & Pitard, B. Galactosylated DNA lipid nanocapsules for efficient hepatocyte targeting. *Int. J. Pharm.* **379**, 293–300 (2009).
414. Tsend-Ayush, A. *et al.* Lactobionic acid-conjugated TPGS nanoparticles for enhancing therapeutic efficacy of etoposide against hepatocellular carcinoma. *Nanotechnology* **28**, (2017).

415. Piazzini, V. *et al.* Formulation of nanomicelles to improve the solubility and the oral absorption of silymarin. *Molecules* **24**, 1–20 (2019).
416. Liu, J., Zeng, F. & Allen, C. Influence of serum protein on polycarbonate-based copolymer micelles as a delivery system for a hydrophobic anti-cancer agent. *J. Control. Release* **103**, 481–497 (2005).
417. Pranatharthihran, S. *et al.* Asialoglycoprotein receptor targeted delivery of doxorubicin nanoparticles for hepatocellular carcinoma. *Drug Deliv.* **24**, 20–29 (2017).
418. Sorafenib | C21H16ClF3N4O3 - PubChem.  
<https://pubchem.ncbi.nlm.nih.gov/compound/Sorafenib#section=Physical-Description>.
419. Sonali *et al.* Transferrin receptor-targeted vitamin E TPGS micelles for brain cancer therapy: preparation, characterization and brain distribution in rats. *Drug Deliv.* **23**, 1788–1798 (2016).
420. Zheng, Y. *et al.* Surface modification of TPGS-b-(PCL-ran-PGA) nanoparticles with polyethyleneimine as a co-delivery system of TRAIL and endostatin for cervical cancer gene therapy. *Nanoscale Res. Lett.* **8**, 1–12 (2013).
421. Tsend-Ayush, A. *et al.* Lactobionic acid-conjugated TPGS nanoparticles for enhancing therapeutic efficacy of etoposide against hepatocellular carcinoma. *Nanotechnology* **28**, 195602 (2017).
422. Agrawal, P. *et al.* TPGS-chitosan cross-linked targeted nanoparticles for effective brain cancer therapy. *Mater. Sci. Eng. C* **74**, 167–176 (2017).
423. Tao, W. *et al.* Docetaxel-loaded nanoparticles based on star-shaped mannitol-core PLGA-TPGS diblock copolymer for breast cancer therapy. *Acta Biomater.* **9**, 8910–8920 (2013).
424. Liang, C. *et al.* Self-controlled release of Oxaliplatin prodrug from d- $\alpha$ -tocopheryl polyethylene glycol 1000 succinate (TPGS) functionalized mesoporous silica nanoparticles for cancer therapy. *J. Colloid Interface Sci.* **525**, 1–10 (2018).
425. Uster, P. S. *et al.* Insertion of poly(ethylene glycol) derivatized phospholipid into

- pre-formed liposomes results in prolonged in vivo circulation time. *FEBS Lett.* **386**, 243–246 (1996).
426. Mare, R. *et al.* Post-insertion parameters of PEG-derivatives in phosphocholine-liposomes. *Int. J. Pharm.* **552**, 414–421 (2018).
427. Ashok, B., Arleth, L., Hjelm, R. P., Rubinstein, I. & Önyüksel, H. In vitro characterization of PEGylated phospholipid micelles for improved drug solubilization: Effects of PEG chain length and PC incorporation. *J. Pharm. Sci.* **93**, 2476–2487 (2004).
428. Ishida, T., Iden, D. L. & Allen, T. M. A combinatorial approach to producing sterically stabilized (Stealth) immunoliposomal drugs. *FEBS Lett.* **460**, 129–133 (1999).
429. Wei, M. *et al.* Hepatocellular carcinoma targeting effect of PEGylated liposomes modified with lactoferrin. *Eur. J. Pharm. Sci.* **46**, 131–141 (2012).
430. Allen, T. M., Letters, M. B., Sapra, P. & Moase, E. Use of the post-insertion method for the formation of ligand-coupled liposomes. *Cell. Mol. Biol. Lett.* **7**, 889–894 (2002).
431. Wei, M. *et al.* Lactoferrin-modified PEGylated liposomes loaded with doxorubicin for targeting delivery to hepatocellular carcinoma. *Int. J. Nanomedicine* **10**, 5123–5137 (2015).
432. Bourseau-Guilmain, E. *et al.* Development and characterization of immunonanocarriers targeting the cancer stem cell marker AC133. *Int. J. Pharm.* **423**, 93–101 (2012).
433. Béduneau, A. *et al.* Brain targeting using novel lipid nanovectors. *J. Control. Release* **126**, 44–49 (2008).
434. Formica, M. L. *et al.* Novel hybrid lipid nanocapsules loaded with a therapeutic monoclonal antibody – Bevacizumab – and Triamcinolone acetonide for combined therapy in neovascular ocular pathologies. *Mater. Sci. Eng. C* **119**, 111398 (2021).
435. Perrier, T., Saulnier, P., Fouchet, F., Lautram, N. & Benoît, J. P. Post-insertion into Lipid NanoCapsules (LNCs): From experimental aspects to mechanisms. *Int.*

- J. Pharm.* **396**, 204–209 (2010).
436. Vonarbourg, A., Passirani, C., Saulnier, P. & Benoit, J. P. Parameters influencing the stealthiness of colloidal drug delivery systems. *Biomaterials* **27**, 4356–4373 (2006).
437. Sun, K., Bligh, S. W. A., Nie, H. L., Quan, J. & Zhu, L. M. Lectin recognizing thermoresponsive double hydrophilic glycopolymer micelles by RAFT polymerization. *RSC Adv.* **4**, 34912–34921 (2014).
438. Roger, E., Lagarce, F. & Benoit, J. P. The gastrointestinal stability of lipid nanocapsules. *Int. J. Pharm.* **379**, 260–265 (2009).
439. Roger, E., Lagarce, F. & Benoit, J. P. Development and characterization of a novel lipid nanocapsule formulation of Sn38 for oral administration. *Eur. J. Pharm. Biopharm.* **79**, 181–188 (2011).
440. Eissa, M. M. *et al.* Miltefosine lipid nanocapsules for single dose oral treatment of schistosomiasis mansoni: A preclinical study. *PLoS One* **10**, 1–22 (2015).
441. Ullio Gamboa, G. V. *et al.* Albendazole-lipid nanocapsules: Optimization, characterization and chemoprophylactic efficacy in mice infected with *Echinococcus granulosus*. *Exp. Parasitol.* **198**, 79–86 (2019).
442. Moretton, M. A. *et al.* A glucose-targeted mixed micellar formulation outperforms Genexol in breast cancer cells. *Eur. J. Pharm. Biopharm.* **114**, 305–316 (2017).
443. Palchetti, S. *et al.* The protein corona of circulating PEGylated liposomes. *Biochim. Biophys. Acta - Biomembr.* **1858**, 189–196 (2016).
444. Pozzi, D. *et al.* Surface chemistry and serum type both determine the nanoparticle–protein corona. *J. Proteomics* **119**, 209–217 (2015).
445. Verderio, P. *et al.* Delivering Colloidal Nanoparticles to Mammalian Cells: A Nano-Bio Interface Perspective. *Adv. Healthc. Mater.* **3**, 957–976 (2014).
446. Kobayashi, H., Watanabe, R. & Choyke, P. L. Improving conventional enhanced permeability and retention (EPR) effects; What is the appropriate target? *Theranostics* **4**, 81–89 (2014).

447. Ngoune, R., Peters, A., von Elverfeldt, D., Winkler, K. & Pütz, G. Accumulating nanoparticles by EPR: A route of no return. *J. Control. Release* **238**, 58–70 (2016).
448. Su, Y. *et al.* Sorafenib-loaded polymeric micelles as passive targeting therapeutic agents for hepatocellular carcinoma therapy. *Nanomedicine* **13**, 1009–1023 (2018).
449. Wei, J. C. *et al.* Sorafenib inhibits proliferation and invasion of human hepatocellular carcinoma cells via up-regulation of p53 and suppressing FoxM1. *Acta Pharmacol. Sin.* **36**, 241–251 (2015).
450. Damiani, E., Solorio, J. A., Doyle, A. P. & Wallace, H. M. How reliable are in vitro IC<sub>50</sub> values? Values vary with cytotoxicity assays in human glioblastoma cells. *Toxicol. Lett.* **302**, 28–34 (2019).
451. Labouta, H. I. *et al.* Understanding and improving assays for cytotoxicity of nanoparticles: what really matters? *RSC Adv.* **8**, 23027–23039 (2018).
452. Zhai, Q. *et al.* Preparation and Optimization Lipid Nanocapsules to Enhance the Antitumor Efficacy of Cisplatin in Hepatocellular Carcinoma HepG2 Cells. *AAPS PharmSciTech* **19**, 2048–2057 (2018).
453. Szwed, M. *et al.* Biological response and cytotoxicity induced by lipid nanocapsules. *J. Nanobiotechnology* **18**, 1–19 (2020).
454. Liu, X. *et al.* Asialoglycoprotein receptor-targeted liposomes loaded with a norcantharimide derivative for hepatocyte-selective targeting. *Int. J. Pharm.* **520**, 98–110 (2017).
455. Sakai-Kato, K. *et al.* General considerations regarding the in vitro and in vivo properties of block copolymer micelle products and their evaluation. *J. Control. Release* **210**, 76–83 (2015).
456. Zhang, G. *et al.* Glucosylated nanoparticles for the oral delivery of antibiotics to the proximal small intestine protect mice from gut dysbiosis. *Nat. Biomed. Eng.* **6**, 867–881 (2022).
457. Owen, S. C., Chan, D. P. Y. & Shoichet, M. S. Polymeric micelle stability. *Nano Today* **7**, 53–65 (2012).

458. Cagel, M. *et al.* Mixed micelles for encapsulation of doxorubicin with enhanced in vitro cytotoxicity on breast and ovarian cancer cell lines versus Doxil®. *Biomed. Pharmacother.* **95**, 894–903 (2017).
459. Ding, Y. *et al.* Soluplus®/TPGS mixed micelles for co-delivery of docetaxel and piperine for combination cancer therapy. *Pharm. Dev. Technol.* **25**, 107–115 (2020).
460. Piazzini, V. *et al.* Enhanced dissolution, permeation and oral bioavailability of aripiprazole mixed micelles: In vitro and in vivo evaluation. *Int. J. Pharm.* **583**, 119361 (2020).
461. Riedel, J. *et al.* Paclitaxel and curcumin co-loaded mixed micelles: Improving in vitro efficacy and reducing toxicity against Abraxane®. *J. Drug Deliv. Sci. Technol.* **62**, (2021).
462. Wang, L. L. *et al.* Preparation and evaluation of curcumin-loaded self-assembled micelles. *Drug Dev. Ind. Pharm.* **44**, 563–569 (2018).
463. Hou, J. *et al.* Improved oral bioavailability and anticancer efficacy on breast cancer of paclitaxel via Novel Soluplus®—Solutol® HS15 binary mixed micelles system. *Int. J. Pharm.* **512**, 186–193 (2016).
464. Li, X. *et al.* Preparation and evaluation of novel mixed micelles as nanocarriers for intravenous delivery of propofol. *Nanoscale Res. Lett.* **6**, 1–9 (2011).
465. Alopaeus, J. F., Hagesæther, E. & Tho, I. Micellisation mechanism and behaviour of soluplus®–furosemide micelles: Preformulation studies of an oral nanocarrier-based system. *Pharmaceuticals* **12**, 1–23 (2019).
466. Shamma, R. N. & Basha, M. Soluplus®: A novel polymeric solubilizer for optimization of Carvedilol solid dispersions: Formulation design and effect of method of preparation. *Powder Technol.* **237**, 406–414 (2013).
467. Altamimi, M. A. & Neau, S. H. Investigation of the in vitro performance difference of drug-Soluplus® and drug-PEG 6000 dispersions when prepared using spray drying or lyophilization. *Saudi Pharm. J.* **25**, 419–439 (2017).
468. Petters, M. & Kasparoglu, S. Predicting the influence of particle size on the glass transition temperature and viscosity of secondary organic material. *Sci. Rep.* **10**,

- 1–10 (2020).
469. Lee, J. Y. *et al.* Soluplus®/TPGSGS-based solid dispersions prepared by hot-melt extrusion equipped with twin-screw systems for enhancing oral bioavailability of valsartan. *Drug Des. Devel. Ther.* **9**, 2745–2756 (2015).
470. Yusuf, O. *et al.* Design and development of d- $\alpha$ -tocopheryl polyethylene glycol succinate-block-poly( $\epsilon$ -caprolactone) (tpgs-b-pcl) nanocarriers for solubilization and controlled release of paclitaxel. *Molecules* vol. 26 at <https://doi.org/10.3390/molecules26092690> (2021).
471. Roger, E., Lagarce, F., Garcion, E. & Benoit, J. P. Biopharmaceutical parameters to consider in order to alter the fate of nanocarriers after oral delivery. *Nanomedicine* **5**, 287–306 (2010).
472. des Rieux, A., Fievez, V., Garinot, M., Schneider, Y. J. & Pr eat, V. Nanoparticles as potential oral delivery systems of proteins and vaccines: A mechanistic approach. *J. Control. Release* **116**, 1–27 (2006).
473. Society, T. A., Rcc, A., Rcc, A. & Iii, P. *Nexavar: EPAR scientific discussion*. *Emea*  
[http://www.emea.europa.eu/ema/index.jsp?curl=pages/medicines/human/medicines/000690/human\\_med\\_000929.jsp&mid=WC0b01ac058001d124](http://www.emea.europa.eu/ema/index.jsp?curl=pages/medicines/human/medicines/000690/human_med_000929.jsp&mid=WC0b01ac058001d124) (2006).
474. Siepmann, J. & Siepmann, F. Mathematical modeling of drug delivery. *Int. J. Pharm.* **364**, 328–343 (2008).
475. Constantinou, C., Papas, A. & Constantinou, A. I. Vitamin E and cancer: An insight into the anticancer activities of vitamin E isomers and analogs. *Int. J. Cancer* **123**, 739–752 (2008).
476. Neophytou, C. M., Constantinou, C., Papageorgis, P. & Constantinou, A. I. D- $\alpha$ -tocopheryl polyethylene glycol succinate (TPGS) induces cell cycle arrest and apoptosis selectively in Survivin-overexpressing breast cancer cells. *Biochem. Pharmacol.* **89**, 31–42 (2014).
477. Shen, H. *et al.* Preparation, characterization, and pharmacokinetics study of a novel genistein-loaded mixed micelles system. *Drug Dev. Ind. Pharm.* **44**, 1536–1542 (2018).

478. Dintaman, J. M. & Silverman, J. A. Inhibition of P-glycoprotein by D- $\alpha$ -tocopheryl polyethylene glycol 1000 succinate (TPGS). *Pharmaceutical Research* vol. 16 1550–1556 at <https://doi.org/10.1023/A:1015000503629> (1999).
479. Gnoth, M. J., Sandmann, S., Engel, K. & Radtke, M. In vitro to in vivo comparison of the substrate characteristics of sorafenib tosylate toward P-glycoprotein. *Drug Metab. Dispos.* **38**, 1341–1346 (2010).
480. Luiz, M. T. *et al.* Docetaxel-loaded folate-modified TPGS-transfersomes for glioblastoma multiforme treatment. *Mater. Sci. Eng. C* **124**, 112033 (2021).
481. Li, D. *et al.* Folic acid modified TPGS as a novel nano-micelle for delivery of nitidine chloride to improve apoptosis induction in Huh7 human hepatocellular carcinoma. *BMC Pharmacol. Toxicol.* **22**, 1–11 (2021).
482. Tekchandani, P., Kurmi, B. Das, Paliwal, R. & Paliwal, S. R. Galactosylated TPGS Micelles for Docetaxel Targeting to Hepatic Carcinoma: Development, Characterization, and Biodistribution Study. *AAPS PharmSciTech* **21**, 1–11 (2020).
483. Assanhou, A. G. *et al.* Reversal of multidrug resistance by co-delivery of paclitaxel and lonidamine using a TPGS and hyaluronic acid dual-functionalized liposome for cancer treatment. *Biomaterials* **73**, 284–295 (2015).
484. Liu, T. *et al.* Mechanisms of TPGS and its derivatives inhibiting P-glycoprotein efflux pump and application for reversing multidrug resistance in hepatocellular carcinoma. *Polym. Chem.* **9**, 1827–1839 (2018).
485. Singla, P. *et al.* Temperature-Dependent Solubilization of the Hydrophobic Antiepileptic Drug Lamotrigine in Different Pluronic Micelles - A Spectroscopic, Heat Transfer Method, Small-Angle Neutron Scattering, Dynamic Light Scattering, and in Vitro Release Study. *ACS Omega* **4**, 11251–11262 (2019).
486. Lu, Y., Zhang, E., Yang, J. & Cao, Z. Strategies to improve micelle stability for drug delivery. *Nano Res.* **11**, 4985–4998 (2018).
487. Zou, Y. *et al.* Polyglycerol Grafting Shields Nanoparticles from Protein Corona Formation to Avoid Macrophage Uptake. *ACS Nano* **14**, 7216–7226 (2020).

488. Dai, Q., Walkey, C. & Chan, W. C. W. Polyethylene Glycol Backfilling Mitigates the Negative Impact of the Protein Corona on Nanoparticle Cell Targeting. *Angew. Chemie Int. Ed.* **53**, 5093–5096 (2014).
489. Tahir, N. *et al.* Microfluidic fabrication and characterization of Sorafenib-loaded lipid-polymer hybrid nanoparticles for controlled drug delivery. *Int. J. Pharm.* **581**, 119275 (2020).
490. Handké, N. *et al.* Elaboration of Glycopolymer-Functionalized Micelles from an N -Vinylpyrrolidone/Lactide-Based Reactive Copolymer Platform. *Macromol. Biosci.* **13**, 1213–1220 (2013).
491. Zhang, Y. *et al.* mPEG-PDLLA Micelles Potentiate Docetaxel for Intraperitoneal Chemotherapy in Ovarian Cancer Peritoneal Metastasis. *Front. Pharmacol.* **13**, 1–12 (2022).
492. Garg, M., Dutta, T. & Jain, N. K. Reduced hepatic toxicity, enhanced cellular uptake and altered pharmacokinetics of stavudine loaded galactosylated liposomes. *Eur. J. Pharm. Biopharm.* **67**, 76–85 (2007).
493. Yousef, S., Alsaab, H. O., Sau, S. & Iyer, A. K. Development of asialoglycoprotein receptor directed nanoparticles for selective delivery of curcumin derivative to hepatocellular carcinoma. *Heliyon* **4**, e01071 (2018).
494. Feng, L. *et al.* Construction of efficacious hepatoma-targeted nanomicelles non-covalently functionalized with galactose for drug delivery. *Polym. Chem.* **5**, 7121–7130 (2014).
495. Sukkar, F., Shafaa, M., El-Nagdy, M. & Darwish, W. Polymeric Nanocarriers for Effective Synergistic Action of Sorafenib Tosylate and Gold-sensitized Gamma Radiation Against HepG2 Cells. *Int. J. Nanomedicine* **16**, 8309–8321 (2021).
496. Kweon, S. *et al.* Liposomes coloaded with iopamidol/lipiodol as a res-targeted contrast agent for computed tomography imaging. *Pharm. Res.* **27**, 1408–1415 (2010).
497. Freag, M. S., Elnaggar, Y. S. R. & Abdallah, O. Y. Lyophilized phytosomal nanocarriers as platforms for enhanced diosmin delivery: Optimization and ex vivo permeation. *Int. J. Nanomedicine* **8**, 2385–2397 (2013).

